# BINARY DROP COALESCENCE IN LIQUIDS

A DISSERTATION
SUBMITTED TO THE FACULTY OF THE GRADUATE SCHOOL
OF THE UNIVERSITY OF MINNESOTA
BY

**Jungyong Kim**

IN PARTIAL FULFILLMENT OF THE REQUIREMENTS
FOR THE DEGREE OF
DOCTOR OF PHILOSOPHY

Ellen K. Longmire, Adviser

MAY 2009

# Acknowledgements

This work would not have been possible without the support and encouragement of my advisor, Dr. Ellen Longmire. I am deeply indebted to my advisor for her helpful advice and guidance. Her stimulating suggestions, encouragement, and professionalism brought me up one step further in my career. I also would like to thank my final oral exam committee, Dr. Paul Strykowski, Dr. Krishnan Mahesh, and Dr. Jian Sheng for their helpful comments.

I want to thank my colleagues in Longmire group for their help and support: Neelakantan Saikrishnan, Matthew Stegmeir, Qi Gao, Dr. Cecilia Ortiz-Duenas, and Devesh Amatya. I also thank Dave Hultman and his workshop staffs for their help in the machine shop. Special thanks to Dr. Steve Anderson from LaVision for his support and valuable suggestions. I am grateful also to my friends in Minnesota. I specially thank to Timothy McCarthy and my friends in D.C. Their unflinching courage and conviction always inspired me to continue to work this study. There are other many friends and colleagues I like to thank. I would like to express my gratitude to all those who gave me the possibility to complete this work. I specially thank to Dr. Hwanil Huh who showed me a vision to study in US.

I cannot end without thanking my parents, on whose constant encouragement and love I have relied throughout the course of this work.

This research was supported from the American Chemical Society, Petroleum Research Fund through Grant 42939-AC9 and the National Science Foundation through Grant CTS-0320327. I also gratefully acknowledge a fellowship from the Korean Science and Engineering Foundation (KOSEF).

This dissertation is dedicated to my parents and their unending love, support and inspiration.

# Abstract

Experiments on binary drop collisions within an index-matched liquid were conducted for Weber numbers (*We*) of 1-50 and collision angles of 15-80° below the horizontal. Drop pairs of water/glycerin mixture were injected into silicone oil and, due to gravitational effects, traveled on downward trajectories before colliding. A dual-field high-speed PIV measurement system was employed to quantify drop trajectories and overall collision conditions while simultaneously examining detailed velocity fields near the collision interface.

In the *We* range examined, for equal size drops, both rebounding and coalescing behavior occurred. The drops coalesced for $We > 10$ and rebounded for $We < 10$, and this boundary was found to be insensitive to collision angle. Coalescence was found to result from a combination of vortical flow within drops and strong drop deformation characteristic of higher *We*. Flow through the centers of opposing ring vortices, strengthened by drop deformation, enhanced drainage of the thin film in the impact region, leading to film rupture and coalescence. The collision angle affected the eventual location of film rupture, with the rupture location moving higher in the thin film region as the collision angle increased. The film rupture location correlated closely with the location of maximum downward velocity in the thin film. The time between collision and rupture increases with *We* until $We = 30$. For $We > 30$, the time decreases as *We* increases.

Unequal size drop collisions with drop size ratios ($D_s/D_L$) of 0.7 and 0.5 were also examined. Coalescence occurs above $We^* = 11$ similar to equal size drops. As drop size ratio decreases, the intervening film deforms more. If the velocity ratio $u_L/u_s < 1$, the deformed interface becomes flat before coalescence. The rupture location varies due to the asymmetry of the drops. As collision offset increases ($B > 0$), the film rupture time is shortened and mixing of the fluid from both drops is enhanced after coalescence.

The presence of tracer particles in the intervening film does not affect the minimum Weber number for coalescence, but the film ruptures earlier compared with cases lacking tracer particles.

# Table of Contents

# Nomenclature

## Roman symbols

| | |
|---|---|
| $We$ | Weber number for equal size drops |
| $We_s$ | Weber number based on the smaller drop diameter (unequal size drops) |
| $We_{avg}$ | Weber number based on the average diameter of the two drops (unequal size drops) |
| $We^*$ | Weber number based on the momentum of drops (unequal size drops) |
| $U_{rel}$ | Relative velocity between approaching drops |
| $U_f$ | Fluid velocity |
| $U_p$ | Particle velocity |
| $D$ | Drop diameter (equal size drops) |
| $D_s$ | Small drop diameter (unequal size drops) |
| $D_L$ | Large drop diameter (unequal size drops) |
| $D_P$ | Particle diameter |
| $B$ | Impact parameter |
| $Ca$ | Capillary number |
| $G$ | Magnitude of the velocity gradient in the driving shear flow |
| $r$ | Radius of the undeformed drop |
| $t$ | Time |
| $t_i$ | Inertia time scale |
| $t_s$ | Surface tension time scale |
| $t_\nu$ | Viscosity diffusivity time scale |
| $t^*$ | Dimensionless time (equal size drops) |
| $t'$ | Time interval from the time at maximum film length |

| | |
|---|---|
| $t^{max}$ | Dimensionless time from when film length is maximum |
| $Re$ | Reynolds number |
| $r_b$ | Bridge radius |
| $V$ | Thinning velocity |
| $h$ | Average film thickness |
| $F$ | Interaction force between two drops |
| $r_f$ | Film radius |
| $R$ | Resistance |
| $C$ | Capacity |
| $F_D$ | Drag force |
| $m_p$ | mass of particle |
| **R** | Correlation function |
| $I$ | Pixel intensity |
| $\Delta s$ | Particle image displacement |
| $F\#$ | Focal number |
| $x, y$ | Cartesian spatial coordinates |
| $x_c, y_c$ | Drop centroid coordinates |
| $Vol$ | Drop volume |
| $S_d$ | Surface area of drop |
| $S_E$ | Surface area of equivalent spherical drop |
| X | Projection of the distance between the centroid of each drop normal to the direction of the relative velocity |
| $C_D$ | Drag coefficient of drop |
| $R^*$ | Dimensionless film rupture location |

## Greek Symbols

| | |
|---|---|
| $\rho_d$ | Drop Density |
| $\rho_p$ | Particle Density |
| $\sigma$ | Interfacial tension |
| $\mu_s$ | Dynamic viscosity of the suspending fluid |

| | |
|---|---|
| $\mu_d$ | Dynamic viscosity of the drop fluid |
| μ | Film viscosity |
| ν | Kinematic viscosity |
| $n$ | Refractive index |
| $\tau_p$ | Particle time constant |
| $\theta$ | Collision angle |
| α | Stereo camera tilting angle |
| $\omega_z$ | Vorticity in z-direction |

# List of Tables

# List of Figures

# Chapter 1

# Introduction

## 1.1 Motivation

When liquid volumes collide in a gas or liquid where interfacial tension exists, they can either coalesce or disperse. Collisions between liquid drops occur in atmospheric raindrop formation (Abbott 1977, Whelpdale and List 1971), spray combustion (Faeth 1977, O'Rourke and Bracco 1980), and liquid-liquid extraction processes. The following are some examples of practical coalescence applications.

Coalescence in liquid/liquid mixtures occurs in many practical applications involved in the manufacture, transport, mixing, polymer blending, and separation of petroleum, chemical, food, and waste products. Crude oil pumped from a well, for example, exists initially in the form of an oil-water mixture due to the presence of natural surfactants in crude oil. The oil and water must be separated before the oil can be transported to a pipeline or a tanker. Currently, petroleum companies rely on systems that incorporate gravity, surfactants, centrifugation, and electric fields to destabilize and separate water from the oil. In the absence of other effects, water drops settle to the bottom of the container due to density differences. Eventually the individual droplets merge or coalesce to form larger drops. The larger drop size enhances the gravitational separation force and increases separation rate. In general, the system size and its cost depend directly on the separation rate that can be achieved. In order to improve cost effective production, it is key to understand the characteristics of coalescence.

Coalescence occurs within chemical wastes from a wide range of industries. These

wastes are byproducts from steel, aluminum/metal, textile, and petrochemical processes contain emulsions. Vegetable oil extraction, such as palm oil processing, is another good example of a source of this waste. To separate these wastes, chemical demulsifiers are added. Emulsions of fine droplets are generated to enhance the rate of mass transfer of a chemical between liquids. After the mass transfer takes place, the liquids must be separated, and therefore coalescence is necessary.

Understanding coalescence has been one of most challenging problems in fluid dynamics. It occurs when inertia drives two volumes of fluid toward each other. These two volumes could be either separate drops or one drop and a larger fluid volume with a nominally flat interface. When drops collide, they typically deform and a thin film of liquid remains between them. This film must drain away before the bodies can merge. For the film drainage, the inertia must persist over sufficient time in order to overcome the surface tension acting to restore the initial curvature. When the film thickness between the drops becomes small enough, the neighboring interfaces merge so that the drops coalesce.

The coalescence process is difficult to characterize because the flow behavior is typically highly complex, three-dimensional, and unsteady. The coalescence frequently encompasses a wide range of time and length scales coupled in a nonlinear way. While the drop size and its trajectories are of macroscopic scale, the thickness of film between colliding drops becomes submicroscopic. Mackay and Mason (1963) showed that the critical film thickness for coalescence of colliding drops in air is on the order of $10^2$ Å. Colliding drops will actually coalesce only under certain physical conditions that allow the film thickness to reduce to molecular scales and van der Waals forces to become significant.

## 1.2 Previous work

When two drops collide, they may coalesce without deforming, rebound, coalesce after deformation, separate after temporary coalescence near head-on collision (reflexive separation), and separate after stretching coalescence due to an off-center collision (stretching separation). Examples of theses behaviors for Tetradecane drop

collisions in air are shown in Fig. 1.1.

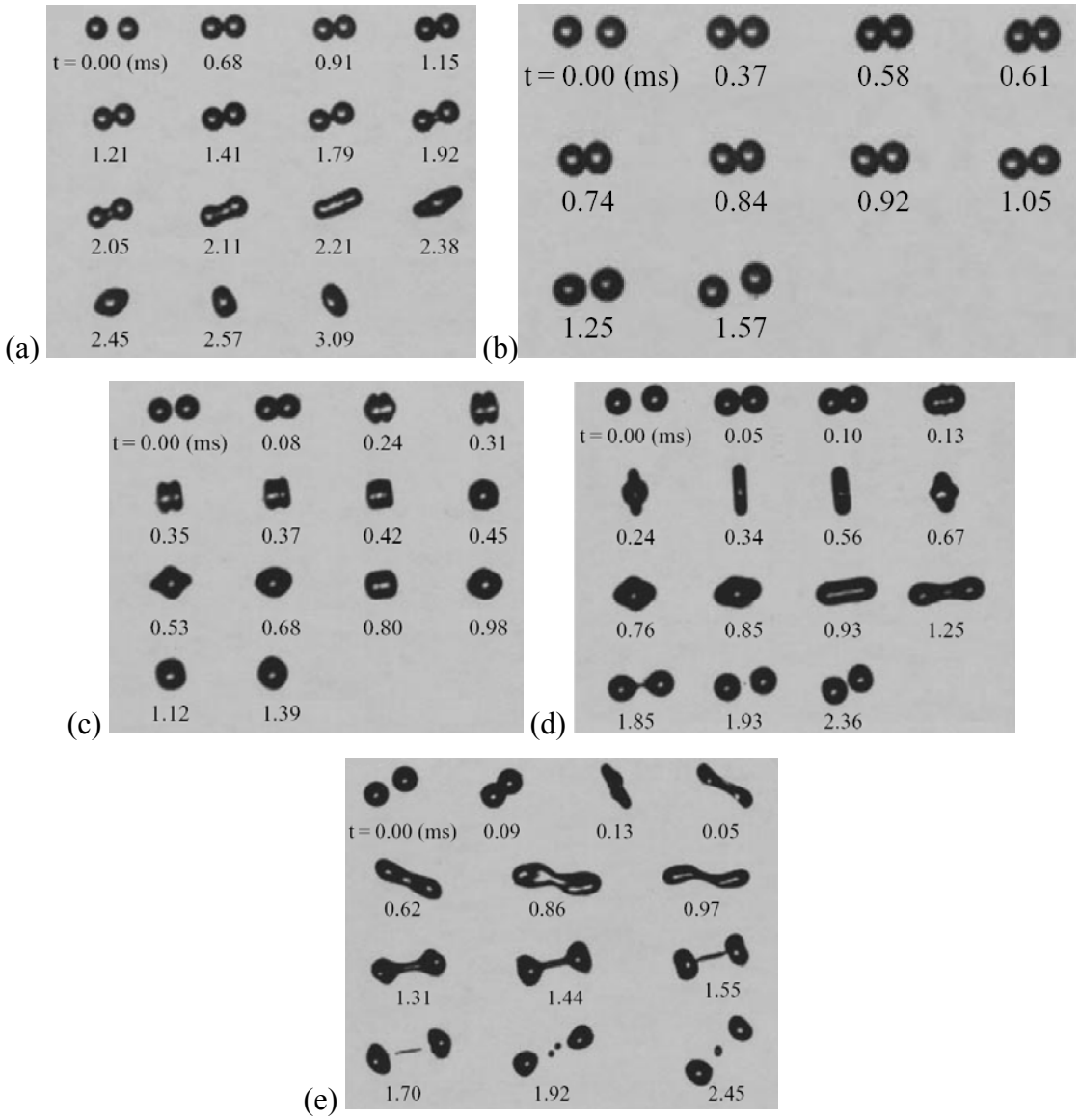


**Figure 1.1** Tetradecane droplet collisions in air (1 atm), (a) Coalescence without deforming, *We* = 0.2; (b) Rebound, *We* = 0.5; (c) Coalescence after deformation, *We* = 19.4; (d) Reflexive separation, *We* = 37.2; (e) Stretching separation, *We* = 60.1 [Images taken from Qian and Law (1997)]

When drops coalesce without deforming as shown in Fig. 1.1a, drop collision is gentle due to low inertia. Drops coalesce due to intermolecular interaction without

deformation. In Fig. 1.1b, rebound occurs even though the inertia is higher than Fig. 1.1a. If the inertia of the drop is sufficient, drops deform after they collide and coalesce when the interfacial film between the drops is drained out as shown in Fig. 1.1c. After drops coalesce into a single drop, the drop oscillates and forms a spherical shape. Some of previous studies defined this regime as 'stable (permanent) coalescence', or coalescence after substantial deformation' (Adam et al 1968, Ashgriz and Poo 1990, Jian et al 1992, Qian and Law 1997). As drop inertia further increases, drops coalesce followed either by reflexive separation into multiple drops for near head-on collision (Fig. 1.1d) or followed by stretching separation into two drops with several satellite drops for an off-center collision (Fig. 1.1e). These regimes are sometimes defined as 'unstable coalescence' because drops coalesce temporarily before they separate into two or more drops. For stretching separation, the kinetic energy of the drop is changed into rotational energy if the drop collision is off-center at sufficiently high inertia. Therefore, the drop rotates, stretches, and finally breaks into two main drops and several satellite drops.

Many previous studies (Adam et al 1968, Ashgriz and Poo 1990, Jiang et al 1992, Qian and Law 1997, Brenn et al 2001, Chen and Chen 2006) characterized the outcome of binary drop collisions in gases based on the value of the Weber number (*We*) and the impact parameter (*B*). The Weber number is defined as,

$$We = \frac{\rho_d U_{rel}^2 D}{\sigma} \tag{1.1}$$

The Weber number quantifies the ratio of inertial to surface tension forces, where $\rho_d$ is the drop density, $U_{rel}$ is the relative velocity between approaching drops, $D$ is the drop diameter, and $\sigma$ is the interfacial tension. Thus, higher *We* values correspond to faster, larger drops with lower surface tension. The impact parameter *B* is the offset distance between approaching drop centers normalized by the drop diameter. Hence, when $B = 0$, the drop collision is head-on, and when *B* is greater than 0, the drop collision is oblique or glancing.

The following literature review divides previous work into experimental,

numerical, and theoretical contributions. Previous experimental research is separated into two sections that consider drop collision in gases and in liquids.

### 1.2.1 Experiments on drop collision in gases

Early binary drop collision studies were motivated by applications for raindrop formation and spray combustion (Gunn 1965, Adam et al 1968, Whelpdale and List 1971, Brazier-Smith et al 1972, Bradley and Stow 1978, and Brenn and Frohn 1989). Those works focused on collision between water or hydrocarbon drops. Gunn (1965) studied the collision of water drops in air and found that drops rebound at low velocities. He suggested that drops coalesce only if there is sufficient kinetic energy. Adam et al (1968) were the first to investigate the effect of impact parameter on water drop collisions. They showed that the transition of coalescence to reflexive separation depends on Weber number and impact parameter. When increasing the drop momentum ($We$), drops temporarily coalesce followed by separation (unstable). With increasing impact parameter, drops have either reflexive separation or stretching separation. They also found a critical $We$ of 7.6 which represents the boundary between coalescence regime (stable) and separation (unstable), in the range of impact parameters greater than 0.8. Brenn and Frohn (1989) first studied the collision of two hydrocarbon drops (Propanol-2). They generally considered effects of impact parameter, drop velocity, and drop size. Equal sized propane-2 drop collision behaved similar to water drop collisions. With increasing drop momentum, the coalesced drop tends to become longer vertically for head-on collisions. For off-center collisions, as the momentum increases, small satellite drops are formed while the drops were separating, similar to water drop collision. The number of satellite drops increased with increasing kinetic energy.

Binary drop collisions in gases were studied extensively by Ashgriz and Poo (1990), Jiang et al. (1992), and Qian and Law (1997) who observed a variety of collision outcomes, including rebounding and coalescence, over a range of Weber numbers ($We$) and impact parameters ($B$). Ashgriz and Poo (1990) studied water drop coalescence and separation following temporary coalescence. Figure 1.2 shows the

collision outcome for two equal size water drops. In this plot depiction, drop collisions may result in coalescence, reflexive separation, or stretching separation. For $5 < We < 18$, the drops always coalesce. Above $We = 19$ (near head-on collision), drops temporarily coalesce followed by separation. As *We* further increases, the vertically elongated liquid volume breaks into several satellite drops during separation. Stretching separation was observed for higher impact parameters.

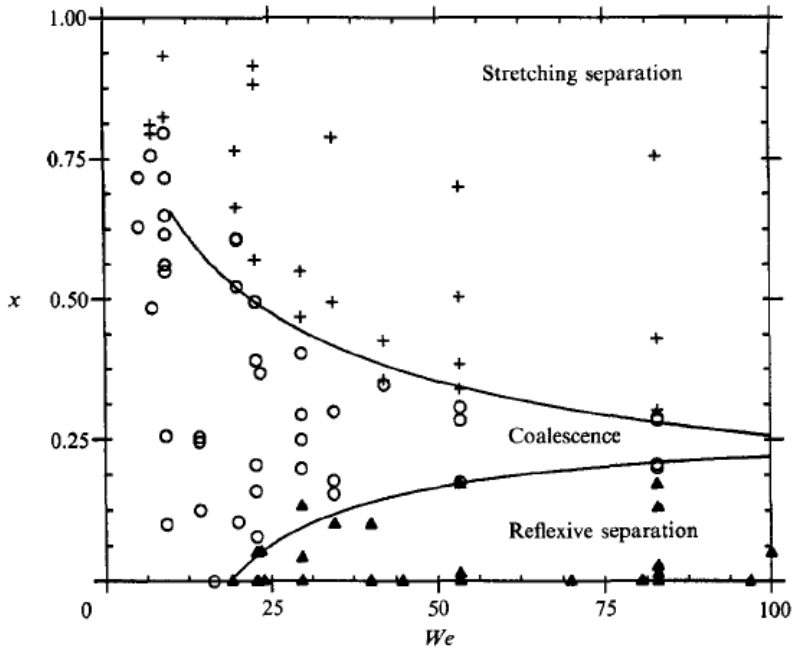


**Figure 1.2** Regions of coalescence, reflexive separation, and stretching separation for water drops. Plot is taken from Ashgriz and Poo (1990).

Jiang et al (1992) quantified hydrocarbon drop collision behaviors and later, Qian and Law (1997) extended the work by varying background pressures, densities, and viscosities. Their works showed that hydrocarbon drop collisions are different from water drop collisions. For water drop collision as shown in Fig. 1.2, the drops always coalesce when *We* is low, up to $We \approx 20$. However, hydrocarbon drops coalesce when $We << 1$ (regime I from fig. 1.3), and then rebound as *We* increases (regime II) (see Fig. 1.2 for water drops and Fig.1.3 for hydrocarbon drops). For head-on collisions with very low *We* as shown in Fig. 1.3, intermolecular interaction causes coalescence. With

this low *We* regime ($We < We_1 = 2.5$ for Tetradecane drops, $C_{14}H_{30}$ in Fig. 1.3), coalescence for head-on collisions could be only observed for hydrocarbon drops. In this *We* regime, Qian and Law (1997) found that water drops did not coalesce unless the impact parameter was greater than zero so that the drops collided off center. This result was not documented by Ashgriz and Poo (1990) (Fig. 1.2). As *We* increased (beyond $We_1 = 2.5$ for Tetradecane drops in Fig. 1.3), drops rebound even though the inertia is higher than coalescence regime I ($We < 2.5$). If the inertia of the drop is sufficient by increasing *We*, drops coalesce with deformation (Regime III). As *We* further increases ($We_3 = 35.5$ for Tetradecane drops in Fig. 1.3), drops coalesce either followed by reflexive separation into multiple drops for near head-on collision (small B) or followed by stretching separation into two drops with several satellite drops for larger B similar to the result from Ashgriz and Poo (1990).

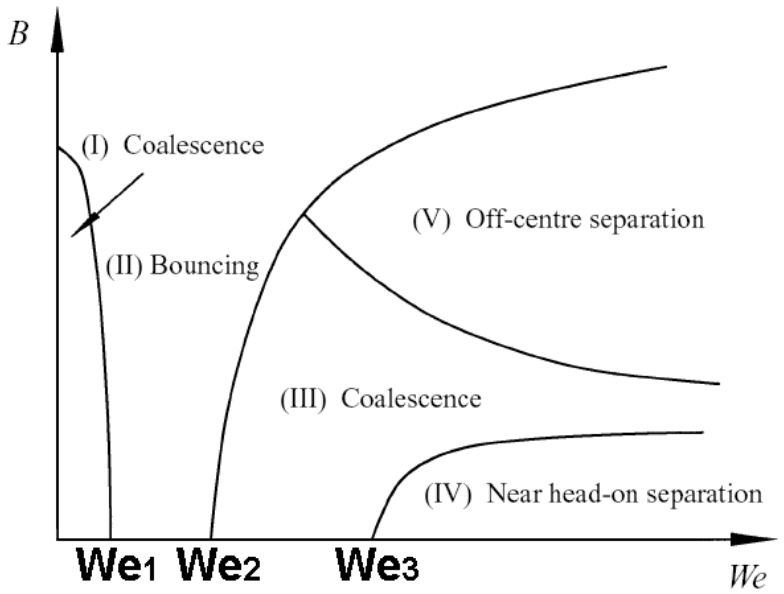


**Figure 1.3** Schematic of various collision regimes of hydrocarbon droplets in 1 atm. air. Plot is reproduced from Qian and Law (1997).

Willis and Orme (2000, 2003) studied the collision of liquid drops with a high viscosity in a vacuum chamber to understand the collision dynamics due to aerodynamic and viscosity effects. Their experiments showed that the order of critical

*We*, between stable coalescence and coalescence followed by separation, was different for hydrocarbon drops and water drops. Water drop collisions have a critical *We* of the order of 100 while the critical *We* of 30 cSt fluid is approximately 3000. As drop viscosity increases, the critical *We* increases. They computed energy dissipation based on kinetic energy and surface energy changes. Changes of the total of kinetic energy and surface energy before collision and the time of maximum deformation were considered. They found that the percentage of energy dissipated increases with increasing fluid viscosity.

Brenn et al (2001) and Brenn and Kolobatic (2006) investigated the formation and breakup of drops in off-center collisions by varying the impact parameter. Based on their experiments, they developed a numerical model of satellite drop formation. They found that the number of satellite drops increases, up to 7 satellite drops, as colliding drop size increases.

Unequal size drops collision

More realistically, drop collision usually occurs between two different drop sizes. However, for unequal size drop collisions, the collision event becomes more complex. Few studies have been conducted with unequal size drop collision. Since size of the drops is different, the Weber number must be modified to characterize the unequal size drop collision. Brazier-Smith et al. (1972) and Ashgriz and Poo (1990) used the smaller drop diameter as the characteristic length. The $We_s$ based on the smaller drop diameter is defined as,

$$We_s = \frac{\rho_d U_{rel}^2 D_s}{\sigma} \tag{1.2}$$

where $D_s$ is the diameter of the small drop. The drop size ratio is defined as $D_s/D_L$. Some people defined the Weber number ($We_{avg}$) for unequal size drop based on the average diameter of the two drops (Orme 1997 and Premnath and Abraham 2005).

Brazier-Smith et al. (1972) used 150-750 μm diameter drops colliding at velocities range of 0.3-3.0 m/s$^2$ ($20 < We_s < 90$). They analyzed the results based on

angular momentum considerations and made an attempt to relate the ratio of drop sizes to the coalescence efficiency (percentage of collisions resulting in coalescence). They found that coalescence efficiency increases with drop size ratio.

Low and List (1982) studied breakup and coalescence of 6 different size ratios of drop pairs ($D_s/D_L$ = 0.22, 0.10, 0.09, 0.40, 0.06, 0.03). They provided the collision outcomes with a wide range of drop ratios for breakup and coalescence. Their experiment showed that coalescence occurs significantly when the small drop is less than 0.06 cm in diameter. Beard, and Ochs (1983) investigated 15 different drop size ratios of drop collision and resulting coalescence efficiency. The drop sizes were in the range of 63-98μm and 11-26μm. The *We* cannot be estimated due to lack of velocity information. The efficiency decreases with increasing small drop size, which agrees with Low and List (1982) and Brazier-Smith et al (1972). They did not provide photographs, but observed coalescence with deformation in their experiment. They conclude that increasing the size of the small drop may cause rebound instead of coalescence with deformation.

Ashgriz and Poo (1990) also investigated the collision of different size drops. They provided the collision outcomes for drop size ratios ($D_s/D_L$) of 0.75 and 0.5, where $D_s$ is the small drop diameter and $D_L$ is the larger drop diameter, and provided photographs of the evolution of collision. Figure 1.4 shows the outcomes of water drop collision for the drop size ratio of 0.5. Overall outcomes in Fig. 1.4 are similar to outcomes in equal size drop collisions (Fig. 1.2). However, Fig. 1.4 (compared to Fig. 1.2 for equal size drop collision) shows that both the reflexive and stretching separation regions become smaller as the drop size ratio decreases. The drops coalesce in a wider range of impact parameter. In Fig. 1.4 the boundary between coalescence and separation shifted to higher $We_s$ when compared to equal size drop collisions (Fig. 1.2). Figure 1.5 shows two examples of unequal size drop collisions. Fig. 1.5a is reflexive separation with *We* = 56 and the drop ratio is 0.5. Fig. 1.5b is coalescence with *We* = 25 and the drop size ratio is 0.6. The color shows the mass transfer between small drop and large drop after collision. The coalesced volume in Fig. 1.5b loses its symmetry and moves in the direction of the larger drop trajectory similar to the result of Brenn and

Frohn (1989). Brenn and Frohn also found that after reflexive separation with generation of small satellite drops, the satellite drops can recombine with the larger drop.

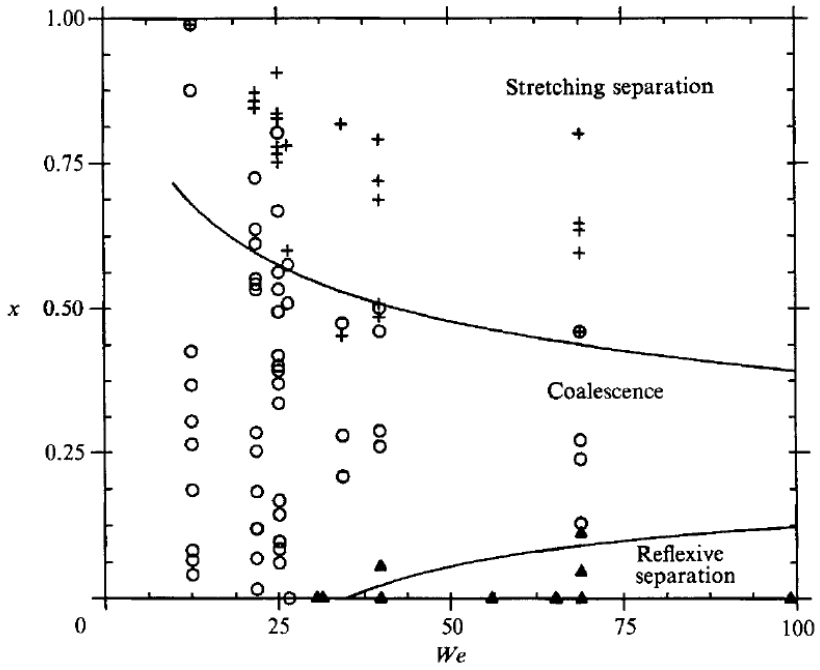


**Figure 1.4** Regions of coalescence, reflexive separation, and stretching separation for drop size ratio, $D_s/D_L = 0.5$. Plot is taken from Ashgriz and Poo (1990).

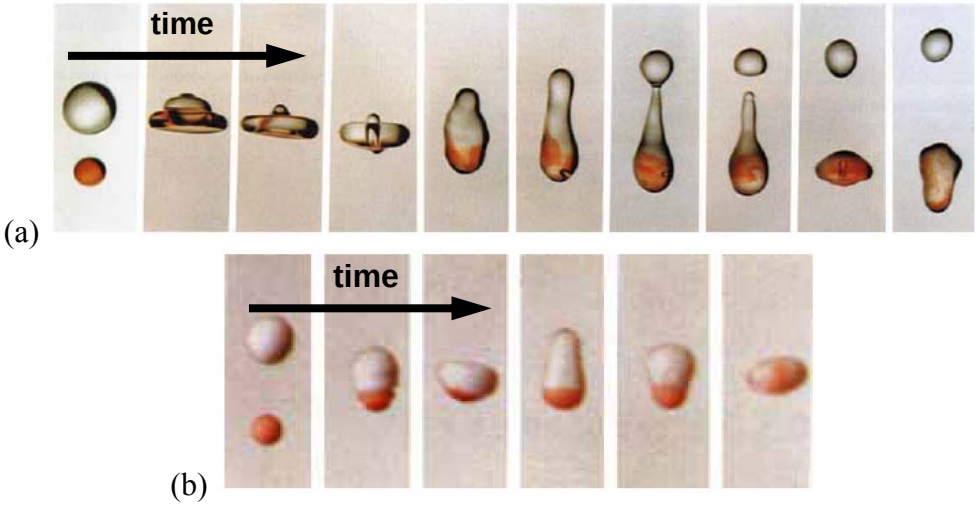


**Figure 1.5** Unequal-size drop collision: (a) Reflexive separation collision, *We* = 56, $D_s/D_L$=0.5 and (b) coalescence, *We* = 25, $D_s/D_L$=0.6. Images are taken from Ashgriz and Poo (1990).

Mass transfer during collision

Ashgriz and Poo (1990) colored one drop to observe the mass transfer between the two drops during the collision event. At $We$ = 23, B=0, a very small amount of mass transfer occurs during reflexive separation. The mass transfer increases with $We$. Authors also found that mass transfer increases with the impact parameter for stretching separation. For higher impact parameters, the colored drop moves to the opposite side after separation. However, for reflexive separation colored drop does not move to the opposite side after separation. Recently, Chen and Chen (2006) studied collisions between equal size diesel oil and water drops using different color dyes. They observed the diesel oil drop moves toward the water drop during collision and eventually they switched their initial positions, which is consistent with the results of Ashgriz and Poo (1990) for stretching separation. Authors also observed the drop switching for rebound and reflexive separation which is not viewed by Ashgriz and Poo (1990). Gerzina (2005) observed this drop position switch for reflexive separation and stretching separation in liquid.

Mass transfer (or dye transfer) can also be observed in reflexive separation for unequal size drop collision (Fig. 1.5). During reflexive separation for unequal size drop collision (Fig. 1.5a), the large drop becomes smaller and small drop becomes larger after collision. Part of the volume of the large drop is transferred to the smaller drop. For coalescence (Fig. 1.5b), the mixing between two drops during the initial period of collision is similar to most of low $We$ equal size drop collisions. As the combined volume oscillates to form a spherical drop, the small drop flows into the large drop and mixing occurs.

### 1.2.2 Experiments of drop collision in liquids

Extensive experiments on binary drop coalescence in liquids have been conducted in flows with negligible inertia ($We << 1$) by Guido and Simeone (1998) and Leal's group (Hu et al 2000, Yang et al 2001, Ha et al 2003, Borrell et al 2004, Yoon et al 2005, 2007). These previous studies used a capillary number ($Ca$) as a criterion for coalescence, where $\mu_s$ is the viscosity of the suspending fluid, $G$ is the magnitude of the

velocity gradient in the driving shear flow, and $r$ is the radius of the undeformed drop.

$$Ca = \frac{\mu_s G r}{\sigma} \tag{1.3}$$

Guido and Simeone (1998) studied two equal size drops (polyisobutylene, PIB) colliding in shear flow. Their *Ca* was fixed at 0.13 (similar to the regime I in Fig. 1.3) and drop radius was 17-20 μm. They studied the collision trajectories and found that the collision in shear generally acted to separate the two drops along the velocity gradient direction. They observed coalescence when the drops were about to separate, but did not provide any extended results in order to understand the coalescence process. Leal and coworkers studied the coalescence of equal-sized polybutadiene (PB) drops in polydimethylsiloxane (PDMS). Typically, the drops impacted and rotated about their center of mass. For their experimental conditions, drop pairs coalesce when collisions are gentle: the drops do not deform significantly (*We* << 1), and coalescence occurs at a point of contact. This is similar to the regime I shown in Fig. 1.3 for *We* << 1. Above *Ca* = 0.012, the drops deformed slightly and moved apart without coalescing. The authors measured film drainage time for head-on collisions and found that the film drainage time at a fixed *Ca* increased with viscosity (Hu et al (2000), Yang et al (2001)). Verdier and Brizard (2002) first quantified local velocity field within drop during a coalescence event by PIV (Particle Image Velocimetry) measurement. For their experiment, polydimethylsiloxane (PDMS) drops (a diameter of ~5-20 μm) collided in polyisobutylene (PIB). The collision was very gentle so that drops did not deform. The authors observed film drainage vectors near a 'neck' (the region where two drops merged. Sometimes it is called 'bridge') from PIV image. However, the time and spatial resolution were limited to determine when and where the thin film ruptured.

Salber (2004) examined drop collisions in liquid at *We* where inertia was significant and observed a boundary between rebounding and coalescence for which *We* was of similar order to that observed for drop collisions in a gas as shown in Fig. 1.6. She found that the boundary between rebound and coalescence shifts to higher *We* with increasing viscosity ratio ($\mu_d/\mu_s$ where $\mu_d$ is the dynamic viscosity of the drop fluid and

$\mu_s$ is the dynamic viscosity of the surrounding fluid). This trend is similar to the result for drop collisions in gas from Willis and Orme (2000). She conducted PIV measurements, but the data was only preliminary to understand the detailed coalescence mechanism.

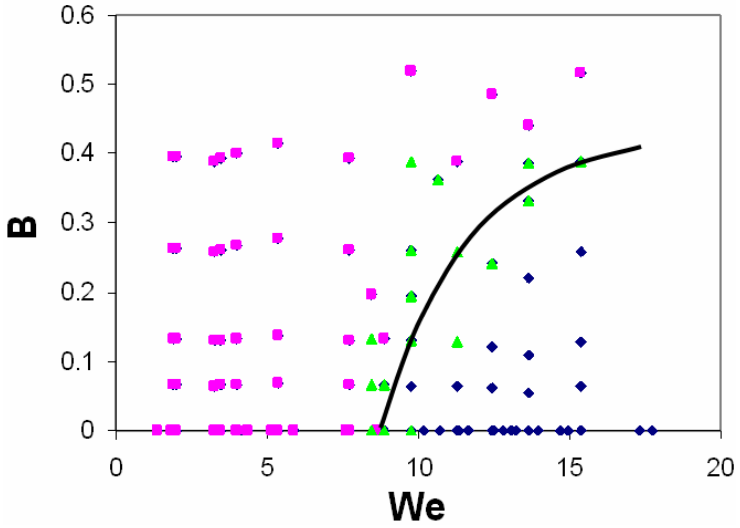


**Figure 1.6** Regions of rebounding (left) and coalescence (right) for $\mu_d/\mu_s = 0.33$. Pink = rebound, blue = coalescence, green = mixed behavior (rebound/coalescence). Plot is reproduced from Salber (2004).

Some researchers studied the drainage behavior of the thin film between two drops in a liquid (Klaseboer et al. 2000, Chevaillier et al 2006, Zdravkov et al 2006). Inertia is negligible in these experiments, so that *We* << 1. Klaseboer et al. (2000) found by comparing experimental data and numerical results that the interfaces of the drops were immobile. Later Chevaillier et al (2006) further studied the influence of mass transfer on the film drainage mechanism. They explained that a different solute concentration at the interface induces an interfacial tension gradient and this gradient enhances the interface thinning or thickening by reducing or increasing the interfacial shear stress. Experiments on single drop coalescence at liquid interfaces showed that the film ruptures when it reaches a minimum thickness of about 10 microns (Charles and Mason 1960, Hartland 1967a, 1967b). Mohamed-Kassim and Longmire (2003) visualized the drop coalescence with index matched fluids and observed that drop

rupture was always off-axis toward the rim of the interface.

### 1.2.3 Numerical studies

Computations of multiphase flows are difficult because conventional continuum models have failed numerically to simulate coalescence. These models interpret the interface between two fluids as a sharp discontinuity in density and stress. Therefore, when the distance between fluid layers is too close, the code blows up and there is no physical way of rupturing an interface. The computations are challenging since the interface is generally evolving and unknown and must be determined in conjunction with the flow field. Also, the highly complex, three-dimensional, and unsteady flow during the coalescence event make the numerical simulation quite difficult and challenging. Drop coalescence is simulated as the large motion of two volumes of drops and the smaller flow behavior of film drainage between the drops. Various approaches have been developed to overcome multiphase flow computation problems in coalescence. Most numerical studies have been studied using two standard methodologies: front tracking methods and front capturing methods. They differ primarily in the interpretation of boundary conditions on the interface.

Earlier numerical studies of the dynamics of drop collision, with application to the raindrop formation and liquid/liquid dispersion problems, have previously been performed by several researchers (Foote 1975, Tobin et al 1990, Tsouris et al 1994). Essentially models for raindrop formation involve drop coalescence, and it is important to understand the mechanism in order to predict drop growth accurately. One of the earliest numerical studies was conducted by Foote (1975). Foote numerically simulated axisymmetric drop head-on collisions with $We < 5$. In his simulation, after a drop impacted on a rigid wall, it flattened on the bottom and started to bounce upward. He was able to simulate internal motion and forces, and compared the computed drop shape with experimental results. Yet the results are limited, since there is no existing experimental data available to compare the computed internal flow motion inside of the drops. Tobin et al. (1990) numerically studied the drop size dependence of coalescence rate in purely coalescing dispersions (negligible drop break-up). They assumed that

coalescence occurs when the interface film between the drops reaches a critical thickness. They uses cut and connect method to simulate the film rupture. Authors found that the drop size plays an important role in coalescence, the coalescing rate increase as the drop size increases.

The front tracking method typically uses an ad hoc cut-and-connect technique such as when two interfaces reach an arbitrary separation, they coalesce. Discrete representation of the interface is employed to track the interface on a grid. This method includes surface marker function to connect the marker particles to determine the boundary. Since the interface is represented more accurately compared to other methods, the surface tension force can be estimated more precisely. However, this method has difficulty dealing with interactions between the topologies of the interface, either coalescence or rebound, because there is no physical way to change interface topology (Tryggvason et al. 2001 and de Sousa et al. 2004).

Nobari et al (1996) used the front tracking method to simulate axisymmetric head-on drop collision. They resolved bouncing, coalescence, and reflexive separation cases using a cut-and-connect procedure. They ruptured the interface film between the drops before the separation of two interfaces reaches too close. Therefore the details of the rupturing of the film between the drops were unresolved. They reported that the rupture time depends on how fast the film is drained. In a three-dimensional (3D) simulation, Nobari and Tryggvason (1996) varied the impact parameter at a fixed *We*. They observed rebound for head-on collisions and B = 0.75. Similar to their axisymmetric simulation, details regarding the film rupture could not be resolved because the rupture was simulated by removing the thin layer between the drops. Similar to their axisymmetric computation, they concluded that rupture time was an important factor to determine the collision outcome. Mashayek and Ashgriz (1995) and Mashayek et al (2003) studied binary drop coalescence using the spine-flux method (SFM) for the free surface tracking. A moving grid method was used. The interface is represented as a boundary between two sub-domains of the grid. Changes in the topology of the interface are represented by changes in the shapes of the grid cell near the interface. Mashayek and coworkers showed the liquid drop deformation on a very

low *We* (*We* < 3.2). They found that the initial internal circulation affects the oscillation of the coalesced drop. Dai and Schmidt (2005) used a 3D moving-mesh finite-volume solver to simulate head-on drop collision and compared the results with those of Willis and Orme (2003). In this method, two drops are connected by a bridge as they approach to avoid the singularity problems when drops coalesce. They showed that the maximum deformation increases with increasing Reynolds number.

Front capturing methods, such as the Volume of Fluid (VOF) method and the level set (LS) method, include an additional conservation equation. The interface is represented by capturing it on fixed grid. Sometimes, it is called a fixed-grid method since the grid does not move with the interface. The VOF method uses the volumetric fraction of a given fluid within each grid cell. Cells containing fractional values representing two regions are considered the interface. The VOF method represents surface tension as a boundary condition by taking the product of surface tension and local curvature (James and Lowengrub 2004 and de Sousa et al. 2004). The VOF method is able to preserve overall mass-conservation. However, due to numerical smoothing or limited diffusion of sharp discontinuities near the interface, the accuracy of collision outcomes may be affected. Another front capturing method is the Level Set method (LS). LS method involves the computation of the level set function to describe the interface between two fluids. LS method can easily simulate topology changes in the interface like merging and breaking in both 2D and 3D geometries. However, a major disadvantage of this method is the interface diffusion over several cells resulting in a loss of accuracy (Sethian 1999).

Rieber and Frohn (1995) and Schelkle and Frohn (1995) discussed the numerical techniques for some three-dimensional simulations of binary drop collisions using the VOF method and the lattice Boltzmann model, but did not show any practical results. Recently, Tanguy and Berlemont (2005) simulated liquid drop collisions in gas using the level set method and compared their results with the experimental results of Ashgriz and Poo (1990). The authors simulated coalescence and reflexive separation for axisymmetric head-on collisions. For off-centered collisions, they used a full 3-D configuration.

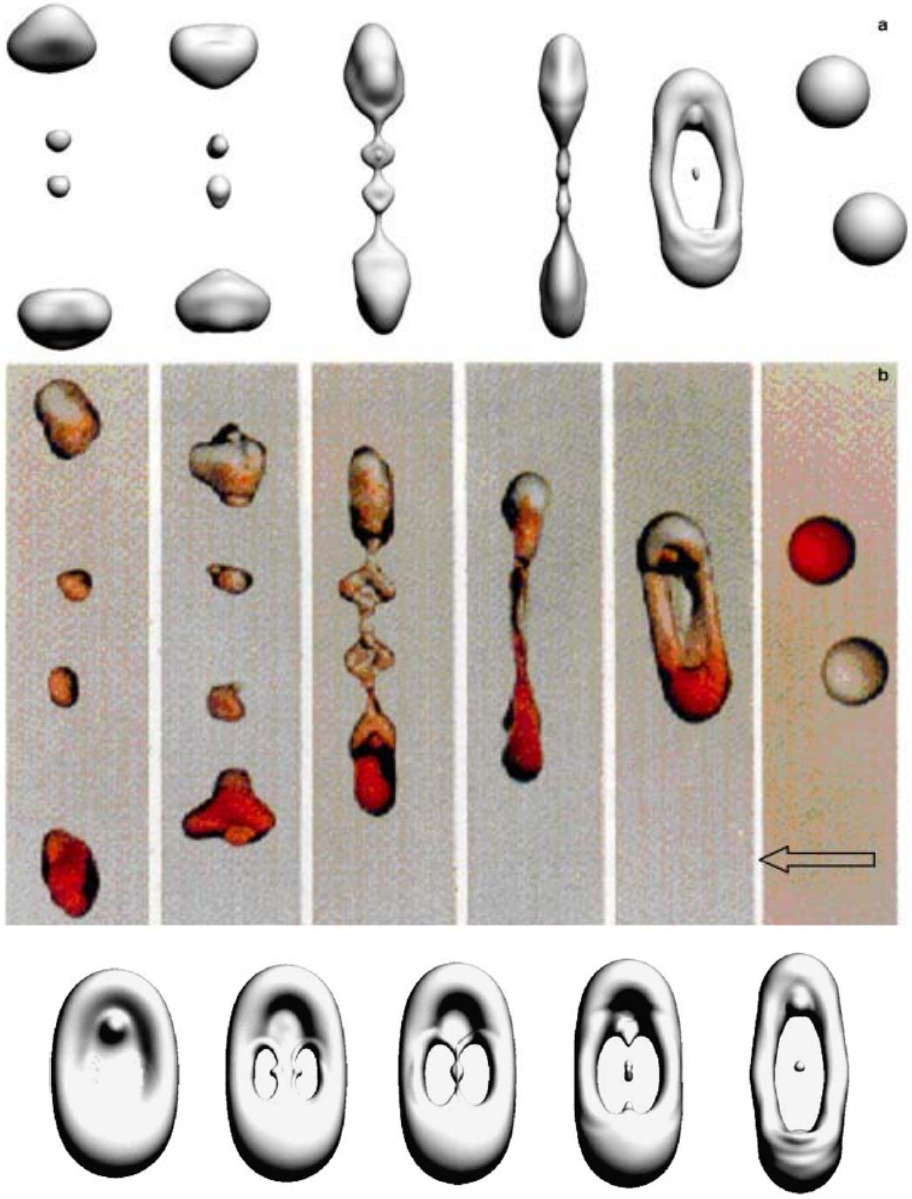


**Figure 1.7** 3D simulation, ethanol droplet, *We* = 60, impact parameter, B = 0.5 (top). Water droplet, *We* = 83, B = 0.43 from Ashgriz and Poo (1990) (middle). Thin membrane break in 3D simulation (bottom). This figure is reproduced from Tanguy and Berlemont (2005).

Figure 1.7 shows an example of their simulation. The drops temporarily coalesce followed by separation into several drops. As shown in Fig. 1.7, the simulation results agree well with the experiment results from Ashgriz and Poo (1990).

They also observed the thin membrane break in the three-dimensional simulation for coalescence followed by separation, which was not observed in the results from Ashgriz and Poo (1990), as shown in Fig. 1.7 (bottom). Their 2D and 3D results using the level set method agreed well with experimental results. However, limitation of the grid size in this simulation failed to conserve mass in their 3D computation. The lack of mass conservation is a severe limitation of the level set method. Pan and Suga (2005) also performed 3D dynamic simulations of binary drop collisions using the level set method. They investigated the complete process of water drop and Tetradecane drop collisions in nitrogen gas for a wide range of the Weber numbers and impact parameters. They compared their results with Ashgriz and Poo (1990) and Qian and Law (1997). Their results for the macroscopic dynamics of drop collision are consistent with experimental results. However, similar to Tanguy and Berlemont (2005), the mass loss during rebounding was noted in this simulation. Also, the computation failed to simulate the regime of coalescence with minor deformation (similar to regime I in Fig. 1.3) due to absence of the intermolecular forces.

The above methods are generally based on solution of the continuum-based Navier-Stokes equations coupled with a representation of the interface. However, when the surfaces of two drops approach to within microscopic scales, the intermolecular forces between the drops become important, and the continuum assumption may no longer be valid. The Lattice Boltzmann method (LBM) uses the lattice Boltzmann equation which represents a kinetic equation to describe the microscopic particle interactions. The behavior of particles corresponds to the dynamics of fluid motion. LBM can simulate intermolecular force interactions. Post and Abraham (2002) studied binary drop collisions in diesel sprays. They calculated the collision frequency based on the number density and relative velocity of the drops. Their numerical model showed the outcomes of bouncing, reflexive separation, and stretching separation. The shattering of colliding drops was observed for high *We*, in which numerous tiny drops are formed from the interfaces of the drops. However, this shattering was not observed in previous experiments (Ashgriz and Poo 1990, Qian and Law 1997). Premnath and Abraham (2005) computed drop collisions using a lattice Boltzmann Method. They

showed coalescence with small deformation (similar to regime III in Fig. 1.3) and reflexive separation with or without the formation of satellite drops. They also simulated off-center collisions. The results were in good agreement with experiments seen in Ashgriz and Poo (1990) and Qian and Law (1997).

Meleán and Sigalotti (2005) applied the smoothed particle hydrodynamics (SPH) method to simulate van der Waals forces and liquid drop coalescence in axisymmetric geometry. The SPH method is a grid-free method capable of computing large surface deformation problems, such as a single drop coalescing at an underlying surface and binary drop collisions. Meleán and Sigalotti (2005) simulated the evolution of drop coalescence in a vacuum for low impact parameter cases. When drops reach a minimum distance, a liquid bridge connects the drops and broadens in a similar way to the Dai and Schmidt (2005) simulation. The bridge expands faster with increasing *We*.

Unequal size drop collision

Fujimoto et al. (1997) simulated equal and unequal size drop collisions and showed the time sequence of the velocity vector and pressure contour of liquid drop. They used a single phase 2D MAC type solution method to solve a finite-differencing approximation of Navier-Stokes equations. MAC method is one of the pioneering front capturing methods to predict a moving surface. The drop size ratio was 0.5 and relative velocity was 2 m/s ($We_s$ = 20.2). The velocity of the large drop is much faster than of small drop (about 8 times higher). Figure 1.8 shows that, unlike equal size drop collisions where the thin film is flat, the film drains at an angle toward the upper and lower sides of small drop (t = 0.5 and 1.0). The curvature of the coalesced volume changes completely from one side to the opposite side between t = 1.5 sec and t = 3.0 sec. This is because the larger drop still has enough inertia after collision to lead the coalesced volume in the direction of the initial larger drop trajectory. The coalesced volume becomes cylindrical for t = 4.0-6.0.

Unequal size drop simulation is difficult because the collision involves asymmetric evolution. Unlike equal size drop collision, the interface film between the drops is not symmetric due to asymmetric drop collision. Numerical computations are

usually performed with fixed coordinates based on an assumption of symmetric evolution.

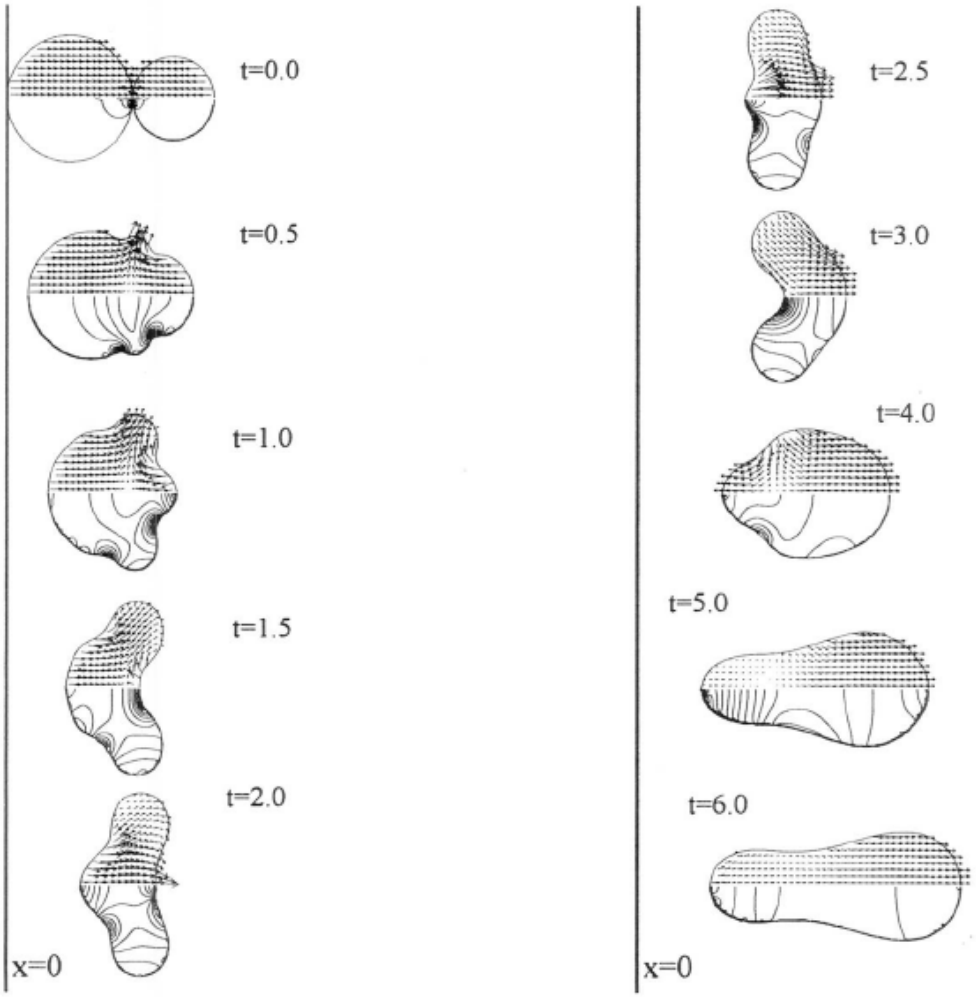


**Figure 1.8** Collision behavior of unequal size drop collision: $D_s/D_L$ = 0.5, relative velocity is 2 m/s ($We_s$ = 20.2). Image taken from Fujimoto et al (1997).

Mashayek et al (2003) used a coordinate shift methodology based on the initial axial velocity of the center of mass to overcome the fixed coordinate problem. The time evolution of unequal size drop coalescence behaves similar to the numerical result from Fujimoto et al (1997). They found that with increasing velocity ($U_{rel}$), the penetration of the smaller drop inside the larger drop become larger. They also investigated the mixing of the fluids between drops by tracing fluid particles. Mass transfer from

increases with decreasing drop size ratio. The majority of mixing occurs during the coalescence process. Mass transfer between drops is small while the coalesced drop oscillates to become spherical.

Premnath and Abraham (2005) simulated unequal size drop collisions (drop size ratio, $D_s/D_L$ is about 0.5) using a lattice Boltzmann model for multi-relaxation-time multiphase flow and compared their numerical results with the Qian and Law (1997 results. The multi-relaxation-time model modifies the standard lattice Boltzmann equation to enable drop collision computation at lower fluid viscosities without increasing the lattice resolution. They examined drop collisions for $We_{avg}$ = 20 and 60. Their computation shows that high pressure develops at the interface between the drops, and causes the interface of the larger drop contacting the smaller drop to curve inward. This curvature trapped gas between the drops, and a small bubble was observed in the coalesced volume. With increasing $We_{avg}$, the larger drop deforms more during collision than the smaller drop. In the $We_{avg}$, where drops separate following coalescence for equal size drops, unequal size drops do not coalesce since a portion of the kinetic energy of the small drop transfers to larger drop. They also reported that at high impact parameters, drops coalesce temporarily and then separate, which is consistent with previous experiments (Brazier-Smith et al 1972, Ashgriz and Poo 1990). Recently, Sakakibara and Ianmuro (2008) simulated unequal size drop collisions in gas using the lattice Boltzmann method for two phase fluid flow with large density ratios. They examined the diameter ratios of 0.5 and 0.25 for $30 < We_s < 140$, and $0 < B < 0.75$. They showed the time evolution of drops and surrounding gas velocity vectors for $We$ = 51.3 but did not provided any additional detail. They also investigated the mixing between drops during collision by tracing and counting fluid particles in drops. They calculated the mixing rate based on counting the number of two different color particles. The mixing rate represents the penetration of small drop fluid into the larger drop. With increasing $We$, the mixing rate for the small drop increases while the mixing rate for the larger drop decreases. This trend is similar to the results observed by Ashgriz and Poo (1990) and Chen and Chen (2006).

Theoretical studies

Several theoretical studies have been conducted to understand the outcomes of drop collision in gas (Eggers et al. 1999, Chesters and Bazhlekov 2000, and Yeo et al. 2003). These studies found that the minimum radius of the bridge connecting the drops varies with time. Eggers et al (1999) investigated the early-time behavior of the radius of the small bridge between drops ($Re << 1$). They observed neck-size evolution and reported that the coalescence may occur at any point along the dimple, the deformed interfacial film between the drops. They also investigated the early time evolution of the shape and proposed a scaling law for the bridge radius and the gap width for early time. The bridge radius $r_b$ follows a scaling law of $r_b \propto \ln(t)$.

The first step of coalescence is the approach and collision of two or more drops. After this step, the surfaces of the colliding drops flatten in the near-contact region, and drainage of the intervening film leads to film rupture. Chesters (1991) reported that collisions do not always result in coalescence and that drop deformation tends to decrease the probability of coalescence. The film drainage is very important process and element of the coalescence mechanism. Reynolds (1886) was the first to develop a drainage time model based on experiments on parallel plane disks. His drainage time was derived as Eq. 1.4 for immobile surfaces and no deformation at the interface.

$$\boldsymbol{V} = -\frac{\boldsymbol{dh}}{\boldsymbol{dt}} = \frac{2\boldsymbol{h}^3\boldsymbol{F}}{3\pi\mu\boldsymbol{r}_f^4} \tag{1.4}$$

where V is the thinning velocity, h is the average film thickness, F is the interaction force between two drops, $r_f$ is the film radius, and μ is the film viscosity. Based on Eq. 1.4, the film thinning velocity increases with increasing film thickness or decreasing viscosity. The mobility of the interface between the drops is also important to determine the film drainage time. If the interface is mobile, the drainage time is shortened. Chesters (1991) reported the approximation of immobile interfaces is valid if the continuous phase contains surfactants in sufficient concentration. Later, Chesters and Bazhlekov (2000) revealed that film drainage was unaffected by the presence of

surfactants which corresponds with the immobile interface assumption matching more closely to experimental results regardless of surfactants. Klaseboer et al. (2000) confirmed the conclusion of Chesters (1991) that the experimental film thickness and the thinning rate were well predicted by the model with immobile interfaces. In this case, Eq. 1.4 can be modified to the following,

$$V = -\frac{dh}{dt} \cong \frac{8\pi\sigma^2 h^2}{3\mu r^2 F} \tag{1.5}$$

where σ is the interfacial tension and r is drop radius. In case of a mobile interface, Chesters (1991) suggested that drainage is controlled by the resistance of the film to deformation or acceleration. Hence, viscosity and inertia needed to be considered for Reynolds' parallel-film model. If the viscosity is dominant, the film thickness is defined,

$$h = h_0 \exp\left(-\frac{t}{t_{ch}}\right) \tag{1.6}$$

where $t_{ch} = 3\mu r/2\sigma$.

If the inertia forces are dominant, Eq. 1.6 is still valid but the characteristic time changes to $t_{ch} = \rho U_{rel} r^2/8\sigma$ where $U_{rel}$ is the relative velocity of the drops. The coalescence efficiency depends on the ratio of two characteristic time scales: the contact time which is mainly controlled by the external flow, and the drainage time of the film thinning between drops until rupture by molecular forces (Chesters 1991).

Film rupture occurs at some point during the film drainage. Yiantsios and Davis (1991) categorized the film rupture mechanism as either "nose rupture" (film rupture on the axis of symmetry) or "rim rupture" (film rupture at the edge of a dimple). Nose rupture occurs when the film thickness is relatively large so that there is no significant deformation or dimple. When dimpling occurs before the film breaks, rim rupture occurs at the rim of the dimple (away from the axis of symmetry). Yeo et al. (2003) also classified the rupture events as rim rupture and nose rupture. Most experiments did not observe the rupture location due to their limited resolution. Some studies showed

rim rupture for a drop coalescing onto a liquid surface (Charles and Mason 1960, Hartland 1967, Mohamed-Kassim and Longmire 2004, Aarts and Lekkerkerker 2008, Lekkerkerker et al. 2008). A few experiments showed a nose rupture for coalescing drops in gas (Kapur and Gaskell 2007, Thoroddsen et al. 2007) with very gentle collisions. For example, in the experiments of Thoroddsen and coworkers, drop velocity was 100 μm/s and the diameters were ≈ 1-4 mm. In these experiments, the drops approach, collide gently, and form a bridge to coalesce, but it is unclear where the film rupture occurs since they do not provide the film rupture location.

For studies on reflexive separation and stretching separation, Roisman (2004) theoretically studied head-on binary drop collision. The model described temporal evolution of the diameter and stretching length. He identified the various stages of the deformation of the collision complex prior to breakup by reflexive separation. The theoretical results were compared with experimental data from Willis and Orme (2000, 2003) and were in good agreement. Ko and Ryou (2005) used results of Ashgriz and Poo (1990) to develop a new model to predict the size and number of satellite droplets in the stretching and reflexive separation regimes. Their model consists of equations derived from the conservation of drop mass, momentum, and energy before and after collision. The results were compared with experimental data (Ashgriz and Poo 1990, Brenn et al. 2001). The number of satellite drops after stretching separation and reflexive separation was in good agreement with the experimental results.

Summary

Previously, some experiments were conducted on liquid drop collisions in gases and in liquids. Most of the experiments on binary drops collision examined collision only. All of the experiments in liquids were with $We << 1$ and therefore negligible inertia similar to the regime I in Fig. 1.3 for drop collisions in gases except those of Salber (2004). Currently there has been little experimental study that viewed the flow in interiors during the collision events (Verdier and Brizard 2002 and Salber 2004). Further, these results had only a limited resolution. Some numerical studies (Fujimoto et al. 1997, Eggers et al 1999, Dai and Schmidt 2005, Meleán and Sigalotti 2005,

Sakakibara and Ianmuro 2008) have viewed the velocity vector distribution within drops. However for most of these studies, the results were limited because the computations had a limited resolution and a singularity problem when drops coalesced. Some numerical studies simulating coalescence in gases (Pan and Suga 2005, Premnath and Abraham 2005, Tanguy and Berlemont 2005) suggested that their simulation could be extended to higher *We* regimes, but currently no liquid-liquid experiment has been conducted to validate such simulations.

## 1.3 Objectives

As mentioned in above paragraph, some experiments and numerical simulations were previously conducted on liquid drop collisions in liquid at very low *We*. Thus far, no experiments quantify inertia-driven binary drop collisions in liquid, and no experiments have shown the internal flow motion within drops during collision events.

The main objective of the current study was to investigate further the regime explored by Salber (2004) specifically to understand the dynamic behavior of coalescing drops and the mechanism behind coalescence in flows with significant inertia. The current study focused on B = 0 and $We > 1$, similar to regimes II and III in Fig. 1.3. In these regimes, the drops deform significantly upon collision, and the internal flow within drops is expected to be significant. The current study will investigate the characteristics of a rebound and coalescence.

The second objective is to provide quantitative test cases useful for the validation of numerical simulation methods. In industrial and environmental applications, accurate predictive models for coalescence or rebound flows are highly desirable because of their great potential for cost savings. A barrier to the development of such models, however, is our current lack of understanding of coalescence transitions in even the simplest flow geometries. Therefore the quantitative measurements of simple coalescence/rebound experiments will not only improve our understanding of the collision behavior but also provide detailed test cases against which numerical models can be compared.

Answers to the following questions are sought:

- How can the collision behaviors be parameterized?
- How does internal drop motion affect the coalescence, and what is the coalescence mechanism?
- How do particles at the intervening film affect the coalescence behavior?
- How is the unequal size drop collision different from equal size drop collision?
- How is off-center drop collision different from head-on collision?

To characterize the drop trajectories and internal circulation patterns through the collision process, effects of the Weber number, collision angle, drop size ratio, impact parameter and presence of contaminant particles will be considered.

To understand the coalescence process, the velocity field near the thin film that separates colliding drops needs to be considered. The thin film has a microscopic length scale, and the drop trajectories span a much larger length scale. A large field of view can observe the drop trajectories of the collision event, but smaller scale flow behavior at the interface cannot be resolved due to the resolution limit. Therefore, a dual-field PIV measurement system was employed to capture both larger and smaller scale fields of view simultaneously. Chapter 2 describes the experimental setup and methods used in this study. The results will be discussed in Chapter 3.

# Chapter 2

# Experimental Methods and Facilities

## 2.1 Drop collision facility

2.1.1 Tank

A plexiglas tank with a cross-section of 203 mm × 406 mm and a height of 305 mm held a layer of silicone oil on top of a layer of water/glycerin mixture. Figures 2.1 and 2.2 show the detailed diagrams of the experimental setup. The height of each layer was approximately 114 mm. The secondary tank has a cross-section of 180 mm × 180 mm and a height of 305 mm and held a drop fluid (water/glycerin mixture). Drop fluid from the secondary tank flows into a pump as described below.

For equal size drop collisions, a magnetic-drive pump (Little Giant, 1.5-MD-SC, 1/30 hp) was used to pressurize the drop fluid (water/glycerin mixture) within the tubes, and a series of needle valves and ball valves were adjusted to control flow rate as shown in Fig. 2.1. For unequal size drop collision as shown in Fig. 2.2, an additional pump (Little Giant, 3-MD-SC, 1/12 hp) and valves separately generated a larger drop. By adjusting valve opening which controls the pressure at the tube location, the velocity of each drop is controlled. A series of ball valves and needle valves downstream of the pump controlled the main pressure. The fluid is separated into two paths with each path having a needle valve and ball valve. The needle valve was used primarily to control precise flow rate while the ball valve was use to control the coarse flow rate. A separate bleed valve was used to ventilate undesired air bubbles in the fluid before it flowed into the solenoid valve. If the air was not removed before solenoid valve, bubbles could be seen in the drop when it was injected from a tube. A drop is injected from a tube by

opening the solenoid valve. The solenoid valve was mainly used to control the size of the drops by controlling the volume of fluid. Adjusting valves to generate proper drop volume and velocity was difficult even though several valves were used to control the fluid. Fluid only flows when solenoid valve is opened. When solenoid valve is not opened, high pressure is built within the tubes. Therefore, a jet of fluid was ejected when the solenoid was first opened. When this fluid formed a drop, a fraction of surrounding fluid (Silicone oil) was trapped in the drop. After a few drops were released from the tube, this phenomenon was no longer observed.

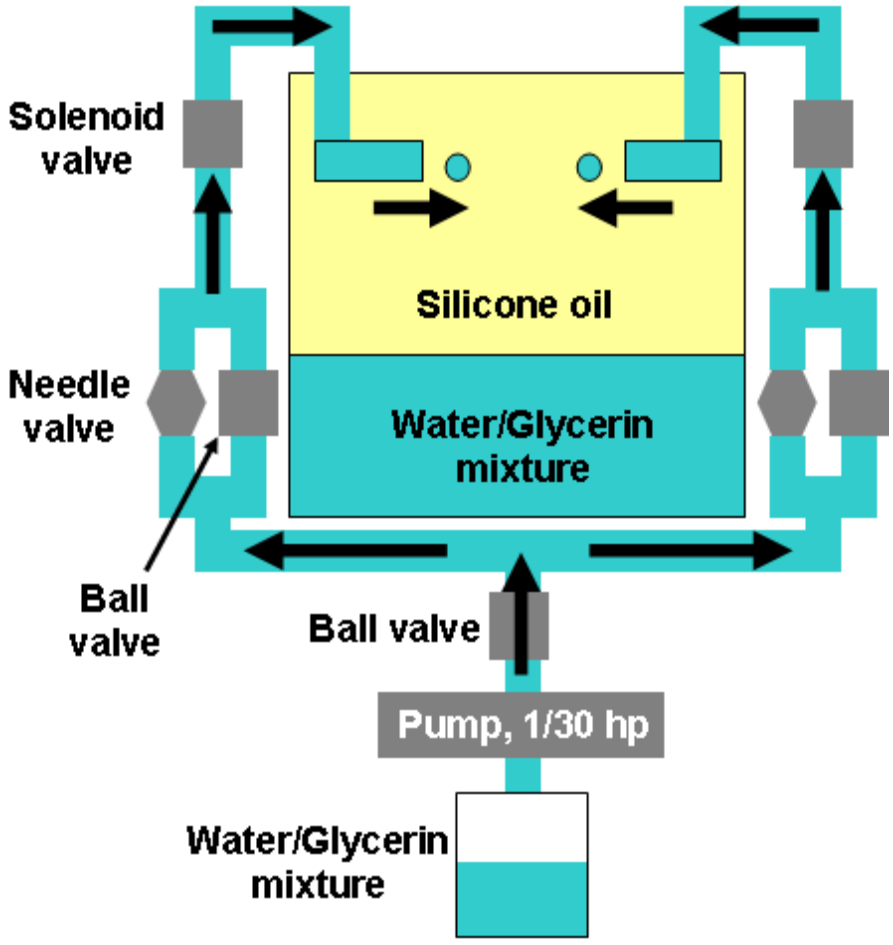


**Figure 2.1** Schematic of flow facility for equal size drop collision

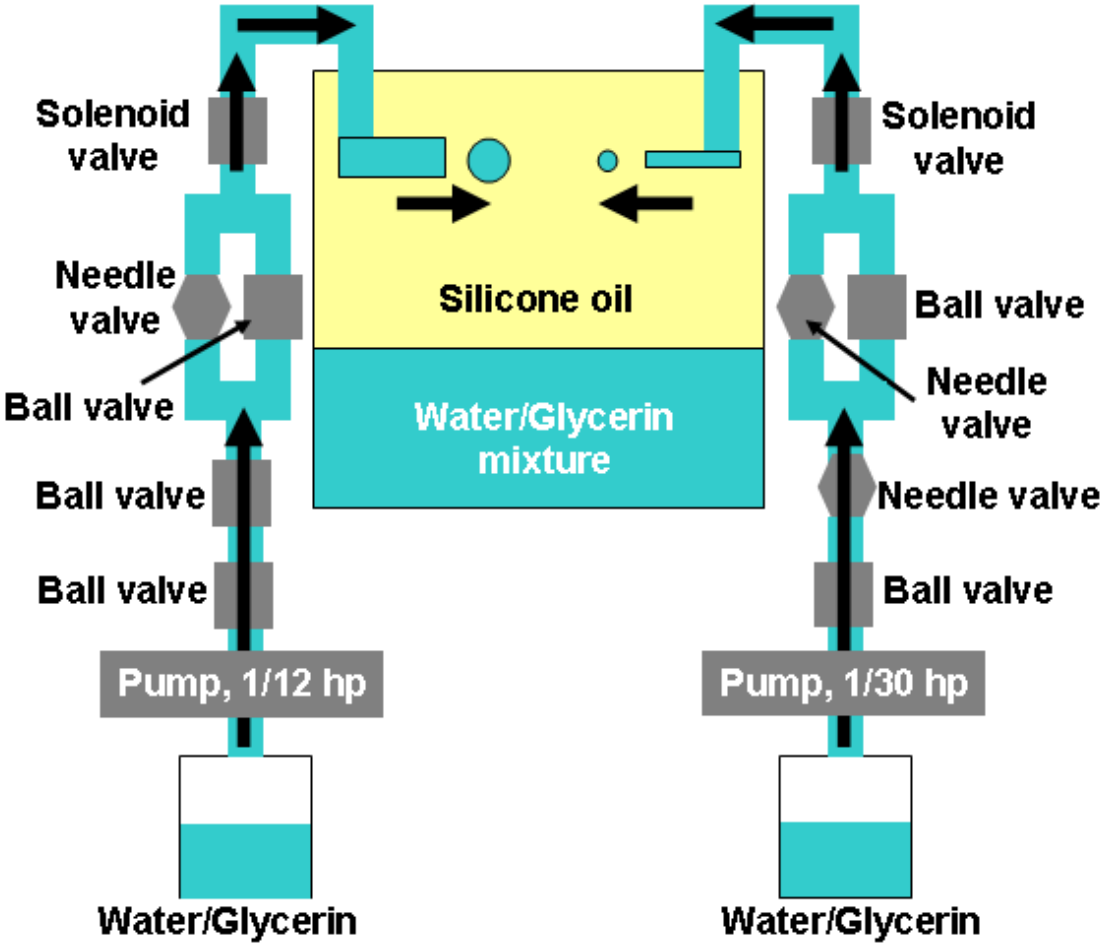


**Figure 2.2** Schematic of flow facility for unequal size drop collision

2.1.2 Drop generator

Two aluminum tubes were directed horizontally and positioned opposite each other in the silicone oil layer to generate drop pairs. The tubes were immersed in silicone oil at least 50 mm below the top of the silicone oil layer to prevent the undesired reflection at the top surface due to laser light. The aluminum tubes were also painted black to minimize the reflection of laser light. For equal-size drop collisions, the inner diameter was 6.1 mm. The distance between the two tubes was adjusted from approximately 56 mm to 80 mm. Translation stages with mounted micrometers allowed a precise adjustment of both tubes as shown in Fig. 2.3.

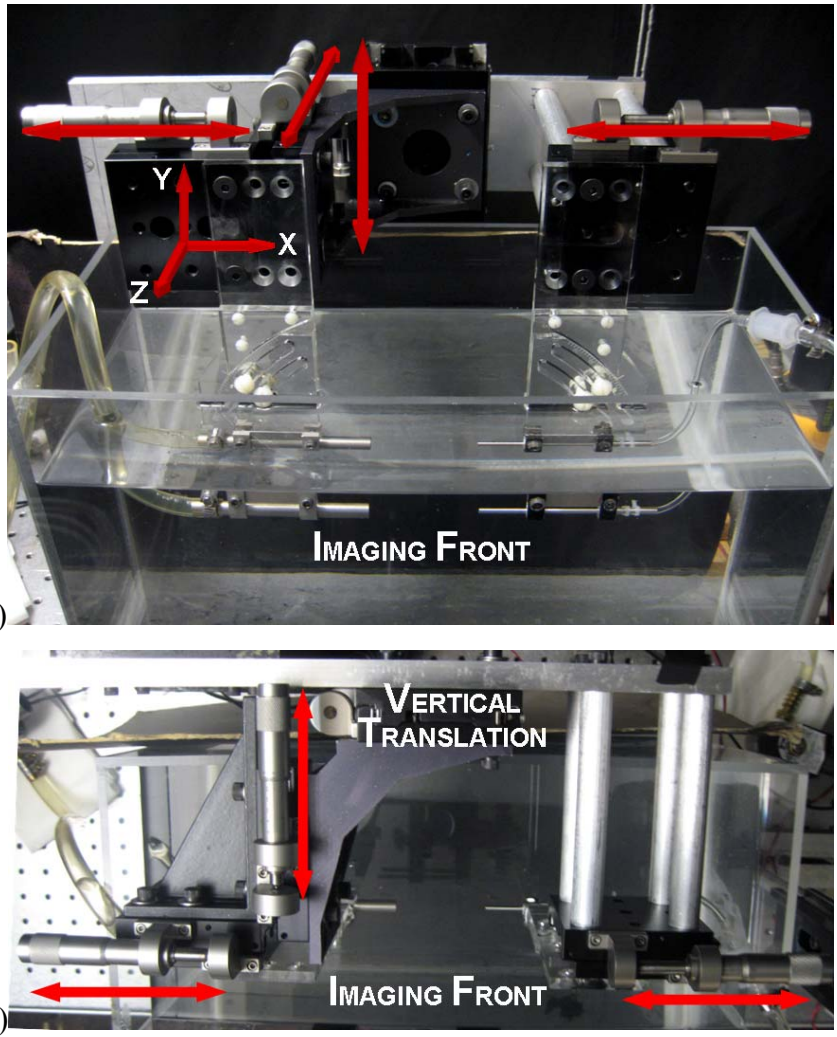


(a)

(b)

**Figure 2.3** Micrometer translation stages; (a) front view, (b) top view

Two horizontal micrometers controlled the tube separation distance. The other micrometer on the top adjusted the out-of-plane translation (z-direction) of the left tube for the drops to collide in the measurement plane. The vertical micrometer controlled the height of the left tube for unequal size drop collisions. The right tube was only adjustable to horizontal direction.

The drop collision angle was varied independently of the Weber number by controlling the angle and separation distance of the drop injection tubes as shown in Fig. 2.4. Injection tube angle was varied from -10° (downward direction) to +15° (upward direction). By adjusting tube separation distance and injection angle, the collision angles were controlled. The tubes were aligned using a precise laser level to achieve a head-on collision. Figure 2.5 shows an image of injection tubes in the fluid tank with camera setup. The setting of the valves and solenoid open time could greatly change the collision behavior at a particular separation distance. For example, if the initial drop velocity is low, the drops move on more downward trajectories and will collide at a slow velocity. To obtain the same drop collision outcome at a higher initial velocity, the tubes would need to be moved closer. Adjustments of the flow rate, solenoid open time, and separation distance were traded off to obtain the desired shape and velocity at collision. If coalescence was desired, drop velocity and open time of solenoid valve (= drop size) were needed to be higher, and separation distance needed to be small. Although these adjustments are dependent on each other, flow rate control is the better option when a large adjustment is desired, while solenoid valve open time contributes a small adjustment.

The drop size was limited by the tube diameter. For unequal-size drop collision experiment, tubes with inner diameter of 2.4 and 4.5 mm (right side) and inner diameter of 8.5 mm (left side) were positioned opposite each other. For the smaller tubes, spherical drops could be obtained only to a certain Weber number, otherwise the drop appeared more like a jet of fluid. To attain larger Weber numbers with a larger tube, the larger pump was used. Since each drop had a different size, each drop had a different trajectory. Due to this reason, tube alignment was more difficult than that for the equal size drop collision. The tube height and injection angle were adjusted separately by

mounted micrometers to have proper drop collisions.

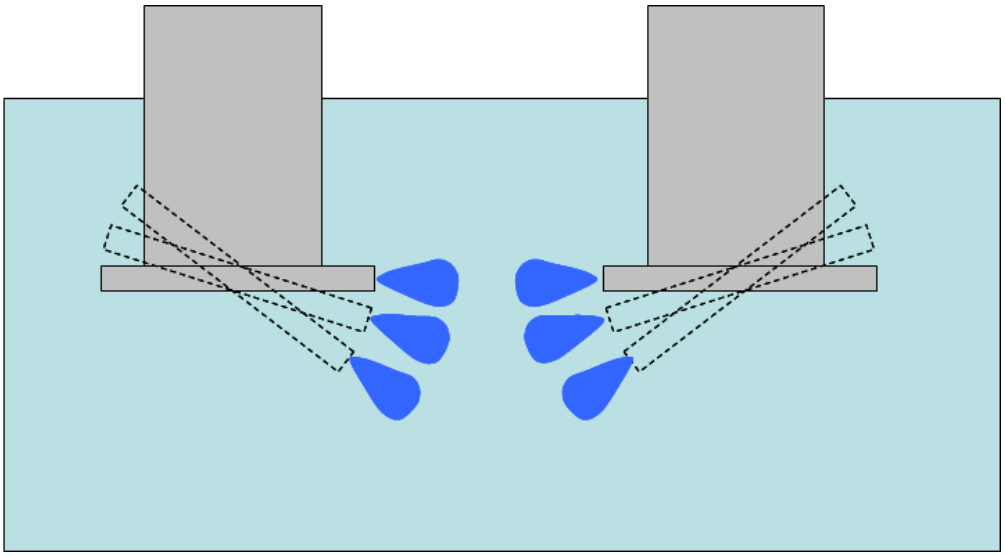

(a) Illustration of trajectory angle variation

(b) Image of trajectory angle adjustment units

**Figure 2.4** Trajectory angle adjustments

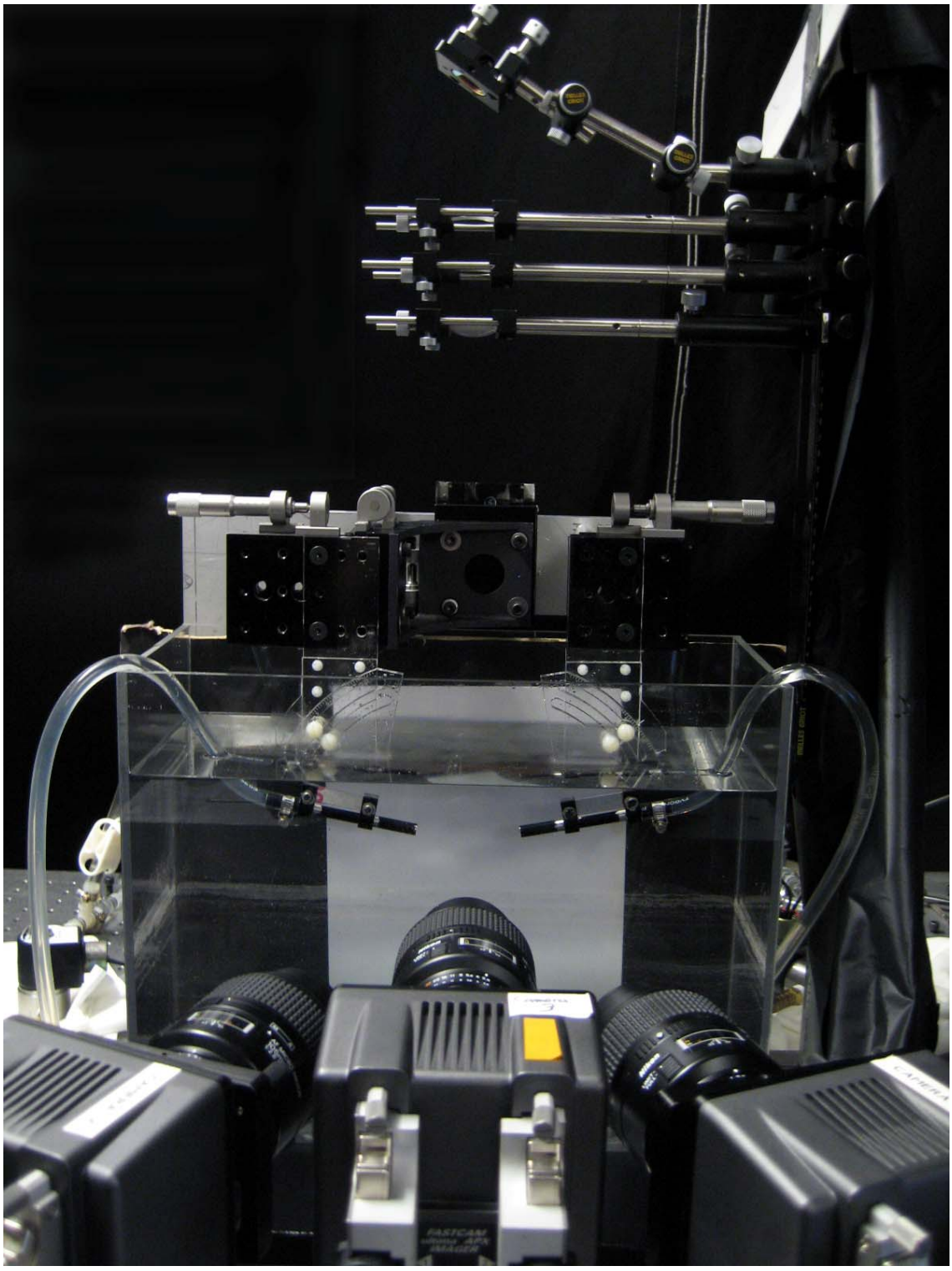

**Figure 2.5** Flow facility with adjustable injection tube

A timing circuit controlled both the opening and closing times of the solenoid valves downstream. A circuit using a 555 monostable timer chip was built to output the necessary signals to operate the solenoid valves for equal size drop collisions (see Fig. 2.6). A switch in the circuit was pressed to open the valves at the desired time. A monostable circuit produced a single pulse when triggered. PNP transistors (2N3055) were added to the circuit to trigger the monostable timer from a rising edge of signal as shown in Fig. 2.7. The open time of the output pulse was calculated from Eq. 2.1.

$$t = 1.1 \times R \times C \tag{2.1}$$

where R is total resistance (Ω) in circuit and C is capacity (F). In Fig. 2.7, the trigger pulse results in a normal ouput pulse with a period determined by t=1.1*RC*. In this case, capacity C was 1 μF and the total resistance R varied in the range of 15 ~ 20 kΩ. The timing capacitance is fully discharged during the trigger pulse as shown in Fig. 2.7. The timing period starts when the trigger input goes high. By adjusting a variable resistance in circuit, the valve open time was controlled (on the order of ~10 ms). For unequal size drop collisions, two separate 555 timing circuits were set up to open both valves at once, yet allow different opening times (Figs. 2.8 and 2.9). A single switch was shared for the two circuits to open both valves at the same time. The capacitance C in each circuit was 1 μF. The range of total resistance R was 32 ~ 40 kΩ for the large drop and 9 ~ 12 kΩ for the small drop. By adjusting the pressure in the tube location and total open time of each valve, the volume and initial velocity of each drop were varied. Typically the circuit was actuated to generate pairs of single drops.

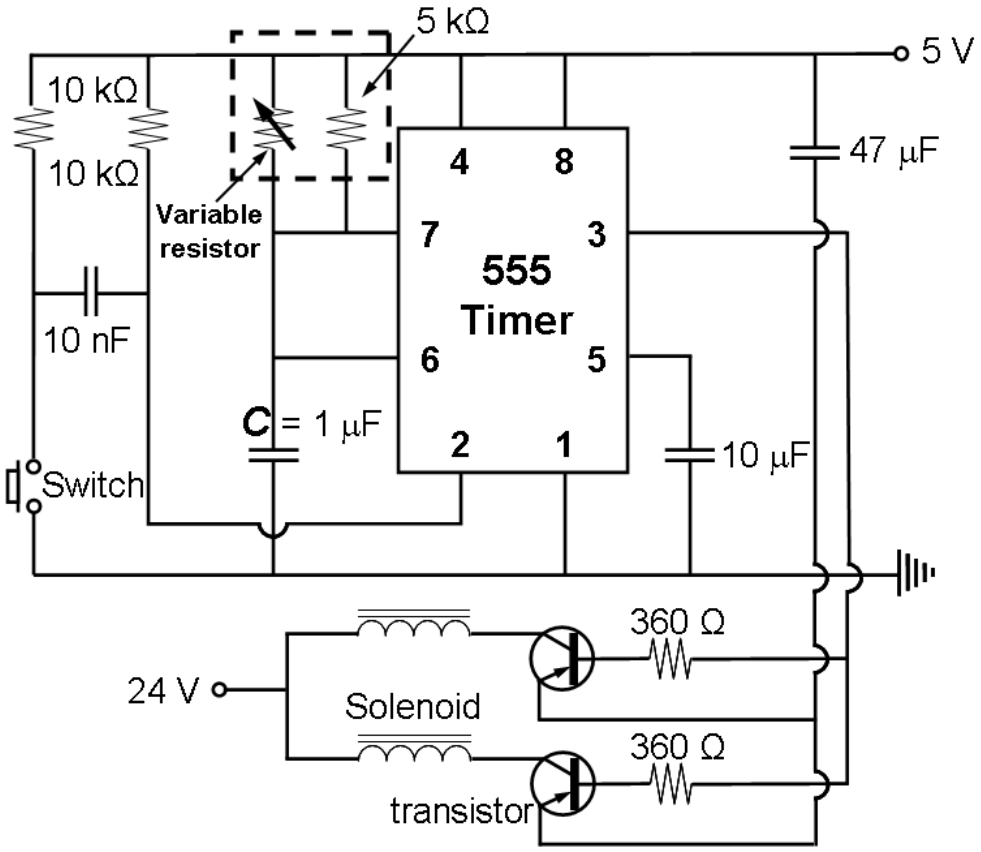


**Figure 2.6** 555 monostable timing circuit diagram for equal size drop collision. Solenoid valve open time, $t = 1.1RC$

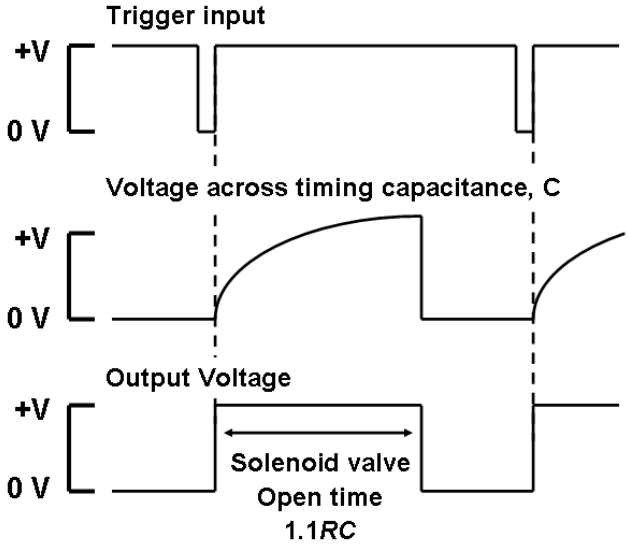


**Figure 2.7** Timing signal diagram for monostable circuit

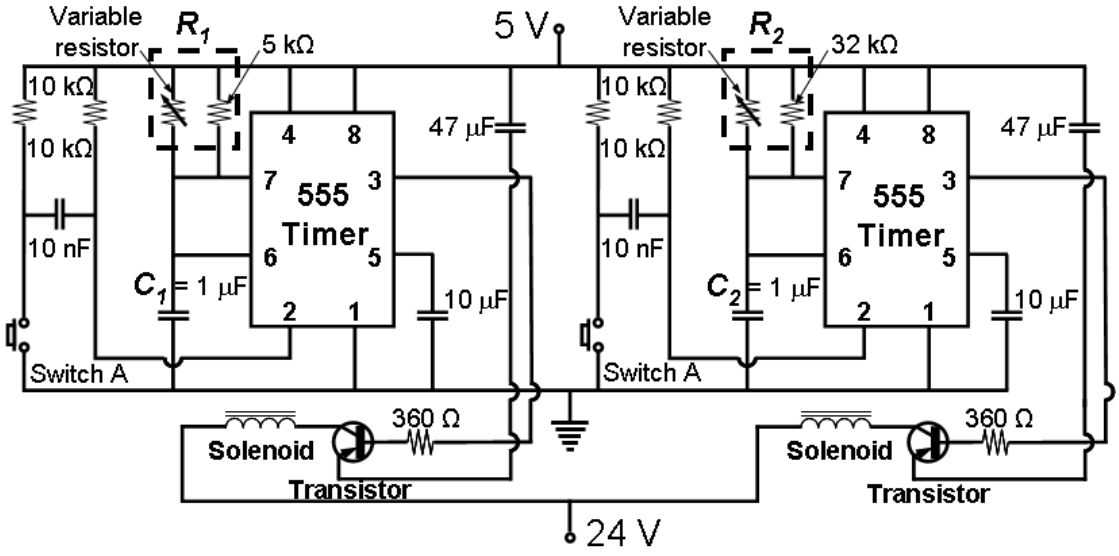


**Figure 2.8** 555 monostable timing circuit diagram for unequal size drop collision. $t_1$ = $1.1R_1C_1$ (the solenoid valve open time for small drop). $t_2$ = $1.1R_2C_2$ (the solenoid valve open time for large drop).

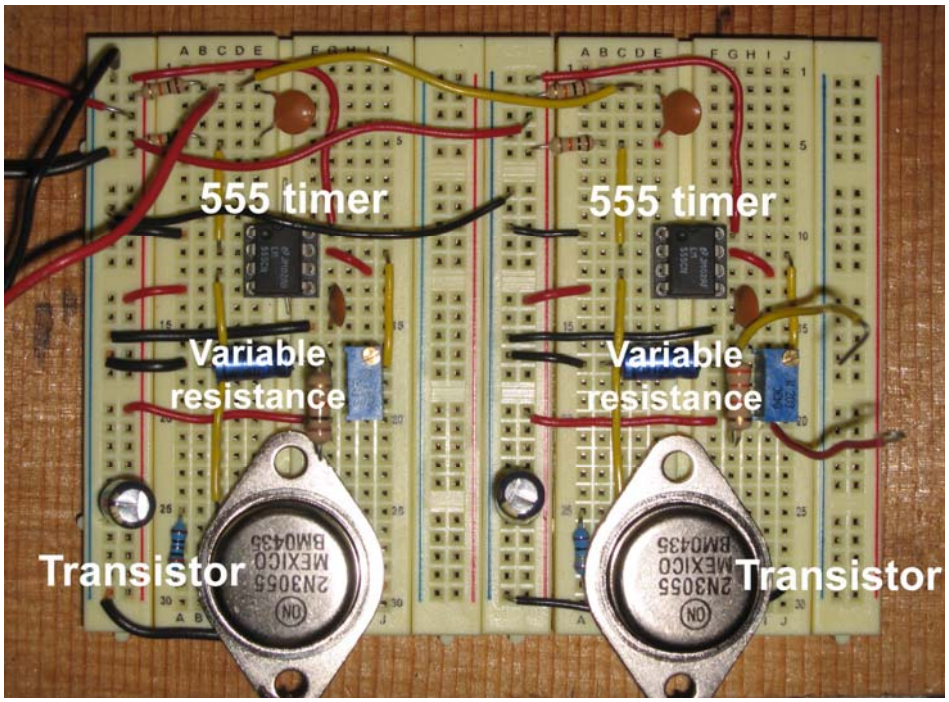


**Figure 2.9** Timing circuit for unequal size drop collision

2.1.3 Fluids

The silicone oil was Dow Corning 200 fluid with viscosity of 50 cS (50 $mm^2/s$). Table 2.1 gives the fluid properties. Some of these properties were obtained from tables in the *CRC handbook of Chemistry and Physics* (Lide 2008). By adjusting the glycerin concentration in the water, the refractive index of the drop fluid was matched with that of the silicone oil to eliminate optical distortion. Therefore velocity variations inside of the drops could be observed. This index matching technique was demonstrated previously by Mohamed-Kassim and Longmire (2003) for multiple drop/ambient viscosity ratios. Water and glycerin were mixed in a graduated cylinder with pre-determined quantities (52 percent water and 48 percent glycerin by volume). A hand-held refractometer (Atago N-2E) was used to measure the index of refraction. Although an error of refractive index is very small (an accuracy of ~ 0.02%), the indices of refraction of liquids were not perfectly matched. When the incident viewing angle was large, the liquid/liquid interface between fluid layers in the tank could be observed due to imperfect indices of refraction. However, PIV (Particle Image Velocimetry) measurements in this study were not affected by this slight mismatch. Surface tension empirically measured by Mohamed-Kassim and Longmire (2003). They found that the particles did not affect the surface tension.

| | **Dow Corning 200 fluid (50 $mm^2/s$ [50 cS])** | **Water/glycerin mixture (46.2% glycerin by volume)** |
|---|---|---|
| Density, $\rho$ ($g/cm^3$) | 0.960 | 1.131 ± 0.001 |
| Kinematic viscosity, $\nu$ ($cm^2/s$) | 0.50 | 0.059 ± 0.001 |
| Dynamic viscosity, $\mu$ (g/cm s) | 0.48 | 0.067 ± 0.001 |
| Refractive index, n | 1.401 | 1.401 ± 0.0004 |
| Interfacial tension, $\sigma$ (mN/m) | 29.5 | |

**Table 2.1** Material properties of fluids

2.1.4 Tracer particles

The accuracy of the velocity field determination is ultimately limited by the

ability of the scattering particles to follow the instantaneous fluid motion. Proper seeding is critical for PIV because PIV required high energy density over a laser sheet using high energy pulse laser and a high spatial concentration of particles to observe sufficient detail in the flow field. Particle size must be small enough to follow the fluid motion and not to alter the flow or the fluid properties. Reducing the particle size improves flow tracking, but reduces light scattering. In this study, titanium dioxide ($TiO_2$) particles of ~1μm diameter (a density of 3.5 g/cm$^3$) were added to both fluids to act as tracer particles for PIV measurement. Based on the assumption of Stokes flow (*Re* << 1), tracer particle motion within the flow can be estimated. The drag force around a spherical particle is derived as Eq.(2.2)

$$\boldsymbol{F_D} = 3\pi\mu_s \boldsymbol{D_p}(\boldsymbol{U_f} - \boldsymbol{U_p}) = \boldsymbol{m_p}\frac{\boldsymbol{dU_p}}{\boldsymbol{dt}} \tag{2.2}$$

where, $\mu_s$ is the fluid viscosity of ambient fluid, $D_p$ is the particle diameter, $U_f$ is the fluid velocity, $U_p$ is the particle velocity, and $m_p$ is the mass of particle. Then, Eq. (2.2) can be rewritten as,

$$\frac{\boldsymbol{U_p(t)}}{\boldsymbol{U_f}} = 1 - \exp\left(-\frac{\boldsymbol{t}}{\boldsymbol{\tau_p}}\right) \tag{2.3}$$

$$\boldsymbol{\tau_p} = \frac{\boldsymbol{D_p^2}\boldsymbol{\rho_p}}{18\boldsymbol{\mu_s}} \tag{2.4}$$

where, $\rho_p$ is the particle density and $\tau_p$ is a particle time constant which represents the time the particles responds to a change in fluid motion. $\tau_p$ must be smaller than the smallest time scale in a flow to ensure that the particle accurately tracks the flow. The particle time constant for $TiO_2$ used in this study was 4 ns; $D_p$ = 1 μm, $\rho_p$ =3.5 g/cm$^3$, $\mu_s$ = 0.48 g/cm s. The smallest flow time scale was of order of 0.1 s. Therefore, it is assumed that particles track the flow well.

A fairly dense particle concentration was required in order to resolve velocity

vectors in small interrogation areas ($0.2 \times 0.2$ mm$^2$ for $16 \times 16$ pixel$^2$) corresponding with the smaller field of view ($\sim 13 \times 13$ mm$^2$). The seeding of fluids was challenging in this experiment. It was difficult to have uniform seeding through the entire fluid layer. $TiO_2$ easily clumped together while mixing in liquids, especially in water/glycerin mixture. If the particles clumped together in liquid, they appear overly bright and large in the PIV image. To prepare the fluid for PIV measurement, water and glycerin were first mixed in gallon bottles. The particles were introduced into a smaller container of water/glycerin. At this stage, a fine strainer lined with cheesecloth was used to break up the initially clumped dry particles before they were added into the liquid. The particles were mixed in the container by stirring with a rod. It has to be mixed very well otherwise the particles clump. Initially mixing particles with a large volume of fluid is inefficient. After a small amount of water/glycerin was seeded, this suspension was poured into the volume of unseeded water/glycerin in the gallon bottle and mixed. Seeding in the silicone oil was easier than in water/glycerin since the particles disperse more easily and mix well. The seeding procedure for silicone oil was exactly the same as for water/glycerin. Note that an electric mixer generated lots of undesired bubbles, especially for viscous silicone oil. These bubbles stayed for several days and made fluid visibly unclear.

The mixed particles in the fluid float for days but then clump together to either float as a group or settle on the bottom of the fluid layer. Also, some particles were trapped in the pump motor and valves. Sometimes particles were intentionally over-seeded in the fluid to achieve a desired particle density for small field of view measurement. If the fluid is too over-seeded, it needs to be left for days until the particles sink to the bottom of the fluid layer to reach the proper particle concentration. If necessary, additional particles were added to either the silicone oil or water/glycerin mixture in the secondary tank. In either case, new particles were mixed with a sub volume of new liquid that was then added to the existing fluid volume. The fluids in the tank needed to be cleaned occasionally. The fluids in the tank were poured into 5 gallon containers through a commercial air filter. This filter generally captures a diameter of $0.3 \sim 1\mu$m particle in air. The air filter did not remove particles except

some clumped groups of particles because the fluid is highly viscous compared to the air. Sometime a peristaltic pump was used to remove the clumped particles or dust in the fluid.

2.1.5 Laser fluorescing dye

The drops were not distinguishable from the silicone oil since the indices of refraction of the two fluids were matched. Hence, the drop fluid was made visible by adding a small amount of Rhodamine 6G ($C_{26}H_{27}O_3N_2Cl$) laser fluorescing dye. The dye is a red powder. It is soluble in water and fluoresces an orange color in a green Nd:YLF laser light (wavelength of 527 nm). Light is absorbed by this fluorescing dye at wavelength ranging from 480 nm to 590 nm. The molecules then fluoresced in the range from 536 nm to 602 nm.

(a) 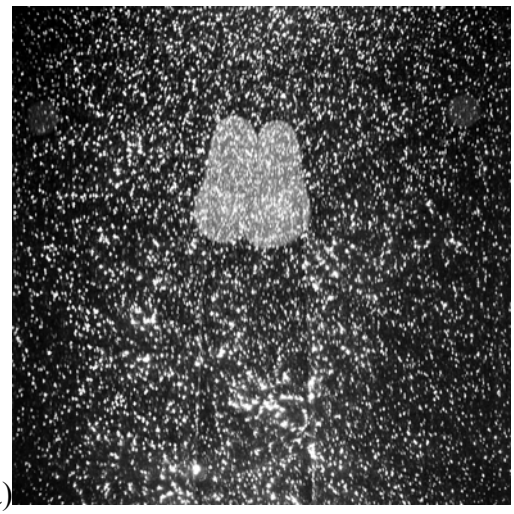 (b) 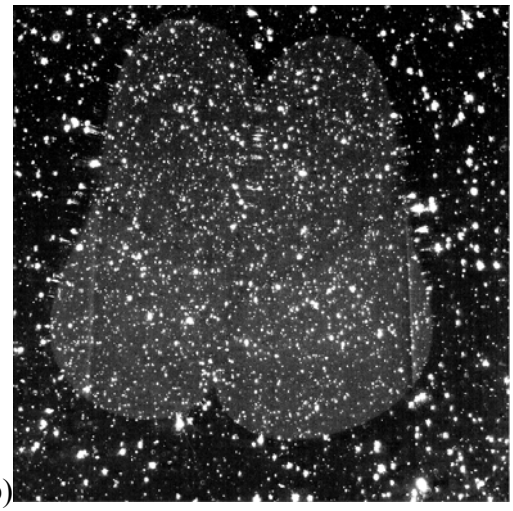

**Figure 2.10** Sample images of fluid mixed with $TiO_2$ tracer particle and Rhodamine 6G laser fluorescing dye; (a) a large field of view, (b) a small field of view. White dots show the $TiO_2$ particles. Grey color shows the drop fluid.

To dye fluid, a small amount of Rhodamine 6G (weight of ~150 mg) was mixed with 100 ml of water/glycerin mixture to make a highly concentrated solution. Using a syringe, one or two drops of this concentrated solution (a volume of ~0.1 ml) was added into water/glycerin mixture in the secondary tank (a volume of ~4800 ml) and stirred

thoroughly. If too much dye is added, an image scatters too much light, and PIV vector computation is difficult to process. In this study, the dye concentration in water/glycerin was approximately $3.1 \times 10^{-6}$ g/cm$^3$. Figure 2.10 shows the sample PIV images with seeded and dyed fluids for both large and small fields of view.

## 2.2 Dual-field Particle Image Velocimetry (PIV)

Particle image velocimetry (PIV) is a method used to measure the instantaneous velocity in the field of interest indirectly. The fluid is seeded with tracer particles which generally follow the flow. Typical PIV require of a high power laser, optics to make a laser light sheet, and a camera. The thin laser sheet illuminates the particles in the fluid, these particles scatter the light, and the camera records this scattered light over short time interval $\Delta t$. The recorded image is divided into a large number of interrogation areas to calculate a displacement by cross-correlation algorithm. The displacement of particles over $\Delta t$ converts to velocity vector.

In this section, the general concept of stereo PIV and the correlation algorithm will be discussed. Then, laser and optic alignment, dual-field PIV camera setup, and calibration technique used in this study will be described.

### 2.2.1 Stereoscopic PIV

Stereoscopic PIV enables one to measure three components of velocity in a plane. Two cameras view a flow field from two perspectives as shown in Fig. 2.11. The two cameras record different images according to their perspective. For example, true velocity vector in Fig. 2.11 will be measured as a projected velocity vector either imaged from the right camera (blue) or from the left camera (red). It shows only in-plane velocity component, but it does not show out-of-plane velocity component. The out-of-plane velocity component can be obtained by reconstructing velocity components based on 2-D velocity components from each camera.

For stereoscopic camera setup, the digital image sensor in camera must be tilted in order to properly focus the entire field of view. A Scheimpflug mount makes it possible to rotate the image sensor into the plane of best focus without moving the

camera lens as shown in Fig. 2.12. The Scheimpflug arrangement allows keeping the plane of best focus in the plane of light sheet while having the camera view the light

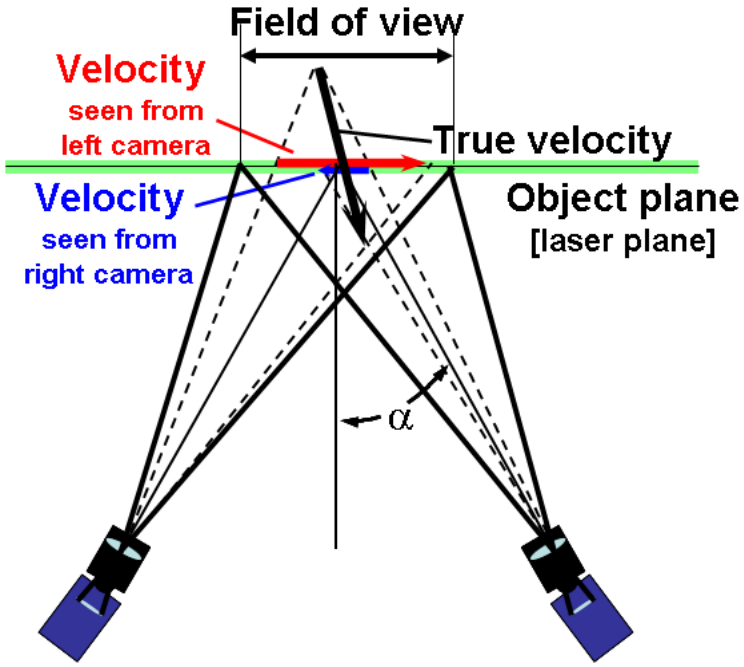


**Figure 2.11** Schematics of stereoscopic PIV setup

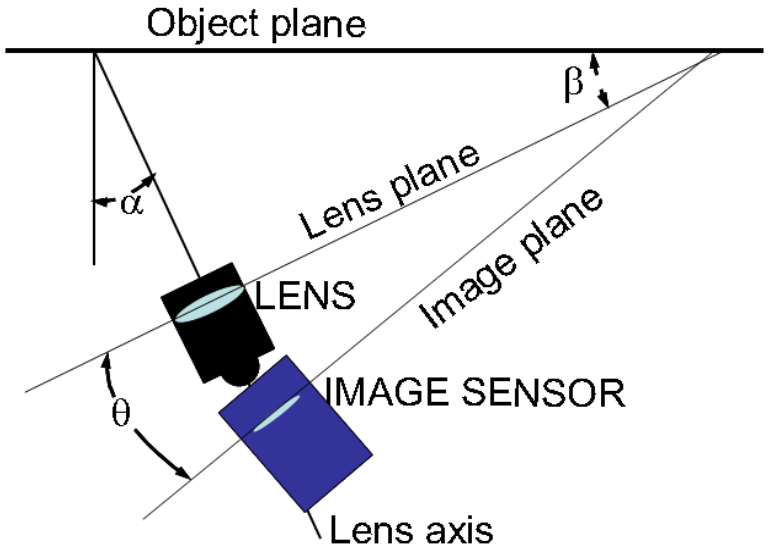


**Figure 2.12** Scheimpflug arrangement of the camera. Diagram shows the right camera of stereoscopic PIV setup from Fig. 2.11

sheet from off-axis angle. This configuration introduces perspective distortion to the images causing a rectangle in the light sheet plane to be imaged as a trapezoid on the image sensor. The most accurate determination of the out-of-plane displacement is accomplished when the angle between the two cameras is 90° ($\alpha$ = 45° in Fig. 2.11). However, the image is difficult to focus since the lens is not parallel to the object plane. Smaller angles $\alpha$ can be used with reduced but reasonable accuracy. In general, a range of $20° < \alpha < 30°$ is favorable to achieve reasonable PIV accuracy.

### 2.2.2 Cross-correlation algorithm

PIV images are analyzed by subdividing the image into small areas called interrogation areas. Each interrogation area contains many particle-image pairs. It is not possible to find individual matching pairs, because the displacement is greater than the mean spacing between particle images. Therefore a statistical method is used to find the particle-image displacement. The correlation domain contains a dominant peak as shown in Fig. 2.13 by computing the spatial cross-correlation of intensities for two interrogation areas in a time interval $\Delta t$. This peak can be found by computing Eq. 2.5 where $R$ is the correlation function, $I_1$ is the intensity at t, and $I_2$ is the intensity at $t+\Delta t$.

$$\boldsymbol{R}(\Delta\vec{\boldsymbol{x}},\Delta\vec{\boldsymbol{y}}) = \int \boldsymbol{I}_1\left(\vec{\boldsymbol{x}},\vec{\boldsymbol{y}}\right)\boldsymbol{I}_2\left(\vec{\boldsymbol{x}}+\Delta\vec{\boldsymbol{x}},\vec{\boldsymbol{y}}+\Delta\vec{\boldsymbol{y}}\right)\boldsymbol{d}\,\vec{\boldsymbol{x}}\boldsymbol{d}\,\vec{\boldsymbol{y}} \tag{2.5}$$

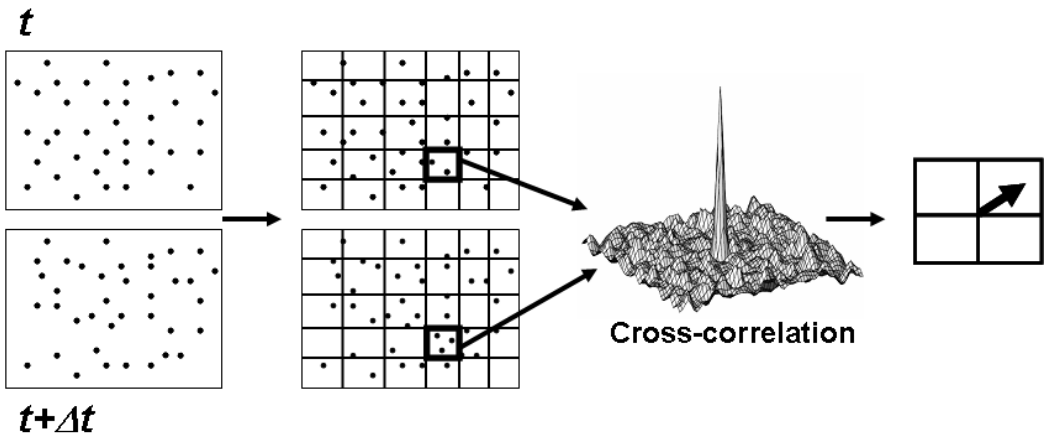


**Figure 2.13** Concept of cross-correlation algorithm

A sharp peak in *R* will appear that reflects the location (Δx, Δy) of the dominant particle displacement in the interrogation area.

2.2.3 Laser and optic alignment

Two high frequency Nd:YLF lasers (Quantronix 527 DQE, and Photonics DM30-527) were used as light sources. The output wavelength for both lasers was 527 nm. The pulse energy for Quantronix laser was approximately 20 mJ/pulse and for Photonics laser was 30 mJ/pulse. Most of head-on collision data acquisitions were performed using Quantronix laser. Photonics laser was used for unequal size drop collision experiments. Each was operated at a repetition rate of 1 kHz (Δt = 0.001 sec). If the pulse separation Δt is too large, the signal to noise ratio in the correlation algorithm is low decreasing the accuracy. On the other hand, if Δt is too small, the particle image displacement Δs is very small, which causes large uncertainty in vector computation.

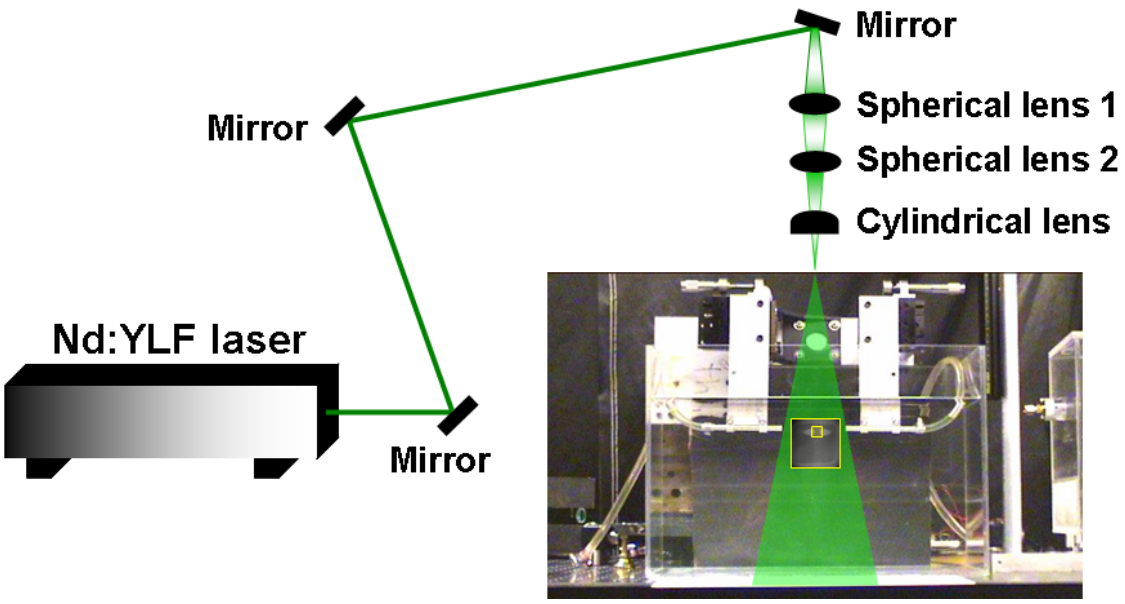


**Figure 2.14** Diagram of laser sheet optic alignment

Figure 2.14 shows the diagram of the optic alignment. The laser beam was focused using two spherical lenses. For Quantronix laser setup, the focal length of

spherical lens 1 was 500 mm and of spherical lens 2 was 1000 mm. Different spherical lenses were used for Photonics laser setup since the beam diverges faster than for Quantronix laser; the focal length of spherical lens 1 was 1000 mm and of spherical lens 2 was 600 mm. The laser beam was formed into a sheet with a cylindrical lens of focal length 60 mm for Quantronix laser and 125 mm for Photonics laser directed vertically downward through the plane bisecting the tube outlets as shown in Fig. 2.14. The light sheet thickness was approximately measured using laser alignment paper in the field of view. The sheet thickness at the measurement location was approximately 1 mm. The sheet light was partially reflected at the upper surface of silicone oil layer and the interface between and oil and water/glycerin layers. These reflections caused undesired saturation of light on the images. To eliminate this effect, the height of the upper fluid layer was adjusted to move the top surface up higher.

### 2.2.4 Dual-field camera setup

During the binary drop coalescence event, length scales of drop motion and the interface film between the colliding drops are different. Because of resolution limit, the scales can not be obtained with conventional PIV system. In this study, a dual-field PIV system was proposed to overcome the resolution limit to characterize two different length scales. The large field of view was set to capture drop shape evolution and trajectory, while the small field was focused on the thin film region that developed during a coalescence or rebounding event. The large field was captured in stereo to enable assessment of the importance of out-of-plane motion and whether or not drops were in fact bisected by the laser sheet during a given sequence. The small field, captured by one camera, observed only in-plane motion.

Three high-speed monochrome CMOS digital cameras (Photron Fastcam Ultima APX) were mounted as shown in Fig. 2.15 and operated at 1 kHz framing rate synchronized with laser pulse repetition rate. Each camera has an array of 1024 × 1024 pixels with 10-bit depth. Each camera can record 2048 consecutive frames at 1 kHz. Two cameras with Nikon Micro-Nikkor 105mm lenses, oriented at $\alpha = \pm 20°$ to the plane bisecting them for stereo PIV, viewed a ‘large’ field of 40 mm × 40 mm, yielding

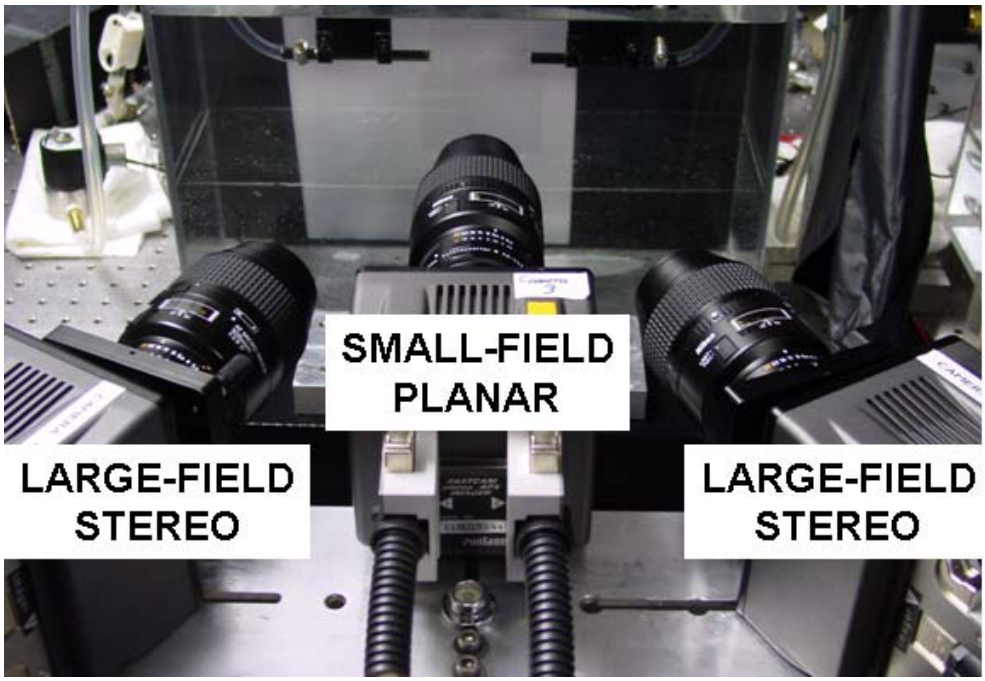


**Figure 2.15** Camera arrangements for dual-field particle image velocimetry

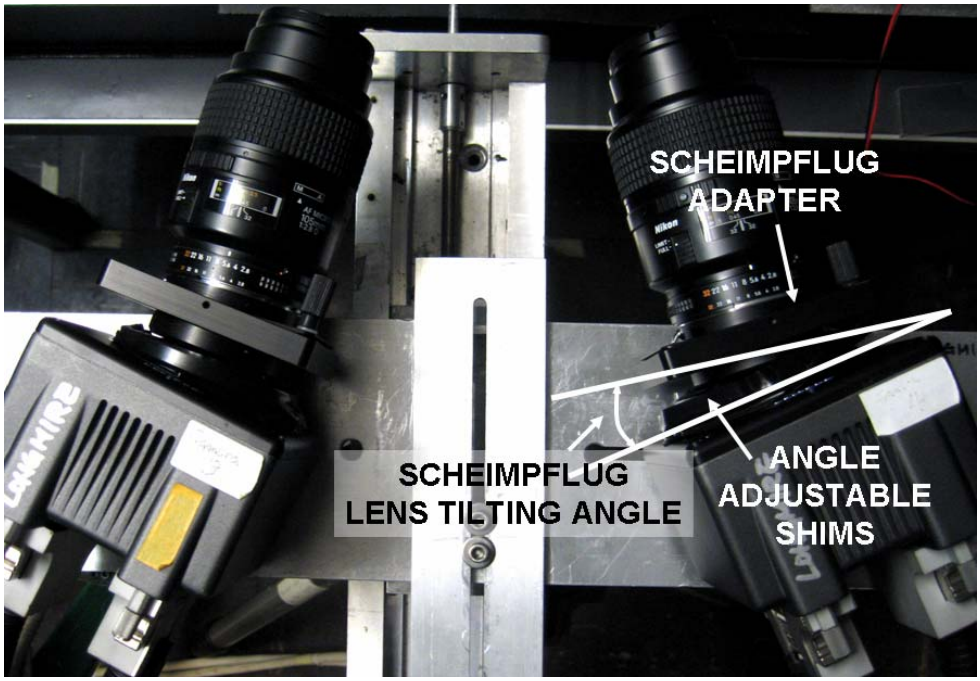


**Figure 2.16** Top view of Scheimpflug angle adjustments for stereo camera

a spatial resolution of 26 pixel/mm. F# of the stereo cameras were 2.8 ~ 4 and of the zoomed planar camera was 2.8. A Scheimpflug arrangement was used between each camera sensor and lens to achieve good focus across the field of view. The rotation angle of the current Scheimpflug angle adapter limited to ± 7°. Thin shims were inserted to one of the mounting screws to achieve reasonable stereoscopic angle ($\alpha = \pm$ 20°) as shown in Fig. 2.16. The resulting lens tilting angle $\theta$ in Fig. 2.12 was ~15°. The correct focus and tilt angles were achieved when all of the particles within the field of view were in good focus.

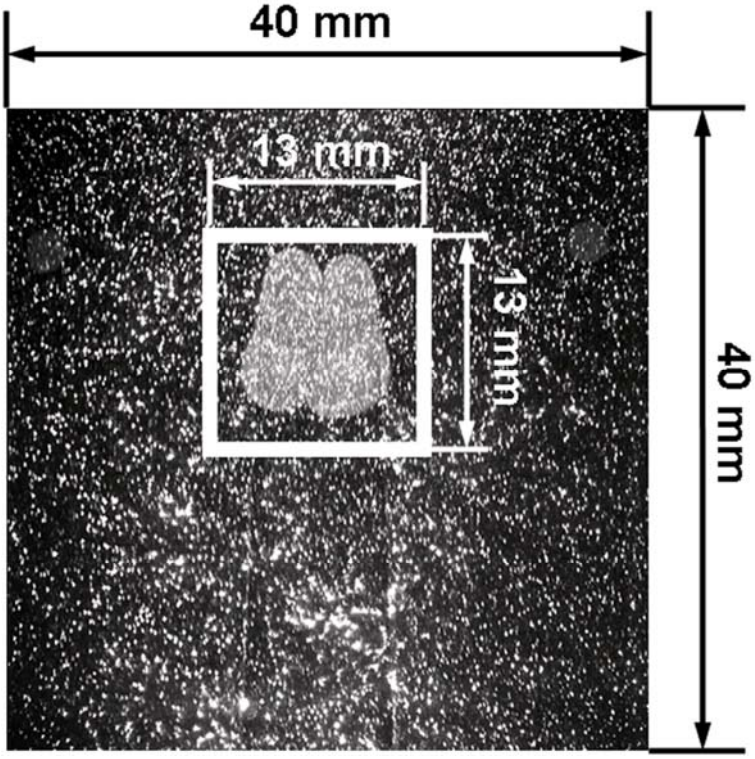


**Figure 2.17** Fields of view for dual-field PIV

A single camera with Nikon Micro-Nikkor 105 mm lens, 1.4X teleconverter, and extension ring, oriented for planar PIV, resolved a 'small' field of 13 mm × 13 mm yielding a spatial resolution of 79 pixel/mm. Somewhat smaller fields were possible under the current illumination conditions (e.g. with a 2X teleconverter), but, in the current flow, it became difficult to center the field consistently on the zone of interest.

When arranging dual-field PIV system, planar PIV camera needed to be setup first before stereo camera setup. Using translation stages, the small field camera was positioned to capture thin interface film region while the field of view was examined during the collision event with laser beam illumination. Observation of the small field was challenging due to a relatively thin depth-of-focus (~45 μm). After the planar PIV camera was aligned, the stereo cameras were setup. Figure 2.17 shows the two fields of view for dual-field PIV including their locations relative to a pair of colliding drops.

A LaVision timing unit (Programmable Timing Unit [PTU], version 8) controlled by *DaVis 7.1* software synchronized the laser pulsing and camera framing. The timing of cameras and laser is shown in Fig. 2.18.

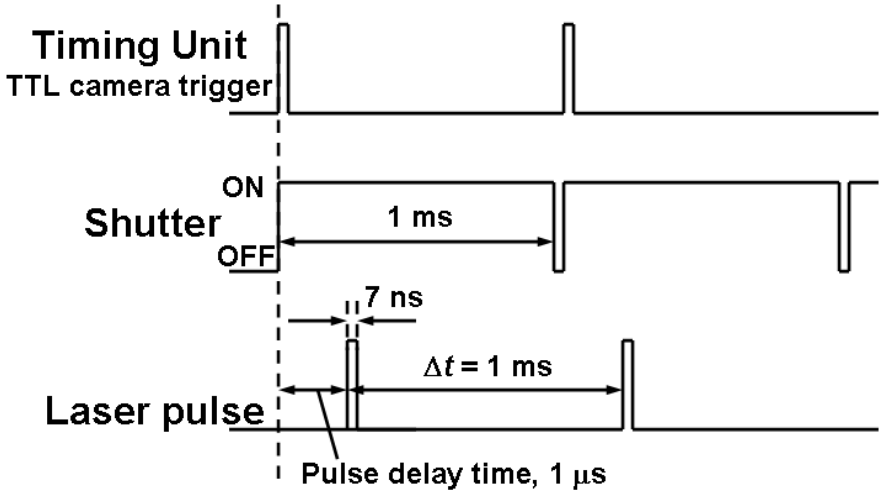


**Figure 2.18** Timing synchronization diagram of camera and laser

When an external trigger signal from timing unit is sent to camera, the camera initializes the shutter opening. Then, the camera triggers the laser. Pulse delay time is the time between initial timing of TTL trigger signal and laser firing. If it is too small, each has multiple exposures, and if it is too large, a laser pulse can be detected only every 2$^{nd}$ image. The delay time for this setup was adjusted to 1μs. Shutter speed and laser pulse repetition rate is synchronized at 1 kHz. Figure 2.19 shows the camera and laser connections to timing unit. The timing unit output a trigger signal and sent it as an external trigger signal (OUT2 cable) to the cameras through Trigger TTL IN cable. The

timing unit set pulse width and time delays between theses outgoing signals. Camera shutter opening and laser firing was synchronized using Ext_V IN (CAM1 cable) and Q1 cable in response to external triggers from PTU. The recorded images temporarily saved into buffer memory in camera and they were transferred into the computer through IEEE1394 cable.

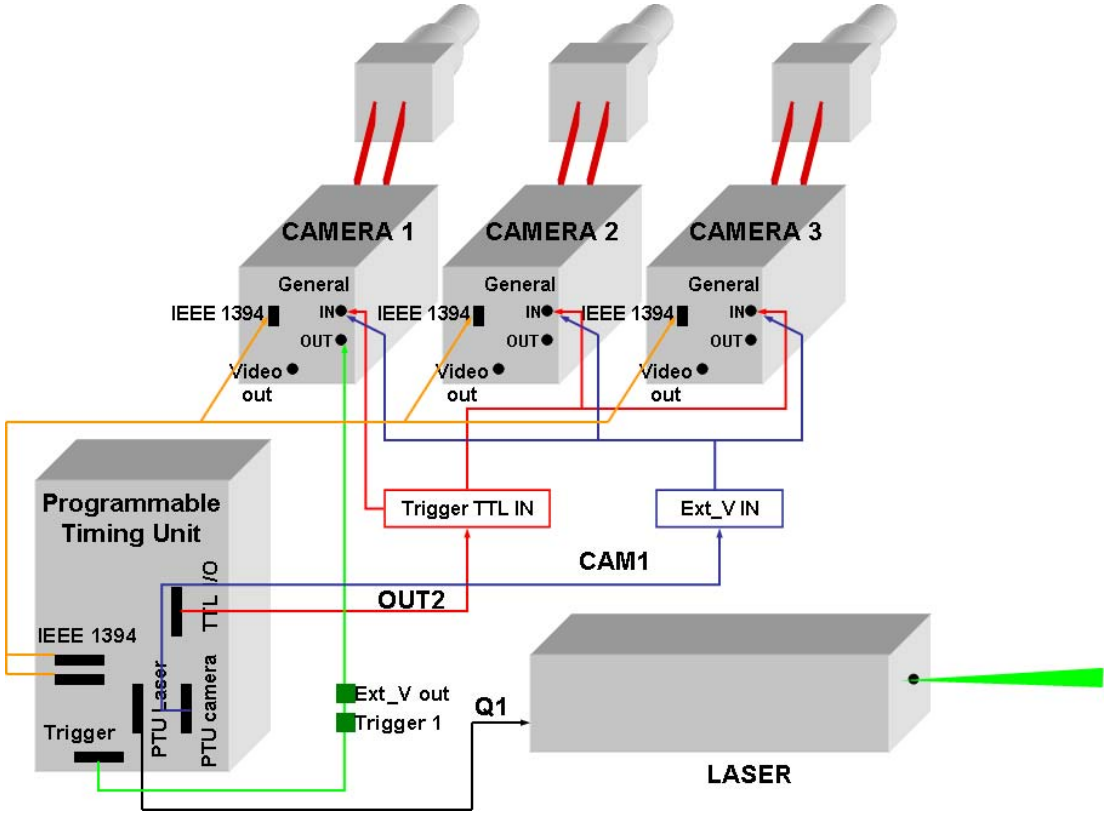


**Figure 2.19** Layout of camera and laser connection to the timing unit

2.2.5 Calibration

For stereoscopic PIV, each image is distorted due to the oblique viewing angle. The Schiempflug configuration helps focus the image. However, the area of interest in the image plane is still distorted and the magnification is nonuniform over the field of view. Thus, a calibration is necessary to measure and correct the perspective distortion due to the camera tilt and other image distortions in the optical system.

A three-dimensional calibration target with equally spaced marks was developed as shown in Fig. 2.20. The target has two planes of marker points on front and back side. In general, a two-level calibration target enables to calibrate the stereoscopic image without traversing the target in the out-of-plane direction. This is convenient to calibrate the stereoscopic setup in liquid because traversing and positioning the target are difficult in liquid.

A square grid of crosses was used for the marks on a white background. The thickness of the mark lines is ~0.1 mm (2 to 3 pixel in the large field of view image). The total size of the cross is 1.67 mm × 1.67 mm; the spacing between centers of the crosses is 3/2 of 1.67mm = 2.5 mm. The spacing of target was limited by the maximum resolution of a conventional laser printer (1200 dpi, dot per inch) and the image distortion due to nonuniform magnification of the oblique view. The mark spacing of 2.5 mm is the minimum spacing to print uniformly with current laser printer. Below this limit, the spacing between the marks was not uniform. Also, marks on front and back planes overlapped if the spacing was finer than 2.5 mm since camera viewed with oblique angle to the measurement plane. The target marks were drawn by Freehand® Software. The target image has a cross-section of 57.5 mm × 57.5 mm. It was printed on transparency film. Printed transparency films were mounted on both sides of a transparent plastic piece with thickness of 1.4 mm as shown in Fig. 2.20a. When attaching films, the grids were staggered in the two planes with shifting ½ of the spacing. The target is placed such that the two planes of markers are not overlapped at the viewing angle. The thickness of target was determined by trial and error to eliminate the overlapped marks on two levels due to the viewing angle of ±20°. A bold dot (red dot shown in Fig. 2.20b) in the front plane represents a reference mark.

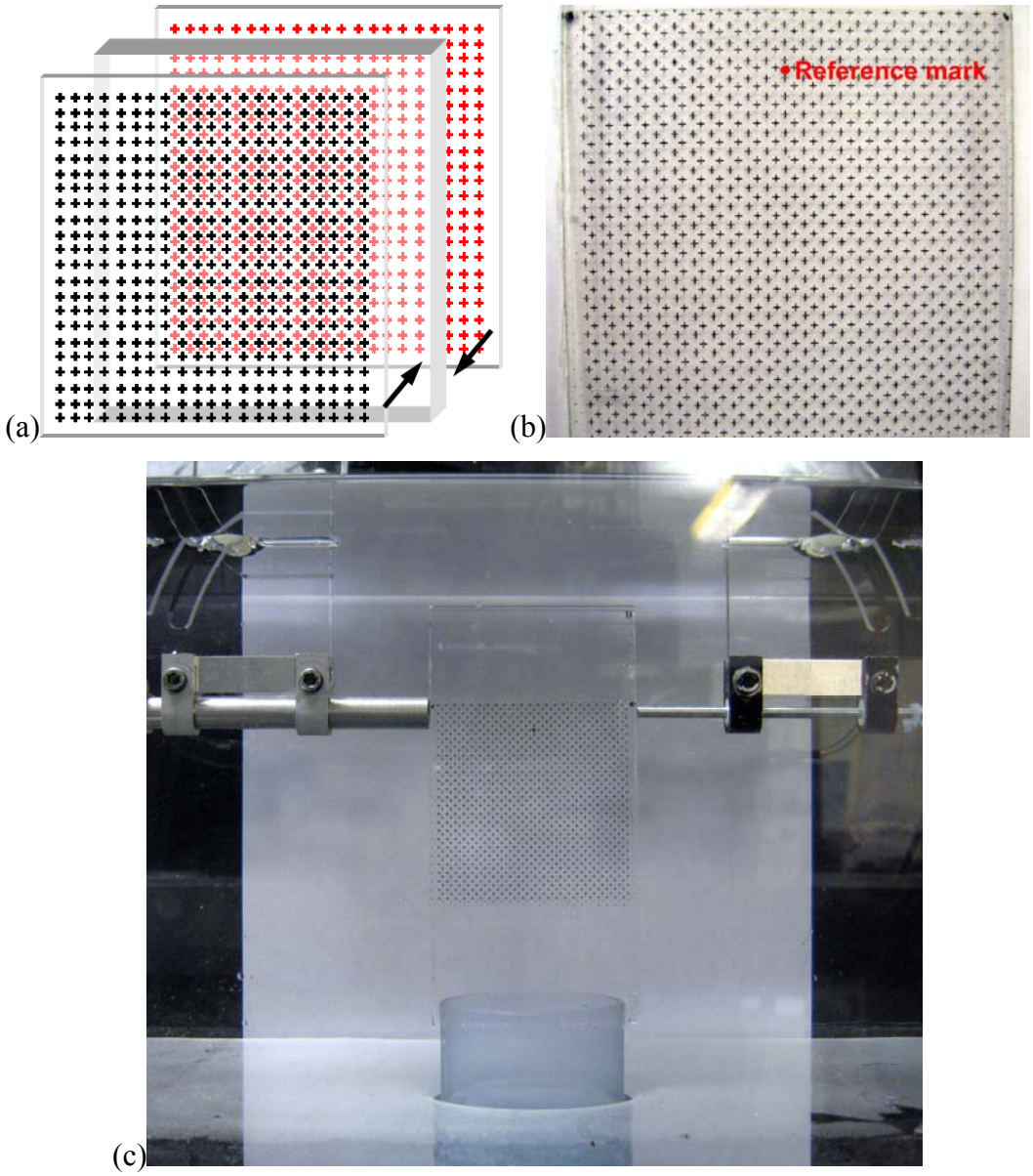


**Figure 2.20** Calibration target; (a) Calibration target assembly. The regular lattice of black crosses, 2.5 mm apart, is printed on top of the transparency film. Actual target grid colors for both front and back films are black. (b) Photograph of calibration target. Red dot shows the reference mark. (c) Calibration target when it is placed in the measurement plane.

The planes are actually separated by 1.5 mm in depth (the thickness of plastic piece is ~1.4 mm and the transparencies add additional thickness). The target is fixed to a base so it can be positiond in liquid (Fig. 2.20c).

The calibration plate needed to be arranged carefully in the object plane aligned with laser sheet beam. If the calibration target was immersed in liquid, it was difficult to align. In this case, there was always some misalignment between the calibration target plane and the laser sheet plane. Therefore, it was necessary to do self-calibration technique. This will be discussed later.

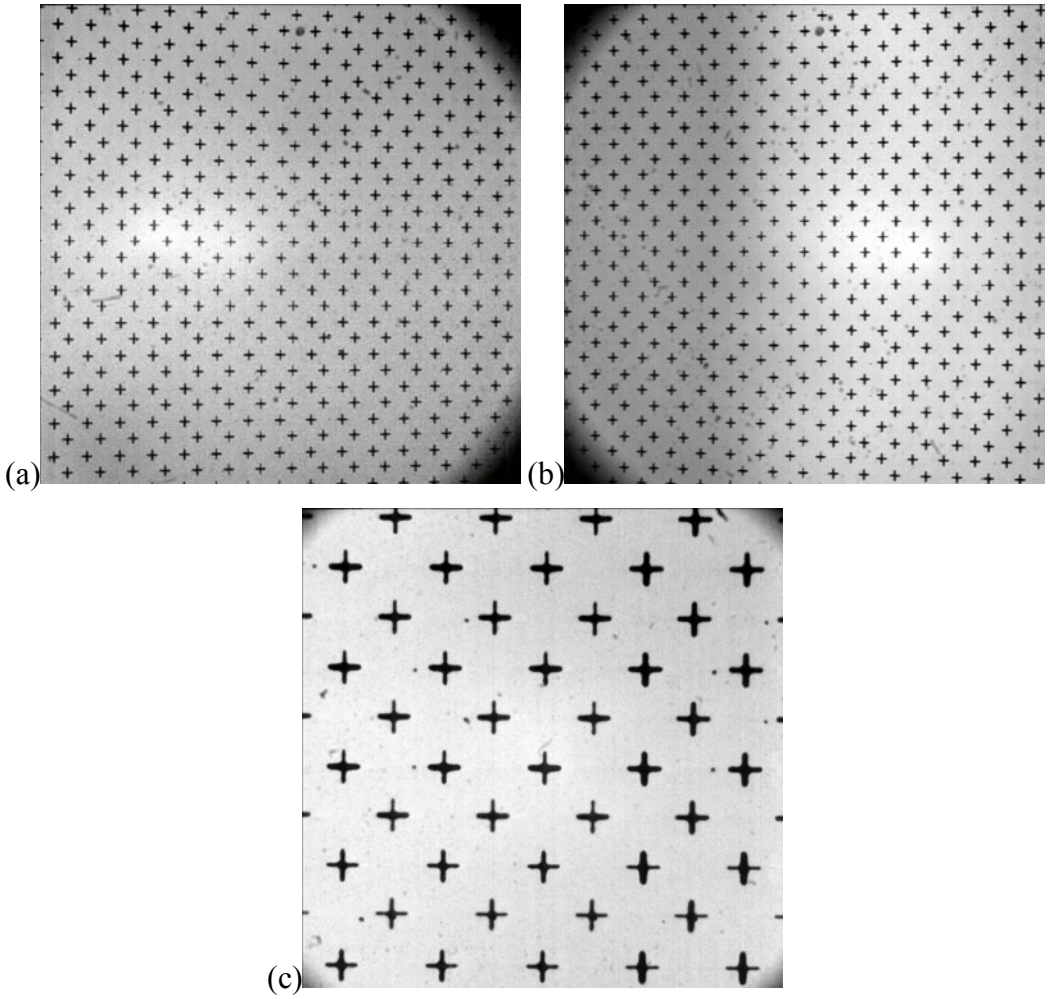


**Figure 2.21** Calibration target images; (a) stereo image from left camera, (b) stereo image from right camera, (c) planar image from small-field camera

After the target was situated, it was illuminated by white light. This lighting is critical for the calibration because nonuniform illumination on target sometimes causes poor calibration results. Figure 2.21 shows the target images in dual-field system. Black areas shown in Fig. 2.21a and b were due to lens tilting with Scheimpflug condition. But, it did not affect the calibration or vector processing. In the calibration the reference mark needed to be first indicated. It was always chosen on the front plane and defined the location of z = 0. Before calibration procedure, the image must be in focus using Scheimpflug adapters. The viewing angle to the calibration plane between the two cameras must be greater than 10° to perform stereo camera calibration. Based on the target image, the marks on the target were searched to calculate the imaging parameters as shown in Fig. 2.22. The software showed squares for the position of the search. A green square indicates that the mark position was detected and a red square indicated that the mark detection failed.

(a) (b)

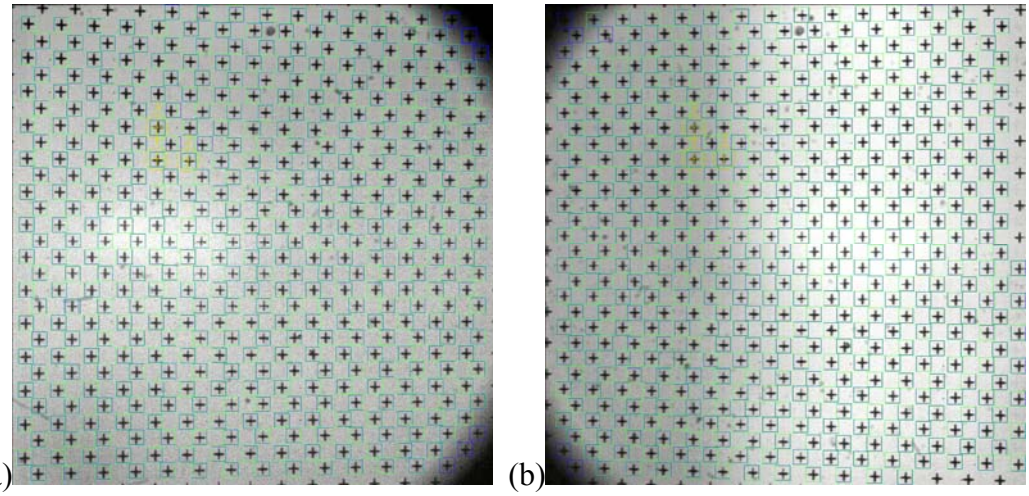

**Figure 2.22** Identified marks on target image; (a) left image, (b) right image

The calibration software attempts to match the pixel location in the object plane to the location in the image plane using a mapping function. A minimum number of 20 marks must be detected over the entire image to compute the mapping function. The software reconstruct the vectors based on outputs of calibration, such as the lens focal length, the angles among the image plane, lens plane, object plane, and the magnification along the

principal optical axis. The mapping algorithm maps the recorded image to the reconstructed image and computes a corrected image from the recorded image under perpendicular view. This process allows calculating the image correction coefficients. In this study, the stereo calibration was performed with the pinhole model. The pinhole model is a mathematical model and provides a complete mapping of volume. During the calibration process, the position and orientation of two cameras relative to the calibration plate can be estimated. Figure 2.23 shows the mapping of volume with pinhole model. This model assumes that all the light from the object plane passes though a single point in space to the image sensor. Dewarping the image is done in this process.

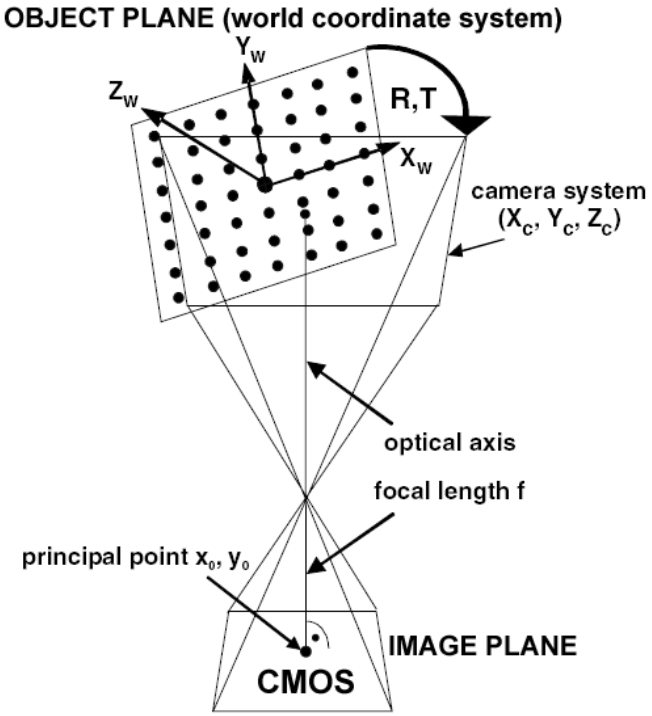


**Figure 2.23** Camera pinhole model. Figure is reproduced from Wieneke (2005)

After a mapping function has been generated, the RMS of pinhole fit was shown. The calibration was determined acceptable if the RMS is smaller than 3 pixels. If the RMS of the fit is larger, the calibration is inaccurate. In this case, either target image was refocused or the reference mark was changed. If the front and back marks are viewed

too close at the viewing angle due to image distortion, the calibration is less accurate. The calibration of the camera images has to be repeated every time the distance between camera and object plane is changed.

Self-calibration for stereo PIV

After the initial calibration, a self-calibration procedure is performed. A procedure is to adjust the coordinate system and the camera calibration of the 3D stereo PIV setup such that the plane of z = 0 will lie exactly in the middle of the laser light sheet. The plane of z = 0 (coincident with the surface of calibration plate) was determined by the initial calibration process. In general the laser sheet is difficult to align perfectly with calibration target plane (plane of z = 0) as shown in Fig. 2.24.

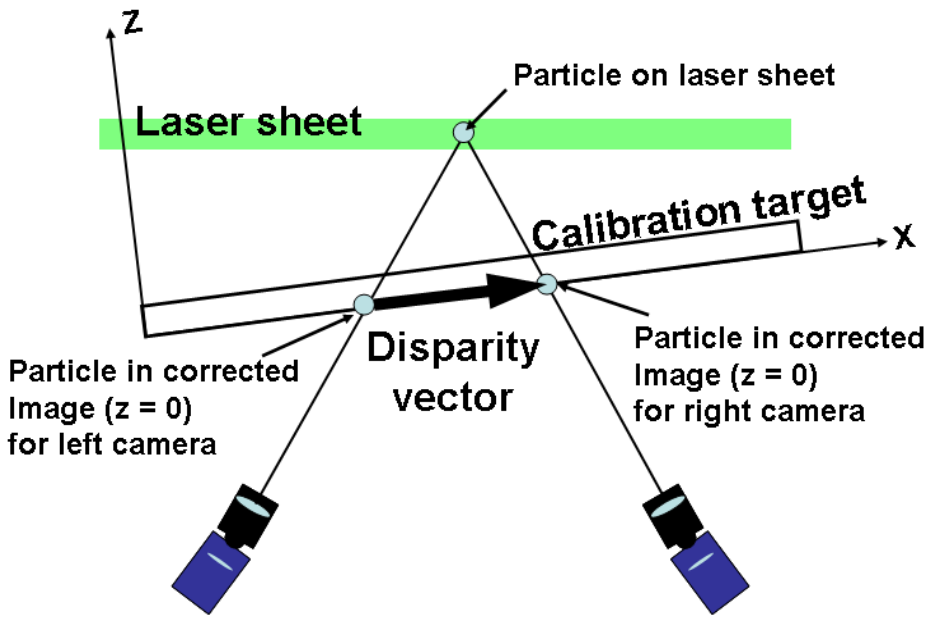


**Figure 2.24** Misalignment of laser sheet and calibration target for stereo PIV setup

The self-calbration is performed on pairs of particle images illuminated by the laser sheet. By correcting an image, the image had been captured on z-axis (plane of z = 0). It is assumed that all particles locate in-plane or z = 0 plane. If there is no misalignment of laser sheet and calibration target and the laser sheet is placed at z = 0 plane, the corrected image of both camera shows the particles at the same location. However, if

laser sheet is misaligned, a particle imaged by each camera shifts to the left for left camera and vice versa for right camera. The vector between these corrected positions is the disparity vector as shown in Fig. 2.24. The corrected image is divided into small windows, and a disparity map is created. A disparity vector was computed for each window. For processing, at least 20 PIV raw image pairs were required for correlation. More images provided better results.

The disparity map was determined based on cross-correlation of stereo images. The disparity vector of a window corresponded to the location of the correlation peak. If the disparity map showed zero or very small vectors, the calibration was accurate. Once the disparity map has been computed, the difference between the laser sheet and calibration target positions was determined by triangulation. Then, the calibration, which was based on a pin-hole model, was corrected to fit the laser sheet position as explained in Wieneke (2005). The previous mapping function was then updated based on the laser sheet plane. The resulting outputs were the average length of the disparity vectors, the plane parameters such as rotation angles for x and y axis, the translation in the z-direction and the average deviation from the plane, and the new camera calibration parameters. The calibration is acceptable if the average deviation of computed disparity vector was less than 3 pixels.

## 2.3 Vector processing

The pixel displacement within each interrogation region was obtained from cross-correlation of two images. For each vector, three true displacements ($\Delta x$, $\Delta y$, $\Delta z$) were extracted from a pair of 2-D displacements ($\Delta X$, $\Delta Y$) as seen from the left and right cameras respectively. Each particle recorded in image sensor had information of particle in object plane ($x$, $y$, $z$), and the mapping functions $f$ correlate two plane profiles.

$$X_{left\ image} = f_1(x, y, z) \tag{2.6}$$

$$Y_{right\ image} = f_2(x, y, z) \tag{2.7}$$

$$X_{left\ image} = f_3(x, y, z) \tag{2.8}$$

$$Y_{right\ image} = f_4(x, y, z) \tag{2.9}$$

Basically the 3-D velocity components were computed by cross-correlation. It is then solved the system of 4 equations (Eq. 2.10 -2.13) with 3 unknowns ($x$, $y$, $z$) is then solved in a least square minimization.

$$\Delta X_{left\ camera} = \Delta x\left(\frac{dX_{left\ camera}}{dx}\right) + \Delta y\left(\frac{dX_{left\ camera}}{dy}\right) + \Delta z\left(\frac{dX_{left\ camera}}{dz}\right) \quad (2.10)$$

$$\Delta Y_{left\ camera} = \Delta x\left(\frac{dY_{left\ camera}}{dx}\right) + \Delta y\left(\frac{dY_{left\ camera}}{dy}\right) + \Delta z\left(\frac{dY_{left\ camera}}{dz}\right) \quad (2.11)$$

$$\Delta X_{right\ camera} = \Delta x\left(\frac{dX_{right\ camera}}{dx}\right) + \Delta y\left(\frac{dX_{right\ camera}}{dy}\right) + \Delta z\left(\frac{dX_{right\ camera}}{dz}\right) \quad (2.12)$$

$$\Delta Y_{right\ camera} = \Delta x\left(\frac{dY_{right\ camera}}{dx}\right) + \Delta y\left(\frac{dY_{right\ camera}}{dy}\right) + \Delta z\left(\frac{dY_{right\ camera}}{dz}\right) \quad (2.13)$$

Vector computation was performed using *DaVis 7.2* software. In this study, PIV recording contained a sequence of images from each camera with a constant time delay. Vector computation was processed with PIV time-series operation letting $\Delta t$ = 1 ms. Therefore, the vector computation was executed on each consecutive pair of images in the sequence as shown in Fig. 2.25.

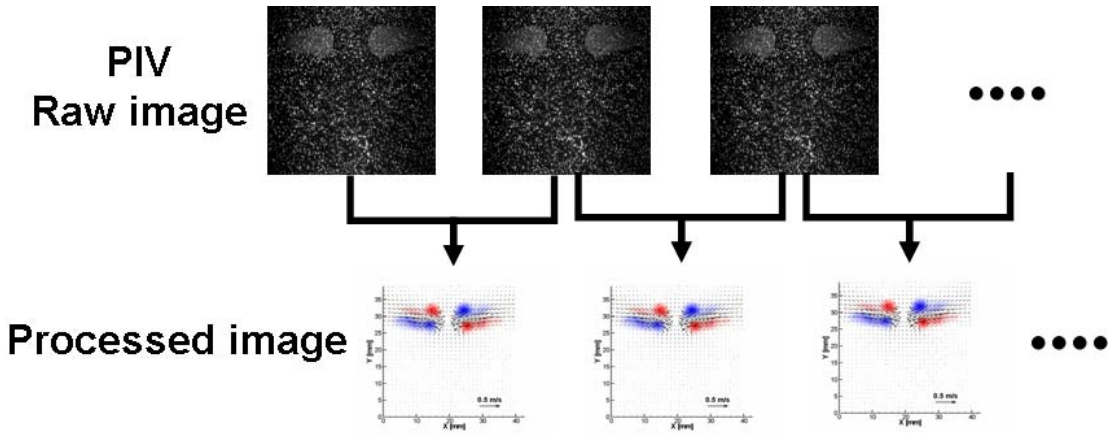


**Figure 2.25** Vector computation operations

The maximum pixel displacement for large field of view, for example of $We$ = 15 ($U_{rel}$ = 21.7 cm/s), was 9 pixels when drops approached and 14 pixels for small field of view during the film rupture event.

Pre-image processing helped to optimize the particle image before the vector computation was performed. It improved the vector computing results by removing background intensity fluctuations. In Fig. 2.10, for example, the recorded PIV image has an inhomogeneous intensity in the background due to reflections at the interfaces. The added fluorescence dye in the drops also caused intensity variations. By subtracting high intensity in the background with a high pass image filter, the large intensity variation was filtered such that the image had constant background intensity without affecting the particle intensity for vector computation as shown in Fig. 2.26. The processed image (Fig. 2.26b) shows that the tracer particles have uniform size, and the background has a relatively uniform intensity over the entire image. The subtracting scale length of the image filter in pixel used in DaVis7.2 was at least twice the size of the mean particle diameter (which was ~4 pixels for the large field of view).

(a) 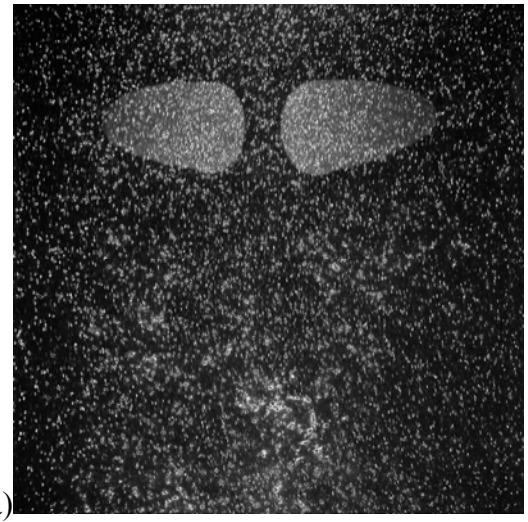 (b) 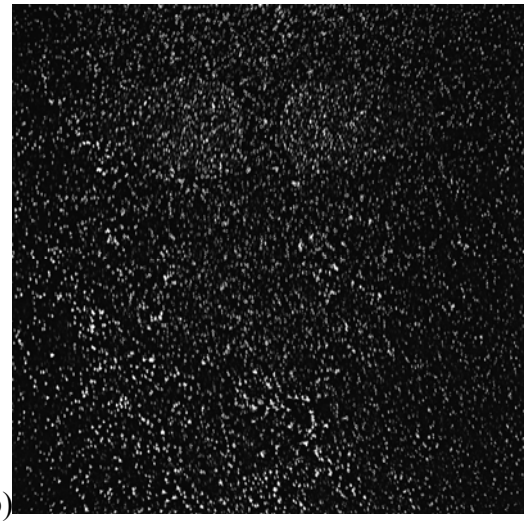

**Figure 2.26** Raw PIV image; (a) before and (b) after image processing

For the case with no tracer particles in the surrounding fluid, 'mask' was applied before the vectors were processed. A mask defined an area of interest and consisted of an image with zero and non zero intensity regions. The area of non zero intensity were

only evaluated in batch processing.

Both large and small view vector fields were obtained using a multi-pass algorithm starting with 64×64 pixel interrogation areas and finishing with 16×16 pixel areas overlapped by 50%. Thus, the velocity was resolved to 0.63 mm × 0.63 mm areas in the large field of view and 0.20 mm × 0.20 mm areas in the small field. In addition, an interrogation area with a round weighting factor was applied to compute the vectors. The weighted interrogation areas had an advantage over square interrogation areas because the Gaussian weighting function decreased the importance of corner zones which contribute relatively more noise and fewer signals. A round Gaussian weighting function was almost always more accurate than a simple window, but took about 5 times longer to compute vectors. The interrogation area with a weight function worked especially well at resolving velocities in high gradient regions.

The multi-pass algorithm enabled the computation of the full vector field that included velocity variations. The first pass with the initial interrogation window size (64 × 64) calculated a reference vector field. In the next pass, a 32 × 32 window size which was half the size of the previous pass was applied. In each pass a reference vector for each interrogation area was processed. The reference vector was interpolated between neighbor vectors at the position where the vectors were computed in the interrogation area. The vector calculated in the first pass was used as a best-choice window shift based on the reference vector. In this manner, the adaptive window achieved better spatial resolution of the vector field and produced fewer erroneous vectors. The relative and absolute vector range restrictions were applied to restrict the allowable vector range. Relative restriction limited the computed vector relative to the reference vector within the interrogation area. Absolute restriction limited the vector depends on pixel displacement. Both restrictions were important to optimize the allowable vector range. The settings varied with each case. To find the optimum values, these restrictions needed to be tested with sample vector computation before batch processing was performed. For example, for a coalescing case with $We$ = 15 ($U_{rel}$ = 21.7 cm/s), a relative vector range restriction was set at reference vector ± interrogation area size/16. Therefore, if the interrogation area size is 32×32 pixels, the

deviation of the calculated vector relative to the previously calculated reference vector is limited by ± 2 pixels. This restricted the allowed range of the vector related to the reference vector because in most cases, the computed vectors were related to the reference vectors. The absolute vector range restriction was reference vector ± 3 pixel. This restriction was not dependent on the size of interrogation area.

A median filter was also employed to remove erroneous vectors. The median filter computed a median vector from the 8 neighboring vectors and compared the center vector with the median vector ± an allowable deviation of the neighboring vectors. The center vector was removed when it was outside the allowed range. Figure 2.27 shows an example of a spurious vector identified using a median filter. In this study, the regional median filter scheme was used. Groups of bad vectors had a high standard deviation of the velocity vector and did not remove spurious vectors surrounded by a few false vectors. Regional median filter allowed removing groups of bad vectors.

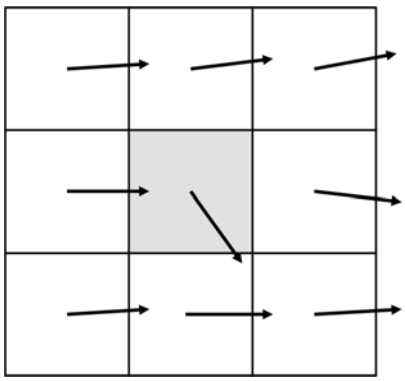

Figure 2.27 Example of local median filter.

The disadvantage of this method is some good vectors are also removed. However, this method was useful in the multi-pass algorithm, when the interrogation area became smaller and generated more false vectors. When the spurious vectors were detected in the pass, if these vectors were not removed, these will propagate the errors in the later passes and resulted in inaccurate final vector field. The adjustment of median filter and vector range restrictions were directly related each other, such that the optimum

adjustment must be tested with a sample vector calculation. Removed vectors were filled with interpolated neighboring vectors. In this study, the 4 passes of the regional median filter ('strongly remove and iteratively replace' option in DaVis 7.2) were applied. The 1st pass removed all spurious vectors using median filter. The 2nd pass removed the vectors without at least 3 neighboring vectors. In the 1st and 2nd passes, vectors were removed that derivated by more than 2 times of RMS value of neighboring vectors. The 3rd pass filled in new interpolated vectors. The filling in was performed by the same method as median filter removal. If the vectors were in the allowable range of the median average ± 3 times of standard deviation of the existing neighbor vectors, the vectors were considered as good vectors and filled in. The 4th pass finally removed any groups of vectors with less than 3 neighbors. Typically, the large field of view yielded 99% valid vectors, and the small field of view yielded 96%. Bad vectors in the small field resulted mainly from areas lacking tracer particles.

## 2.4 Vorticity calculation

Vorticity fields were determined from the velocity fields using a central difference scheme based on the overlapping vectors in the velocity fields. Thus, the vorticity was resolved to smaller length scales in the smaller field of view. The differentiation of the velocity gradients are,

$$\frac{\partial u}{\partial y} = \frac{u_{i,\,j+1} - u_{i,\,j-1}}{y_{i,j+1} - y_{i,j-1}} \tag{2.14}$$

$$\frac{\partial v}{\partial x} = \frac{v_{i+1,j} - v_{i-1,\,j}}{x_{i+1,\,j} - x_{i-1,j}} \tag{2.15}$$

where the vorticity normal to the light sheet is,

$$\omega_z = \frac{\partial v}{\partial x} - \frac{\partial u}{\partial y} \tag{2.16}$$

## 2.5 Parameter computations

2.5.1 Drop interface identification

To compute the volume, diameter, surface area, and relative velocity, MATLAB code was developed to identify the drop interface from a raw PIV image. Automated edge finding technique was first applied to identify the interface. But, it failed to recognize the edge because a light reflection on drops with fluorescing dye made difficult to identify the boundary between the drop and surrounding fluid. Therefore, the drop interface was manually identified by overlaying raw PIV images using the MATLAB code. The boundary of drop was specified by marking dots, and a spline curve fit made a smooth interface as shown in Fig. 2.28. The identified drop was white drop shape with black background, such that each pixel in white area was assigned to 1 and 0 in black background.

(a) 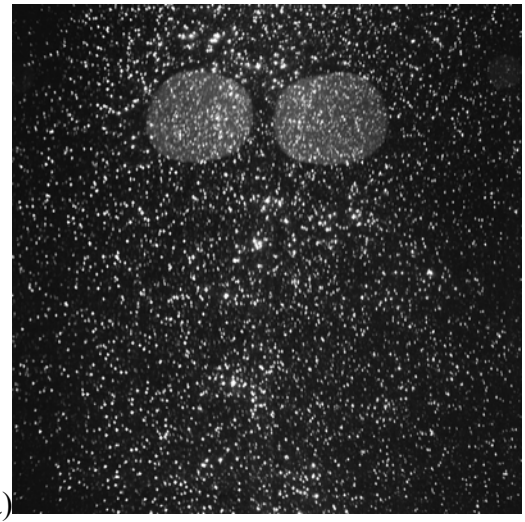 (b) 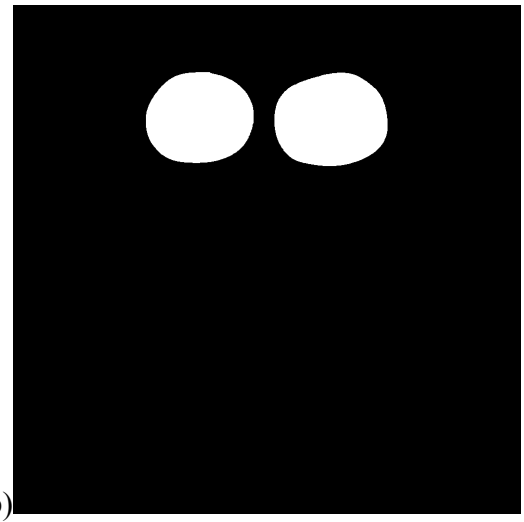

**Figure 2.28** Drop interface identification; (a) raw PIV image, (b) identified drop interface (white area).

2.5.2 Volume, surface area, diameter, and centroid of drop, and kinetic and deformation energy

Image processing software was used to characterize drop properties within image sequences. The local vertical cross section normal to the measurement plane was assumed to be circular everywhere along the horizontal extent of the drop. The volume

and surface area of drop were calculated from the identified drop interface image by summing up the volume and surface area of each cross section. In a given frame, a spherical-equivalent drop diameter was determined from the drop volume calculated based on the imaged cross section. For a specific flow sequence, a drop diameter was calculated from each of the 10 sequential images acquired immediately before the drops deform due to impending collisions, and the results were averaged. A centroid position was determined based on the projected volume of a given drop. The centroid of the volume of drop was calculated using Eq. 2.17 and 2.18.

$$x_c = \frac{\int x dVol}{V} = \frac{\int x\left[\pi\left(\frac{y}{2}\right)^2 dx\right]}{V} \tag{2.17}$$

$$y_c = \frac{\int y dVol}{V} = \frac{\int y\left[\pi\left(\frac{y}{2}\right)^2 dx\right]}{V} \tag{2.18}$$

where *Vol* is the volume of drop.

Kinetic and deformation energy were calculated using Eq. 2.19 and 2.20.

$$KE = \frac{1}{2}mu^2 = \frac{1}{2}(\rho_d Vol)u^2 \tag{2.19}$$

$$DE = \sigma(S_d - S_E) \tag{2.20}$$

Note that m is mass of drop, $\rho_d$ is density of drop, *Vol* is volume of drop, and u is the horizontal velocity component of the drop at a given time. Deformation energy represents the energy required to change the shape of a drop. $\sigma$ is surface tension of fluid, $S_d$ is surface area of drop, and $S_E$ is the surface area of an equivalent spherical drop.

2.5.3 The relative velocity and collision angle

The relative velocity prior to collision, $U_{rel}$ was computed from the horizontal displacement of centroid of each drop between images separated by 10 frames. The second image was chosen at the time that the drops reach a minimum separation before deforming, and the first image was 10 frames earlier.

As shown in Fig. 2.29, when the trajectories of the two drops form an angle, α, the relative velocity of the two unequal size drops is equal to,

$$\boldsymbol{U_{rel}} = \sqrt{\left(\boldsymbol{u_L^2} + \boldsymbol{u_s^2} - 2\boldsymbol{u_L u_s}\cos\boldsymbol{\alpha}\right)} \tag{2.21}$$

where $u_L$ and $u_s$ are velocity magnitudes.

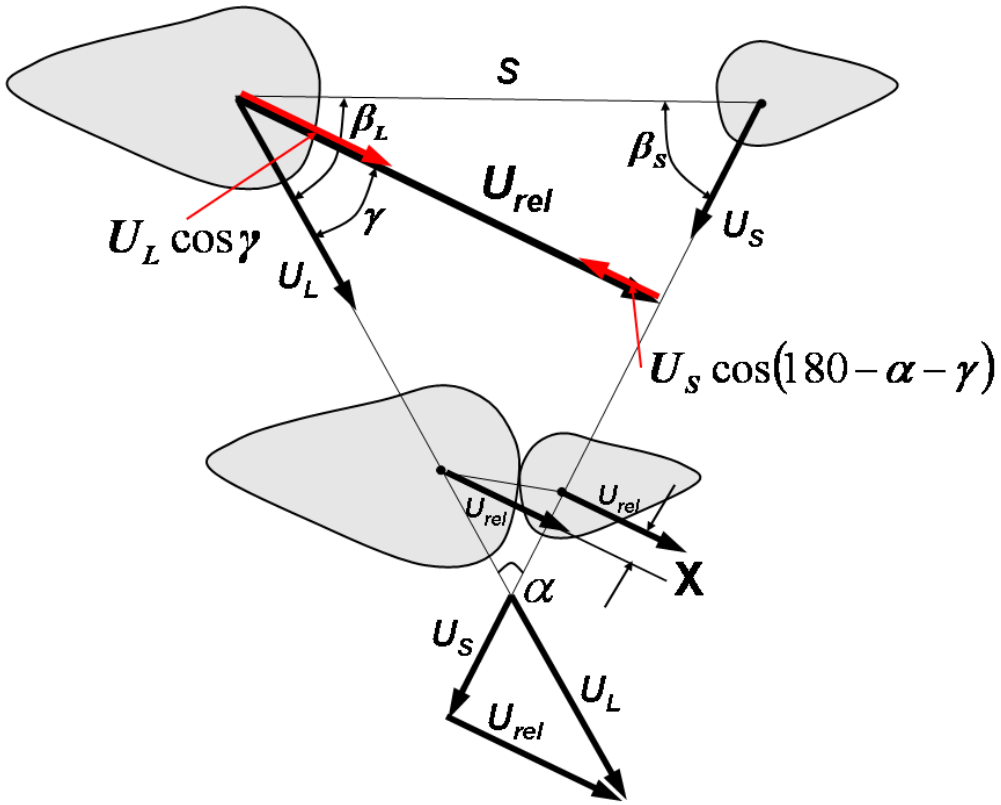


**Figure 2.29** Schematic of unequal size drop collision, $u_L$ is the velocity of large drop (D = $D_L$), $u_s$ is the velocity of small drop (D = $D_s$), and X is the impact parameter.

For head-on collision for equal size drops,

$$U_{rel} = 2u \tag{2.22}$$

where $u$ is the magnitude of the horizontal velocity component.

A collision angle, $\theta$ is defined as the inverse tangent of the vertical velocity divided by the horizontal velocity based on the same two frames described above as shown in Fig. 2.30.

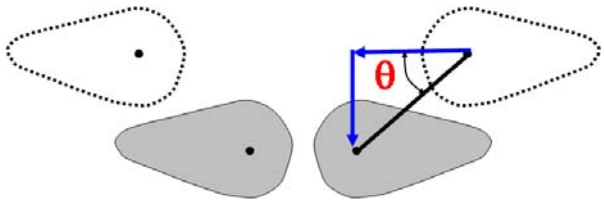


**Figure 2.30** Schematic of equal size drop collision. θ is a collision angle

2.5.4 Dimensional analysis; Weber number, impact parameter, and time scale

The Weber number was defined as Eq. 1.2, $We = \rho_d U^2_{rel} D/\sigma$, in chapter 1. For equal size drop collision, Eq. 1.2 was used. For unequal size drop collision, either the diameter of small drop $D_s$ or average of two drops $(D_s+D_L)/2$ were used as a characteristic lengths for $We_s$ (Brazier-Smith et al 1972, Ashgriz and Poo 1990, Fujimoto et al 1997, and Sakakibara and Ianmuro 2008) or $We_{avg}$ (Orme 1997 and Premnath and Abraham 2005). In this study, the inertia driven Weber number was defined as,

$$\boldsymbol{We^*} = \frac{4\boldsymbol{\rho_d}\left(\boldsymbol{D_L^2 u_L^2} + \boldsymbol{D_S^2 u_S^2}\right)}{\boldsymbol{\sigma}\left(\boldsymbol{D_L} + \boldsymbol{D_S}\right)} \tag{2.23}$$

where the subscript L is for large drop and S is for small drop for horizontal head-on collision. For equal size drop collision (B = 0), Eq. 2.21 is equal to Eq. 1.2. Eq. 2.23

can be rewritten based on Fig. 2.29 as,

$$We^{*} = \frac{4\rho_d \left( D_L^2 (u_L \cos\gamma)^2 + D_S^2 (u_S \cos(180 - \alpha - \gamma))^2 \right)}{\sigma (D_L + D_S)} \tag{2.24}$$

Note that the components $u_L$ and $u_s$ with respect to the $U_{rel}$ plane were used in Eq. 2.24.

The dimensionless impact parameter B was defined as,

$$B = \frac{2X}{D_L + D_S} \tag{2.25}$$

where X is the projection of the distance between the centroid of each drop normal to the direction of the relative velocity (Fig. 2.29).

In this study, equal size drop collisions were all head-on. Therefore the impact parameter was B = 0. For unequal size drop collisions, the impact parameter was calculated by measuring the positions of two drops before collision based on the same two frames described earlier using the following relations:

$$B = \frac{2X}{D_L + D_s} = \frac{2S \sin|\beta_L - \gamma|}{D_L + D_s} \tag{2.26}$$

$$\gamma = \sin^{-1}\left( \frac{u_S}{U_{rel}} \sin\alpha \right) \tag{2.27}$$

where S is the distance between the centroids before the collision, $\beta_L$ is the angle between the trajectory of the large drop and line between the centroids, and $\gamma$ is the angle between the trajectory of the large drop and the direction of relative velocity.

Time scales for inertial, surface tension, and viscous forces were considered. The inertia time scale $t_i$, surface tension time scale $t_s$, and viscous diffusivity time scale $t_v$ were as,

$$t_i = \frac{D}{U_{rel}} \tag{2.28}$$

$$t_s = \sqrt{\frac{\rho_d D}{\sigma}} \tag{2.29}$$

$$t_i = \frac{\rho_s D}{\mu_s} \tag{2.30}$$

where the subscript *d* is drop fluid (water/glycerin) and *s* is surrounding fluid (silicone oil). These time scales were compared in Table 2.2 for the case when drop diameter was 0.84 cm and relative velocity was 21.7 cm/s [*We* = 15].

| | Water/Glycerin (drop fluid) / 50 cS silicone oil (surrounding fluid) |
|---|---|
| $t_i$ (inertial time scale) | 0.039 s |
| $t_s$ (surface tension time scale) | 0.151 s |
| $t_v$ (viscous time scale) | 1.411 s |

**Table 2.2** Inertia, surface tension, viscous diffusivity time scales

The inertial time scale was the smallest among these time scales so that the inertial time scale is most important time scale. In this study, the inertial time scale (Eq. 2.28) was used. Hence, the dimensionless time t* was defined as $tU_{rel}/D$. In all sequences, the value t* = 0 is chosen as the time when the two drops first touch. Therefore, pre-collision times are negative, and post-collision times are positive.

For unequal size drop collision, the dimensionless time t* was characterized as,

$$t^* = \frac{4\left(D_L u_L + D_s u_s\right)}{\left(D_L + D_s\right)^2} t \tag{2.31}$$

where $u_L$ and $u_s$ are horizontal component.

$t_{max}$ were used for a comparison of energy dissipation during the equal size drop collision. When $t_{max} = 0$, interfacial film length between the drops were maximum. In general, drops rebounded or coalesced when they reach the maximum film length. However, if the inertia is higher, drop continuously deformed after the film length was maximum. $t_{max}$ is defined as,

$$t_{\max} = \frac{t' U_{rel}}{D} \tag{2.32}$$

where t' is time interval from the time at maximum film length.

## 2.6 Uncertainty analysis

2.6.1 Uncertainty in drop parameter computations

Volume of drop was obtained by averaging volumes in 10 sequential images before t* = 0. MATLAB volume calculation was examined for several different shapes and the uncertainty in the volume calculation was 2%. The equivalent diameter of drop was computed from volume of drop. The resulting uncertainty in a diameter was estimated to be ±0.01D

The total relative velocity computing error $\delta U_{rel}$ due to centroid displacement error was estimated using the following equations where $\delta x_1$ is the displacement of left drop and $\delta x_2$ is the displacement of right drop,

$$U_{rel} = \left( \frac{U_{x1} - U_{x2}}{\Delta t} \right), \quad U_x = \left( \frac{X_1 - X_2}{\Delta t} \right)$$

$$\delta U_{rel} = \sqrt{\left( \frac{\partial U_{rel}}{\partial U_{x1}} \delta U_{x1} \right)^2 + \left( \frac{\partial U_{rel}}{\partial U_{x2}} \delta U_{x2} \right)^2} = \sqrt{2} \delta U_x = \sqrt{2} \sqrt{\left( \frac{\partial U_x}{\partial x_1} \delta x_1 \right)^2 + \left( \frac{\partial U_x}{\partial x_2} \delta x_2 \right)^2}$$

$$\therefore \delta U_{rel} = \sqrt{2} \left( \frac{\sqrt{2}}{\Delta t} \delta x \right) \tag{2.33}$$

The uncertainty in $U_{rel}$ determined by this method was estimated as $0.02U_{rel}$.

2.6.2 Uncertainty in PIV vectors

Uncertainty of velocity vector in PIV was determined as,

$$\delta u = \sqrt{(\frac{\partial u}{\partial \Delta x}\delta \Delta x)^2 + (\frac{\partial u}{\partial M}\delta M)^2 + (\frac{\partial u}{\partial \Delta t}\delta \Delta t)^2} \tag{2.34}$$

Substituting for the derivatives above equation can be:

$$\frac{\delta u}{u} = \sqrt{(\frac{\delta \Delta x}{\Delta x})^2 + (\frac{\delta M}{M})^2 + (\frac{\delta \Delta t}{\Delta t})^2} \tag{2.35}$$

Assuming that the maximum error in the peak finding algorithm was 0.1 pixels the uncertainty in in-plane velocity components was approximately $0.018U_{rel}$ in the large field (0.0039 mm/pixel resolution). The out-of-plane velocity component in the large field had a corresponding uncertainty of $0.051U_{rel}$. The uncertainty in the small field (0.0127 mm/pixel resolution) was $0.006U_{rel}$.

# Chapter 3

# Results and Discussion

Collision outcomes in liquid will be discussed in this chapter. The characteristics of a rebound and a coalescence are compared for four different *We* cases (*We* = 4 and 9 (rebound) and *We* = 15, 28, and 42 (coalescence)). Drop shape evolutions and corresponding vector fields are presented to gain insights into the coalescence mechanism. Parametric effects, such as Weber number, collision angle, drop size ratio, impact parameter, and presence of contaminant particles, are considered.

## 3.1 Characteristics of binary drop collisions

### 3.1.1 Overall drop trajectories

Figure 3.1 shows results from many cases over which *We* was varied. A trajectory angle θ is defined as the inverse tangent of the vertical velocity divided by the horizontal velocity (where $\theta > 0$ is downward) based on the same frames described in Section 2.5.3 (see Fig. 2.30). In Fig. 3.1, blue and red dots represent coalescence and rebound, respectively. All drop collisions were head-on (B = 0), and in all cases, the two drops were equal-sized. The nozzle separation was varied in order to achieve multiple collision angles for a given value of *We*. All of the drops travel on downward trajectories before colliding because of gravitational effects. As *We* decreases, the vertical velocity becomes more significant. In general, the drops rebound when *We* is below 10 and coalesce when *We* is greater than 10. Based on the current data, this boundary applies for trajectory angles in the range $20° < \theta < 42°$. The boundary tends to shift to higher *We* at even larger downward collision angles. As will be shown below,

as *We* increases, drop deformation increases during collisions.

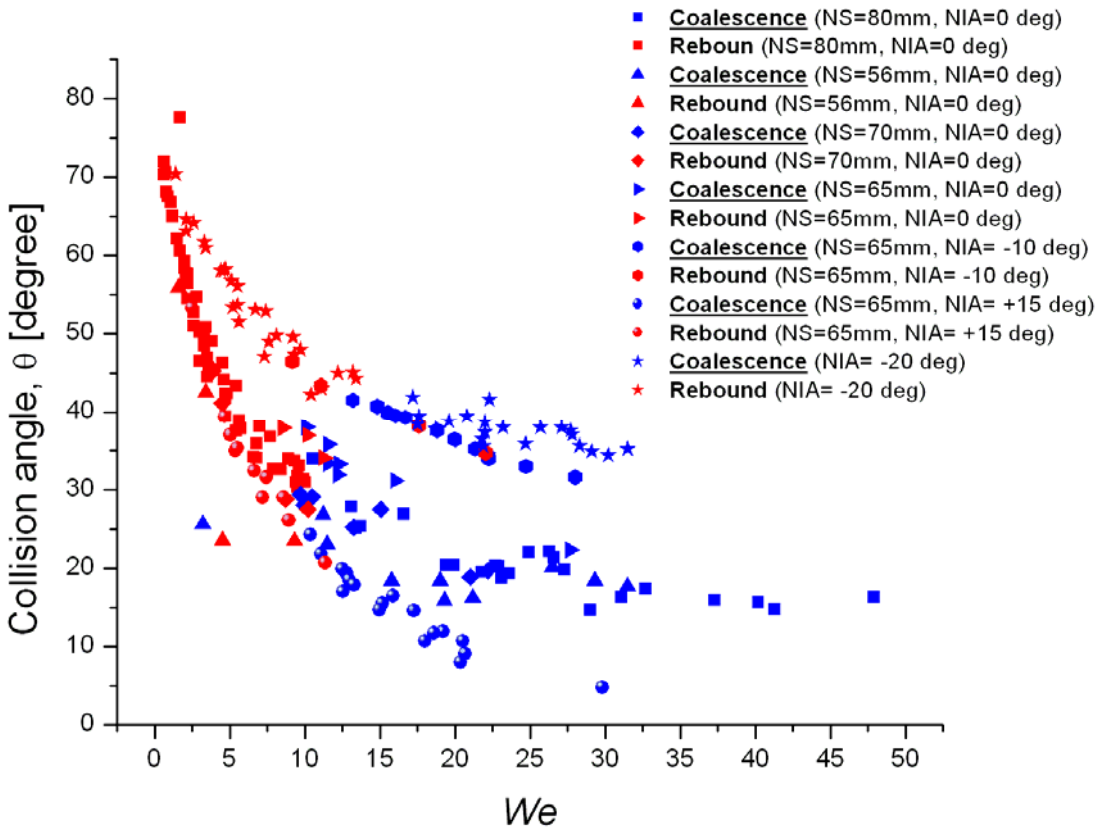


**Figure 3.1** Collision outcomes, B = 0 (head on collisions). NS is the nozzle separation distance and NIA is initial nozzle injection angle.

3.1.2 Rebound

The sequences from the 'large' field of view are shown in Figs. 3.2 and 3.3: a rebound case with *We* = 4 (D = 0.78 cm, trajectory angle θ = 45°, and $U_{rel}$ = 11.5 cm/s) and a rebound case with *We* = 9 (D = 0.80 cm, trajectory angle θ = 32°, and $U_{rel}$ = 16.9 cm/s).

In this study, the decelerating drop motion before impact was influenced by the 'added mass' (or sometimes called 'virtual mass') of liquid volume because the drop motion is unsteady; Note that drops did not reach steady-state velocities before the collision. The total drag on the fluid volume in arbitrary accelerated motion is

generalized as,

$$-\boldsymbol{F}_{D_x} = \frac{\pi \boldsymbol{d}^2 \rho_d}{8} \boldsymbol{C}_D \boldsymbol{V}_x |\boldsymbol{V}| + \frac{\rho_f \boldsymbol{Vol}}{2} \frac{\boldsymbol{dV}_x}{\boldsymbol{dt}} \tag{3.1}$$

where $F_{Dx}$ is Drag force in x-direction, $\rho_d$ is density of drop, $C_D$ is drag coefficient of drop, $V_x$ is horizontal component of drop velocity, $\rho_f$ is density of ambient fluid, and Vol is volume of a drop. The first term is drag term at the instantaneous velocity and the second term is 'added mass' or 'virtual mass' term which is the inertia added to flow because an accelerating or decelerating fluid volume (drops) must move some volume of surrounding fluid. If we assume that the droplet drag term fits empirical correlations and estimate the time scale of deceleration, for example, then the added mass force is approximately 35% and 61% of the drag force in the *We* = 4 and 15 cases respectively (see e.g. development in Clift *et al.* 1978). Therefore, the drag on the drop decreased by added mass term.

In Fig. 3.2, the drops travel on downward trajectories after they are ejected from the tubes. The maximum vertical dimension of the drops in Fig. 3.2a is 7.0 mm compared with the inner diameter of the drop injection tubes of 6.1 mm. The drops are close to spherical before they collide (Fig. 3.2b). The drops initially contact each other at a position above their centers and then rotate toward each other (e.g. right drop rotates clockwise) so that the flat interface between them lengthens (Figs. 3.2c-e). After the collision, the drops become oblate in shape. At t* = 0.79 (Fig. 3.2e), the intervening film length between the drops was maximum and the drops move apart while continuing to rotate. As the drops separate, their shapes revert to spherical.

In Fig. 3.3, a rebound for *We* = 9 behaves similar to the previous case for *We* = 4. The drops are more elongated after they are ejected from the tubes. The maximum vertical dimension of the drops in Fig. 3.3a is 7.2 mm. The tails of the approaching drops are more elongated compared with *We* = 4 (see Figs. 3.2a and 3.3a). After the drops initially contact each other, they rotate less compared to the case for *We* = 4 due to shallower collision angle. The drops reach a longer maximum interfacial film length

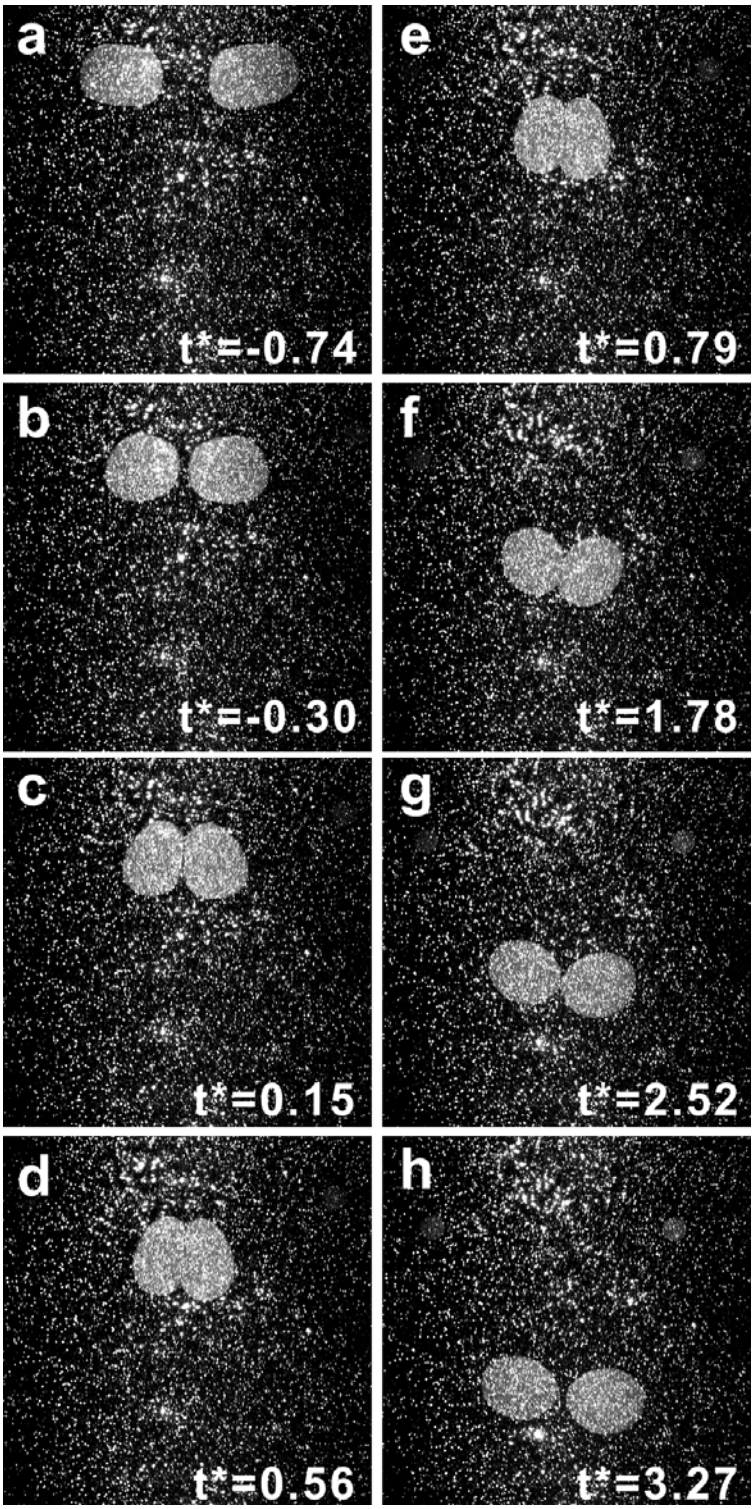


**Figure 3.2** Time evolution of drop collision: *We* = 4 (rebound), θ = 45°. t* = t$U_{rel}$/D, where D is drop diameter and $U_{rel}$ is relative velocity.

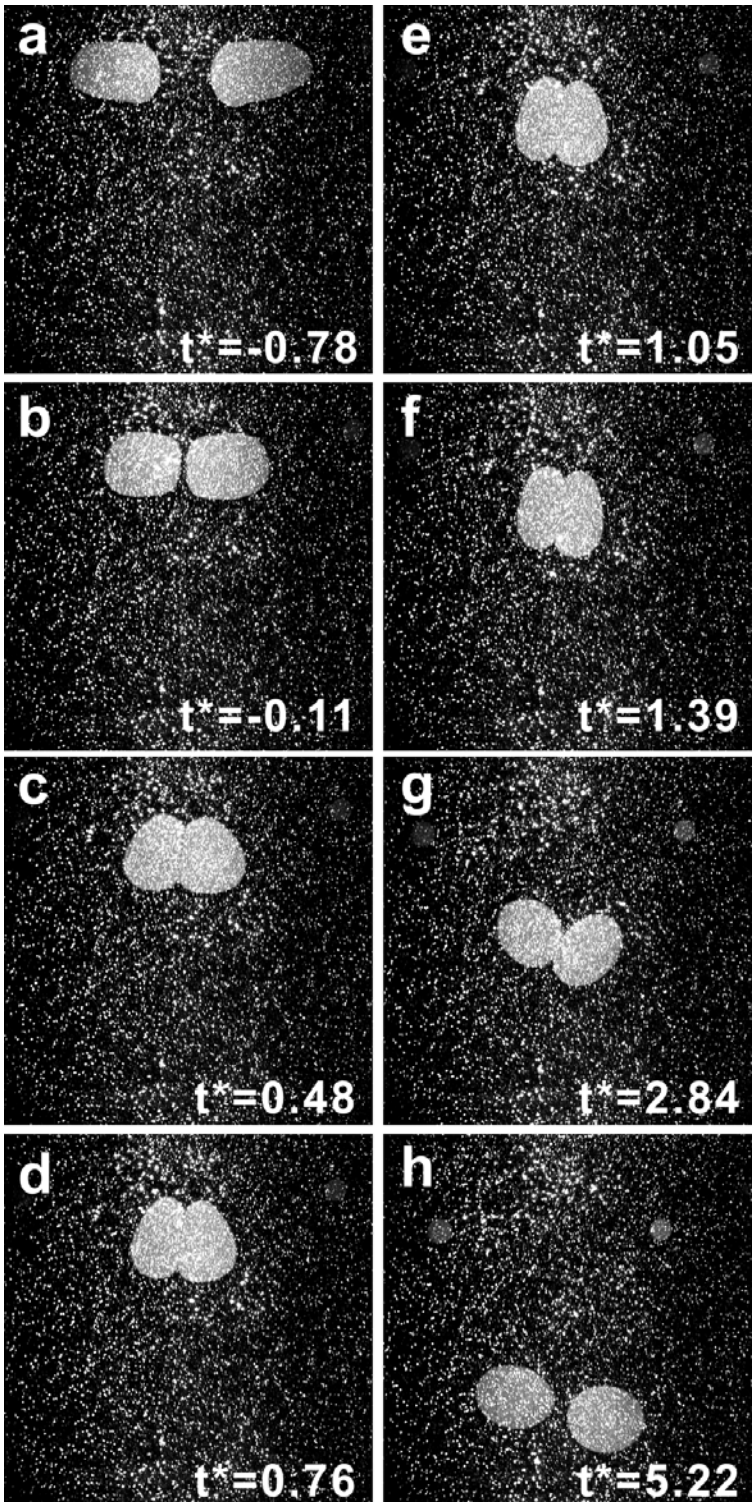


**Figure 3.3** Time evolution of drop collision: *We* = 9 (rebound), θ = 32°. t* = t$U_{rel}$/D, where D is drop diameter and $U_{rel}$ is relative velocity.

at t* = 1.05 (Fig. 3.3e). Drops continuously deform and, beginning at t* = 1.39, the drops move apart (Fig. 3.3f). The time that the film length reached a maximum (t* = 1.05) was later than for *We* = 4 (t* = 0.79). However, the absolute time (t = 50 ms) was slightly earlier for *We* = 4 (t = 53 ms). Also, after the drops reach the maximum film length, they continuously deform and start separating at a later time (t* = 1.39, t = 66 ms) compared with *We* = 4 (t* = 0.79, t = 53 ms) where they start separating immediately after they reach the maximum film length for.

Figures 3.4 and 3.5 show the computed velocity vectors and vorticity contours for the same sequences for the previous cases (only every sixth vector is plotted so that trends are observed more easily). Velocity magnitudes and vectors are normalized by the relative velocity, $U_{rel}$. The vorticity is nondimensionalized using $U_{rel}$ and drop diameter. Red on the color map shows counterclockwise rotation of flow, and blue represents clockwise rotation.

For *We* = 4, the large velocity vectors near the center of each drop during approach are directed toward the symmetry plane and somewhat downward (Fig. 3.4a). These vectors rotate downward as the drops collide and deform. By t* = 0.79 (Fig. 3.4e) when the drops start to rebound, the vectors are directed straight downward. The vorticity contours reveal a vortex ring pattern within each drop. In Figs. 3.4a and d, the angle of vortex ring was illustrated by the black solid line. Each ring rotates during the collision process to align with the local trajectory direction (see Figs. 3.4a with d), and the circulation within each ring appears to decrease. As the drops move apart and continue to fall downward, the weakened rings persist near the drop leading edges. The total circulation is stronger toward the outside of each drop in the pair, most likely a result of each drop continuing to rotate, i.e. the left-hand drop is rotating clockwise and vice versa. The overall circulation associated with each drop has decreased as the propagation speed of the drops has decreased.

Figure 3.5 shows the velocity variations of the rebounding case for *We* = 9. The vortex rings rotate as drops approach and collide in Figs. 3.5a-d. The resulting vortex ring structure rotates less than for *We* = 4 during the collision (see both Figs. 3.4a and d and 3.5a and d). This is because of the shallower collision angle resulting from the

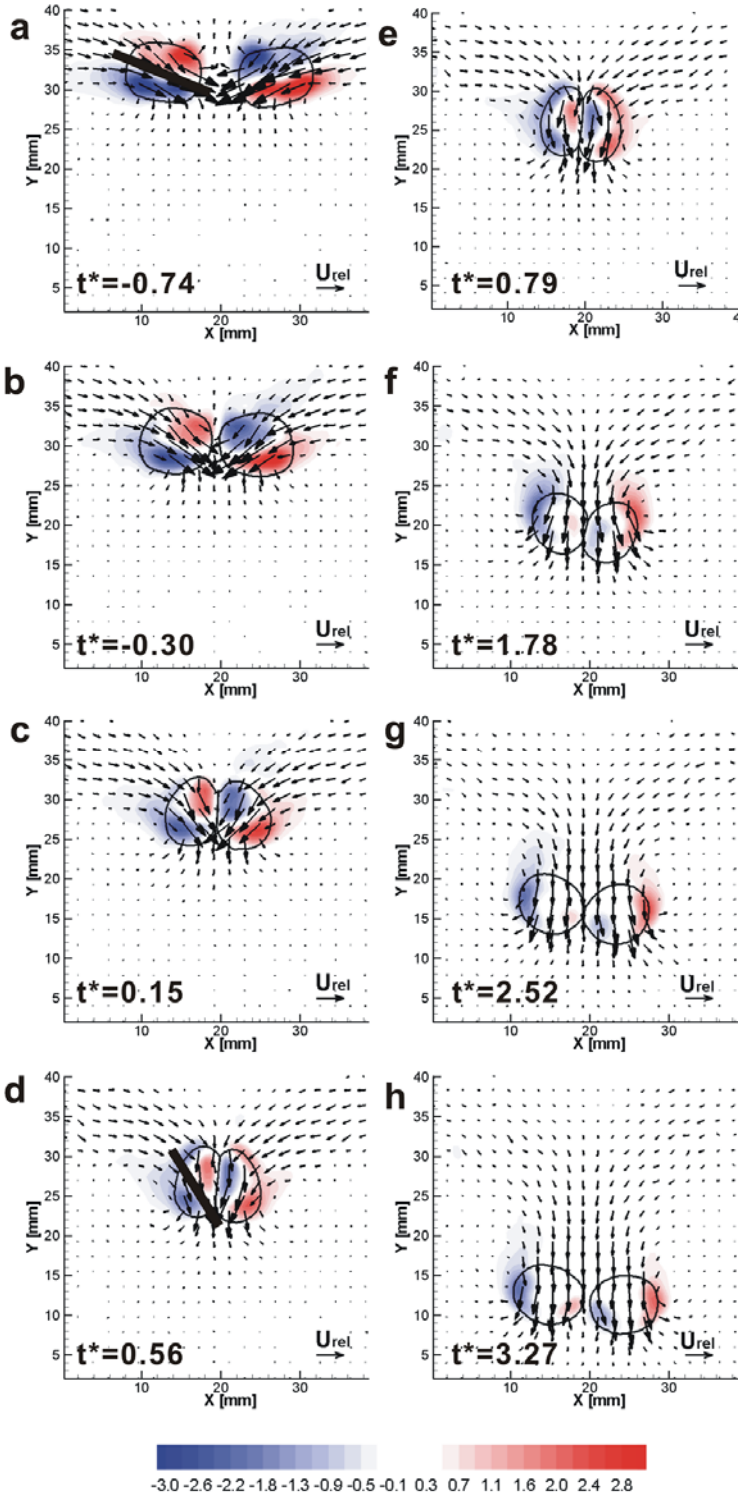


**Figure 3.4** Absolute in-plane velocity vectors and normalized vorticity contours: *We* = 4 (rebound), θ = 45°. Red is counterclockwise, and blue is clockwise.

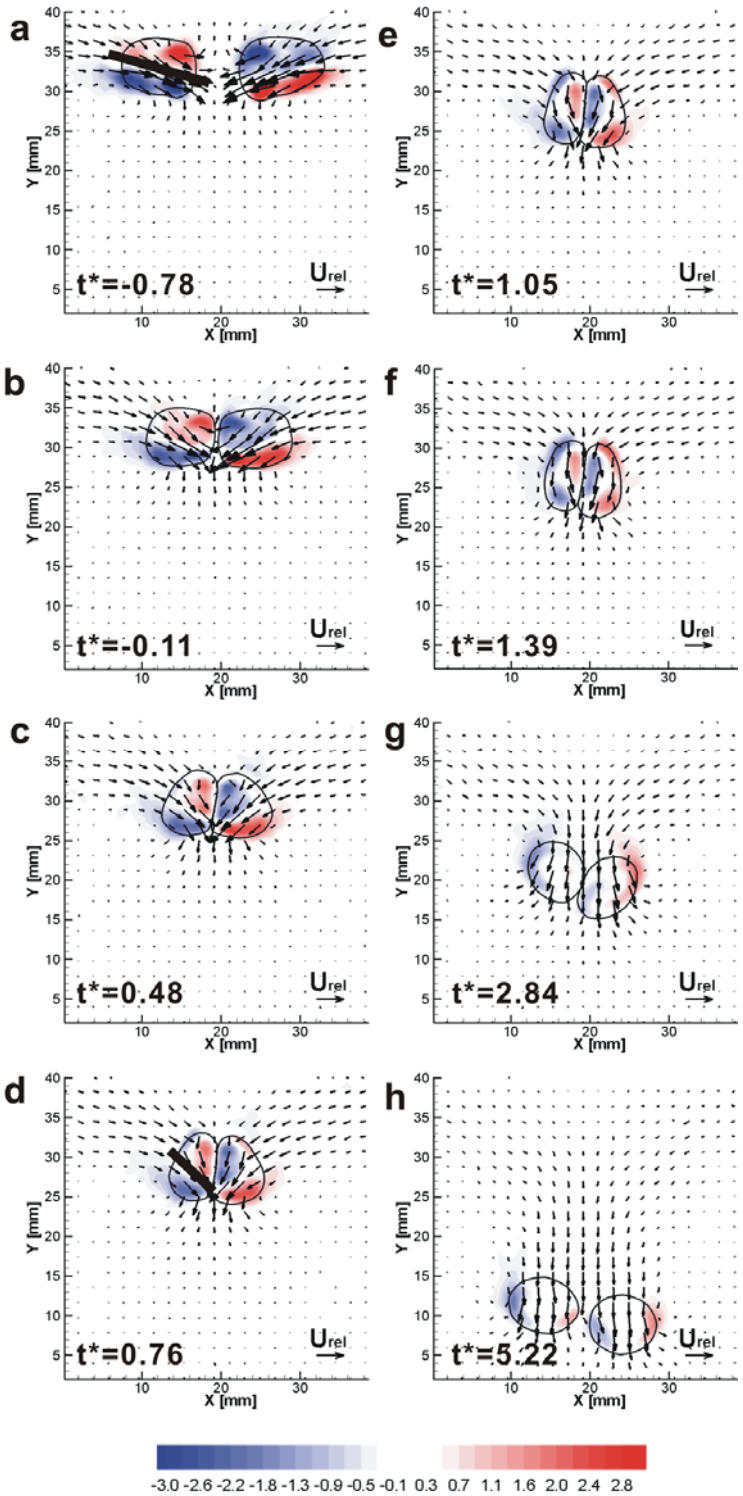


**Figure 3.5** Absolute in-plane velocity vectors and normalized vorticity contours: *We* = 9 (rebound), θ = 32°. Red is counterclockwise, and blue is clockwise.

higher initial injection velocity for *We* = 9. The vectors at t* = 0.76 (Fig. 3.5d) shows that fluid continues to flow toward the centerplane while, for *We* = 4, the vectors point straight downward at t* = 0.79 (Fig. 3.4e). When *We* = 9, the vectors directed downward at t* = 1.05 (Fig. 3.5e) when the drops reach the maximum film length. The downward vectors are somewhat (but, not significantly) directed toward the intervening film.

Normalized vertical velocity contours are plotted in Figs. 3.6 and 3.7 to emphasize patterns of local upflow and downflow as the drops collide in both cases. In the color map, blue represents strong downflow while red is upflow. In both cases, fluid is pushed upward in the zone immediately above the colliding drops (Figs. 3.6a and b, and Figs. 3.7a and b). Meanwhile, two local maxima in downward velocity are observed throughout each sequence shown.

The detailed view of thin film between colliding drops was investigated. Rebounding cases for *We* = 4 and 9 from the small field of view were compared in Figs. 3.8 and 3.9. These images were taken at the time that the film length in the vertical direction was first maximized. For comparison with the large field of view (Figs. 3.4 and 3.5), Figs. 3.8a and 3.9a correspond with t* = 0.79 (Fig. 3.4e) and Figs. 3.8b and 3.9b correspond with t* = 1.05 (Fig. 3.5e). Note that the magnitudes of vorticity and velocity are sometimes higher in these cases than the ones in Figs. 3.4 and 3.5 due to finer resolution. Every fourth velocity vector is plotted. In both cases, each drop contains a tilted vortex ring structure that induces flow downward and inward toward the center plane. In Fig. 3.8, the maximum downward velocity of about $1.3U_{rel}$ for *We* = 4 and $0.8U_{rel}$ for *We* = 9 occurs in the streaming region inside of each vortex ring. Figure 3.9 shows contours of the local vertical velocity component and vectors for the same times in the falling drop reference frame. In these plots, the drop falling velocity has been subtracted from the field. As previously, magnitudes are normalized by $U_{rel}$. In the color map, blue represents downward velocity while red is upward. In this reference frame, which is close to the reference frame moving with the internal drop vortices, the vectors near each core have circulating patterns. In the *We* = 4 rebounding case, the maximum downward velocity of $0.6U_{rel}$ occurs well away from the interface

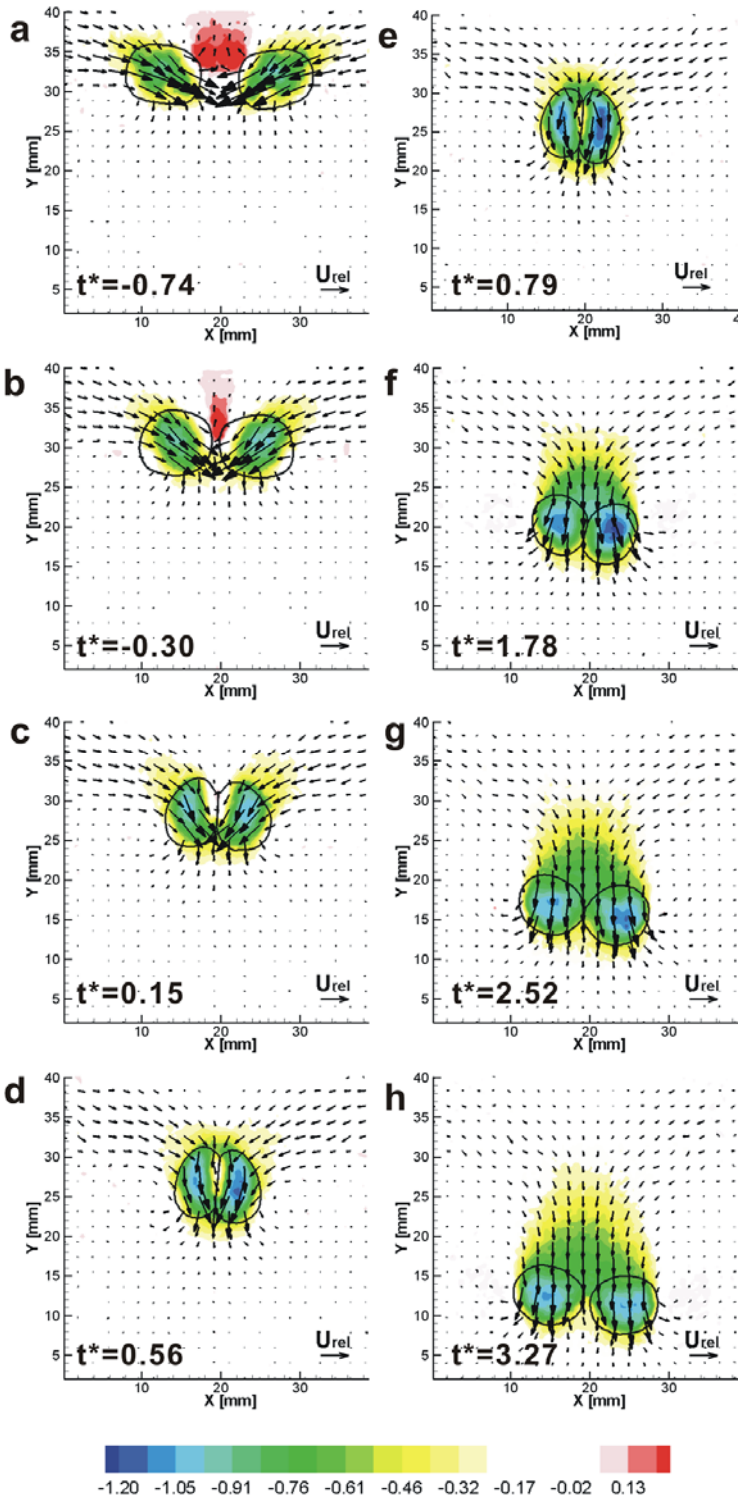


**Figure 3.6** Absolute in-plane velocity vectors and vertical velocity contours: *We* = 4 (rebound), θ = 45°. Red is upflow, and blue is downflow.

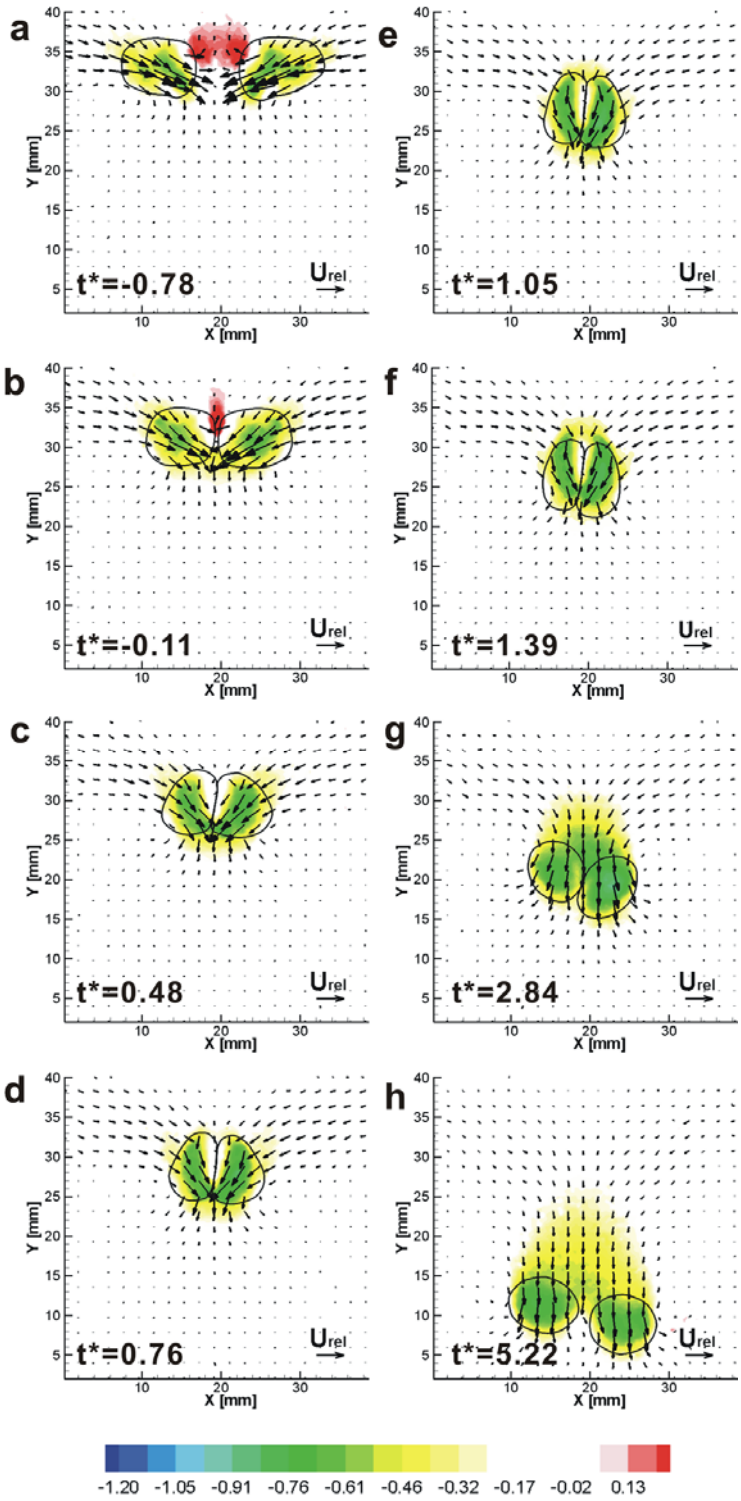


**Figure 3.7** Absolute in-plane velocity vectors and vertical velocity contours: *We* = 9 (rebound), θ = 32°. Red is upflow, and blue is downflow.

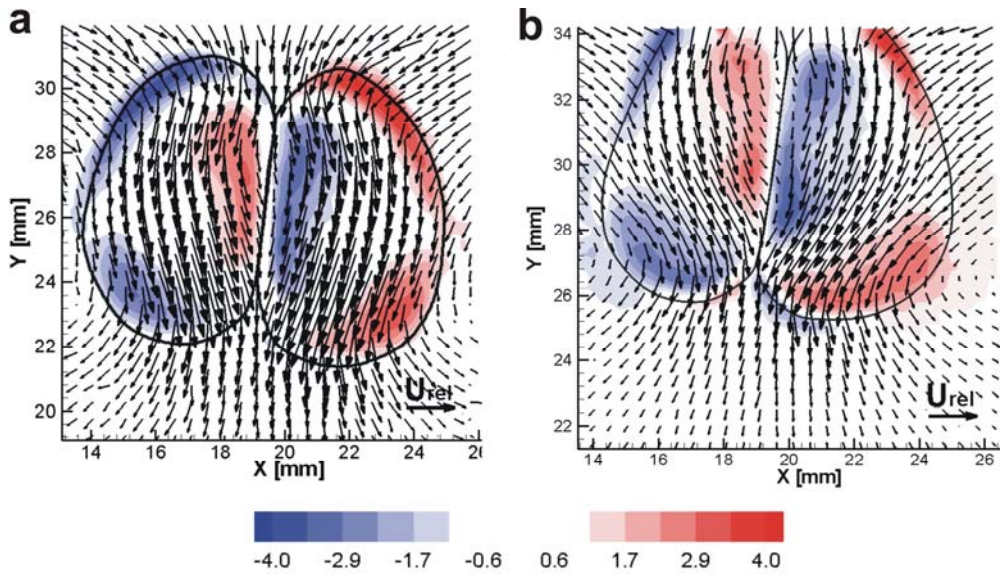


**Figure 3.8** Vector and vorticity fields at the time of maximum film length for rebound: (a) *We* = 4 (t* = 0.79) and (b) *We* = 9 (t* = 1.05). Field of view is 13 × 13 mm$^2$. Vectors show absolute velocity. Colors show normalized vorticity. Red is counterclockwise, and blue is clockwise.

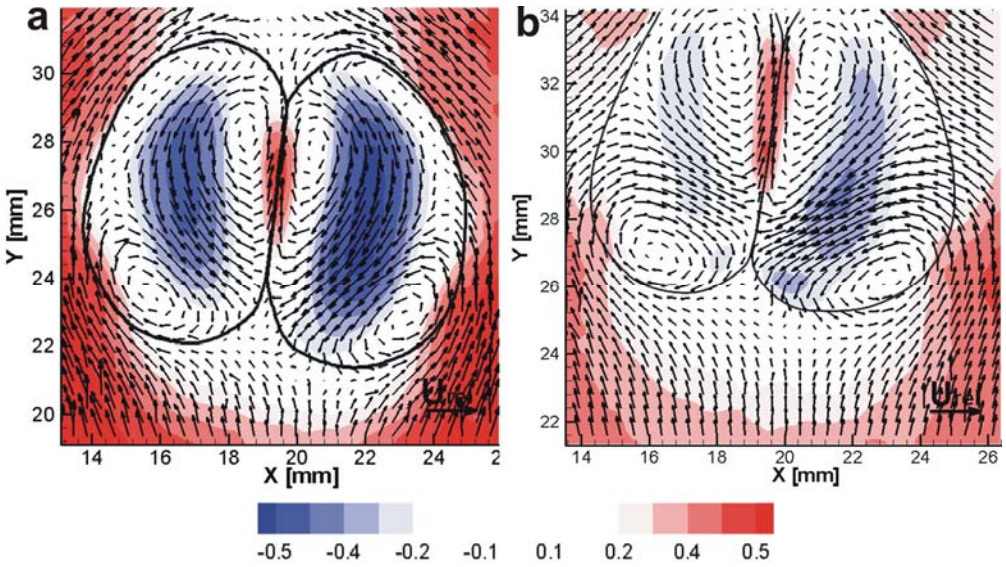


**Figure 3.9** Vector and vertical velocity fields at the time of maximum film length for rebound: (a) *We* = 4, θ = 45° (t* = 0.79), and (b) *We* = 9, θ = 32° (t* = 1.05). Vectors show in-plane velocity relative to falling drops. Colors show normalized vertical velocity relative to falling drops. Red is upflow, and blue is downflow.

while the maximum upward velocity of $0.48U_{rel}$ occurs near the center plane. For *We* = 9, which represents approximately the largest *We* value resulting in rebounding, the maximum relative downward velocity of $0.37U_{rel}$ occurs closer to, but still away from the interface. The maximum relative upward velocity ($0.44U_{rel}$) is limited to a smaller region on the interface downstream of the corresponding regions for *We* = 4.

In the *We* = 4, θ = 45° rebounding case, each ring is tilted more downward as previously described in Fig. 3.4. By contrast, in the case with the shallower angle (θ = 32°), each ring is tilted more inward (see both Figs. 3.8 and 3.9) so that the downstream and upstream core sections are both located close to the center plane and thin film. The inwardly facing rings induce strong inflows toward the interface. For *We* = 9 (Fig. 3.9b), $U_{rel}$ is 16.9 cm/s so that the local downflow has relative speed $0.37U_{rel}$ = 6.3 cm/s and upflow is 7.4 cm/s. By contrast, the strong local upflow on the interface for *We* = 4 (Fig. 3.9a) which has $U_{rel}$ = 11.5 cm/s is $0.48U_{rel}$ = 5.5 cm/s relative to the drop.

### 3.1.3 Coalescence

Sequences from the 'large' field of view are shown in Figs. 3.10-3.12: a coalescing case with *We* = 15 (D = 0.84 cm, trajectory angle θ = 28°, and $U_{rel}$ = 21.7 cm/s), a coalescing case with *We* = 28 (D = 0.94 cm, trajectory angle θ = 22°, and $U_{rel}$ = 27.7 cm/s) and a coalescing case with *We* = 42 (D = 0.92 cm, trajectory angle θ = 15°, and $U_{rel}$ = 34.5 cm/s). The particles near the bottom of the raw PIV images in Fig. 3.10 appear bigger and brighter than others. This is caused by a local increase in laser sheet intensity due to some reflection from the interface beneath the silicone oil. Before computation of PIV vectors, the varying background intensity was subtracted from each image. Figure 3.12 shows the rebounding case without tracer particles in surrounding fluid.

As the drops approach each other (Fig. 3.10a, t* = -0.78), they are initially elongated with tails due to higher injection velocities. As the drops move closer (Fig.3.10b), their heads flatten, and the tails become less prominent. This is significantly different from a rebound case where the drop shapes are more spherical before collision. After collision (Fig. 3.10c), a flat film of silicone oil continues to

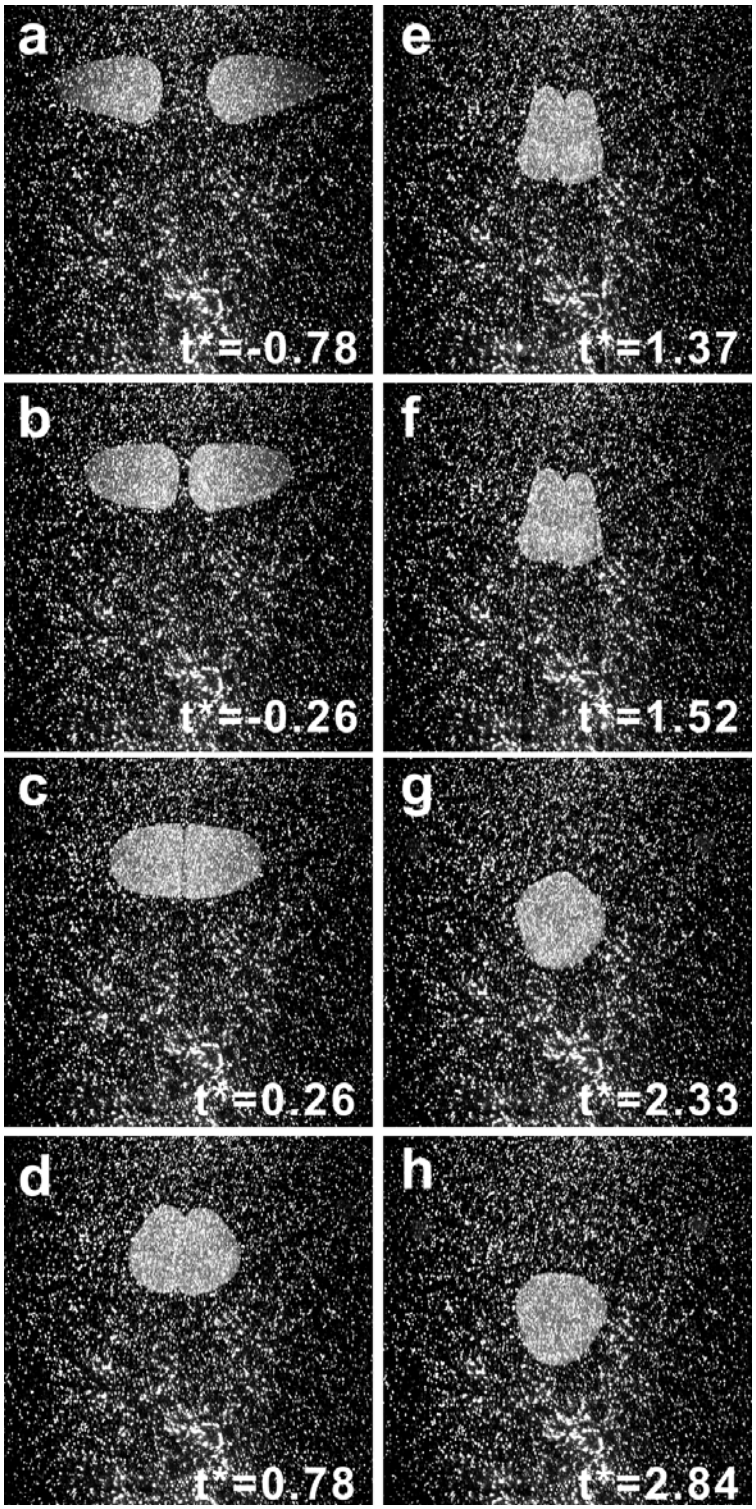


**Figure 3.10** Time evolution of drop collision: *We* = 15 (coalescence), θ = 28°. t* = t$U_{rel}$/D, where D is drop diameter and $U_{rel}$ is relative velocity.

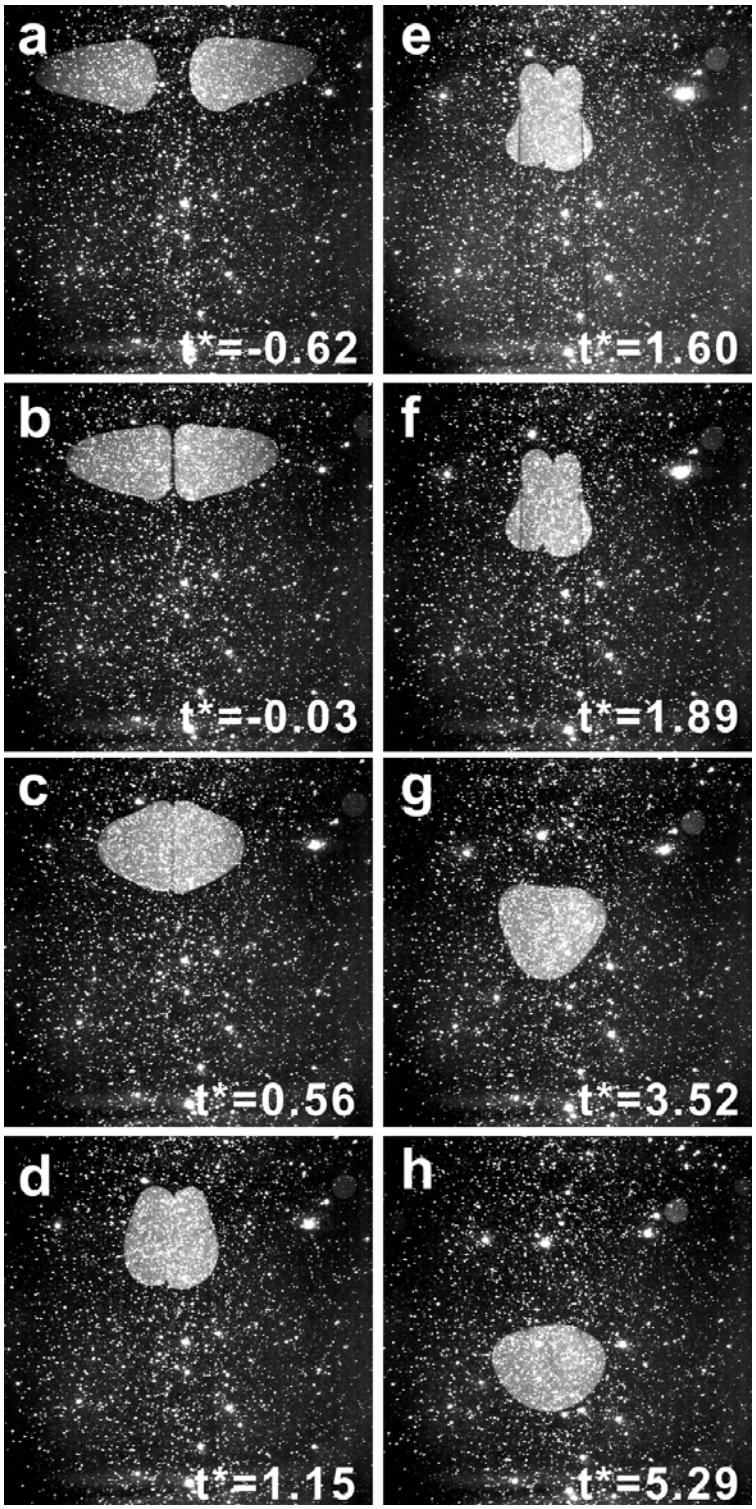


**Figure 3.11** Time evolution of drop collision: *We* = 28 (coalescence), θ = 22°. t* = t$U_{rel}$/D, where D is drop diameter and $U_{rel}$ is relative velocity.

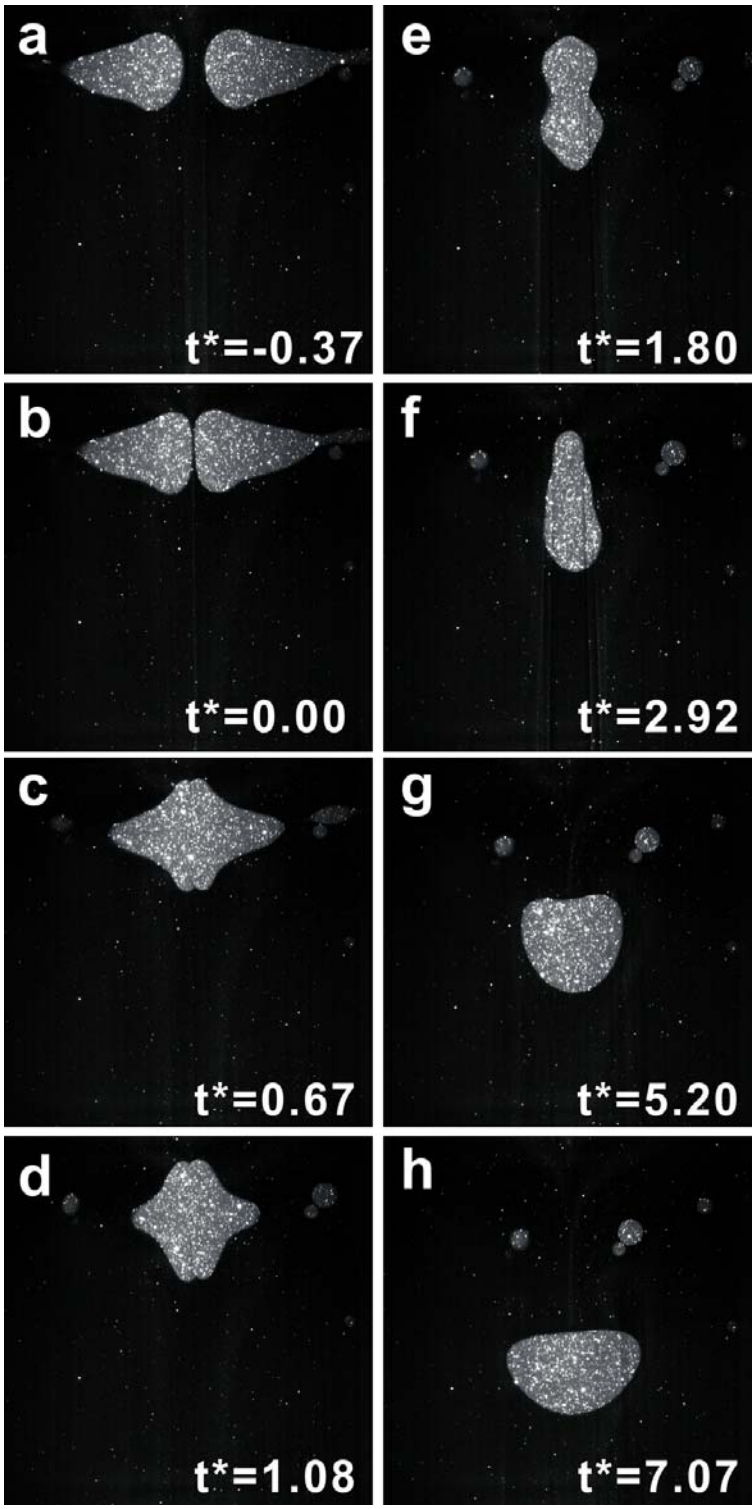


**Figure 3.12** Time evolution of drop collision: *We* = 42 (coalescence), θ = 15°. t* = t$U_{rel}$/D, where D is drop diameter and $U_{rel}$ is relative velocity.

separate the drops. Inertia drives the drop centroids closer together, and the film radius grows while the drops change from prolate to oblate in shape (Fig. 3.10c-e). At this Weber number, the inertia is large enough to generate a local concavity in the curvature (Fig. 3.10e). The film between the drops increases in vertical length until it ruptures at t* = 1.37 (Fig. 3.4e). At t* = 1.52 (Fig. 3.10f), the outer edges of the coalesced drop continues to deform inward. The resulting single drop oscillates in shape as it then falls downward (Figs 3.10g and h). The film rupture will discuss in Section 3.2.

Figure 3.11 shows a coalescence case for *We* = 28. The collision process is similar to the case for *We* = 15, but the drops are more elongated as they approach each other (Fig. 3.11a, t* = -0.62). As the drops move closer (Fig. 3.11b), their heads flatten while the tails are still elongated. The film of silicone oil between the drops reaches a maximum in length at t* = 1.60 (Fig. 3.11e). The drops continuously deform until they coalesce. The intervening film between the drops ruptures at a later time (t* = 1.89, Fig. 3.11e) compared to t* = 1.37 for *We* = 15 (Fig. 3.10e). In absolute time, the time to rupture (t = 53 ms) for *We* = 15 is also shorter than the time (t = 64) for *We* = 28. This is because, for *We* = 28, the drops continue to deform inward after the film between them reaches a maximum in length. For *We* > 15, the deformation is strong enough that the outer side of each drop (distal to the collision location) becomes strongly dimpled before coalescence. In the cut-away view, a local concavity in curvature corresponding with a dimple is easily observed. After the film between the drops ruptures, it takes both longer absolute and dimensionless times for the coalesced drop to oscillate and to form a spherical drop as it falls downward.

For *We* > 30, the coalescence process differs from the previous cases. Figure 3.12 shows a coalescence case with *We* = 42. The initially elongated tails in Fig. 3.12a are still seen in Fig. 3.12d. After collision, the drop heads expand in the vertical direction while the tails move toward the centerplane. Unlike the previous coalescence cases, the drops coalesce at t* = 1.08 (Fig. 3.12d) *before* the drop changes from prolate to oblate in shape. After coalescence, the drop deforms continuously as it expands vertically as shown in Fig. 3.12e (t* = 1.80) and oscillates while it falls. For *We* = 42, the absolute (t = 29 ms) and dimensionless (t* = 1.08) times to rupture are much shorter than for the

previous cases. This is because the approaching velocity is sufficiently high that the drops coalesce before they change their shape.

Cases with $We > 50$ could not be obtained with the 6.1 mm tubes. When the valves and solenoids were adjusted to exceed $We = 50$, a jet of fluid was injected from each tube as shown in Fig. 3.13. Sometimes bubbles of ambient fluid were observed within the resulting drops. Figure 3.13 shows a higher injection velocity case ($We \approx 73$; $U_{rel} \approx 50.92$ cm/s and $D \approx 0.738$ cm). In this case, the liquid volumes do not form drops before impact. After impact, these fluids coalesced and formed a dumbbell shape drop as well as several satellite drops (Fig. 3.13d). The merged drop oscillated and fell downward before becoming spherical as seen in Fig. 3.13h.

One exceptional coalescence case was observed at $We = 3$ as shown in Fig. 3.14. In this case, the drops collided and gently deformed at $t^* = 0.75$ (Fig. 3.14c) similar to the case for $We = 4$ (Fig. 3.2d). While the drops were moving apart, the interface between them suddenly broke, resulting in coalescence at $t^* = 1.58$. Unlike other coalescence cases, the film ruptured in the upper portion of the interface. In other cases, the film ruptured in the lower portion. A similar case was not observed in any previous studies by other researchers. The coalescence mechanism in this case was unclear. Time evolution of velocity vector fields is presented for completeness in Fig. 3.15. Figure 3.16 shows the vorticity and downward velocity contours at the time of rupture at $t^* = 1.58$. The most important point to note is that there are two local downflow maxima through the entire sequence which is exceptional compared with all other coalescence cases examined.

Figures 3.17-3.19 show the computed velocity vectors and vorticity contours for $We = 15$, 28 and 42, respectively (every sixth vector is plotted). Velocity magnitudes and vectors are normalized by the relative velocity, $U_{rel}$. The vorticity is nondimensionalized using $U_{rel}$ and drop diameter. Red on the color map shows counterclockwise rotation of flow, and blue represents clockwise rotation.

For $We = 15$, a leading and trailing vortex ring are apparent in each of the initially elongated drops (Fig. 3.17a). At this time, the leading ring appears more focused than the trailing one. The average vorticity in the leading ring is $\sim 3.9 U_{rel}/D$ while the value

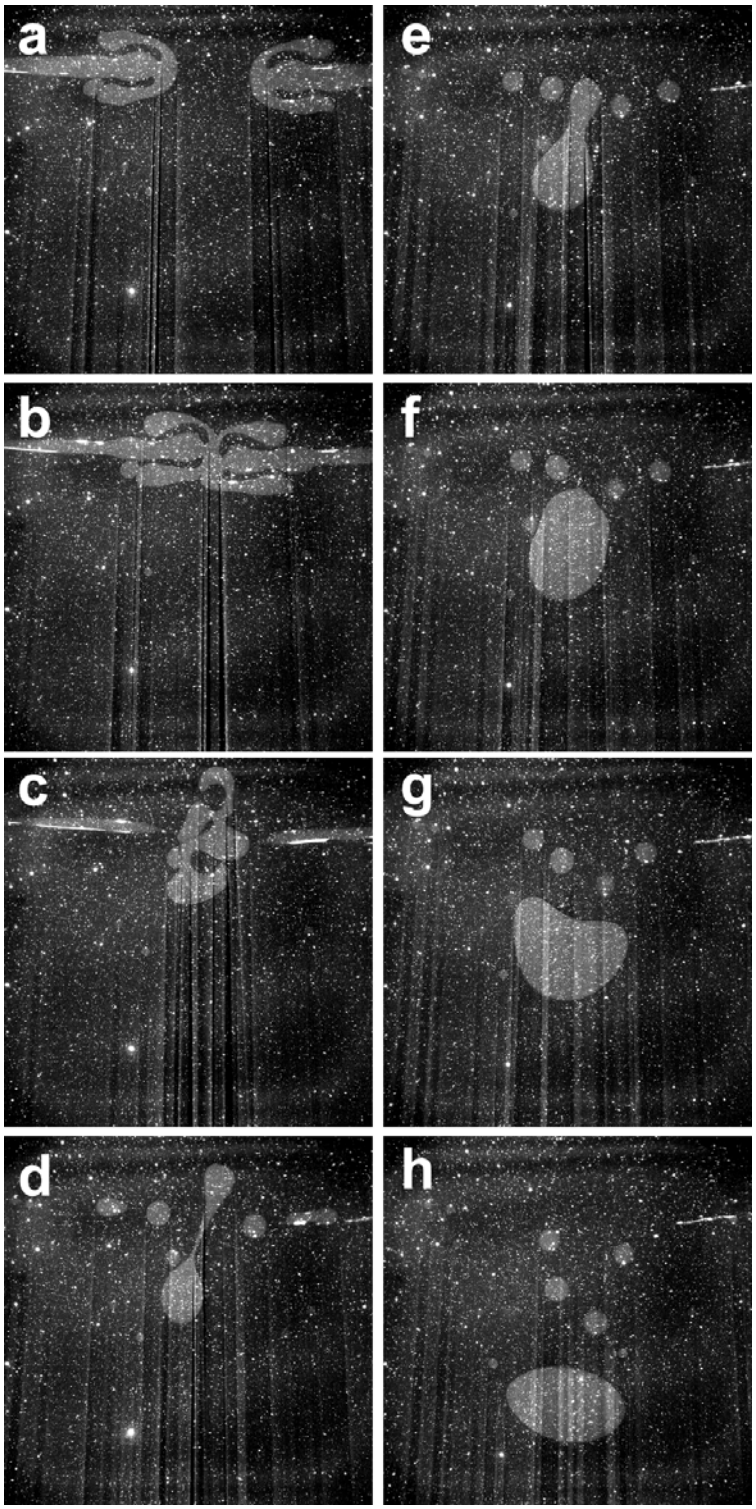


**Figure 3.13** The evolution of drop collision for *We* ≈ 73 (coalescence).

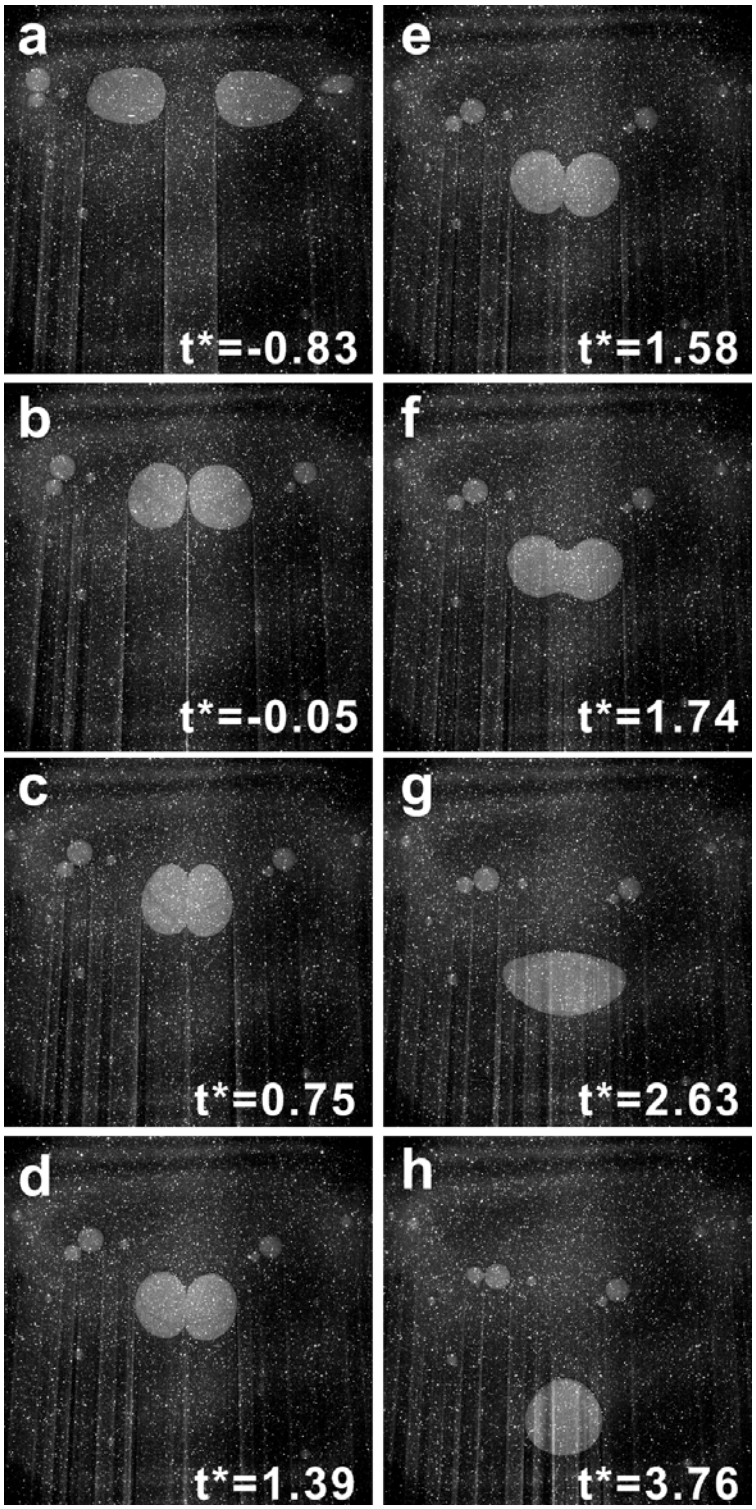


**Figure 3.14** Time evolution of drop collision: *We* = 3 (coalescence), θ = 49°. t* = t$U_{rel}$/D, where D is drop diameter and $U_{rel}$ is relative velocity.

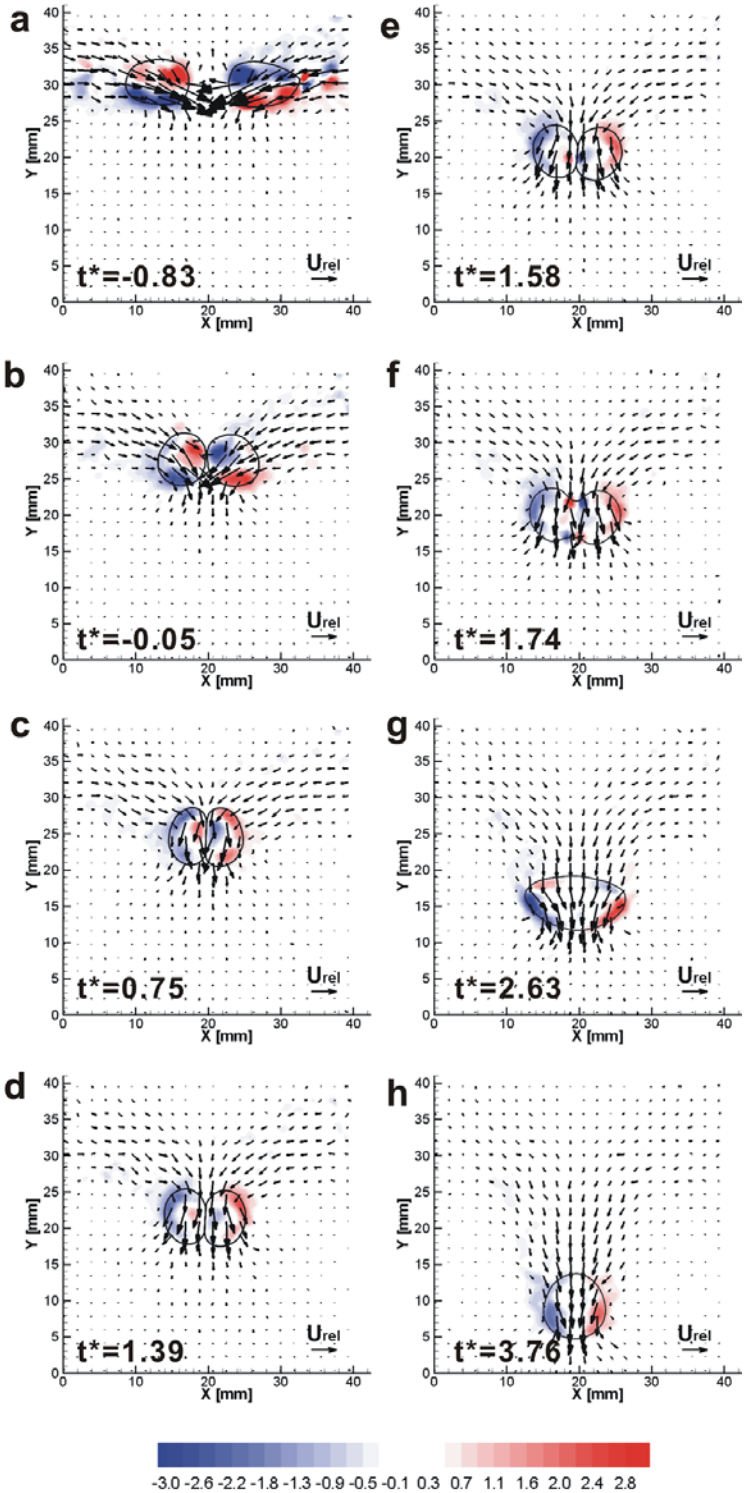


**Figure 3.15** Absolute in-plane velocity vectors and normalized vorticity contours: *We* = 3 (coalescence), θ = 49°. Red is counterclockwise, and blue is clockwise.

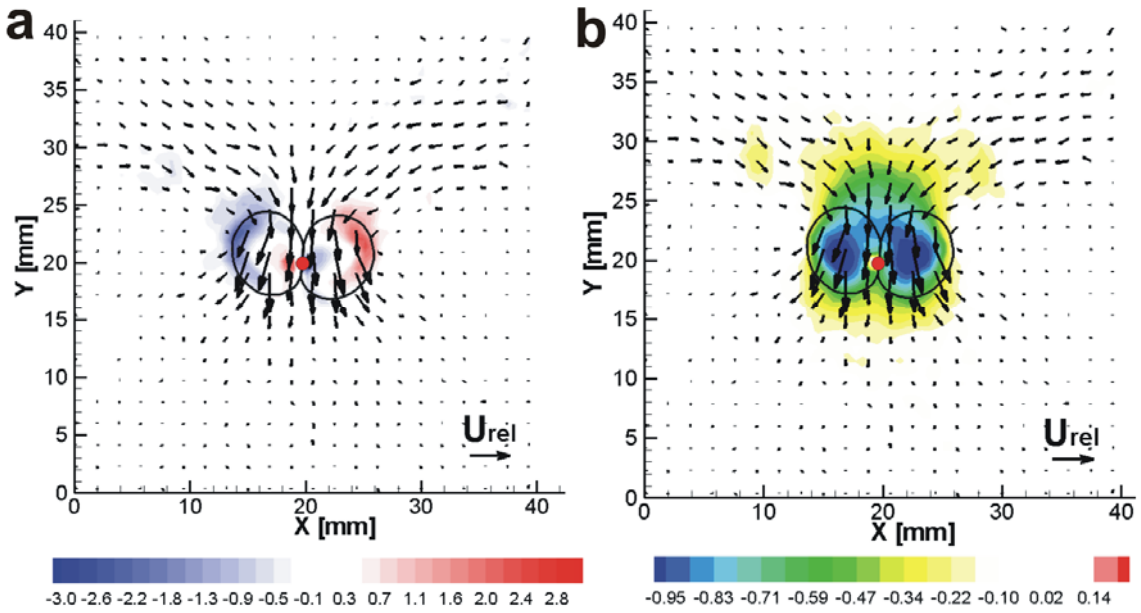


**Figure 3.16** Velocity vectors at the time of rupture (t* = 1.58) for *We* = 3 (coalescence): (a) Normalized vorticity contours. Red is counterclockwise, and blue is clockwise. (b) Normalized vertical velocity contours. Red is upflow, and blue is downflow. Vectors show absolute in-plane velocity. Red dots show the film rupture location.

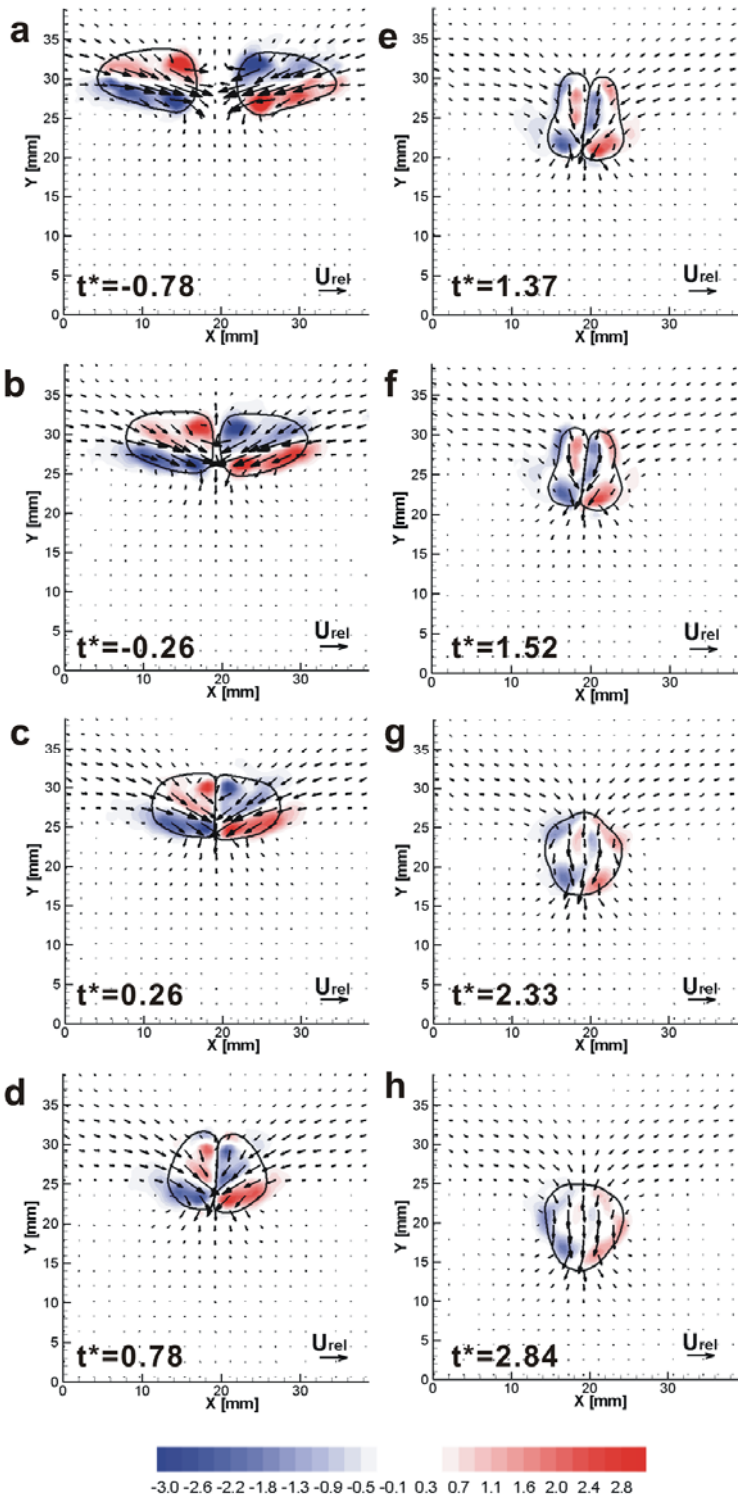


**Figure 3.17** Absolute in-plane velocity vectors and normalized vorticity contours: *We* = 15 (coalescence), θ = 28°. Red is counterclockwise, and blue is clockwise.

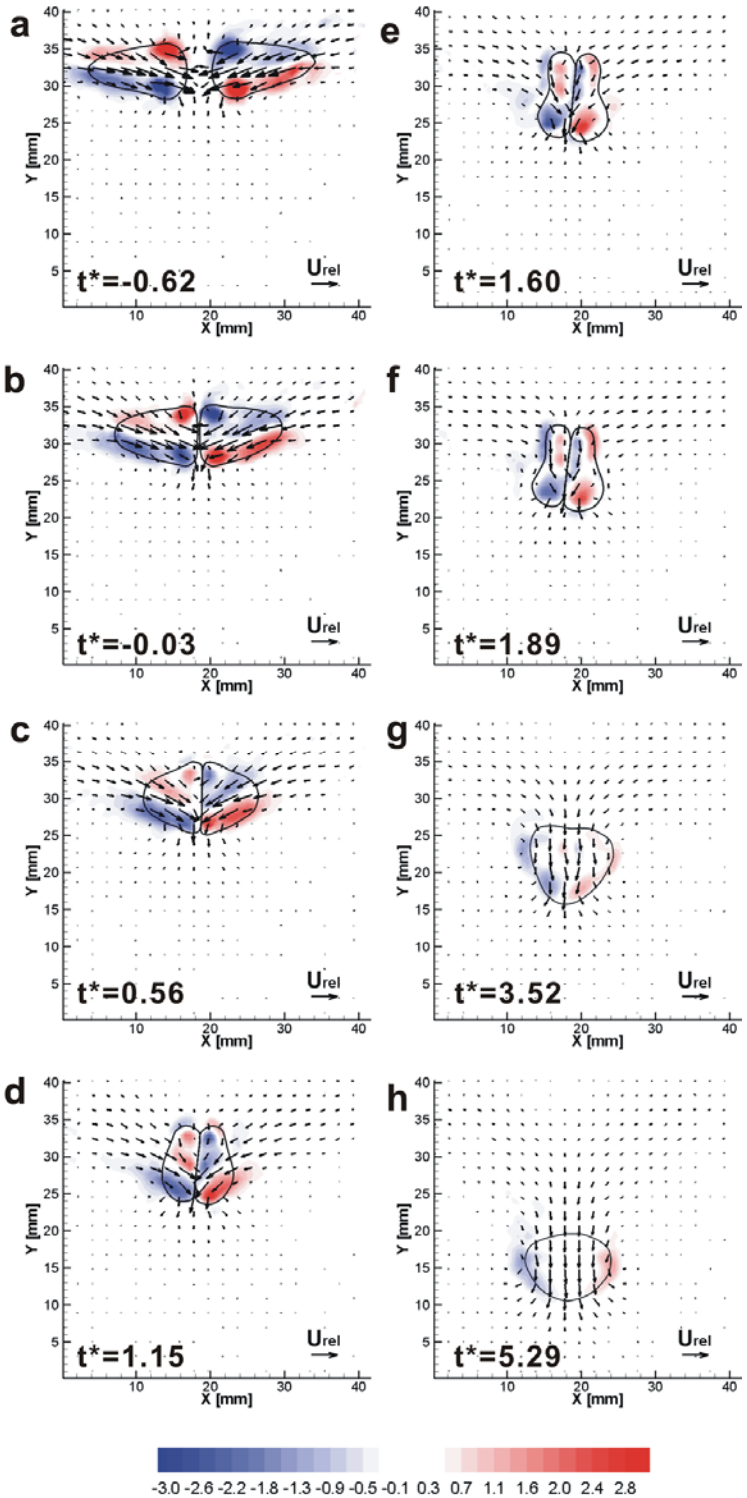


**Figure 3.18** Absolute in-plane velocity vectors and normalized vorticity contours: *We* = 28 (coalescence), θ = 22°. Red is counterclockwise, and blue is clockwise.

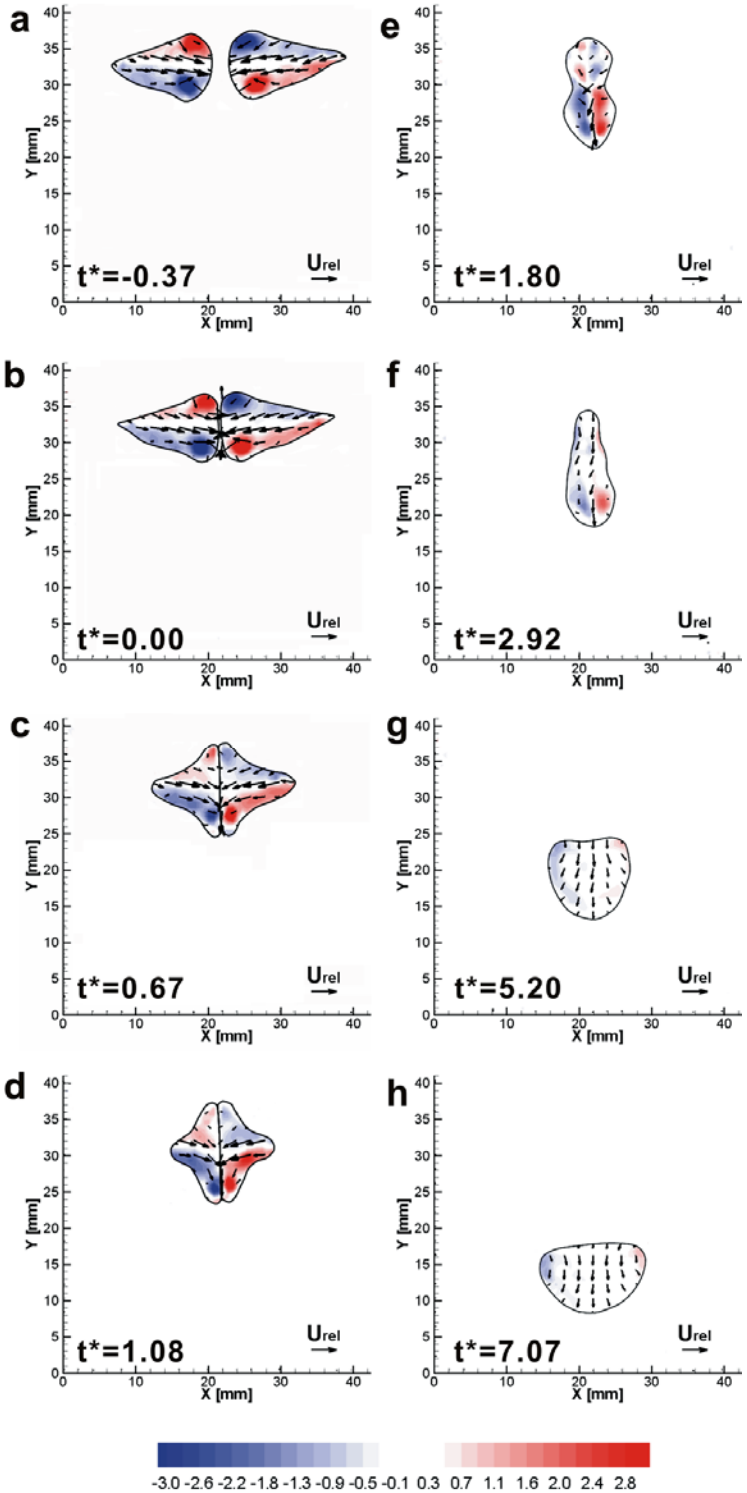


**Figure 3.19** Absolute in-plane velocity vectors and normalized vorticity contours: *We* = 42 (coalescence), θ = 15°. Red is counterclockwise, and blue is clockwise.

in the trailing one is $2.0U_{rel}$/D. However, the trailing ring is spread over a slightly larger area suggesting a significant overall circulation. As the drops collide and start to deform, the higher velocity toward the rear of each drop pushes the trailing fluid closer to the interface. Note that the trailing ring moves forward asymmetrically (top to bottom) as the drop shape changes (Figs. 3.17b-e) resulting in a broader shape near the bottom of each drop and simultaneously an asymmetrical vorticity pattern. The lower portions of the leading and trailing ring appear to overlap or merge, while the upper ends remain distinct (see Fig. 3.17d). Over the same time period, the velocity vectors show that the intervening silicone oil is draining out of the zone between the drops. Also, the fluid streaming through the rings appears to rotate downward somewhat due to the downward drop trajectories before the time of film rupture. The resulting vortex ring structure (and the individual drops) do not rotate significantly during the collision because of the shallow initial trajectory angle of the drops ($\theta$ = 28°). Note that the lower portion of the leading vortex ring lies close to the interface in the coalescing case (Fig 3.17e). The maximum vorticity value in the field decreases as the drops decelerate after impact from ~$4.4U_{rel}$/D at t* = -0.78 to ~$3.0U_{rel}$/D at t* = 1.37. At t* = 1.37, the interface ruptures, and the downflow downstream of the rupture location increases and the interface above the rupture location retracts upward at t* = 1.52 (this effect is not clear in Fig. 3.17f, but will be discussed later in Section 3.2). Afterward, some of the upstream vorticity is dissipated leaving a pattern indicative of a single leading downward-moving ring as shown in Figs. 3.17g and h.

For *We* = 28, a trailing vortex ring apparently stands apart from a leading vortex ring in each of the initially elongated drops (Fig. 3.18a). The leading ring appears more focused than the trailing one similar to the coalescence for *We* = 15. Similar to *We* = 15, the average vorticity in the leading ring is ~$4.2U_{rel}$/D while the value in the trailing one is $1.8U_{rel}$/D. When the drops collide at t* = -0.03 (Fig. 3.18b), the vorticity in the lower portion of the trailing ring ($2.3U_{rel}$/D) is stronger than in the upper portion ($1.2U_{rel}$/D) while the average vorticity in the upper and lower portion of leading ring is similar ($3.2U_{rel}$/D). This trend is similar to *We* = 15: at t* = -0.26 (Fig. 3.17b), the vorticity in the lower portion of the trailing ring ($2.5U_{rel}$/D) is stronger than in the upper portion

(1.3$U_{rel}$/D) while the average vorticity in the upper and lower portion of leading ring is similar (2.9$U_{rel}$/D). This is because the rear part of each drop moves downward relative to the collision interface as each drop compresses. For *We* = 28, when the interface ruptures at t* = 1.89 (Fig. 3.18f), the vortex ring lies closer to the interface than for *We* = 15 (Fig. 3.17e) because of stronger drop deformation. The maximum vorticity value in the field decreases as the drops decelerate after impact from ~4.4$U_{rel}$/D at t* = -0.78 to ~3.0$U_{rel}$/D at t* = 1.37.

The velocity vectors and vorticity contours are different for *We* = 42. The drop shape and vortex ring inside of each drop are nearly symmetric about the horizontal until the drops coalesce at t* = 1.08 (Fig. 3.19d). Similar to previous cases, the average vorticity in the leading ring is ~4.4$U_{rel}$/D while the value in the trailing one is 1.1$U_{rel}$/D at t* = -0.37 (Fig. 3.19a). However, unlike in previous cases, at t* = 0 (Fig. 3.19b), the vorticity in both lower and upper portions of the trails is approximately 1.4$U_{rel}$/D while the lower portion of the leading ring (4.5$U_{rel}$/D) is stronger than the upper portion (3.2$U_{rel}$/D). This is probably because the collision angle is shallower ($\theta$ = 15° compared to $\theta$ = 28° for *We* = 15 and $\theta$ = 22° for *We* = 28), such that the drops do not rotates significantly as they collide. The lower portion of the leading ring becomes relatively stronger as the overall drop velocity becomes more vertical than horizontal (Figs. 3.19c and d). In Figs. 3.19a-d, the trailing vorticity does not dissipate until the film ruptures. The upper portion of the leading ring dissipates when the drops coalesce in Fig. 3.19d.

Normalized vertical velocity contours are plotted in Figs. 3.20-3.22 to emphasize patterns of local upflow and downflow as the drops collide in both cases. In the color map, blue represents strong downflow while red is upflow. The local upflow is observable until t* = 0.78 for *We* = 15 (Fig. 3.20d), t* = 1.15 for *We* = 28 (Fig. 3.21d), and t* = 1.08 for *We* = 42 (Fig. 3.22d). This upflow can be seen over a longer period as initial inertia increases and collision angle decreases (the upflow can be observed until film ruptures for *We* = 42). As the drops approach and collide, the upflow region gets smaller as the fluid layer between the drops drains. Also, in contrast with the rebounding cases shown previously, only one maximum in downward velocity near the

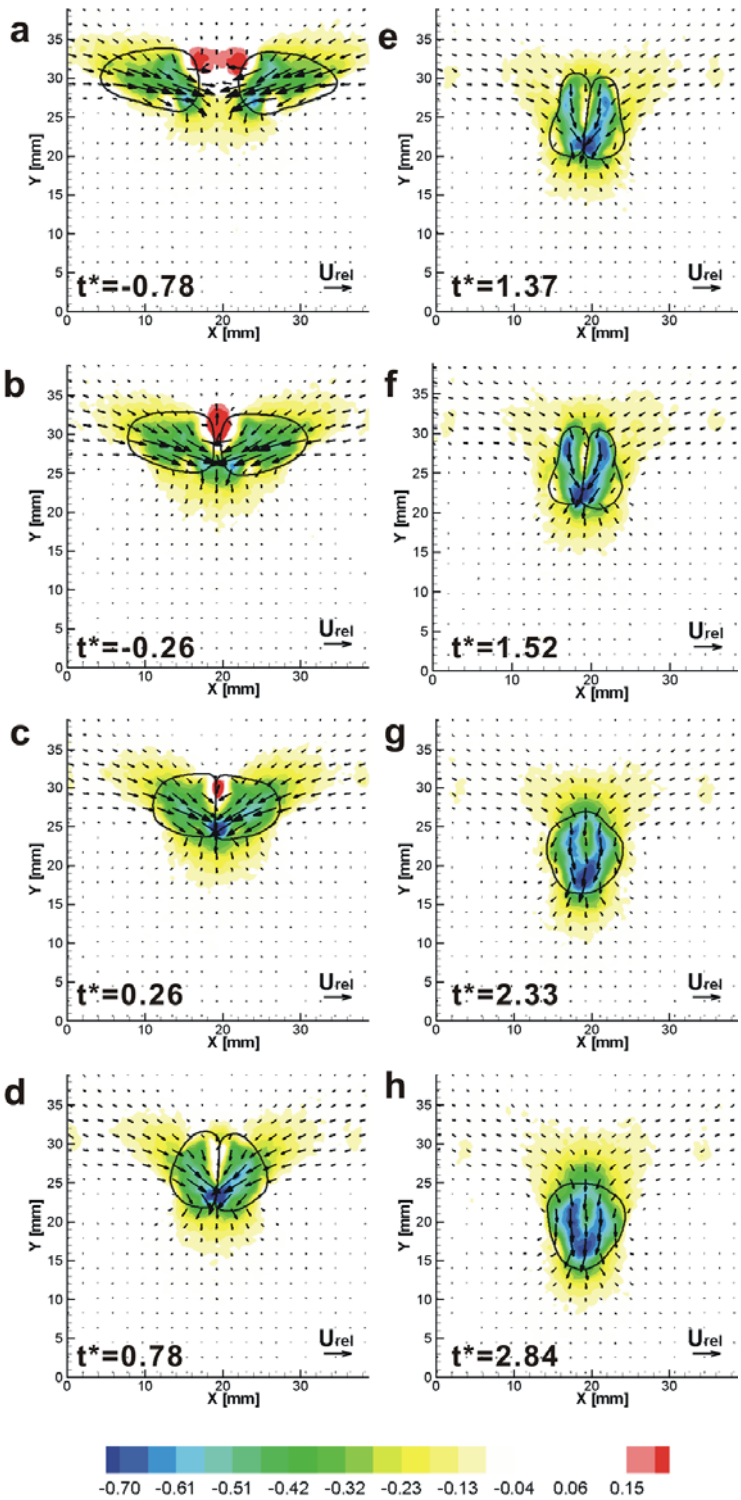


**Figure 3.20** Absolute in-plane velocity vectors and vertical velocity contours: *We* = 15 (coalescence), θ = 28°. Red is upflow, and blue is downflow.

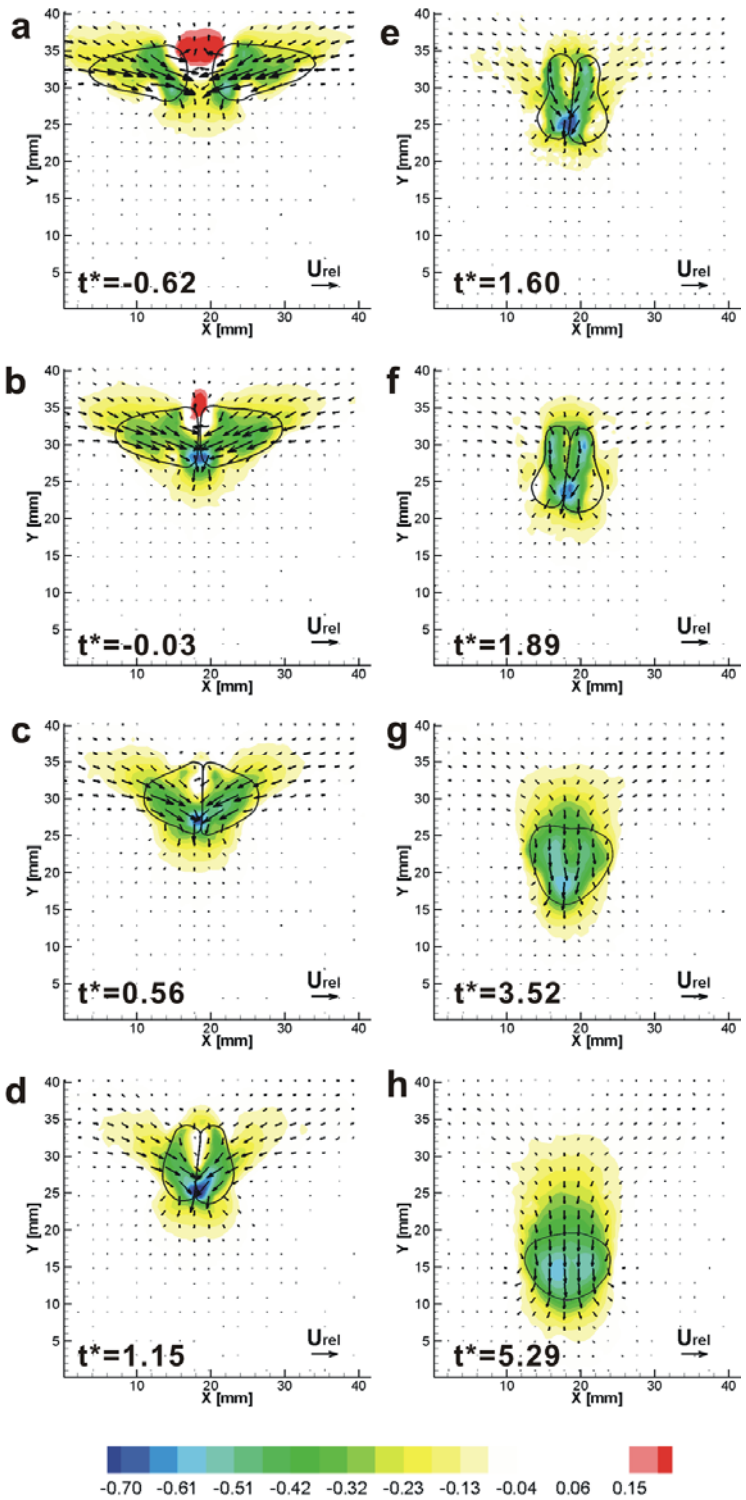


**Figure 3.21** Absolute in-plane velocity vectors and vertical velocity contours: *We* = 28 (coalescence), θ = 22°. Red is upflow, and blue is downflow.

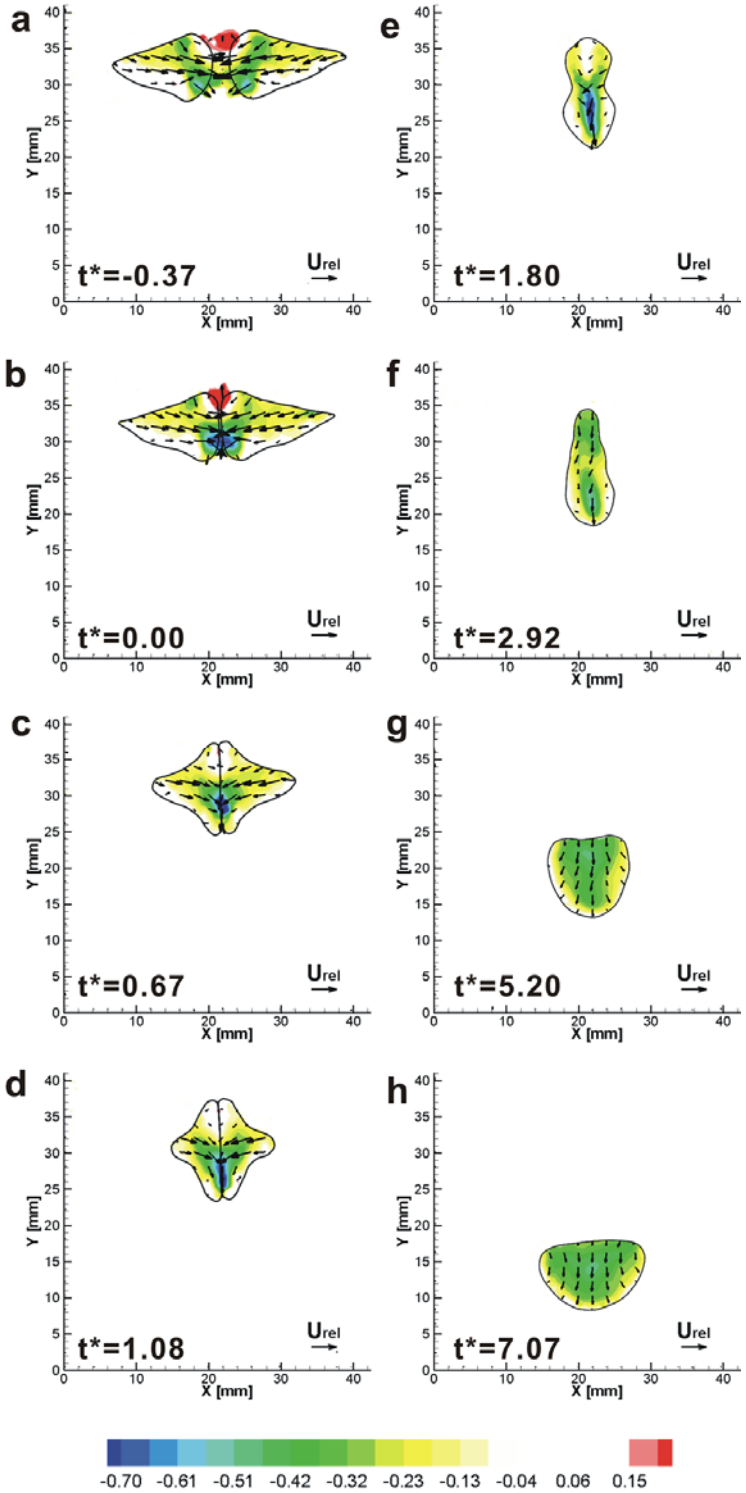


**Figure 3.22** Absolute in-plane velocity vectors and vertical velocity contours: *We* = 42 (coalescence), θ = 15°. Red is upflow, and blue is downflow.

interface is observed beginning at t* = -0.26 for *We* = 15 (Fig. 3.20b), t* = -0.03 for *We* = 28 (Fig. 3.21b), and t* = 0.00 for *We* = 42 (Fig. 3.22b) well before the film rupture. This difference must be attributed to the stronger horizontal inertia and deformation in the coalescing cases. Note especially that, once the drops have deformed significantly and the film between them appears as a flat interface, the local maximum in downward velocity occurs at the interface in the coalescing cases, but away from the interface in the rebounding cases.

The details of coalescence mechanism and effects of the Weber number and collision angle will be discussed in Section 3.2.

### 3.1.4 Out-of-plane velocity profiles

In general, the out-of-plane velocity component provided by the large field stereo sequences was useful for determining the alignment of drops through collision trajectories such that the direct impact or B = 0 condition was satisfied in the out-of-plane direction. To demonstrate the use of the out-of-plane component, a rebounding case is presented in Fig. 3.23 in which the drops appear to collide in-plane and move apart in the out-of-plane direction. Figure 3.23 shows an image during the rebound and the out-of-plane velocity component.

Figure 3.22(a) is zoomed view from large view. The vectors show in-plane velocity (every third vector is plotted). At this time, the size of the right drop is relatively smaller in the measurement plane than that of the left drop. This is because the right drop moves faster out-of-plane than the left drop. The out-of-plane velocity of the right drop is a maximum of $0.16U_{rel}$ toward the viewer. An approximate out-of-plane velocity was also computed ($0.18_{rel}$) by calculating the drop area change with time over several frames. It suggests that the out-of-plane velocity measurement by PIV is valid. In general, all of the cases presented in this chapter did <u>not</u> have a significant out-of-plane trajectory.

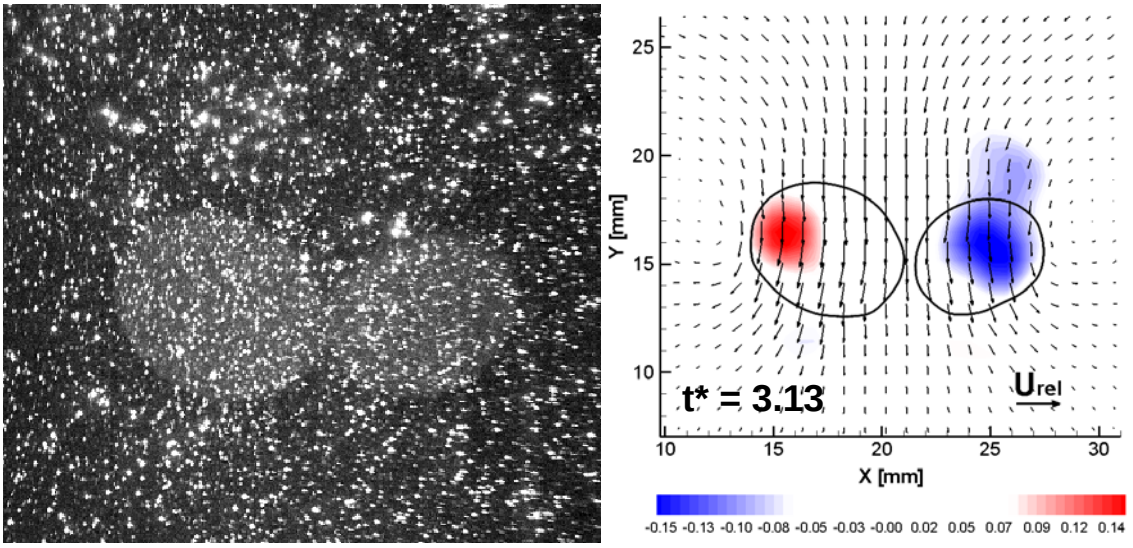


(a) Raw image (b) out-of-plane velocity contour

**Figure 3.23** Out-of-plane velocity when the drops rebound in out-of-plane direction (a rebound with *We* = 8), zoomed view from large field measurements. Color shows normalized out-of-plane velocity. Vectors show absolute in-plane velocity. Blue is toward the viewer, and red is away from the viewer.

The out-of-plane velocity component was also useful in understanding the film rupture process. Figure 3.24 shows the sequence of out-of-plane velocity contours and in-plane vectors shortly before and after film rupture for *We* = 15. In this case, every third vector is plotted. The out-of-plane velocity is generally insignificant before the film breaks (The uncertainty in out-of-plane velocity is of order $0.09U_{rel}$). After the film rupture at t* = 1.37, however, a small zone of out-of-plane velocity (toward the viewer) is observed at the rupture location with maximum magnitude $0.1U_{rel}$. Later at t* = 1.52 (see also Fig. 3.17f), a small zone of out-of-plane velocity moves away from the viewer with magnitude $0.19U_{rel}$ at the location where the ruptured film is retracting upward. At the same time, the downstream section of retracting film (y ~ 20 mm in Fig. 3.24), yields a maximum downward velocity at this resolution of $\sim 0.78U_{rel}$ ($0.46U_{rel}$ relative to the drop falling velocity), and surrounding out-of-plane values are near zero. The velocity gradient normal to the retracting film is so strong that the PIV interrogation areas do not resolve the true film retraction velocity which is of order of

$30U_{rel}$. This velocity is determined by visually tracking particles at the interface and by observing the time between film rupture and the times when the cusped interfaces between the drops become smooth. The pattern observed in this example and other coalescence cases (a local zone with small out-of-plane component followed by another small zone with out-of-plane component in the opposite direction) is consistent with the idea that the film ruptures close to the center of the laser sheet plane, i.e. the plane of symmetry in the flow.

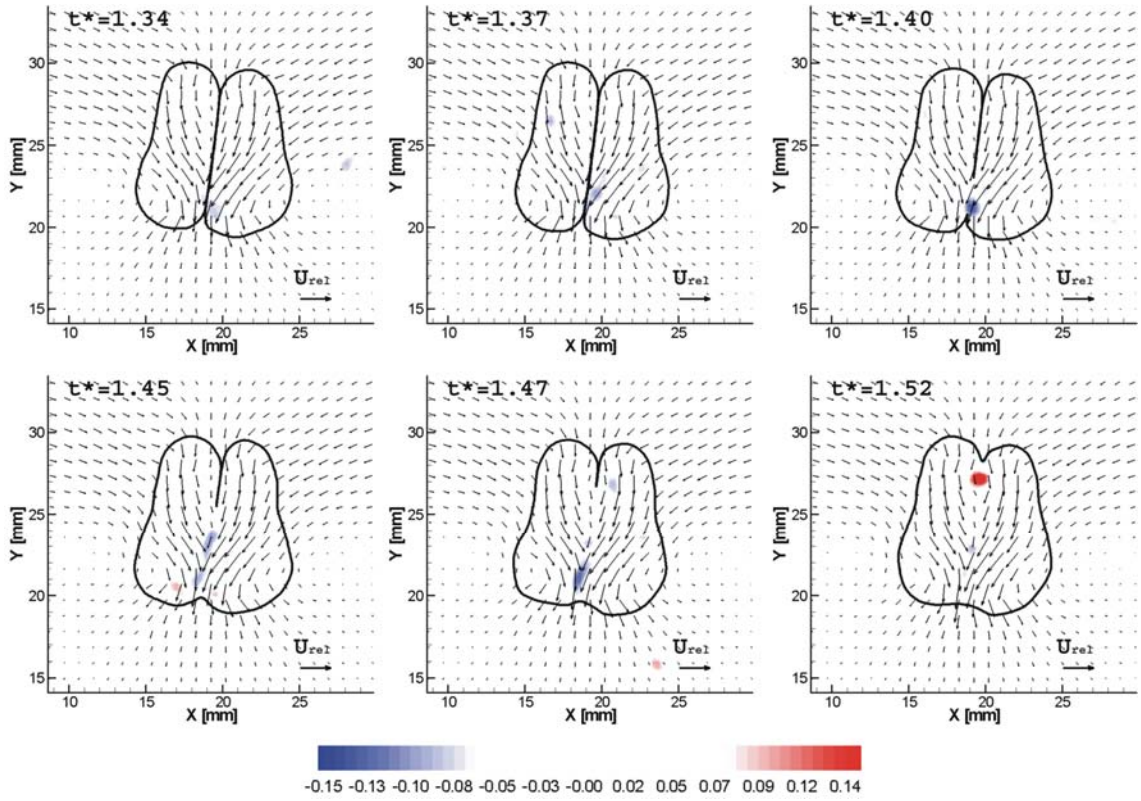


**Figure 3.24** Out-of-plane velocity during the coalescence event (a coalescence with *We* = 15), zoomed view from large field measurements. Color shows normalized out-of-plane velocity. Vectors show absolute in-plane velocity. Blue is toward the viewer, and red is away from the viewer.

By contrast if, due to instabilities for example, the rupture occurred at a location away from the plane of symmetry, out-of-plane velocities associated with the film retraction (all with same direction) through multiple frames would expect to be observed. The

flow sequences of numerous coalescence events with B = 0 were examined, and such organized out-of-plane motion was never observed. Therefore, random instabilities in the flat film between colliding drops probably do not lead to rupture.

### 3.1.5 Variation in kinetic and deformation energy

The variations in kinetic and deformation energy during collisions were considered. The total energy of each drop was assumed as the sum of its kinetic energy and deformation (surface) energy. Only the horizontal component of velocity was considered to compute kinetic energy. Deformation energy is the energy required to change the shape of a drop. Therefore, if the drop is spherical, the deformation energy is zero as discussed in Section 2.5.2. The energy is normalized by surface tension and drop diameter.

In Fig. 3.25, the variation of kinetic and deformation energy during collision sequences is plotted vs. dimensionless time t*. When t* = 0, two drops first touch. A rebounding and coalescing case with similar *We* near the boundary between rebound and coalescence regimes are compared: a rebounding case with *We* = 11 (D = 0.87 cm, trajectory angle $\theta = 34°$, and $U_{rel}$ = 18.3 cm/s), and a coalescing case with *We* = 12 (D = 0.90 cm, trajectory angle $\theta = 32°$, and $U_{rel}$ = 18.8 cm/s). In addition, a coalescing case with *We* = 12 is compared with higher *We* events; a coalescing case with *We* = 28 (D = 0.94 cm, trajectory angle $\theta = 22°$, and $U_{rel}$ = 27.7 cm/s), a coalescing case with *We* = 34 (D = 0.90 cm, trajectory angle $\theta = 16°$, and $U_{rel}$ = 31.6 cm/s), and a coalescing case with *We* = 42 (D = 0.92 cm, trajectory angle $\theta = 15°$, and $U_{rel}$ = 34.5 cm/s).

By comparing a rebound (*We* = 11) and a coalescence (*We* = 12) for similar *We*, the changes in kinetic and deformation energy during the collision event are similar. For both cases, the horizontal kinetic energy dissipates as the drops reach the maximum film length at the center plane. The deformation energy first decreases as the drops approach each other and then increases after the drops touch and deform. In these sequences, each drop changes from prolate to oblate shape. In one case, the drops coalesce at t* = 0.98 shortly after the interface film length is maximum (t* = 0.92) while in the other, the drops deform continuously until t* = 1.05 before rebounding. It is not

clear why one case results in a rebound while the other results in coalescence. It might be because instability arises near the interface when the film length and deformation energy are approximately maximized so that the film ruptures only in some cases. Note that the film length for *We* = 11 (rebound) was maximum at t* = 0.94. In this case, the deformation energy is maximal at t* = 1.05 in Fig. 3.24a, but the bouncing is not observed before this frame. The deformation of the drops continues to increase slightly. The drops start moving apart at t* = 1.32 (t = 63 ms) based on viewing the collision sequence. After t* = 1.32, each drop moves apart and falls downward eventually forming a spherical shape and decreasing the deformation energy.

The comparison of four coalescence cases (*We* = 12, 28, 34, and 42) in Fig. 3.25 reveals the effect of Weber number on the energy. In Fig. 3.25, for *We* = 12, the horizontal kinetic energy decreases as the drops collide and continues to decrease until the drops reach the maximum film length and coalesce (t* = 0.98). For *We* = 28, the kinetic energy of $3.61\sigma D^2$ at t* = -0.89 and decreases to lose its horizontal inertia at t* = 1.77 after the film between the drops is maximal at t* = 1.60. Kinetic energy for *We* = 28 took longer t* (t* = 1.77) to lose its inertia than *We* = 12 (t* = 0.98 when the film ruptures). Although it is not shown in Fig. 3.25, the initial kinetic energy is higher for *We* = 34 than for *We* = 28. The kinetic energy decreases as drops collide and compress each other. However, for this case (also for *We* = 42), the film ruptures before the drops lose all the horizontal kinetic energy. The kinetic energy for *We* = 28 is $0.19\sigma D^2$ at t* = 1.2 when the film ruptures. For *We* = 42, the kinetic energy at t* = -0.22 is $4.59\sigma D^2$ and sharply decreases to $0.89\sigma D^2$ until the film ruptures at t* = 1.08.

The drop deformation increases with an increase of *We* as shown in Fig. 3.25. The deformation energy for *We* = 12 is $0.19\sigma D^2$ at t* = -0.80: the drops are initially elongated with tails. This energy is minimal ($0.07\sigma D^2$) at t* = 0.04 when the drops first touch. Then, the deformation energy increases while the drops change to oblate shape. When the film ruptures, the deformation is $0.28\sigma D^2$ at t* = 0.98. For *We* = 28, the energy at t* = -0.89 is $0.33\sigma D^2$ and decreases to $0.19\sigma D^2$ at t* = 0.44. The energy then increases until t* = 1.63 and then decreases again. At t* = 1.89, the drops coalesce. Note that, for *We* = 28, the drops coalesced when they start moving apart. In Fig. 3.25,

the deformation energy for *We* = 34, unlike for *We* = 12 and 28, increases continuously over the range t* = -0.35 to 0.71. For *We* = 34, the maximum deformation energy ($0.62\sigma D^2$) is similar value to *We* =28 ($0.60\sigma D^2$), but time to reach the maximum deformation energy is earlier than for *We* = 28 (the deformation energy for *We* =34 is maximal at t* = 0.71). After that, the energy decreases until the film ruptures at t* = 1.2. The case with *We* = 42 starts with even higher deformation energy ($0.19\sigma D^2$ at t* = -0.22) than the other cases. Deformation energy for *We* = 42 is much higher than other cases. Because the drops still have long tails at the time of coalescence while, for lower *We* cases, the drops change to oblate shapes. The energy increases without decreasing starting near when the drops first touch (t* = 0). The deformation energy is maximum ($1.2\sigma D^2$) at t* = 1.08 when the film ruptures. The inertia of the drop significantly affects the compression of the drops so that the deformation energy sharply increases as the kinetic energy distinctly decreases.

Figure 3.26 shows the same plot as Fig. 3.25, but a different dimensionless time $t_{max}$ is used. $t_{max}$ is similarly normalized by the relative velocity and drop diameter. When $t_{max}$ = 0, the interface film length of the drops is maximum. $t_{max}$ does not represent the maximum deformation of drop during collisions, but it approximately gives an idea how much the drops deform before they coalesce. The drops coalesce either after they reach the maximum film length ($t_{max}$ = 0) or when $t_{max}$ = 0. In Fig. 3.26, the kinetic energy for *We* = 28 collapses with *We* = 11 and 12. The *We* = 34 and 42 cases do not collapse. This is because the drop shape evolution is <u>different</u> during the coalescence event for *We* > 30. The tails of the drops for *We* = 34 and 42 remain at the time of coalescence (see Fig. 3.12 for *We* = 42) and inertia continuously drives the fluid to the center. By contrast, the drops change from prolate to oblate before they coalesce for *We* < 30. Therefore, any trails have disappeared by the coalescence time. The deformation energy increases as *We* increases. The deformation energy is maximal near $t_{max}$ = 0 except for *We* = 34. For coalescence, the film ruptures either at $t_{max}$ = 0 or shortly after.

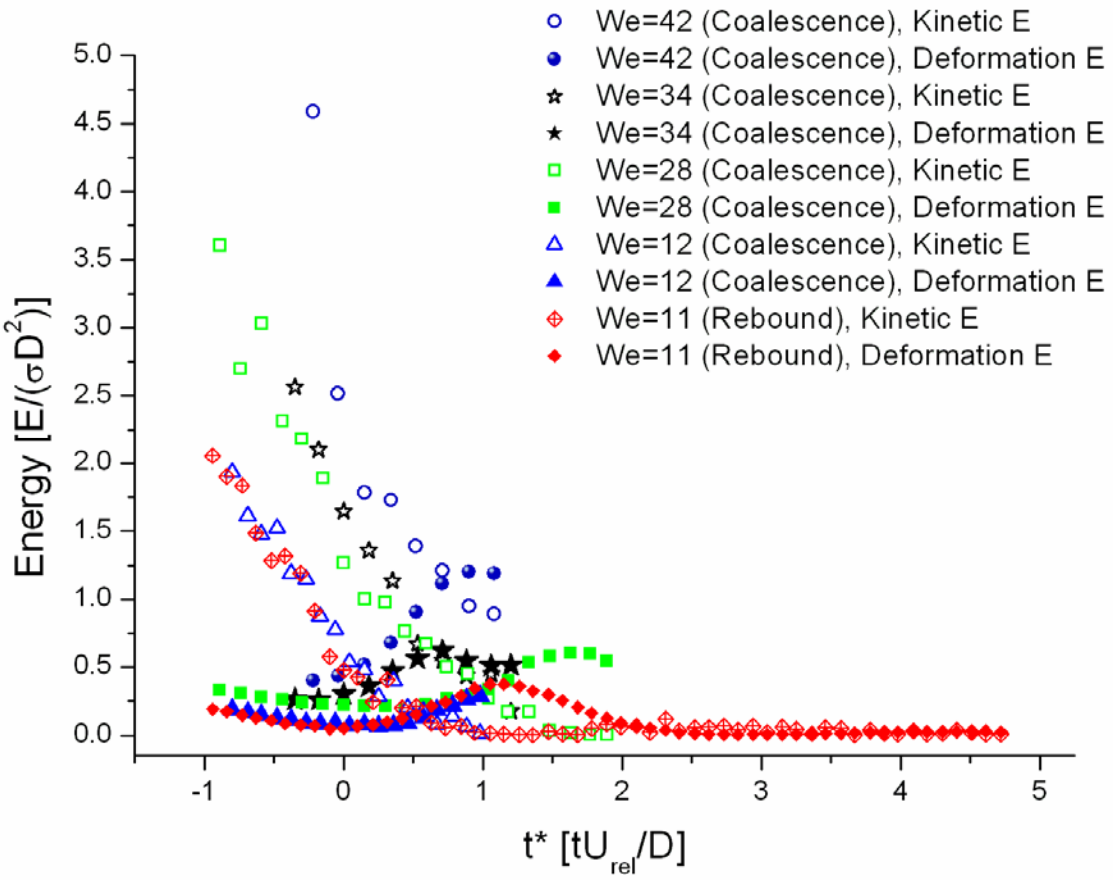


**Figure 3.25** Time evolution of kinetic and deformation energy of a drop. Open symbol is kinetic energy at the time of frame. Solid symbol is deformation energy at the time of frame. t* = t$U_{rel}$/D where D is diameter of drop and $U_{rel}$ is relative velocity.

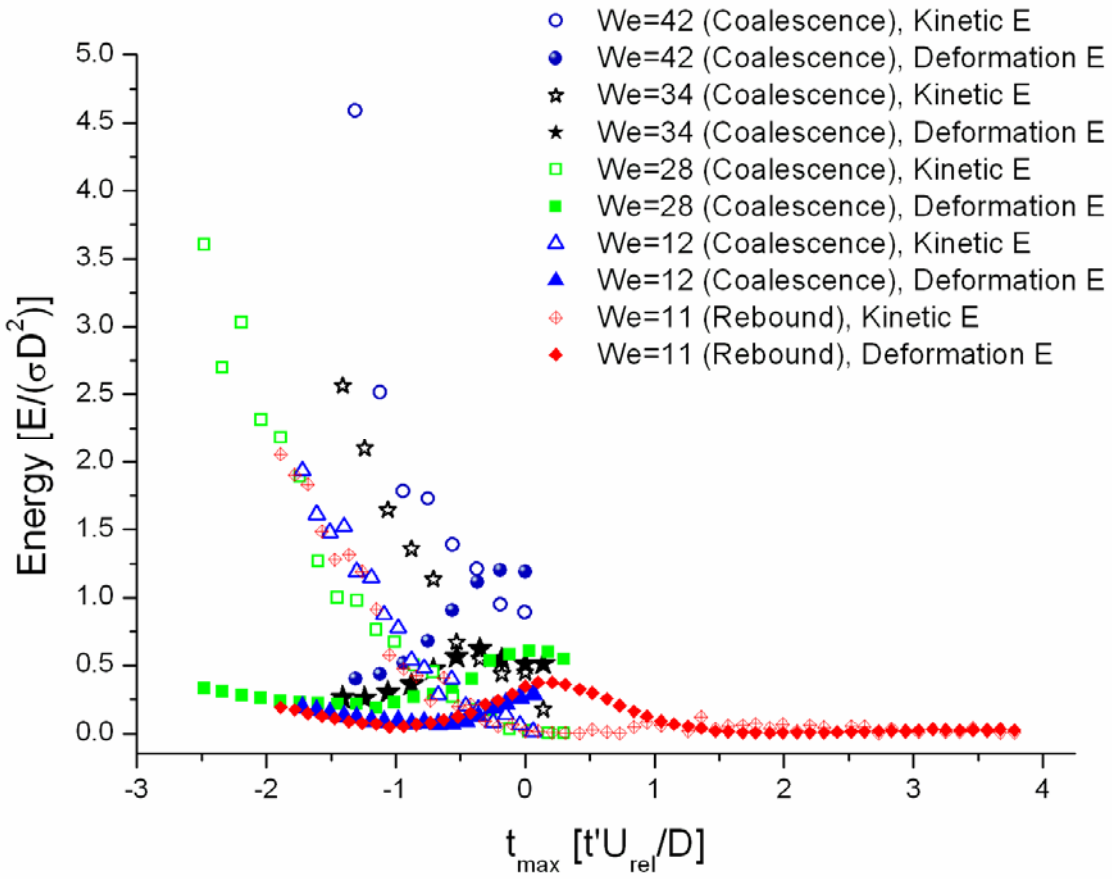


**Figure 3.26** Time evolution of kinetic and deformation energy of a drop. Open symbol is kinetic energy at the time of frame. Solid symbol is deformation energy at the time of frame. $t^{max} = t'U_{rel}/D$, where D is diameter of drop and $U_{rel}$ is relative velocity.

3.1.6 Characteristic times for rebounding and coalescence

Figure 3.27 shows the dimensionless and absolute times of maximum film length and rebound/coalescence for several collision cases. Drops rebound or coalesce sometimes at the maximum film length. In other cases, the drops continue to deform after the film length is maximum before they rebound or coalesce.

In Fig. 3.27, the dimensionless time of the maximum film length generally increases as *We* increases. This is because collision angle becomes shallower and the velocity of drop is higher as *We* increases, such that the drops took longer to reach the maximum film length. As *We* increases, the drops deform slightly after the film is a maximum in length and delay rebound or coalescence. Depending on other parameters, this delay varies for each case. For $9 < We < 12$, time to reach the maximum film length varies in Fig. 3.27. This is probably caused by case-to-case variation or maybe by other parameters that affect the film draining time. For coalescing cases for $We < 30$, the times of the maximum film length and rupture increase in both dimensionless and absolute time as *We* increases.

Figure 3.28 shows the time to reach the maximum interfacial film length ($t_{max} = 0$) vs. collision *We*. The drops took longer to reach the maximum film length as *We* increases until $We = 30$. The line in Fig. 3.28 gives the general trend. Above $We > 30$, coalescence occurs earlier in absolute and dimensionless time than for $We < 30$. This is because higher inertia drops do not change shapes the same as $We < 30$ cases; the drops are elongated when coalescence occurs. Note that theses drops have shorter film draining times, but still coalesce; for example, drops coalesce for $We = 34$ at $t^* = 1.2$ ($t = 34$ ms) while drops start moving outward to rebound for $We = 9$ at $t^* = 1.39$ ($t = 66$ ms). For $We = 9$, although the drops are in contact for a longer time to drain the intervening film than for $We = 34$, the film does not rupture. The results show that film drainage time is not the only parameter that determines whether the film breaks.

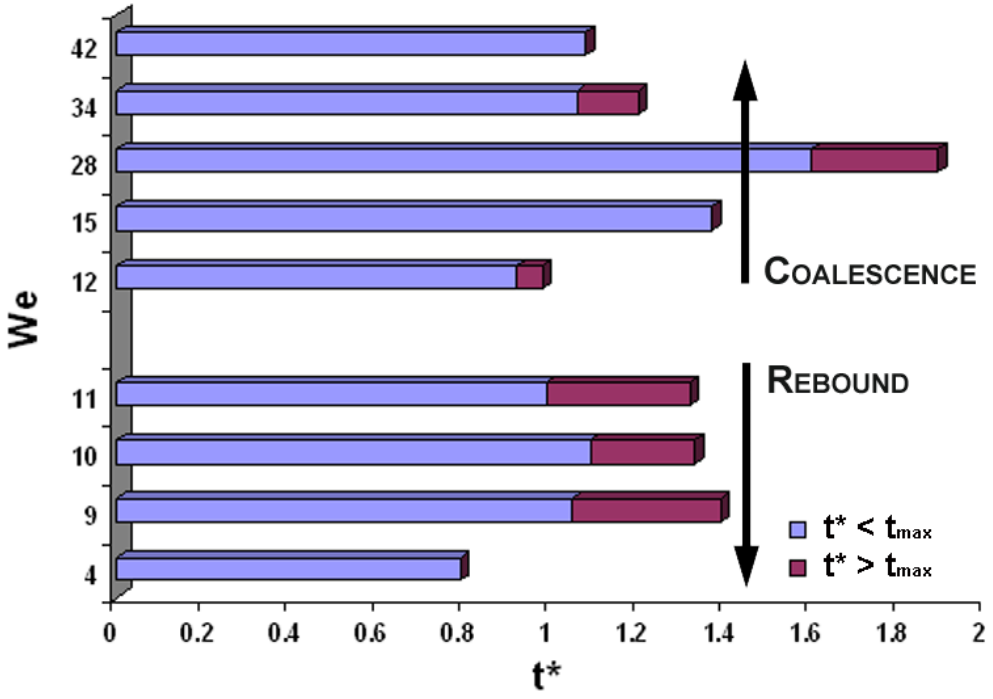


(a)

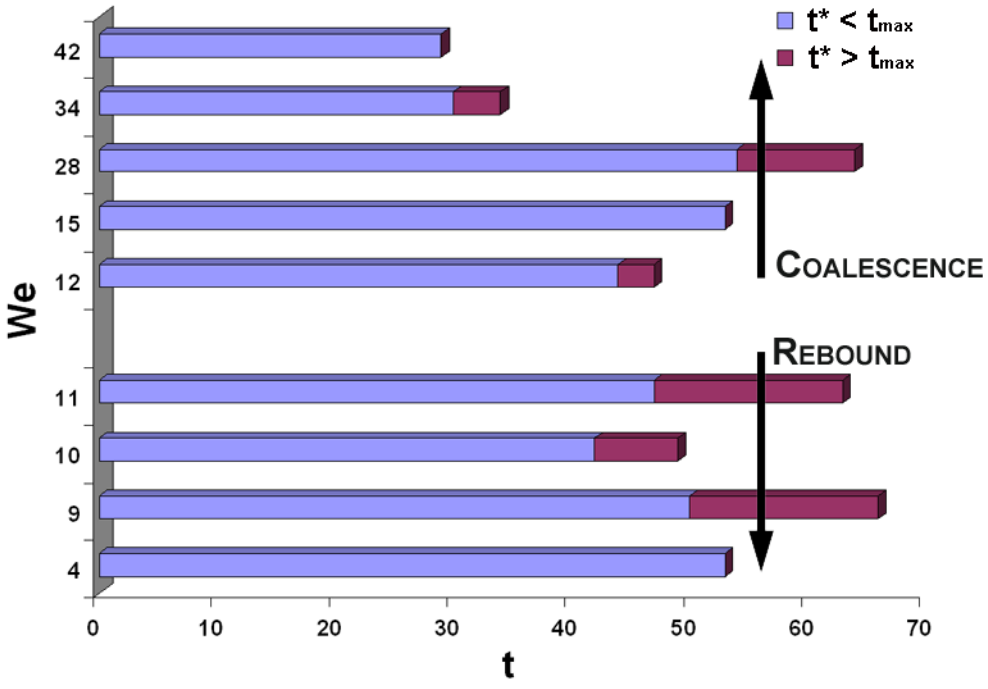


(b)

**Figure 3.27** Time to reach maximum film length ($t^{max}$) and either rupture (coalescing cases) or beginning of outward motion (rebounding cases): (a) Dimensionless time t* and (b) Absolute time t.

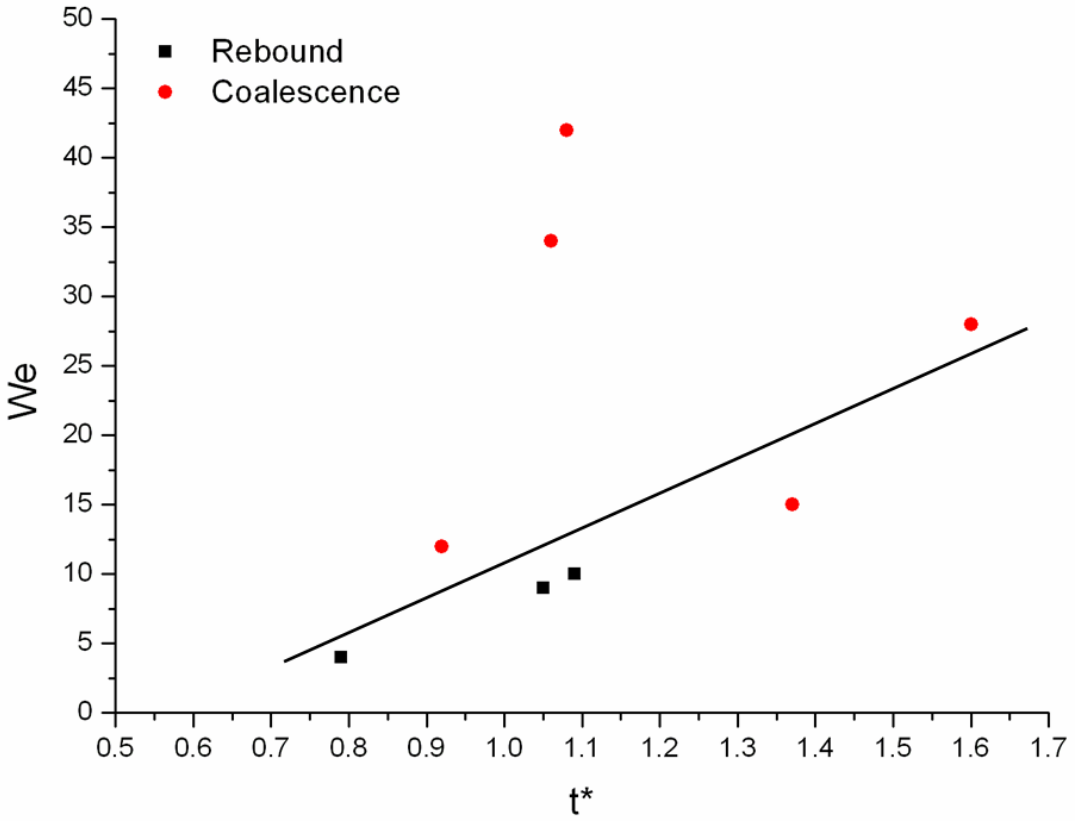


**Figure 3.28** Time at the maximum interfacial film length ($t^{max}$) in dimensionless time t*

## 3.2 Coalescence in detail

3.2.1 Coalescence mechanism

The thin film between colliding drops for *We* = 15 through film rupture was viewed in detail to understand motion near the interface between drops and characterize the coalescence mechanism. Data from the small field of view is presented in Figs. 3.29 and 3.30. These images were taken at the time that the film length in the vertical direction was maximized. For comparison with the large field of view (Fig. 3.17), Figs. 3.29 and 3.30 correspond with t* = 1.37, the time of film rupture (Fig. 3.17e). Note that the magnitudes of vorticity and velocity are higher in these cases than the ones in Fig. 3.17 due to finer resolution. Every fourth velocity vector is plotted. Each drop contains a tilted vortex ring structure that induces flow downward and inward toward the center plane similar to the rebounding cases in Fig. 3.8. In Fig. 3.29, the maximum downward velocity of approximately $0.8U_{rel}$ occurs at the center plane between the vortices in the coalescing case. Figure 3.30 shows contours of the local vertical velocity component and vectors for the same times in the falling drop reference frame. The drop falling velocity has been subtracted from the field. As previously, magnitudes are normalized by $U_{rel}$. In the color map, blue represents downward velocity while red is upward. The maximum relative downward velocity ($0.47U_{rel}$) occurs immediately adjacent to the interface, with the region of strongest relative downflow located near the downstream edge of each drop. The maximum relative upward velocity ($0.34U_{rel}$) is limited to a smaller region on the interface downstream of the corresponding regions for rebound for *We* = 4 and *We* = 9 (see Fig. 3.9).

In the *We* = 15, $\theta = 28°$ case, each vortex ring is tilted inward so that the downstream and upstream core sections are both located close to the center plane and thin film. The inwardly facing rings induce strong inflows toward the interface. The inflow has been enhanced by the deformation of the inwardly moving interface on the outside of each drop. A very strong downflow that is maximized at the center plane results which acts to thin the film between the drops eventually causing the film to rupture in this region. By examination of these fields as well as related sequences, it can be concluded that strong drop deformation combined with vortex induction yields

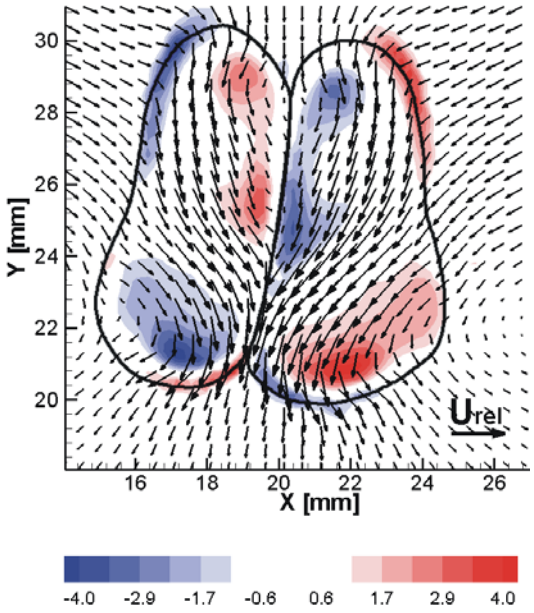


**Figure 3.29** Vector and vorticity fields at the time of maximum film length for coalescence: *We* = 15 (t* = 1.37). Field of view is 13 × 13 mm$^2$. Vectors show absolute velocity. Colors show normalized vorticity. Red is counterclockwise, and blue is clockwise.

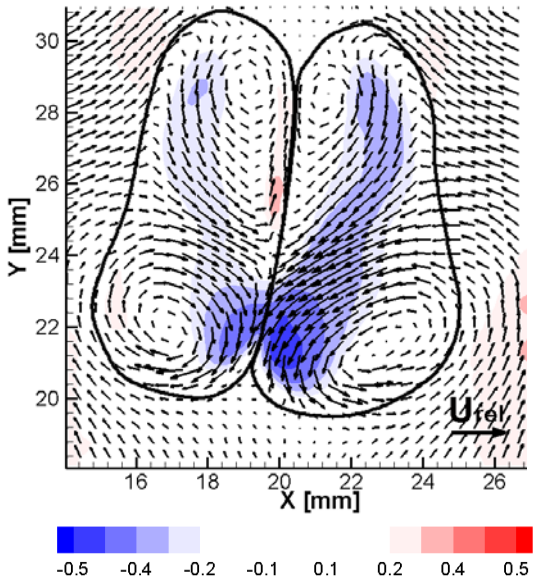


**Figure 3.30** Vector and vertical velocity fields at the time of maximum film length for coalescence: *We* = 15, θ = 28° (t* = 1.37). Vectors show in-plane velocity relative to falling drops. Colors show normalized vertical velocity relative to falling drops. Red is upflow, and blue is downflow.

the appropriate conditions for thin film rupture and drop coalescence.

Figure 3.31 shows a time sequence surrounding the coalescence event for *We* = 15. As in Fig. 3.30, the vectors show velocity in the reference frame relative to the falling drops. At t* = 0.88 (Fig. 3.31a), each drop is deforming, and the flow within moves toward the center plane. The patterns of the original pair of vortex rings are present in each drop. Figure 3.31b shows the frame immediately after film rupture (t* = 1.40), and the rupture location is marked by a red dot. Over the course of this interval, the vorticity magnitudes associated with the upper and lower parts of each vortex ring decrease (maximum vorticity strength $\omega^* = \omega D/U_{rel}$ decreases from 5.1 to 4.7 in the lower part of each leading vortex). Also, the circulation in the upper part of the leading rings clearly decreases with increasing time as the vortical motion is dissipated, possibly by the presence of the nearby interfaces and intervening ambient fluid which has a significantly higher viscosity than the drop fluid ($\mu_{drop}/\mu_{oil}$ = 0.14). The dissipation of the vorticity in the upper part of the rings is also aided by the opposing vorticity developing on the outer part of the drops' trailing edges (Fig. 3.31b) as the drops accelerate downward due to gravity. After the film ruptures, strong localized vorticity is observed at the top of the remaining single drop due to the rapid upward motion of the retracting interface (Fig. 3.31c). The vorticity strength in this region then decreases as the local curvature smoothes out (Fig. 3.31d). The vorticity pattern at the drops' leading edges also changes through the coalescence sequence. Whereas some reverse vorticity, i.e. counterclockwise for lefthand drop, is present in Figs. 3.31a and b, it disappears after the retraction of the interface downstream of the rupture point. This reverse vorticity appears to be caused either by the rotation of the interface itself or by opposing shear stresses along the interface related to drainage of the thin film.

The film rupture event is examined in more detail in Fig. 3.32. The two frames presented are separated by 1 ms. In the image before coalescence, the tracer particles within and bounding the thin film appear distorted (elongated in the horizontal direction) due to imperfect index matching which becomes apparent when the camera views a relatively flat section of interface at a glancing angle (see e.g. Mohamed-Kassim and Longmire, 2003). Nevertheless, viewing of individual particles within

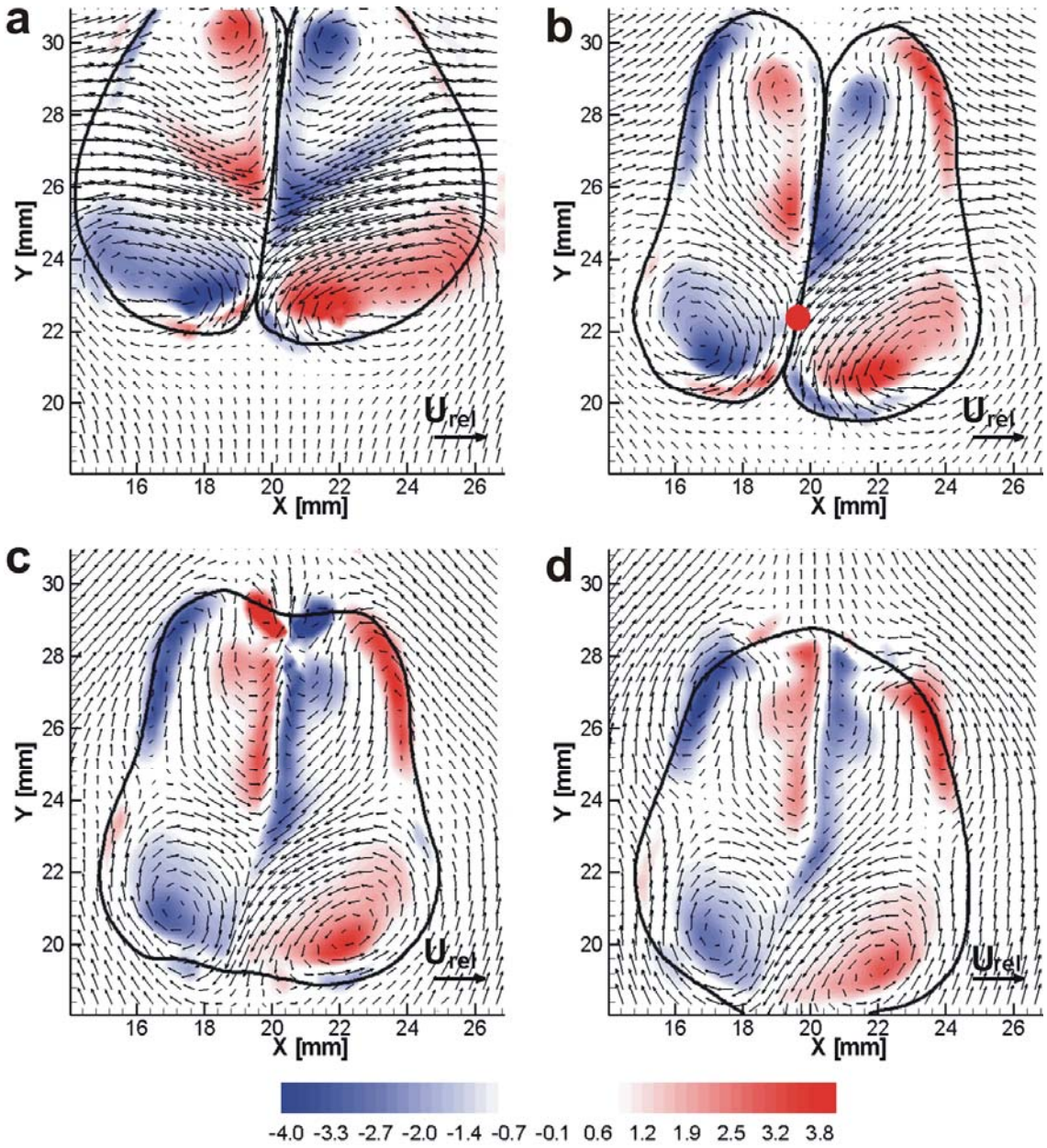


**Figure 3.31** In-plane vectors and normalized vorticity contours during coalescence event (*We* = 15), (a) t* = 0.88; (b) t* = 1.40, Red dot marks film rupture location; (c) t* = 1.66; (d) t* = 1.92. Vectors show velocity relative to falling drops. Colors show normalized vorticity. Red is counterclockwise, and blue is clockwise. Red dot in b shows the film rupture location.

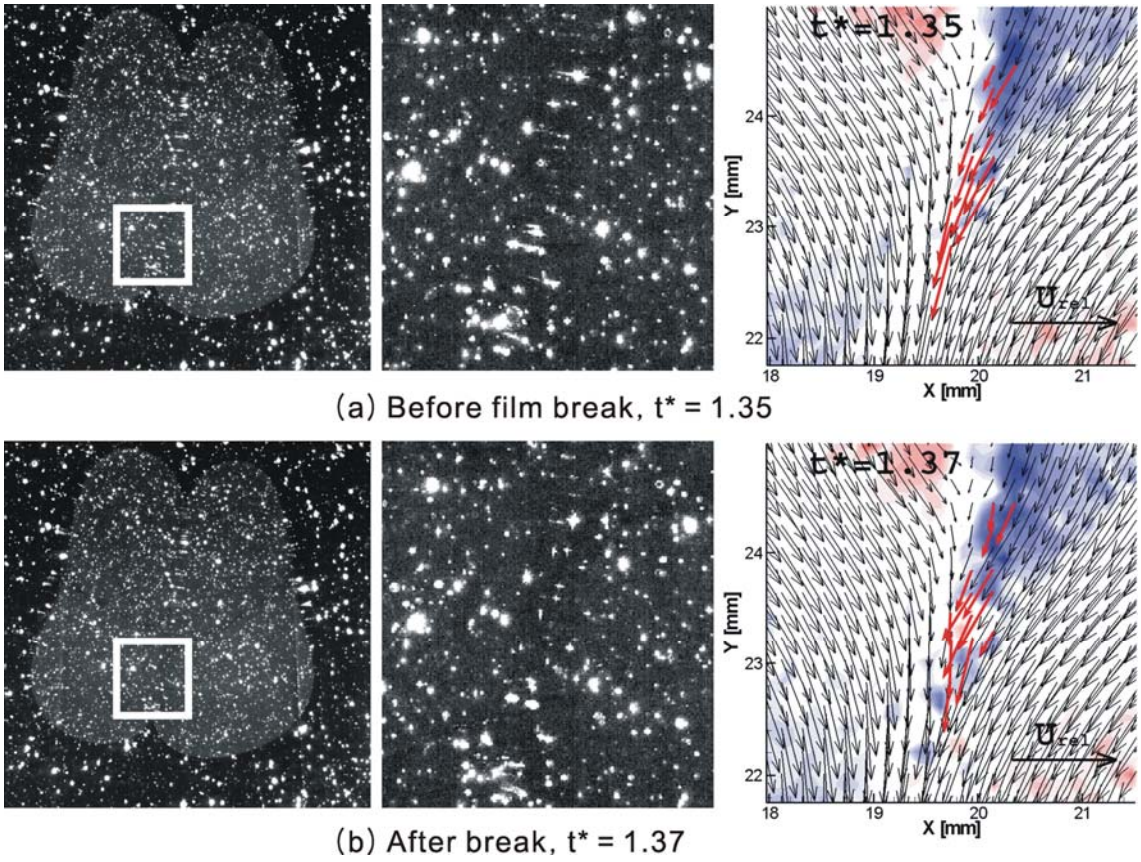


**Figure 3.32** Film rupture and coalescence (*We* = 15). White squares show magnified regions for which velocity fields are plotted. Vectors show absolute velocity. Color contours show normalized vorticity. Red is counterclockwise, and blue is clockwise.

image sequences indicates that the velocity vectors in this zone are accurate (and that most of these particles are associated with the drop fluid).

The magnified views of velocity and vorticity fields are centered on the location of film rupture which occurs near the downstream end of the thin film and coincident with the strong downflow region described above. When Fig. 3.32b is compared with Fig. 3.32a, the velocity vectors in the vicinity of the interface have begun to vary in a wave-like form. This variation probably occurs because of the sudden localized change in velocity associated with the film rupture. In fact, the film has ruptured in the lower portion of the magnified zone in Fig. 3.32b. From the raw image in Fig. 3.32b, the rupture is observable by distorted tracer particles that have reverted to spherical shapes, and the disappearance of the cusp in interface curvature at the downstream edge of the thin film. It is also clear that particles near the interface experience sudden changes in velocity. Figure 3.33 shows the full field shortly after film rupture (t* = 1.52).

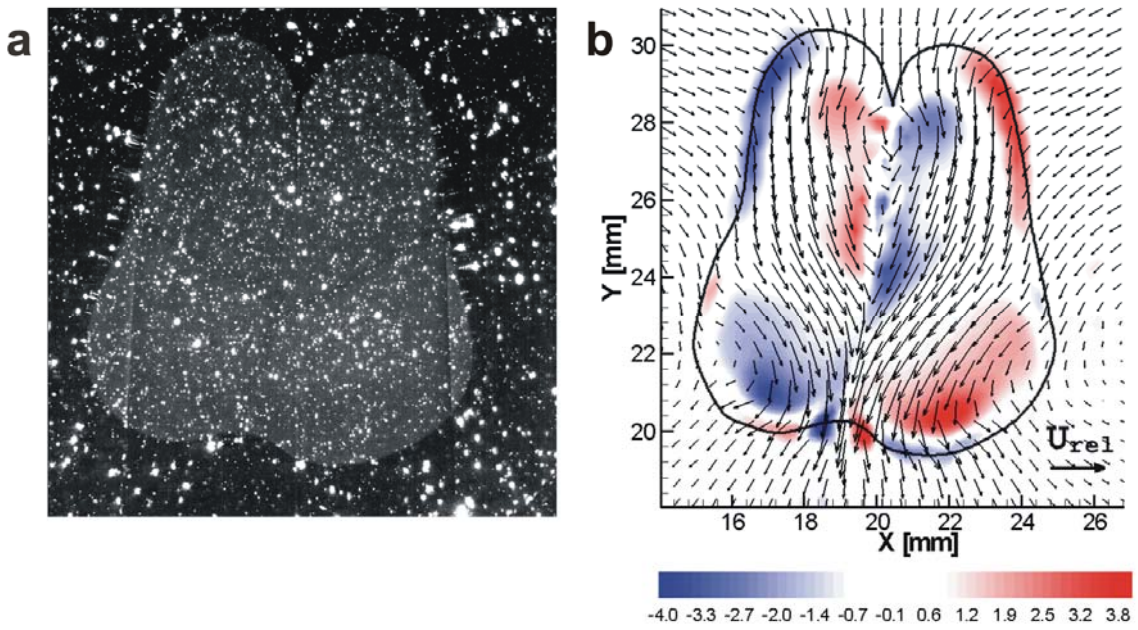


**Figure 3.33** Field shortly after film rupture (*We* = 15), t* = 1.52. Vectors show absolute velocity. Colors show normalized vorticity. Red is counterclockwise and blue is clockwise.

Note the sudden increase in downflow downstream of the rupture location (local

downward velocity changes from $0.33U_{rel}$ in Fig. 3.30b to $0.94U_{rel}$ in Fig. 3.31) caused by the local increase in surface tension and strong increase in curvature generated by the rupture. In subsequent images, the sharply curved interface above the rupture location retracts rapidly upward. The disappearance of the upper 'cusp' in curvature occurs within 7 ms of the film rupture at t* = 1.55.

Previously, the characteristics of several rebounding and coalescing cases were investigated. In the following sections, effects of the Weber number and collision angle in drop collision are discussed further. Rebounding and coalescing cases for different Weber numbers at a constant collision angle are compared. Then, two coalescing cases for different collision angles with the same Weber number are examined.

### 3.2.2 Effects of the Weber number

Time evolution in shape

Collisions between pairs of drops were investigated by varying initial injection angles to control the eventual collision angles. Figure 3.34 and 3.35 show visualizations of two sequences from the large field of view with the same collision angle $\theta = 34°$: a rebounding case with $We$ = 11 (D = 0.87 cm, $U_{rel}$ = 18.3 cm/s) and a coalescing case with $We$ = 22 (D = 0.96 cm, $U_{rel}$ = 24.6 cm/s). The initial injection angles were 0° in the rebounding case and -10° (downward direction) in the coalescing case respectively.

In the rebounding case (Fig. 3.34), the drop shapes appear symmetric about the horizontal at t* = -0.76. The shapes evolve so that the drops are close to spherical before they collide (t* = 0). The drops initially contact each other at a position above their centers due to their downward trajectory angle and then rotate toward each other so that the flat interface between them lengthens. After the collision, the drops become oblate in shape (Figs. 3.34c-e). At t* = 0.94 (Fig. 3.34e), the film length between the drops reaches a maximum, and at t* = 2.22 the drops are moving apart while continuing to rotate. As the drops separate, their shapes revert to spherical.

In the coalescence case (Fig. 3.35), the drops are initially more elongated with tails due to higher injection velocities (t* = -0.51). Also, the drops do not display

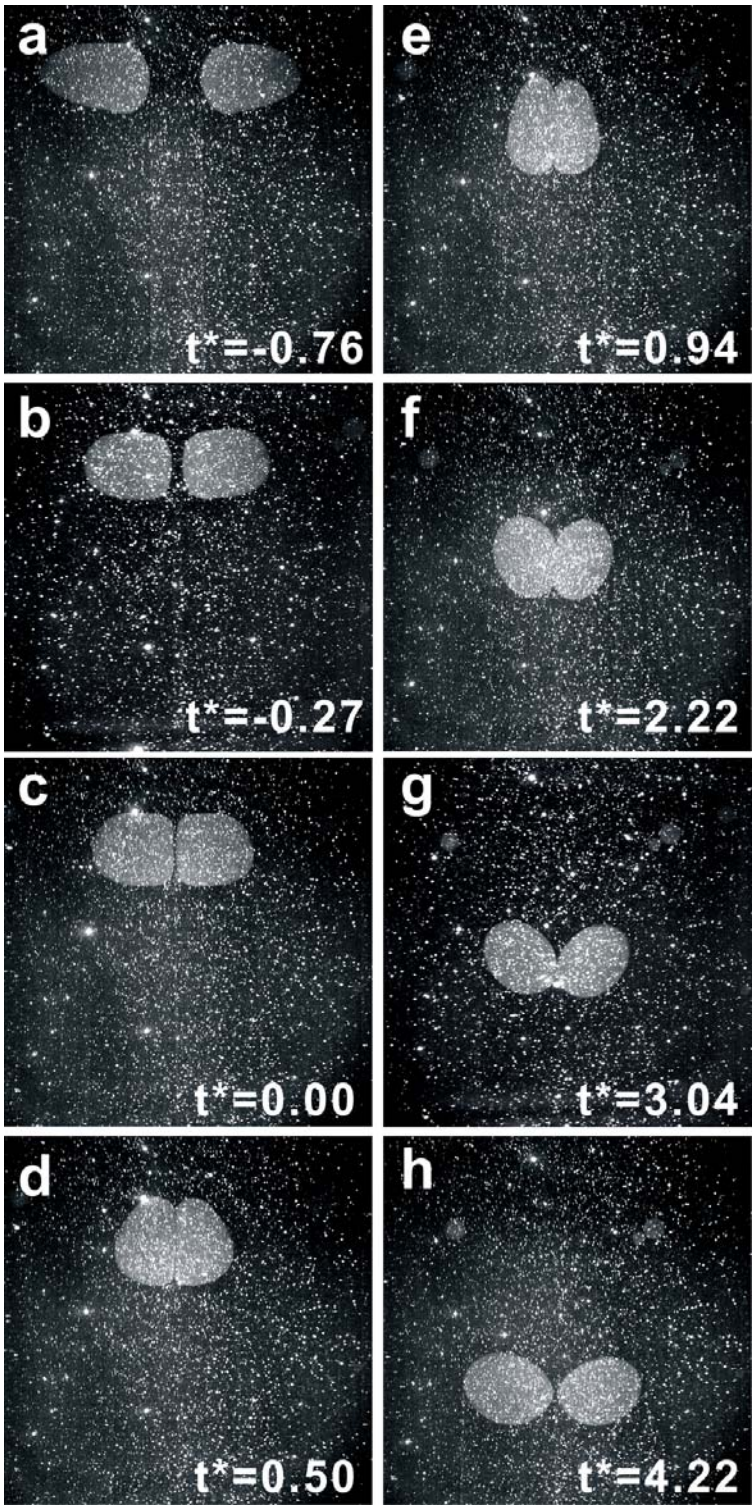


**Figure 3.34** Time evolution of drop collision: *We* = 11, θ = 34° (rebound). t* = t$U_{rel}$/D, where D is drop diameter and $U_{rel}$ is relative velocity.

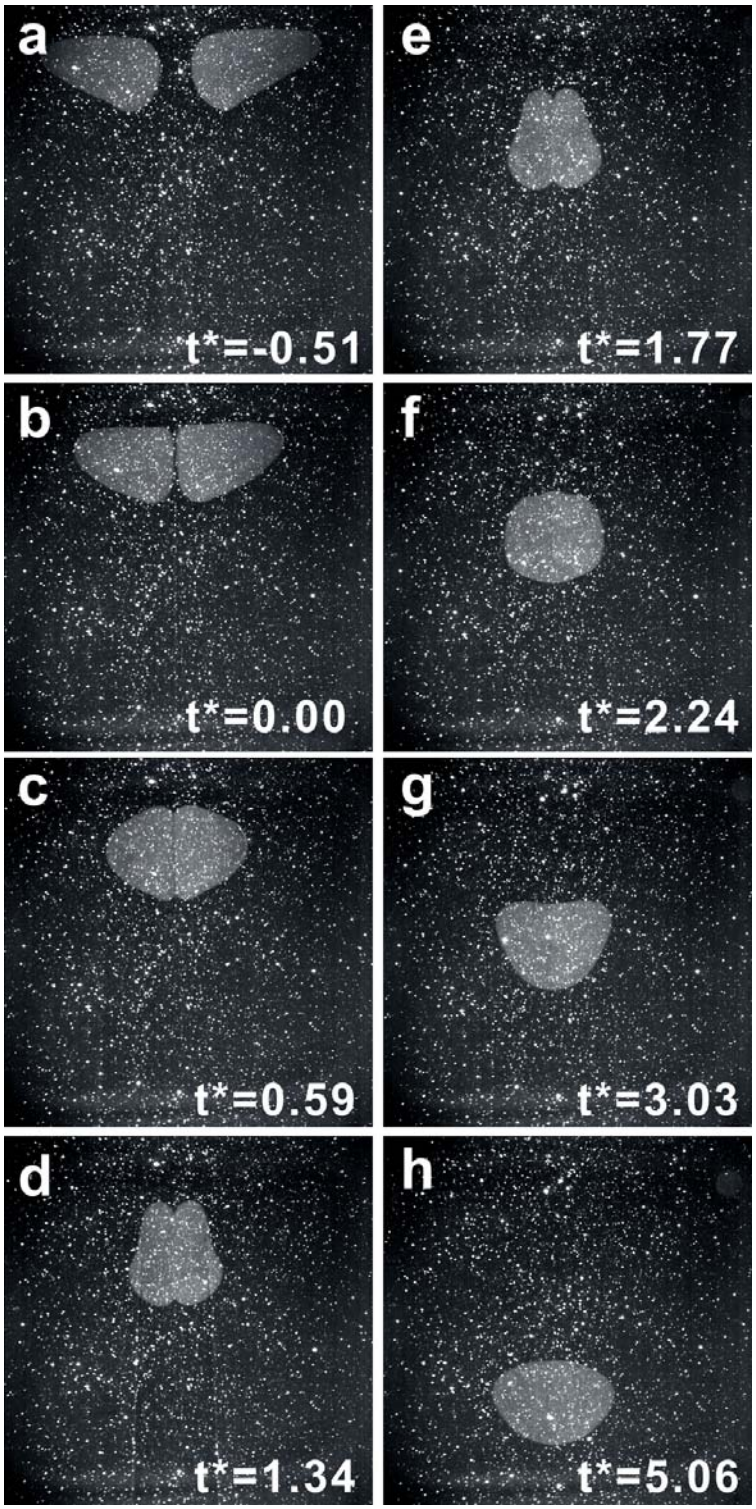


**Figure 3.35** Time evolution of drop collision: *We* = 22, θ = 34° (coalescence). t* = t$U_{rel}$/D, where D is drop diameter and $U_{rel}$ is relative velocity.

horizontal symmetry and initially travel on a more downward trajectory due to the downward injection angle (-10°). As the drops move closer (t* = 0), their heads flatten, and the tails become less prominent. Inertia drives the drop centroids closer together, and the film area grows while the drops change from prolate to oblate in shape (t* = 0.59). At this Weber number, the inertia is large enough to generate a local concavity in the curvature (t* = 1.34). At t* = 1.34 (Fig. 3.35e), the film length reaches a maximum, and the drops coalesce at t* = 1.78. After the film ruptures, the resulting single drop oscillates in shape as it then falls downward. The most striking difference between the two cases is the stronger deformation that occurs in the higher *We*, larger inertia case.

Detailed view of thin film region

In this study, even though the thin film between drops is not observable, a zoomed smaller field of view centered on the film as described in 3.2.1 is used to view the coalescence event. To understand motion near the thin film, data from the 'small' field of view are presented in Figs. 3.36-3.38. These images correspond with the time of maximum film length for the rebounding case and the time of film rupture for the coalescing case. Only every fifth vector is plotted in Fig. 3.36, and every fourth vector is plotted in Fig. 3.37 and 3.38. Figure 3.36 shows the normalized vorticity and the normalized absolute velocity vectors. In Fig. 3.37, the drop falling velocity has been subtracted from each field in Fig. 3.36 in order to understand the velocity pattern relative to each drop. The drop falling velocities are $0.44U_{rel}$ in the rebounding case (Fig. 3.37a) and $0.42U_{rel}$ in the coalescing case (Fig. 3.37b). Figure 3.38 shows the in-plane velocity vectors relative to the falling drops and normalized vertical velocity relative to falling drops. In Figs. 3.37b and 3.38b, a red dot shows the film rupture location.

The velocity vectors and vorticity contours in Fig. 3.37 indicate that the two lower core sections in both cases have merged into one. The fact that the vectors swirl about these cores indicates that the cores are propagating with the same velocity as the drops. The plots also show more clearly the locations of strong inflow toward the interface.

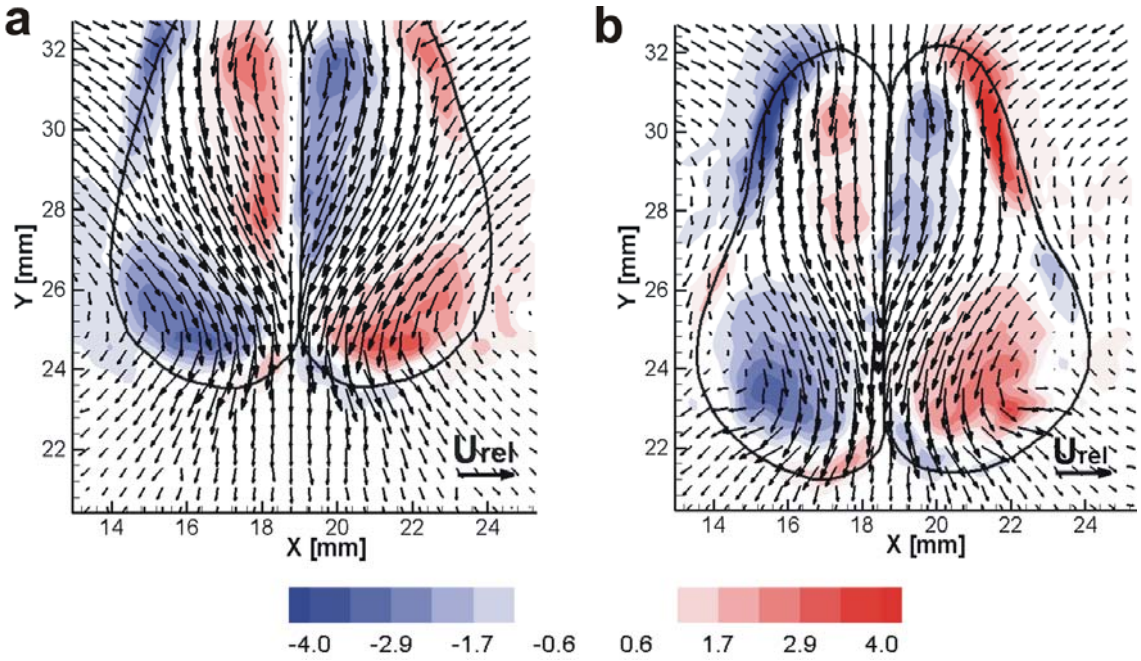


**Figure 3.36** Vector and vorticity fields at the time of maximum film length, (a) *We* = 11, θ = 34°, t* = 0.94, and at the time of film rupture, (b) *We* = 22, θ = 34°, t* = 1.77. Vectors show normalized velocity. Colors show normalized vorticity. Red is counterclockwise rotation and blue is clockwise rotation.

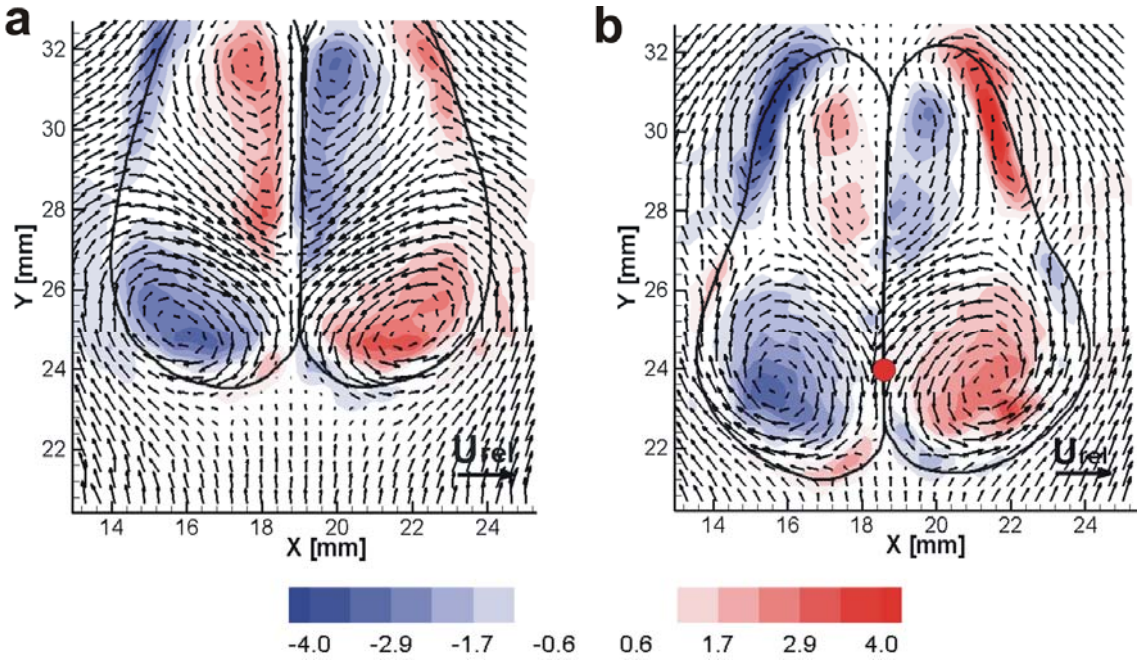


**Figure 3.37** Vector and vorticity fields at the time of maximum film length, (a) *We* = 11, θ = 34°, t* = 0.94, and at the time of film rupture, (b) *We* = 22, θ = 34°, t* = 1.77. Vectors show in-plane velocity relative to falling drops. Colors show normalized vorticity. Red is counterclockwise rotation and blue is clockwise rotation. Red dot in b shows the film rupture location.

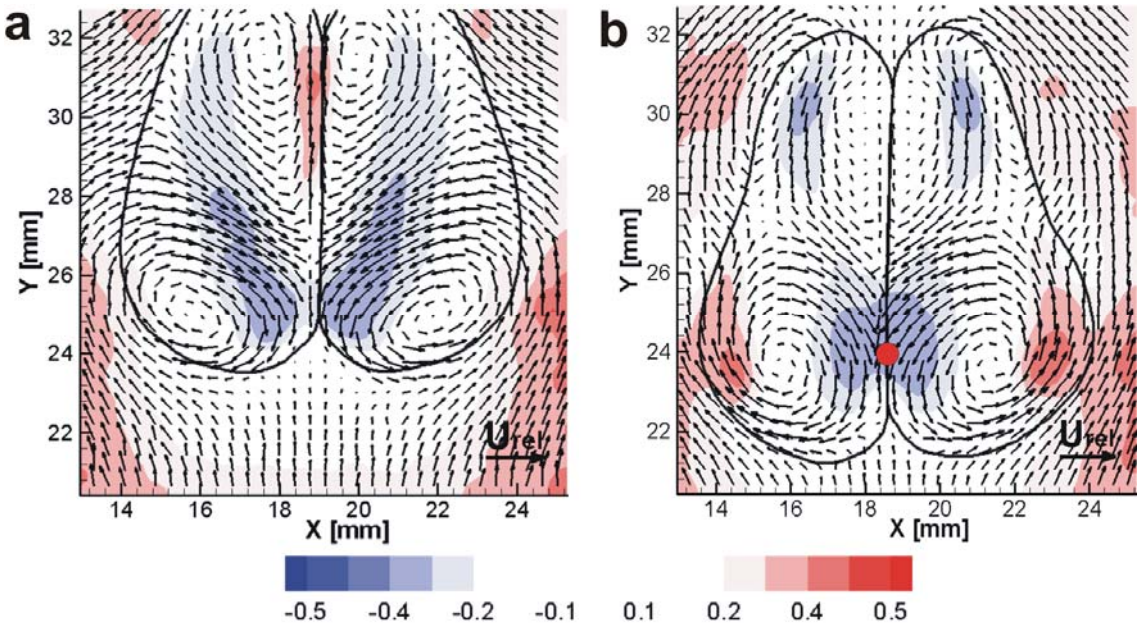


**Figure 3.38** Vector and vertical velocity fields at the time of maximum film length, (a) *We* = 11, θ = 34°, t* = 0.94, and at the time of film rupture, (b) *We* = 22, θ = 34°, t* = 1.77. Vectors show in-plane velocity relative to falling drops. Colors show normalized vertical velocity relative to falling drops. Red is upflow, and blue is downflow. Red dot in b shows the film rupture location.

It is also interesting to note the directions of the vectors crossing the interface at the outer portion of each drop. The inward pointing vectors in the rebounding case indicate that locally the drop deformation is continuing to increase while the outward pointing vectors in the coalescing case indicate that the local deformation is beginning to decrease. (Typically, the film rupture occurs *after* the film length is maximized). Notice also the sharp changes in velocity near the outer trailing edges of the drops that generate strong vorticity. This vorticity is generated by the upper cores within each drop and the trailing drop surface which combine to drive drop fluid downward relative to the fluid immediately outside each drop.

The velocity variation near the thin film can be examined in more detail in this smaller field of view. In Fig. 3.36, the maximum downward velocity of ~0.73$U_{rel}$ for rebounding occurs away from the interface in the streaming region inside of each vortex ring while the maximum downward velocity of approximately 0.76$U_{rel}$ occurs at the center plane between the vortices in the coalescing case. When comparing downflow and upflow at the centerplane, for *We* = 22 (Fig. 3.38b), the maximum downward velocity (0.36$U_{rel}$) in the thin film region is stronger than the maximum upward velocity (0.08$U_{rel}$) immediately before film rupture. By contrast, for *We* = 11, the maximum downward velocity of 0.26$U_{rel}$ is weaker than the upward velocity (0.40$U_{rel}$). In the coalescing case, the thin film ruptures in the lower portion where the local downflow is strong. The remaining film above the rupture location then has a much stronger distortion than the film below the rupture location, and it retracts upward at a very large velocity. In this case, the film retracting velocity is ~1.1 m/s. The film retracting velocity is computed by visually tracking a particle at the interface or by observing the time between film rupture and the time when the upper cusp between the drops becomes smooth. The velocity gradient normal to the retracting film is very strong so that the 16 × 16 PIV interrogation area does not resolve the true maximum.

For both cases in Figs. 3.36 and 3.37, the vortex ring structure is tilted downward. For *We* = 11, the maximum vorticity in the upper (2.9D/$U_{rel}$) and lower portion (3.1D/$U_{rel}$) of each vortex ring are similar. The largest magnitude of inward velocity is higher for *We* = 11 than *We* = 22: 0.48$U_{rel}$ for *We* = 11 and 0.35$U_{rel}$ for *We* = 22. For

*We* = 22, the lower portion of each vortex ring (3.6D/$U_{rel}$) is more focused and generates stronger rotation than the upper portion (2.2D/$U_{rel}$). The vortex pair and the previously deforming interface on the outside of each drop in the higher inertia case induce a local downflow that is maximized at the center plane as shown in Fig. 3.36b and 3.37b. Although the maximum normalized magnitude of inward (horizontal) velocity for *We* = 22 is lower than *We* = 11, the lower parts of vortex ring are tilted so that they induce downflow at the centerplane. By contrast, for *We* = 11, the lower part of each ring is tilted such that the strongest flows are inward, not downward, and the downflow at the interface is weaker than for *We* = 22. For *We* = 22, the downflow acts to thin the film between the drops eventually causing the film to rupture in this region. Strong drop deformation combined with vortex interaction yields the appropriate conditions for thin film rupture and drop coalescence as discussed in 3.2.1. The time t* to reach the maximum film length took longer in the coalescing case; t* = 0.94 (t = 47 ms) for rebounding vs. 1.34 (t = 52 ms) for coalescence. This is consistent with the previous result discussed in Section 3.1.6 that the drops reach the maximum film length later as *We* increases (Fig. 3.27a). For the two cases discussed here, the time when drops coalesce (t* = 1.77, t = 69 ms) is later than the time when drops for the lower *We* rebound (t* = 1.32, t = 63). Thus, the time t* to reach the maximum film length and available time t* for drainage are both longer for the higher *We*. Note that, as described in Section 3.2.1, the absolute times at the maximum film length and the rebound/coalescence vary with *We* so that is not consistent with t*.

### 3.2.3 Effects of collision angle

Time evolution in shape

Two sequences of coalescing cases with like Weber number (*We* = 16) but different collision angles are compared in Figs. 3.39 and 3.40: $\theta = 17°$ vs. $\theta = 40°$. Both $U_{rel}$ = 21.2 cm/s and D = 0.92 cm are matched. The initial injection angles were +15° (upward) for $\theta = 17°$ and -10° (downward) for $\theta = 40°$.

For the shallower collision angle case (Fig. 3.39, $\theta = 17°$), gravitational acceleration causes the drops to move downward at t* = 0, even though their tails are

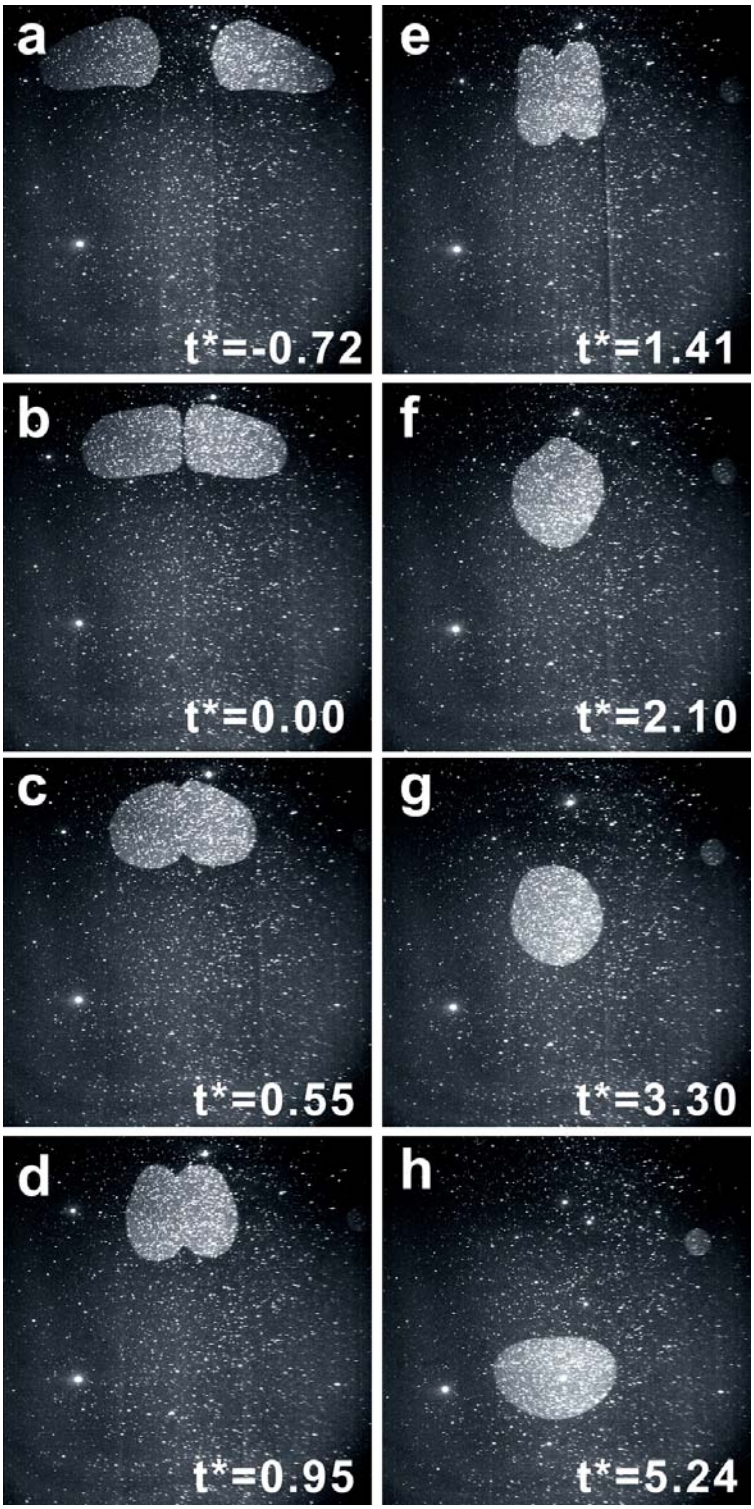


**Figure 3.39** Time evolution of drop collision: *We* = 16, θ = 17° (coalescence). t* = t$U_{rel}$/D, where D is drop diameter and $U_{rel}$ is relative velocity.

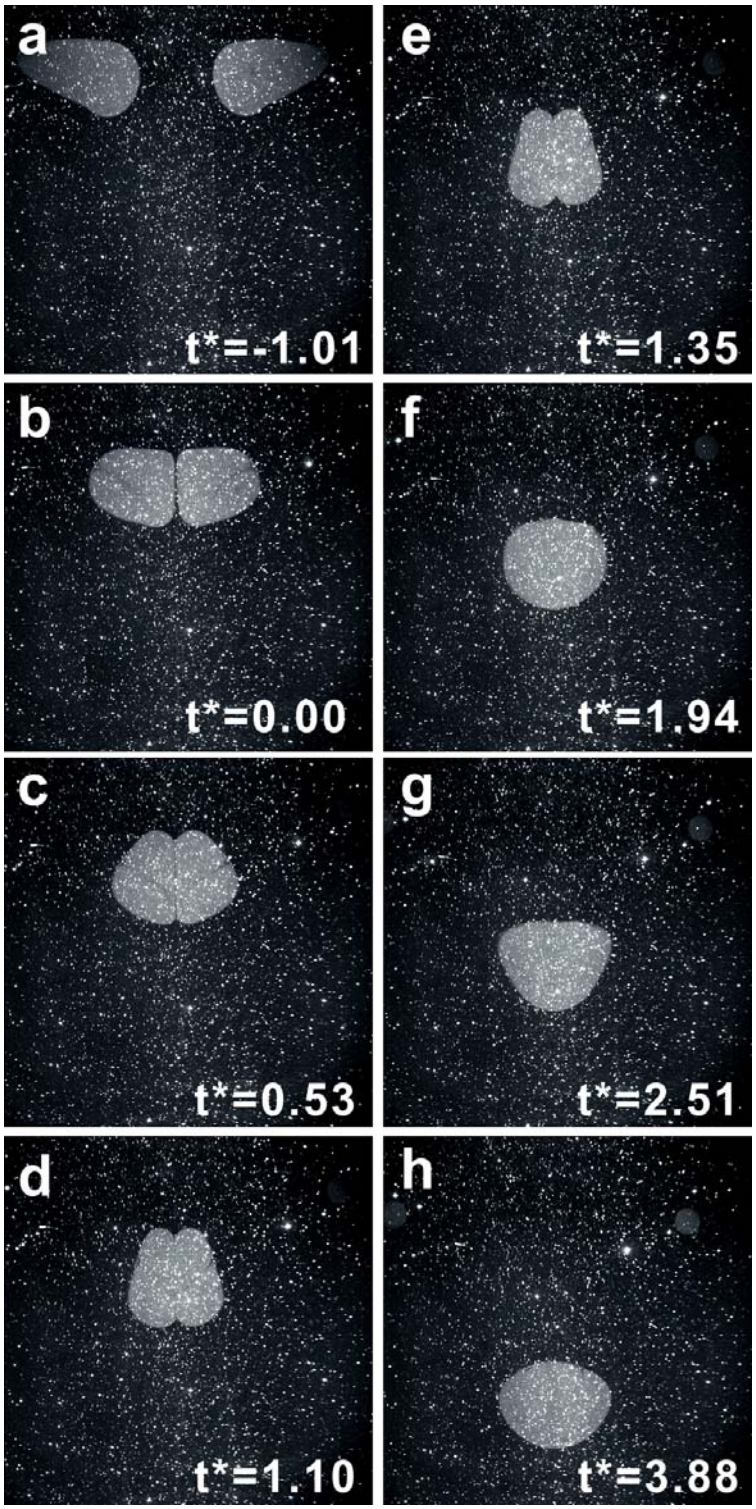


**Figure 3.40** Time evolution of drop collision: *We* = 16, θ = 40° (coalescence). t* = t$U_{rel}$/D, where D is drop diameter and $U_{rel}$ is relative velocity.

still lower than their heads (due to the initial upward injection). The drops initially contact each other at a position near the centers, and the tails rotate downward (t* = 0 and 0.55). When the film length is maximized (t* = 1.41), the drops are horizontally symmetric. In this case, the drops coalesce when the film length is near maximum (t* = 1.43). For the steeper collision angle case (Fig. 3.38, θ = 40°), the drop heads point downward due to the initial downward trajectory (t* = -1.01). The drops initially come in contact at a location above their centers (t* = 0) before they become compressed into oblate shapes. At t* = 1.10, the film length is maximum, and the drops are not horizontally symmetric. Instead, the bottom section of each drop is wider than the top. The drops eventually coalesce at t* = 1.35 after the maximum film length is observed. The times when maximum film length reached is shorter for the steeper collision angle case (t* = 1.10, t = 48 ms) than for the shallower collision angle case (t* = 1.41, t = 61 ms). However, the times when the drops coalesce are similar (t* = 1.43, t = 61 ms for θ = 17°, and t* = 1.35, t = 59 ms for θ = 40°). Thus, the collision angle does not appear to significantly affect the coalescence time.

Detailed view of thin film region

Zoomed views for the two cases are presented in Figs. 3.41-3.43. Figures 3.41a, 3.42a, and 3.43a, and Figs. 3.41b, 3.42b, and 3.43b correspond with the time of film rupture, t* = 1.43 and t* = 1.35 respectively. The drop falling velocities are $0.5U_{rel}$ in Figs. 3.42a and 3.43a, and $0.42U_{rel}$ in Fig. 3.42b and 3.43b.

As observed previously, the drop shapes for the shallow collision angle are close to symmetric about the horizontal while the shapes for the steeper collision angle are broader toward the bottom. In these plots, the different shapes correspond with different vorticity distributions. The paired ring cores near the bottoms of the drops for θ = 40° appear stronger and are focused further from the interface than for θ = 17°. The resulting ring structure is tilted more downward for θ = 40° with the solid lines in Fig. 3.41 showing the angle of each ring. The difference in the direction of the streaming flow moving through each ring is obvious.

In the drop reference frame shown in Fig. 3.42 and 3.43, the streaming flow

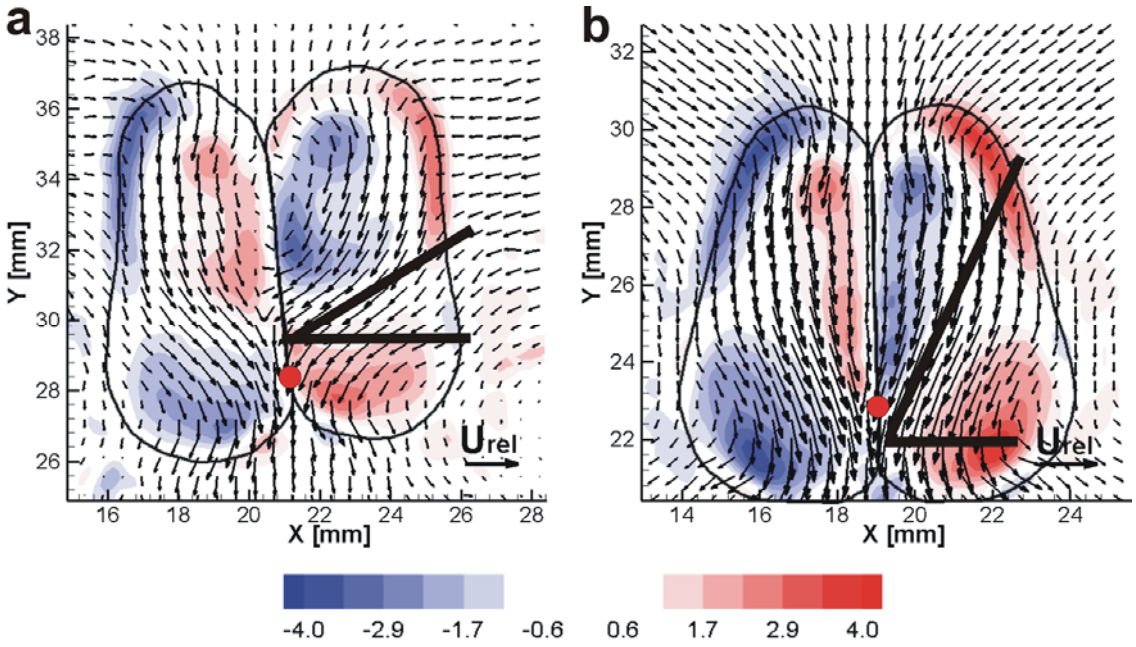


**Figure 3.41** Vector and vorticity fields at the time of rupture: (a) *We* = 16, θ = 17°, t* = 1.43, (b) *We* = 16, θ = 40°, t* = 1.35. Vectors show normalized absolute velocity. Colors show normalized vorticity. Red is counterclockwise rotation and blue is clockwise rotation.

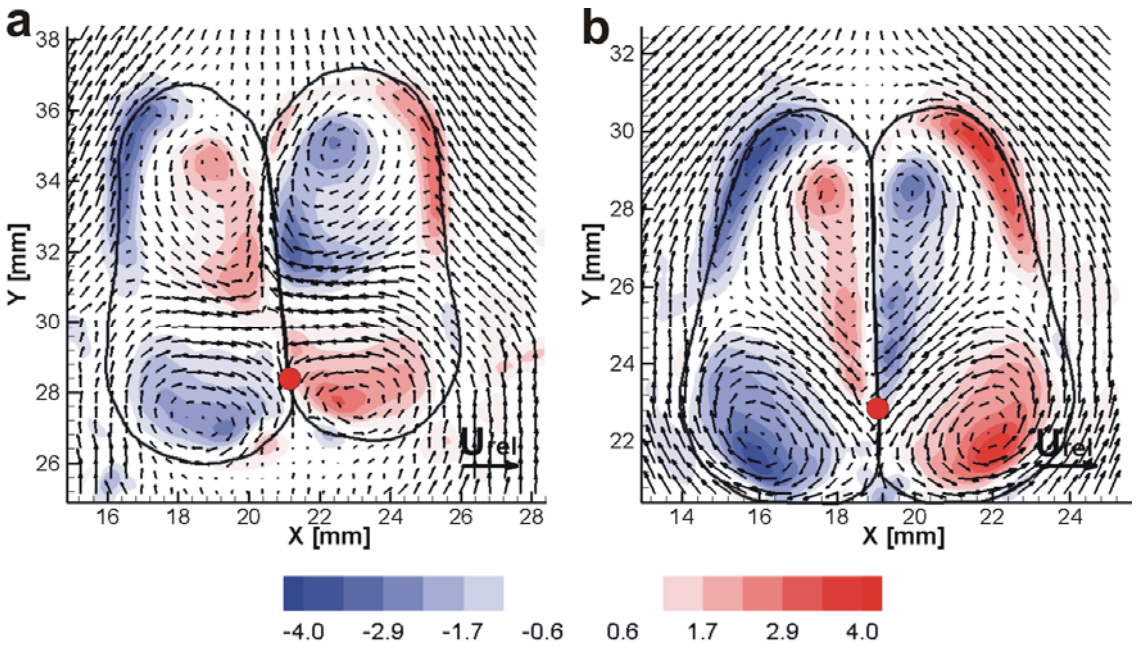


**Figure 3.42** Vector and vorticity fields at the time of rupture: (a) *We* = 16, θ = 17°, t* = 1.43, (b) *We* = 16, θ = 40°, t* = 1.35. Vectors show in-plane velocity relative to falling drops. Colors show normalized vorticity. Red is counterclockwise rotation and blue is clockwise rotation. Red dot shows the film rupture location.

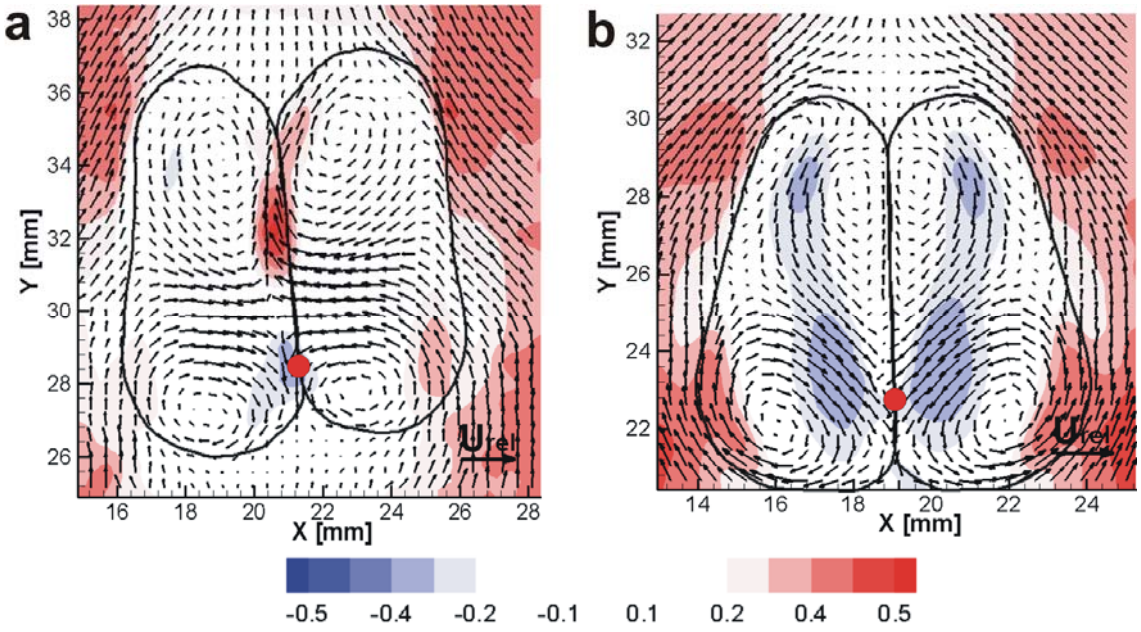


**Figure 3.43** Vector and vertical velocity fields at the time of rupture: (a) *We* = 16, θ = 17°, t* = 1.43, (b) *We* = 16, θ = 40°, t* = 1.35. Vectors show in-plane velocity relative to falling drops. Colors show normalized vertical velocity relative to falling drops. Red is upflow, and blue is downflow. Red dot shows the film rupture location.

moves directly toward the centerplane for θ = 17°, while it tilts downward for θ = 40°. In Fig. 3.43, the maximum downward velocities measured at the center plane are about $0.28U_{rel}$ for θ = 17° and $0.32U_{rel}$ for θ = 40°. The location of this maximum for θ = 17° occurs closer to the bottom of the interface than for θ = 40°. Note that the location of maximum downward velocity is in the centerplane for θ = 17° while the location is slightly away from the centerplane for θ = 40° in Fig. 3.43. For θ = 40°, downward velocity is $0.20U_{rel}$ at the centerplane and 0.30 at the location slightly away from centerplane. This is because the lower portion of vortex ring is away from the interface due to tilting of the ring structure. In Fig. 3.43, upward film draining velocity ($0.46U_{rel}$) is significant for θ = 17° while this upward velocities is not substantial ($0.14U_{rel}$) at the interface.

In Figs. 3.41, 3.42, and 3.43, the red dots show the location of film rupture for each collision angle. If a dimensionless film rupture location, R* is defined as the distance from the bottom of the film divided by the film length, then the case with the shallower angle (θ = 17°) breaks at R* = 0.19 where the local downward velocity is near maximum (see Fig. 3.43a) while the case with the steeper angle (θ = 40°) breaks at R* = 0.27. Therefore the film rupture location moves upward as the collision angle steepens. For each case examined, the film rupture location occurs slightly downstream of the location of maximum downward velocity in the thin film.

## 3.3 Collision of unequal size drops

In the previous section, collisions for equal size drops were investigated. In this section, characteristics of unequal size drop collision are described. First, the rebound and coalescence for unequal size drop collisions are compared. Then, the effect of drop size, the Weber number (*We**), and impact parameters on unequal size drop coalescence will be presented. When generating the drops through the tubes, the inclination angle of each tube was adjusted independently in order to ensure collisions. In general, for head-on collisions of two different sizes of drops, the large drop is heavier that it falls faster than the small drop. Therefore, the initial injection angle and tube height were adjusted to access appropriate impact parameters. In the current study, the collision angle of the large drop was, in general, shallower than that of the small drop. This incidence angle difference resulted in variations in velocity ratio and impact parameters, and therefore affected on the collision outcomes. Typically, if the velocity ratio ($u_L/u_s$) was greater than 1 (the large drop moves faster than the small drop), the intervening film between the drops did not bend significantly. The detailed effects of these parameters are discussed below.

### 3.3.1 Outcomes of unequal size drop collisions

Figure 3.44 shows the results of unequal size drop collisions where *We** and B were varied. The inertia driven *We** is defined in Eq. 2.23.

$$We^* = \frac{4\rho_d\left(D_L^2 u_L^2 + D_S^2 u_S^2\right)}{\sigma\left(D_L + D_S\right)} \tag{2.23}$$

where the subscript L is for the large drop and S is the small drop for head-on collisions. The impact parameter B is defined as the projection of the distance between the centroid of each drop normal to the direction of the relative velocity (Eq. 2.25). Therefore, if B = 0, the drop collision is head-on, and if B > 0, the collision is glancing. In Fig. 3.44, the closed and open symbols represent coalescence and rebound, respectively. The drop pair has an approximate drop size ratio ($D_s/D_L$) of either 0.71 or 0.48. In this study, the

regions of rebound and coalescence are limited to when $We^* < 42$ and $B < 0.6$. When $We^* < 8$, many cases, not shown in Fig. 3.44, were observed, and all rebounded.

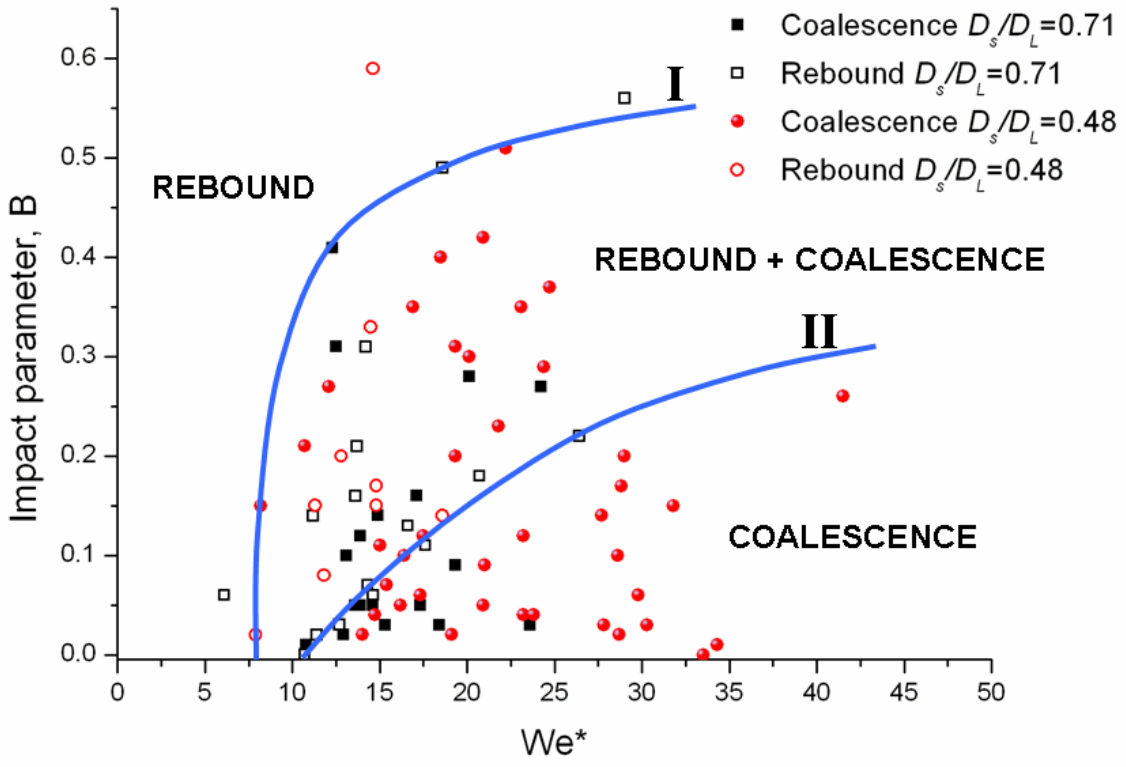


**Figure 3.44** Region of rebound and coalescence for unequal size drops. Closed symbol is a coalescing case and open symbol is a rebound case. The black symbol is for drop size ratio, $D_s/D_L \approx 0.71$ and red is for $D_s/D_L \approx 0.48$.

Two boundaries are drawn in Fig. 3.44. All cases to the left of boundary I rebound. All cases to the right of boundary II coalesce. When $We^* < 8$ at $B = 0$, the drops rebound. Based on the current data, this critical Weber number ($We^* = 8$) applies for impact parameters in the range $0 < B < 0.25$. As B increases, this boundary shifts to the higher $We^*$: critical $We^* = 29$ in the boundary I at $B = 0.56$. Coalescence always occurs for when $We^* > 11$ and $B = 0$. The boundary tends to shift to higher $We^*$ at larger impact parameters: critical $We^* = 42$ at $B = 0.26$. Between the regions of rebound and coalescence (between I and II), the collisions can result in either a rebound or coalescence. By comparing head-on collisions for equal and unequal size drops, the

location of boundary II for unequal size drop collision is similar to the one for equal size drop collision ($We$ = 10).

Figure 3.44 includes two drop size ratios, $D_s/D_L \approx 0.71$ and 0.48. For both ratios, the boundaries and critical $We^*$ of rebound and coalescence are similar. In their studies on water drops in air, Ashgriz and Poo (1990) reported that as the drop size ratio decreases, the critical $We^*$ dividing the coalescence and reflexive separation regions increases and the coalescence region becomes larger while the reflexive and stretching separation regions become smaller (see Figs. 1.2 and 1.4). They did not observe separate regions of rebound and coalescence. In the current study, although the reflexive and stretching separation regions were not assessed, no changes in critical $We^*$ based on drop size ratio were observed.

3.3.2 Details of collisions between unequal size drops

In this section, coalescence cases for two drop size ratios are presented: $We^*$ = 15 ($D_s/D_L$ = 0.69) and $We^*$ = 34 ($D_s/D_L$ = 0.47). A coalescence sequence for $We^*$ = 15 from the large field of view is shown in Fig. 3.46: $D_s/D_L$ = 0.69 ($D_s$ = 0.73 cm and $D_L$ = 1.06 cm), $U_{rel}$ = 20.9 cm/s, $u_s/u_L$ = 0.98 ($u_s$ = 13.1 cm/s and $u_L$ =12.8 cm/s), and B = 0. This different size drop collision can be compared with the equal size drop collision with $We^*$ = 15 (D = 0.84 cm and $U_{rel}$ = 21.7 cm/s) from section 3.2 (Fig. 3.10). Dimensionless time t* from Eq. 2.31 (equivalent to $t^* = tU_{rel}/D$ for equal size drop collisions) is used.

$$t^* = \frac{4\left(D_L u_L + D_s u_s\right)}{\left(D_L + D_s\right)^2} t \qquad (2.31)$$

As the drops approach each other (Fig. 3.45a, t* = -0.64), the smaller drop (right) is initially elongated with a tail while the larger drop (left) is close to spherical. For equal size drops in Fig. 3.10, both drops are elongated with tails. When the drops first contact at t* = 0 (Fig. 3.45b), the tail of the small drop disappears, so that both appear relatively spherical in shape. As the drops collide (Fig. 3.45c), the head of the large

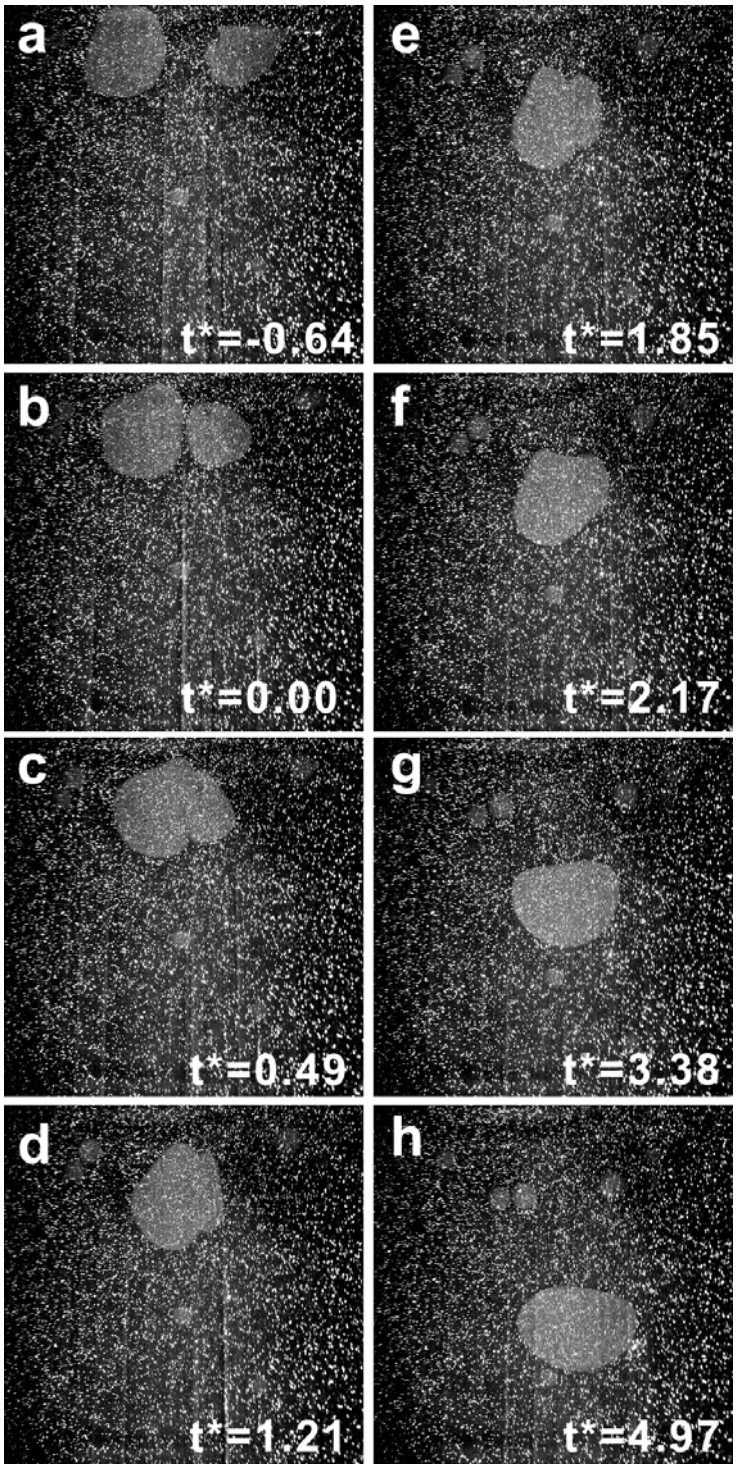


**Figure 3.45** The time evolution of unequal size drop collision: *We** = 15 (coalescence), B = 0, $D_s/D_L$ = 0.69 where $D_L$ and $D_s$ are the diameter of large and small drop, respectively.

drop deforms into a concave shape because the small drop pushes the large drop at the interface. At the same time, the small drop changes from prolate to oblate in shape. This is significantly different from equal size drop collisions where the heads of drops symmetrically flatten at the centerplane until the film ruptures (Fig. 3.10c-e). At t* = 1.21 (Fig. 3.45d), inertia drives the drop centroids closer together and both drops are oblate in shape. The deformed front of the large drop becomes flat, and the small drop elongates in the vertical direction. The drops coalesce at t* = 1.85 while they are moving apart (Fig. 3.45e). At this *We**, in contrast to the dimpled shapes in Fig. 10e, no dimples were observed at the back end of either drop before coalescence. After coalescence, the fluid from the small drop rotates. The resulting drop oscillates in shape and falls downward and to the right (Figs. 3.45f-h). For equal size drop collisions, the coalesced drop falls straight downward (Figs. 3.10f-h).

Figure 3.46 shows the computed velocity vectors and vorticity contours for *We** = 15 (every sixth vector is plotted). Velocity magnitudes and vectors are normalized by the relative velocity $U_{rel}$. The vorticity is non-dimensionalized using $U_{rel}$ and average of drop diameter ($D_L+D_s/2$). Red on the color map shows the counterclockwise rotation of flow, and blue represents clockwise rotation.

The upper portion of the vortex ring on the large drop stands apart from the lower portion (Fig. 3.46a). The maximum vorticity in the upper portion of the ring is ~$4.2U_{rel}/(D_L+D_s/2)$ while the value in lower portion is $3.0U_{rel}/(D_L+D_s/2)$. The fluid flows through the vortex ring and moves downward toward the collision plane. The vectors are directed more downward than for the smaller drop due to the steeper collision angle (42° compared to 31° for the small drop). The leading and trailing vortex ring in the small drop are initially elongated. The average vorticity in the upper portion of the ring is similar to values in the lower portion (~$3.3U_{rel}/(D_L+D_s/2)$). As the drops collide and start to deform, the higher velocity toward the rear of each drop pushes the trailing fluid closer to the interface. Note that both the upper and lower portions of the vortex ring in the small drop lie close to interface while, for the large drop, only the upper portion of the ring is located close to interface. At t* = 0.49, the upper portion of vortex ring ($4.3U_{rel}/(D_L+D_s/2)$) of the large drop is more focused than

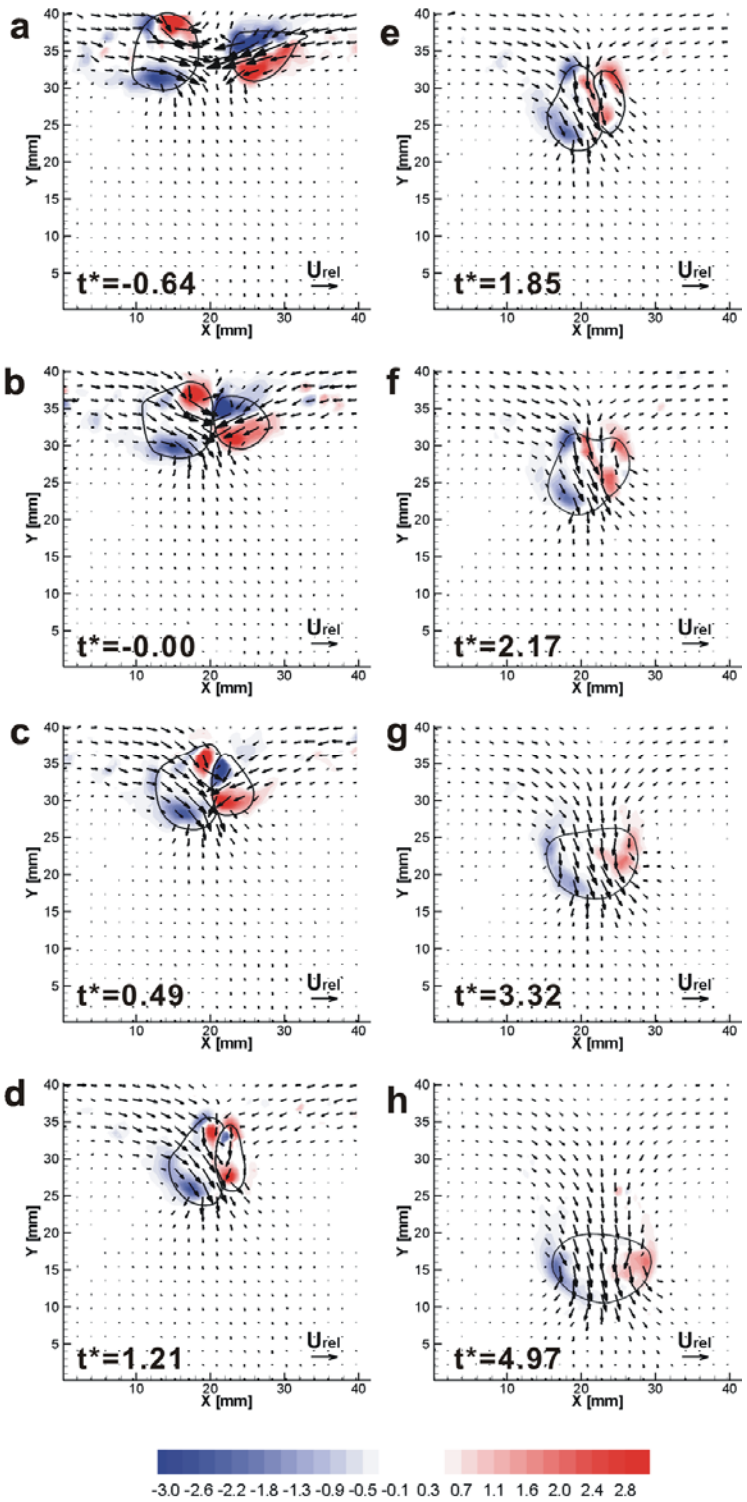


**Figure 3.46** Absolute in-plane velocity vectors and normalized vorticity contours: *We** = 15 (coalescence), $D_s/D_L$ = 0.69. Red is counterclockwise, and blue is clockwise.

the lower portion ($2.5U_{rel}/(D_L+D_s/2)$). Upper and lower portion vorticity of the small drop is similar ($3.0U_{rel}/(D_L+D_s/2)$. This may be because the small drop drives the large drop to deform concavely at the interface during the collision. At the same time, the velocity vectors show that the intervening silicone oil is draining out of the zone between the drops. In Fig. 3.46c, the small drop continuously pushes the larger drop while it changes from prolate to oblate in shape, and for the large drop, the fluid streaming through the rings appears to rotate more downward compare with the vectors in Fig. 3.46b. This concavely deformed interface may direct the fluid more downward. At t* = 1.21 (Fig. 3.46d), the lower portion of the ring in the large drop moves downward as the drop shape changes (Fig. 3.46c and d) resulting in a broader shape at the bottom. At this moment, the upper portion of the large drop and lower portion of the small drop become focused. Note that vortex ring and velocity vectors in the small drop are similar to those in the equal size drop collision in Fig. 3.10e.

In Fig. 3.46e, the small drop vectors are directed downward while larger drop vectors are directed downward and to the right, toward the collision plane. The concavely deformed head of the large drop now changes to be convexly deformed. When the inertia of the small drop dissipates as its centroid comes close to the interface, the large drop still has enough inertia to push the inwardly curved intervening film out toward the small drop. Therefore, a wave-like interface is formed as represented in Fig. 3.46e. While the drops move apart, the interface ruptures at t* = 1.85. Afterward the resulting drop rotates counterclockwise due to the inertia of the large drop and oscillates to form a spherical drop. The drop falls downward with a single downward-moving ring. For unequal size drop collision, the symmetry is lost during the collision due to the unbalanced drop size and velocity, and the coalesced drop moves away from the initial contact plane (Figs. 3.46e-h).

For a pair of equal size drops, the interface did not deform as shown in Fig. 3.10. The drops deformed to form dimples at their back side. The vortex ring pair induces the fluid to move toward the centerplane and strong downflow is experienced at the film. When the downflow is strong, the film ruptures.

Normalized vertical velocity contours are plotted in Figs. 3.47 to emphasize

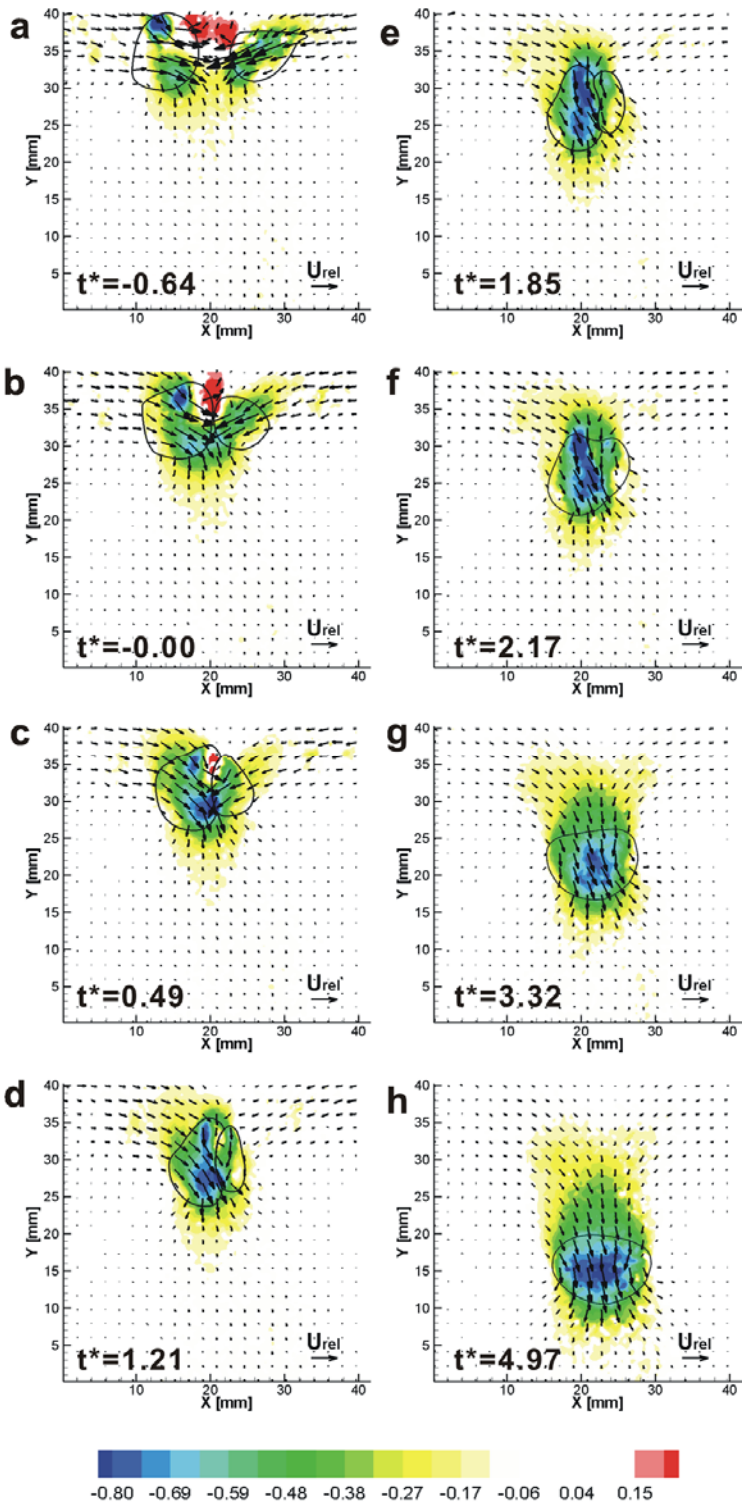


**Figure 3.47** Absolute in-plane velocity vectors and vertical velocity contours: *We** = 15 (coalescence), $D_s/D_L$ = 0.69. Red is upflow, and blue is downflow.

patterns of local upflow and downflow as the drops collide in both cases. In the color map, blue represents strong downflow while red is upflow. As the drops approach and collide, the local upflow is observable until t* = 0.49 (Figs. 3.47a-c). The upflow region gets smaller as the fluid layer between the drops drains. Similar to equal size drop collisions, a single maximum in downward velocity near the interface is observed beginning at t* = 0.49 through t* = 1.21 (Figs. 3.48c-d) before the film ruptures. Note that once the small drop changes its shape to oblate and its horizontal inertia dissipates, downward velocity at the upper portion of the large drop becomes significant as the interface of the large drop changes from concave to convex (Figs. 3.47d-e). At t* = 1.85 when the drops coalesce (Fig. 3.47e), downward velocities at the upper part of the interface ($0.85U_{rel}$) are more focused than at the lower part ($0.76U_{rel}$). The local maximum in downward velocity occurs at the upper portion of the interface in the coalescing case with $We^*$ =15 for unequal size drops, but at the lower portion of the interface in the coalescing case when $We^*$ =15 for equal size drops (see Fig. 3.47e and Fig. 3.10e).

Figure 3.48 shows the time of film rupture for $We$ = 15 ($D_s/D_L$ = 1.00, t* = 1.37) and $We^*$ = 15 ($D_s/D_L$ = 0.69, t* = 1.85). The vectors show velocity in the reference frame relative to the falling drops. The red dots show the film rupture locations. In Fig. 3.48b (unequal size drops), the bottom section of the large drop is wider than the top while the small drop is horizontally symmetrical in shape and somewhat tilted counterclockwise toward the top of the large drop. The flow within the large drop moves toward the collision plane. The flow in the small drop moves outward, away from the collision plane. At this time (compared with large view from Fig. 3.45), the flow within the small drop is moving outward after being deformed vertically. In Fig. 3.48a (equal size drops), the two drops are identical in shape and vertically symmetrical. The flow within both drops moves toward the collision plane. When comparing these two cases, the coalescence time for $We^*$ = 15 ($D_s/D_L$ = 0.69) is later than the time for $We$ = 15 ($D_s/D_L$ = 1.00).

The patterns of the pair of vortex rings in the large drop differ from those in the small drop in Fig. 3.48b. The vortex ring in the large drop tilts downward while the

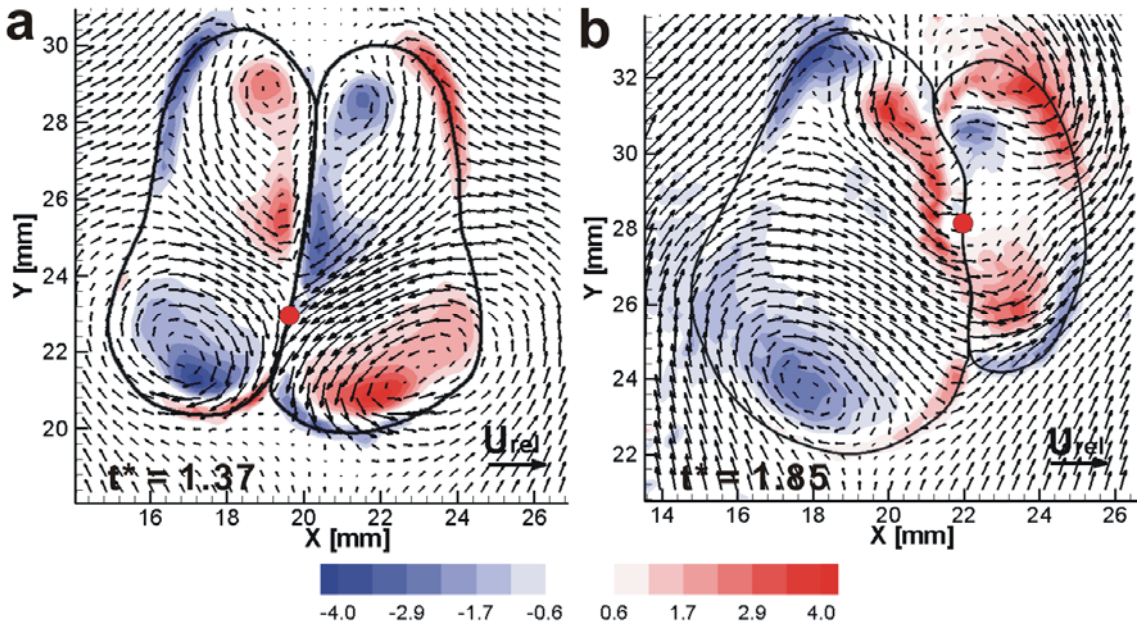


**Figure 3.48** The vector and vorticity fields at the time of rupture: (a) *We* = 15 ($D_s/D_L$ = 1.0), t* = 1.37, (b) *We** = 15 ($D_s/D_L$ = 0.69), t* = 1.85. Vectors show in-plane velocity relative to the falling drops. Colors show normalized vorticity. Red is counterclockwise, and blue is clockwise rotation. The red dots show the film rupture location.

ring in the small drop is horizontally symmetrical. For equal size drops (Fig. 3.48a), the vortex ring of both drops is tilted downward. In Fig. 3.48b, the maximum vorticity strengths in the large drop are 4.2D/$U_{rel}$ and 2.8D/$U_{rel}$ for the upper and lower portion of the ring, respectively. The maximum vorticity strengths in the small drop are 2.5D/$U_{rel}$ and 3.1D/$U_{rel}$ for the upper and lower portion of the ring, respectively. The large drop distribution is therefore different than that observed either in the smaller drop or in the equal size drop pair.

The intervening film between drops is flat for equal size drops (Fig. 3.48a). By contrast, the film is irregularly curved for unequal size drops (Fig. 3.48b). In Fig. 3.49a, the vectors near the interface move vertically along the film. For unequal size drops, the velocity vectors in the vicinity of the curved interface vary. Above the stagnation point (near the center of the film), the flow in the large drop moves upward and warps the film outward (toward the small drop). Below this point, the flow moves downward and causes the drops to rotate slowly counterclockwise. The film ruptures near this center stagnation point for unequal size drops (the red dot in Fig. 3.48b). For equal size drops, the film rupture always occurs near the downstream end of the interface as shown in Fig. 3.48a. The film rupture location for unequal size drop collisions varies and depends on the shape of the intervening film.

Figure 3.49 shows a time sequence during the coalescence event for $We^*$ = 15. As in Fig. 3.48, the vectors show velocity in the reference frame relative to the falling drops. Figure 3.49a shows the field just before the film ruptures. Figure 3.49b shows the frame when the film ruptures, and the rupture location is marked by the red dot. These two fields are separated by 1 ms. When Fig. 3.49b is compared with Fig. 3.49a, sudden changes of the velocity vectors near the interface are observed. The film breaks at this location, and retracts rapidly upward and downward as shown in Figs. 3.49b and c. The fluid in the downstream section of the large drop flows downward into the lower portion of the small drop. In the subsequent image (Fig. 3.49d), the upper and lower apexes in the film disappear, and strong localized vorticity is observed at the top and bottom of the remaining single drop due to the rapid film motion of the retracting interface. The vorticity strength in this region then decreases as the local curvature

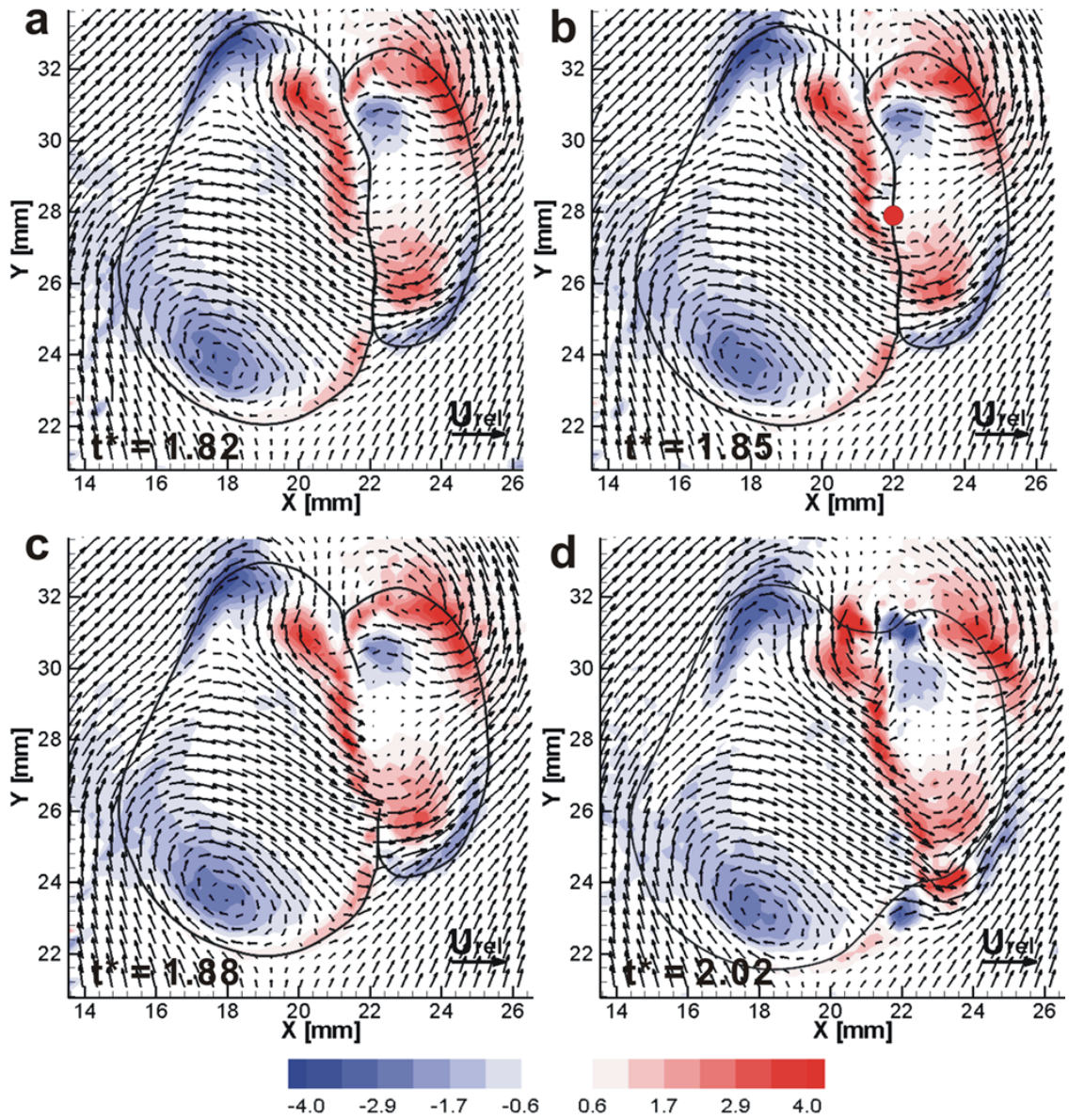


**Figure 3.49** The in-plane vectors and normalized vorticity contours during coalescence event for $We^*$ = 15 ($D_s/D_L$ = 0.69). Vectors show velocity relative to the falling drops. Colors show normalized vorticity. Red is counterclockwise, and blue is clockwise rotation. The red dot in b shows the film rupture location (Film ruptures at t* = 1.85).

smooths out: The vorticity at the upper portion of the large drop decreases from $4.2D/U_{rel}$ at t* = 1.85 to $3.2D/U_{rel}$ at t* = 2.02. The vorticity pairs in the resulting drop rotate counterclockwise while the two drops mix. The upper portions of the ring for each drop eventually disappear. The asymmetry of the resulting vectors and vortex pair of a coalesced drop causes it to oscillate for a longer time before forming a spherical drop as opposed to equal size drop cases.

The coalescence sequence for a smaller size ratio with $We^*$ = 14 is shown in Fig. 3.50: $D_s/D_L$ = 0.47 where $D_s$ = 0.55 cm and $D_L$ = 1.17 cm, B = 0, $U_{rel}$ = 15.7 cm/s, and $u_s/u_L$ = 1.61 ($u_s$ = 7.1 cm/s and $u_L$ =11.4 cm/s). The two drops have slightly different fluorescence dye concentrations so that their colors differ somewhat on the image, and show the mixing of the drops during coalescence.

As the drops approach, they are initially elongated with tails. The small drop is elongated more than the large one. The collision is near head-on (Fig. 3.50b). The small drop changes from prolate to oblate after the two drops initially meet. The inner curvature of the large drop in the intervening film deforms slightly inward but not as significantly as when $We^*$ = 15 ($D_s/D_L$ = 0.69) (Fig. 3.50c). The interface becomes flat as the small drop elongates vertically at t* = 0.98. The tail of the large drop disappears as the drop is compressed, and the drop continues to move to the right. Then, similar to $D_s/D_L$ = 0.69, the large drop causes the small drop to move in the opposite direction. The vertically compressed small drop expands horizontally as it moves apart, and the film ruptures at t* = 1.51. Unlike $D_s/D_L$ = 1.0 for the same *We*, dimpled drops were not observed similar to $We^*$ = 15 ($D_s/D_L$ = 0.69). Afterward, the small drop portion of the resulting volume is horizontally elongated with a tail at t* = 2.14. This elongation of the resulting drop was never observed for $D_s/D_L$ = 1.0 and was not obviously seen for $D_s/D_L$ = 0.69. Afterward, the small drop fluid retracts toward the resulting drop, and the tail disappears (Fig. 3.50g). The small drop fluid moves to the top of the coalesced volume and mixs with the large drop fluid as the coalesced drop oscillates and falls (Figs. 3.50g and h). Rapid mixing shortly after the film rupture is not observed during coalescence.

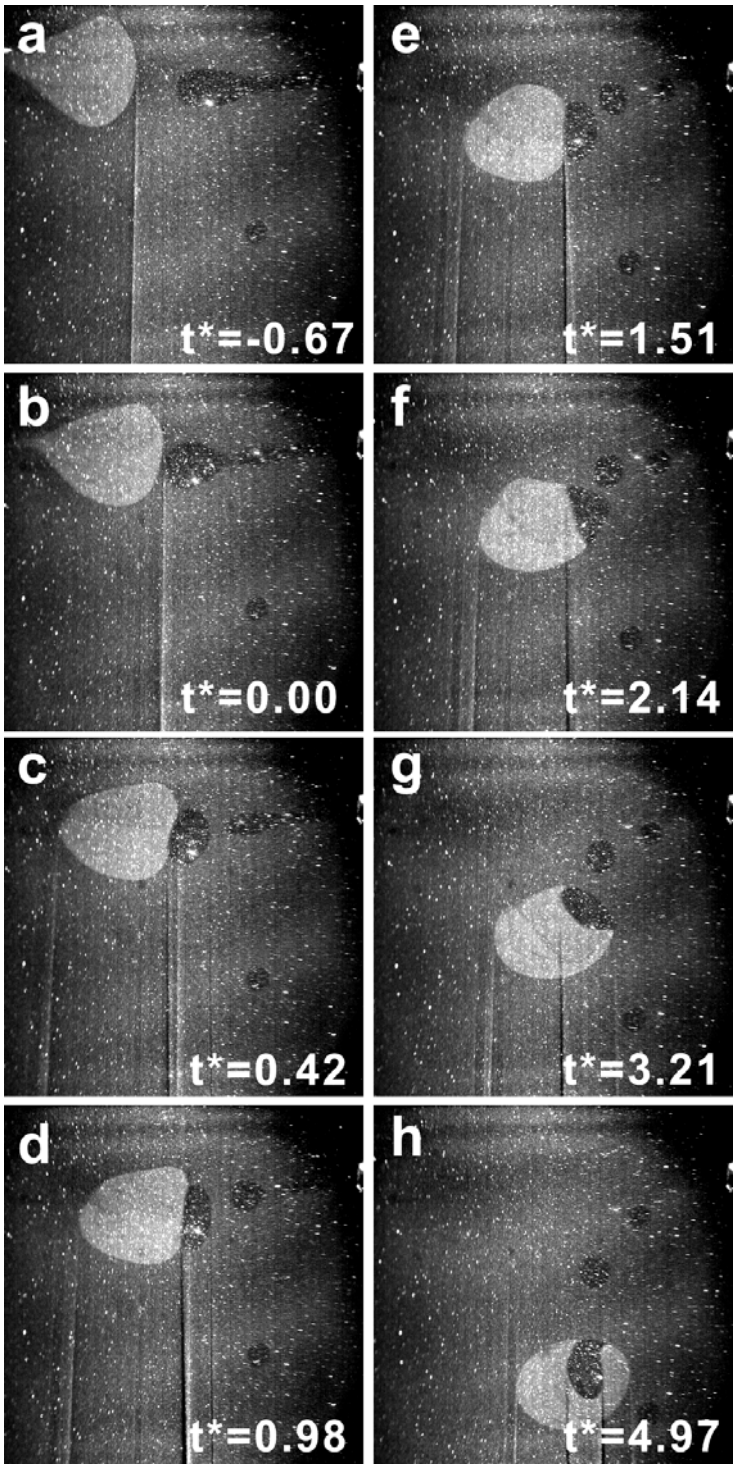


**Figure 3.50** The time evolution of unequal size drop collision: *We** = 14 (coalescence), B = 0, $D_s/D_L$ = 0.47 where $D_L$ and $D_s$ are the diameter of the large and small drops, respectively.

Figures 3.51 and 3.52 show the time sequence during the coalescence event and corresponding vector fields for $We^*$ = 14 ($D_s/D_L$ = 0.47). At t* = 0.93 (Figs. 3.51a and 3.52a), the small drop is near maximum deformation. It is horizontally symmetrical. Both upper and lower portions of the vortex ring in the small drop are close to the interface. The vorticity at the upper and lower portion of the vortex ring are $3.9D/U_{rel}$ and $4.6D/U_{rel}$, respectively. At t* = 0.93, the head of the large drop flattens. The flow moves toward the collision plane. The upper portion of the vortex ring in the large drop is located close to the interface and the lower portion is away from the collision plane. Unlike the small drop, the vorticity in the upper portion of the ring is stronger than that of the lower portion: $4.3D/U_{rel}$ and $3.2D/U_{rel}$, respectively. At t* = 1.51, the small drop broadens horizontally compared to the shape at t* = 0.93 (Figs. 3.51a and b). The large drop continues to drive the small drop to the right that both drops translate to the right. The drops coalesce at t* = 1.51 while the drops are moving apart. At this time, the vorticity magnitudes associated with the upper and lower parts of each vortex ring decrease. The vorticity strength of the large drop decreases from $4.3D/U_{rel}$ to $3.6D/U_{rel}$ in the upper part of the leading vortex (Figs. 3.52a and b). The vorticity of the small drop significantly decreases from $4.6D/U_{rel}$ to $2.6D/U_{rel}$ in the lower part of the vortex ring. The vortex ring of the large drop continues to induce flow inward and toward the right. Unlike when $We^*$ = 15 ($D_s/D_L$ = 0.69), the intervening film is flat through the course of this time interval. The red dot in Fig. 3.52b shows the film rupture location. The location is near the lower end of the film. By comparing this with Fig. 3.53, the film rupture location is lower than the location for $We^*$ = 15 ($D_s/D_L$ = 0.69). It can be concluded that the film rupture location varies for unequal size drop coalescence. By contrast, the rupture location was always in the lower part of the film for equal size drops. After coalescence, the large drop fluid continues to move toward the right and causes the resulting drop to rotate counterclockwise (Fig. 3.52c). The fluid from the small drop elongates horizontally with a tail after the film ruptures as shown in Fig. 3.52c. Afterward, the small drop fluid moves toward the top of the coalesced drop and the tail disappears at t* = 2.79. The circulation in the upper part of the rings decreases with time.

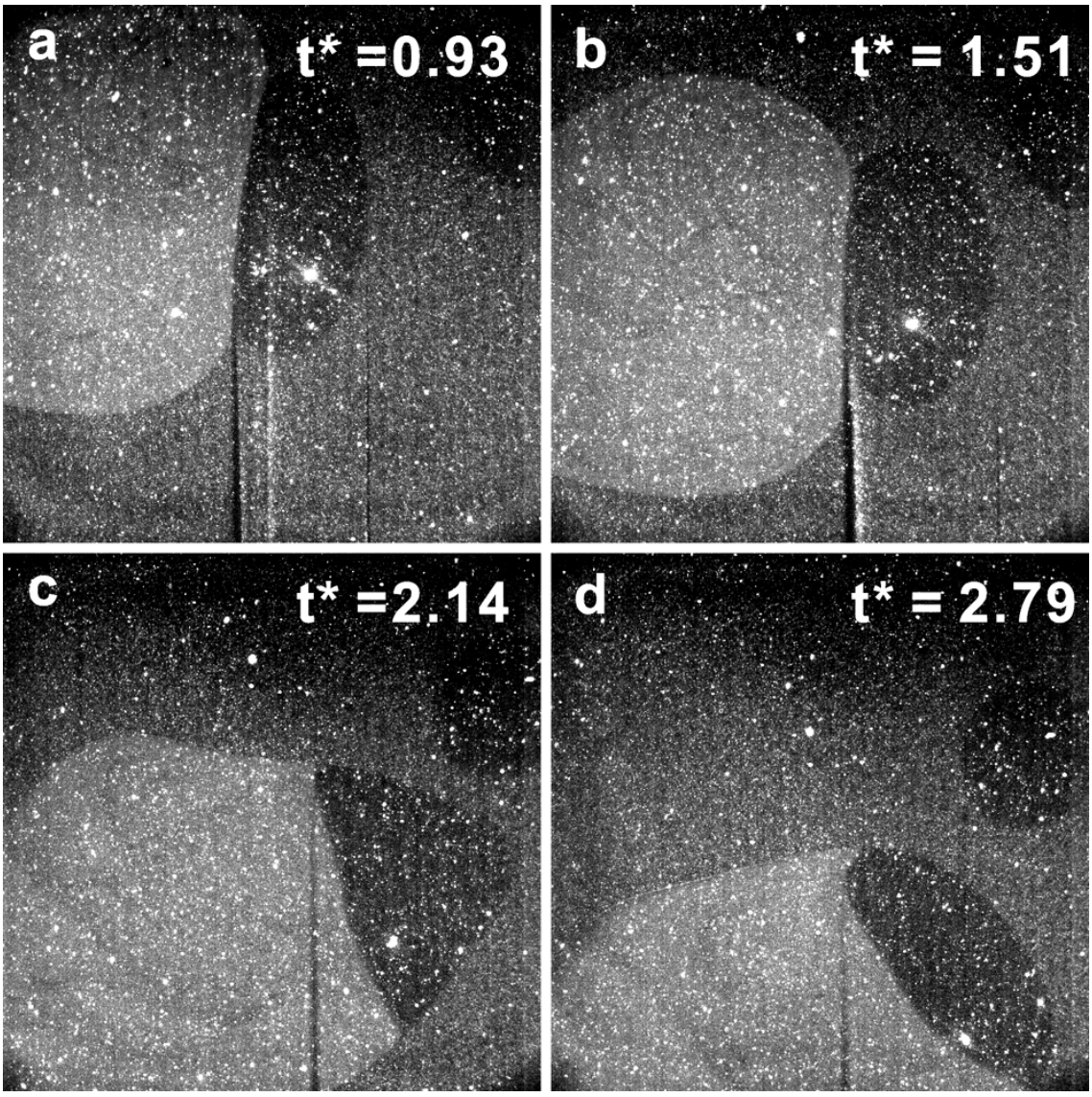


**Figure 3.51** The sequential zoomed views during the coalescence event for when *We** = 14 ($D_s/D_L$ = 0.47).

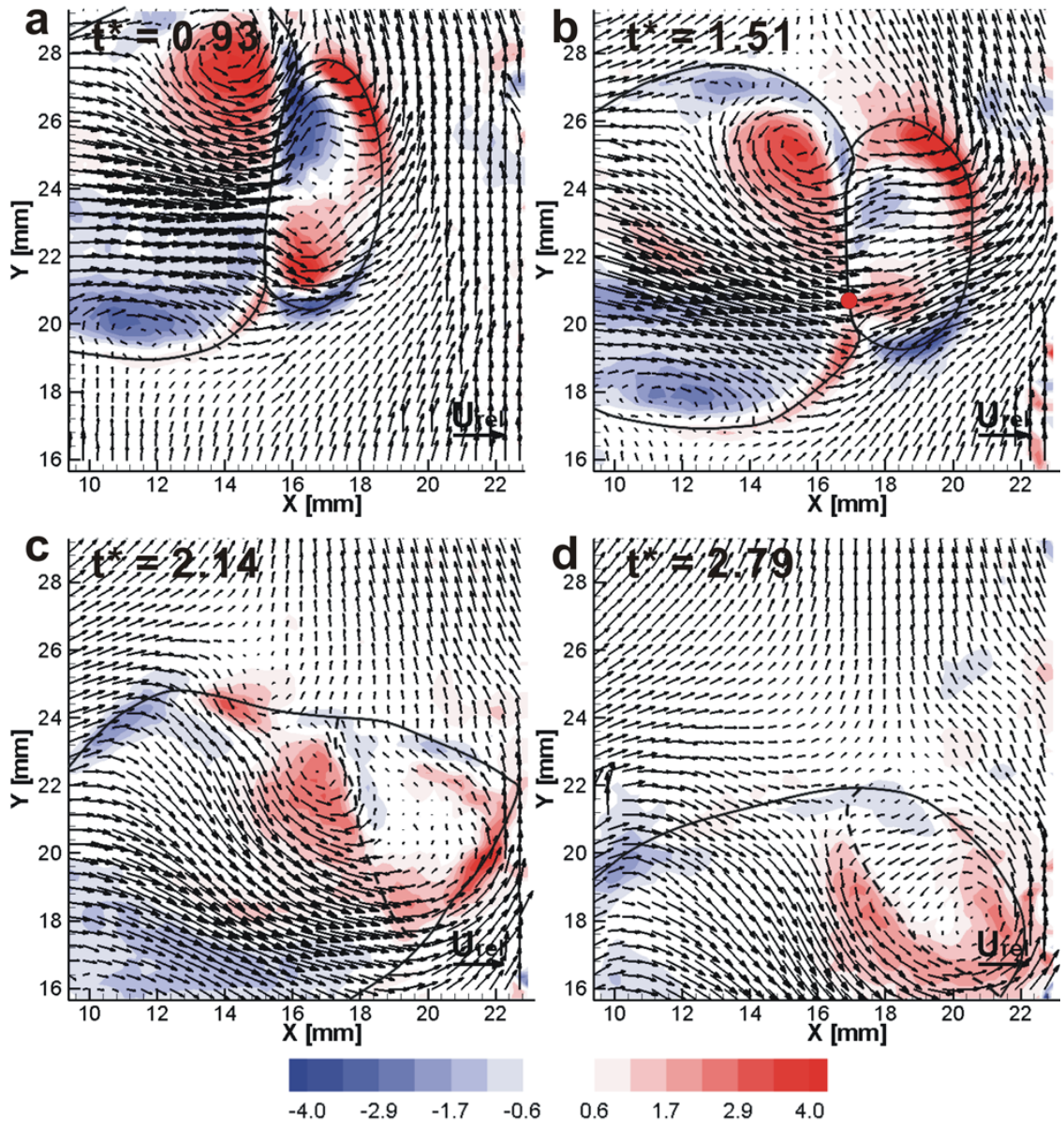


**Figure 3.52** The in-plane vectors and normalized vorticity contours during the coalescence event for *We** = 14 ($D_s/D_L$ = 0.47). Vectors show the velocity relative to the falling drops. Colors show the normalized vorticity. Red is counterclockwise, and blue is clockwise rotation. The red dot in b shows the film rupture location (Film ruptures at t* = 1.51). Dashed line shows boundary of the fluid from small drop.

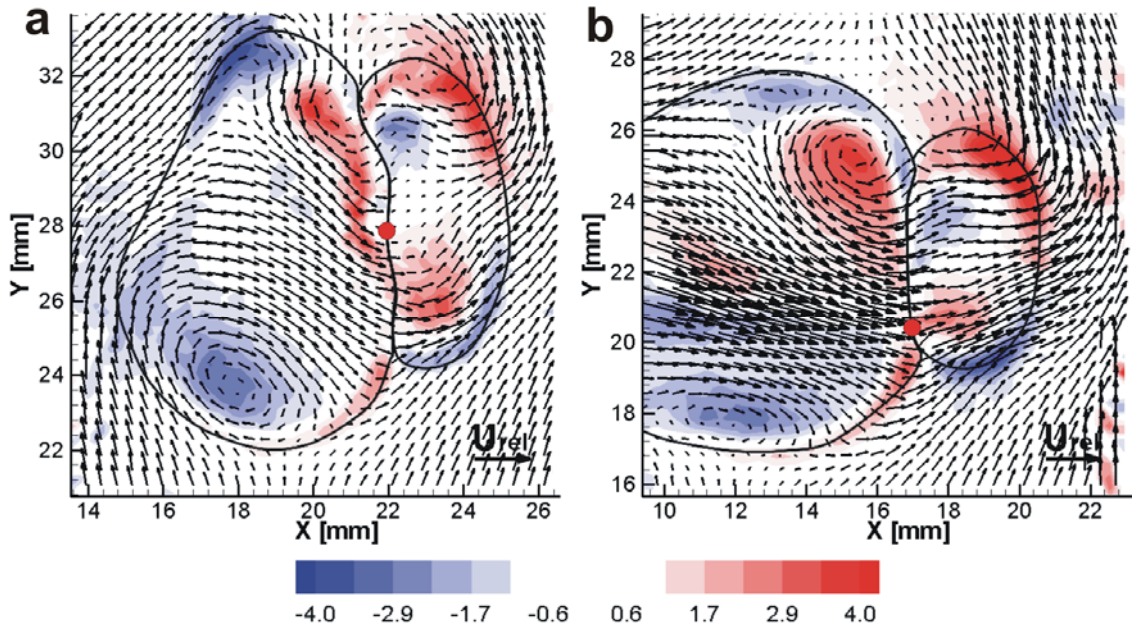


**Figure 3.53** The vector and vorticity fields at the time of rupture: (a) *We** = 15 ($D_s/D_L$ = 0.69), t* = 1.85, (b) *We** = 14 ($D_s/D_L$ = 0.47), t* = 1.51. Vectors show the in-plane velocity relative to the falling drops. Colors show the normalized vorticity. Red is counterclockwise, and blue is clockwise rotation. The red dots show the film rupture location.

3.3.3 Effect of differing Weber numbers

In this section, a higher Weber number $We^* = 34$ ($D_s/D_L = 0.47$) is compared with the previous case of $We^* = 14$ ($D_s/D_L = 0.47$) (Fig. 3.50). Both collisions are head-on (B = 0). The coalescence sequence for $We^* = 34$ from the large field of view is shown in Fig. 3.54: $D_s/D_L = \underline{0.47}$ where $D_s = 0.56$ cm and $D_L = 1.18$ cm, $U_{rel} = 32.3$ cm/s ($u_I/u_s = 0.81$, $u_s = 18.3$ cm/s and $u_L = 14.9$ cm/s), B = 0. Velocity ratio ($u_I/u_s$) is lower than in the $We^* = 14$ case ($u_I/u_s = 1.61$).

As the drops approach, the small drop is initially elongated with tails. This drop later separates into a main drop with three satellite drops during the collision sequence. The collision is head-on as shown in Fig. 3.54b. After the drops make initial contact, the curvature of the intervening film for the large drop is deformed inward as the small drop changes prolate to oblate shape (Figs. 3.54c and d). Note that the deformation of the film also can be seen for $We^* = 14$, but the deformation is weak, and the film becomes flattened before coalescence (Fig. 3.54c through d). Afterward, the large drop continues to move along its trajectory and drives the small drop in the opposite direction of its initial trajectory. The tail of the large drop disappears, and the inwardly deformed interface decreases in curvature at $t^* = 1.62$ (Fig. 3.54e), but is still not flat. The deformation of the small drop is maximized. Although $We^*$ is high, in this case dimpled drops are also not observed. The drops coalesce at $t^* = 1.62$ (Fig. 3.54e). By contrast, dimples were observed when $We = 15$ for equal size drop collisions. Unlike for $We^* = 14$ ($D_s/D_L = 0.47$), a subsequent elongation of the small drop fluid, which can be viewed in Fig. 3.50f and 3.51c for $We^* = 14$, is not observed. Instead, the small drop fluid expands vertically after coalescence as shown in Fig. 3.54f. After coalescence, the small drop fluid moves into the upper part of the coalesced drop as shown in Figs. 3.54f through g. The resulting drop oscillates in shape and falls downward to the right (Figs. 3.54g through h).

Figures 3.55 and 3.56 show a time sequence during the coalescence event and the corresponding vector fields for $We^* = 34$ ($D_s/D_L = 0.47$). At $t^* = 0.77$ (Fig. 3.55a), the small drop moves toward the large drop. The tail of the small drop is still seen at $t^* = 0.77$. The interface is significantly curved toward the large drop. For both drops, the

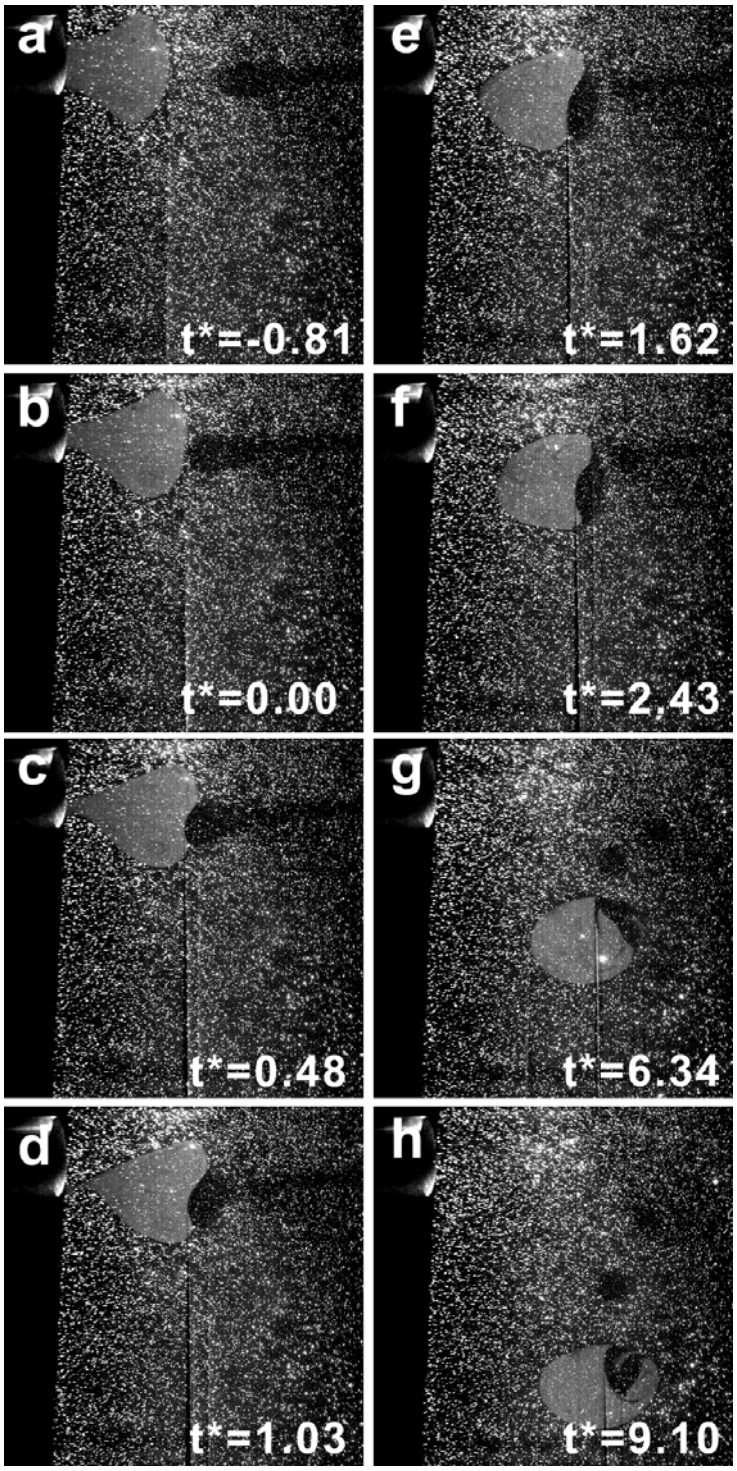


**Figure 3.54** The time evolution of unequal size drop collisions: *We** = 34 (coalescence), B = 0, $D_s/D_L$ = 0.47, and $u_L/u_s$ = 0.81 where $D_L$ and $u_L$, and $D_s$ and $u_s$ are the diameter and horizontal components of velocity for the large and small drops, respectively.

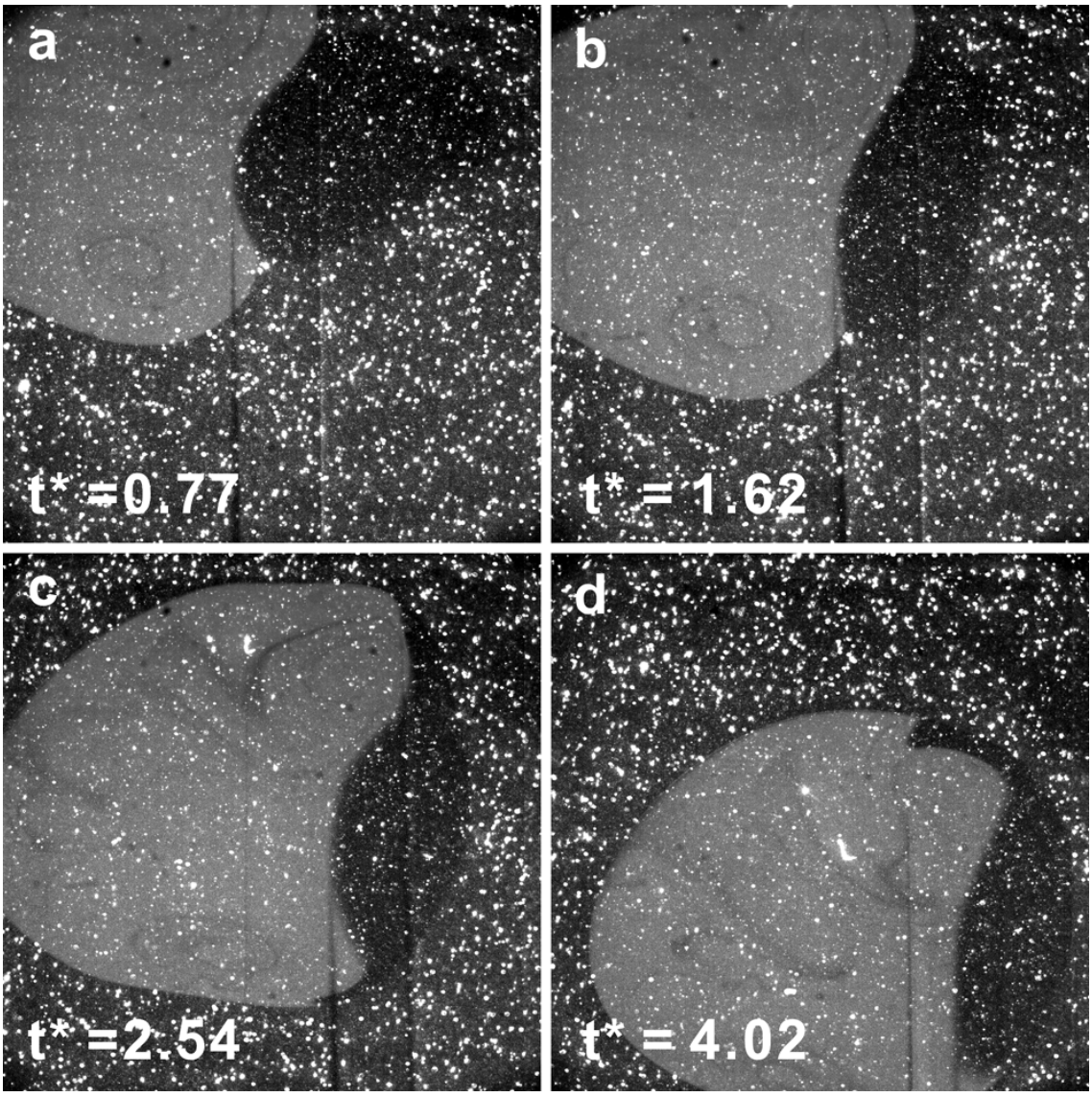


**Figure 3.55** The sequential zoomed views during the coalescence event for *We** = 34 ($D_s/D_L$ = 0.47).

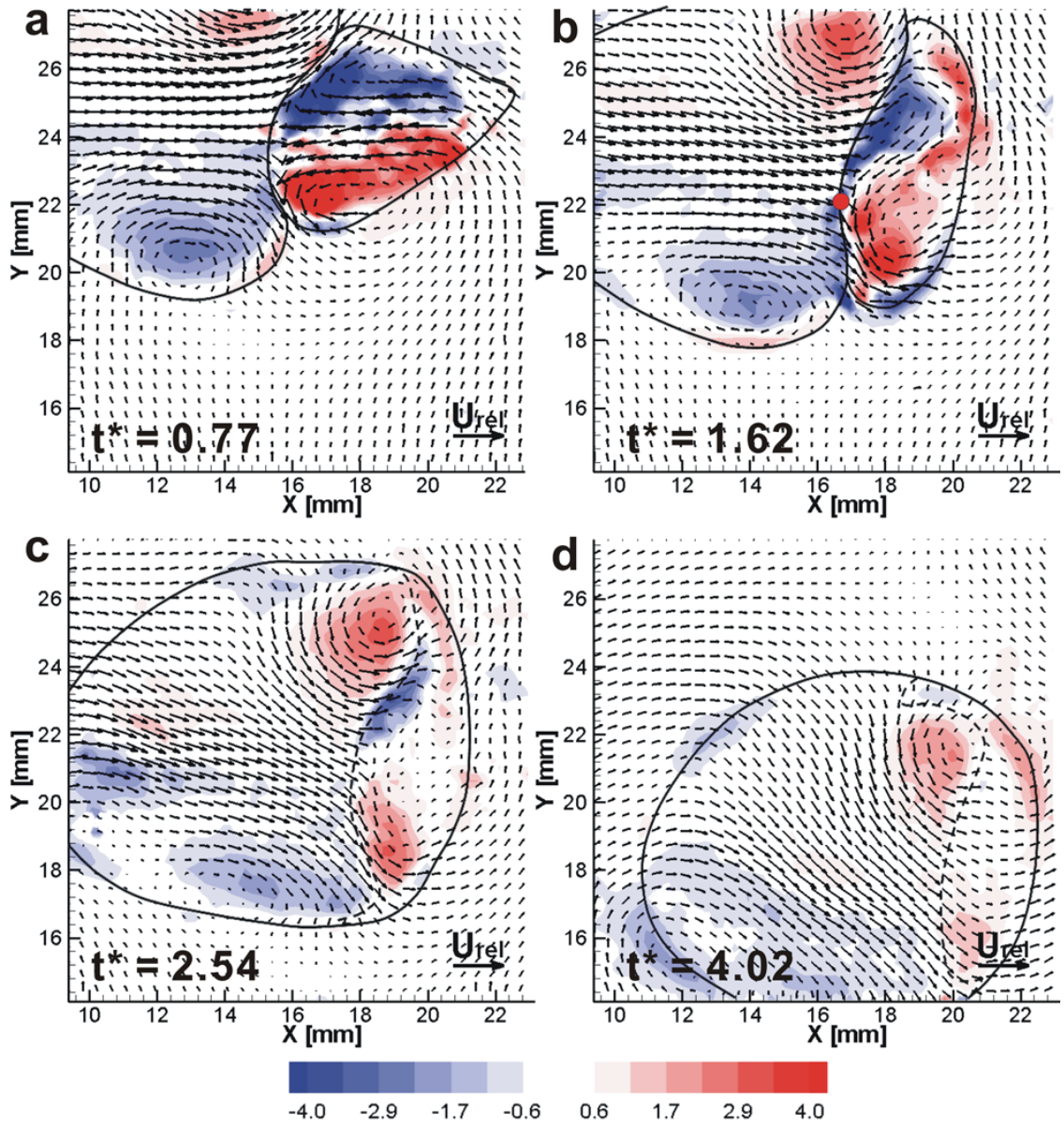


**Figure 3.56** The in-plane vectors and normalized vorticity contours during coalescence event for *We** = 34 ($D_s/D_L$ = 0.47). Vectors show velocity relative to falling drops. Colors show normalized vorticity. Red is counterclockwise, and blue is clockwise rotation. The red dot in b shows the film rupture location (Film ruptures at t* = 1.62). The dashed line shows the boundary of fluid from the small drop.

upper and lower part of the leading ring is close to the interface. The vorticity in the vortex ring of the small drop is stronger than that of the large drop: the vorticity values in the lower part of the vortex ring in the large and small drops are 2.5D/$U_{rel}$ and 6.6D/$U_{rel}$, respectively (Fig. 3.56a). The vorticity magnitudes associated with the upper and lower parts of each vortex ring decrease. In Figs. 3.56a through 3.56b, the vorticity strength of the small drop decreases from 6.6D/$U_{rel}$ to 4.7D/$U_{rel}$ in the lower part of the vortex. For the large drop, the strength of the vortex ring decreases less than in the small drop: the vorticity strength of the small drop decreases from 2.5D/$U_{rel}$ to 2.3D/$U_{rel}$ in the lower part of the vortex ring. In general, for equal size drops, the vortex ring pair in the colliding drops dissipates as they collide and deform. For unequal size drops, the vortex strengths of both drops dissipate, but the small drop dissipates more as the interface changes shape (the shape change generates opposing vorticity).

Similar to when $We^*$ = 14, the upper portion (3.3D/$U_{rel}$) of the vortex ring in the large drop is stronger than the lower portion (2.3D/$U_{rel}$), and the lower portion (4.7D/$U_{rel}$) of the ring in the small drop is stronger than its upper portion (4.2D/$U_{rel}$). However, unlike when $We^*$ = 14, the vortex ring of the small drop is still stronger than the large drop when the film ruptures ($t^*$ = 1.62). By contrast, for when $We^*$ = 14, the strength of vortex ring in the small drop decrease less than the large drop in Fig. 3.57. Also, in Fig. 3.57, the intervening film for when $We^*$ = 14 is vertically flat while the film for $We^*$ = 34 remains curved. When $We^*$ = 34, the film is less curved at $t^*$ = 1.62 than $t^*$ = 0.77 since the large drop pushes out the small drop at the interface as it moves toward the small drop. However the film is obviously not flat when the film ruptures. Since the velocity ratio for $We^*$ = 34 ($u_I/u_s$ = 0.81) is lower than for $We^*$ = 14 ($u_I/u_s$ = 1.61), the interface for $We^*$ = 34 is initially more bent, and although the curvature decreases with time, the interface is still bent when the drops coalesce. With this curved interface, the vortex ring of each drop dissipates somewhat, but the upper part of the ring in the large drop and the lower part of the ring in the small drop are focused more. In Fig. 3.56b, the interface motion opposes the vorticity in the small drop. In contrast, for $We^*$ = 14, the interface initially deforms less and is almost flat before coalescence as shown in Fig. 3.57a since the velocity of the large drop is faster than that

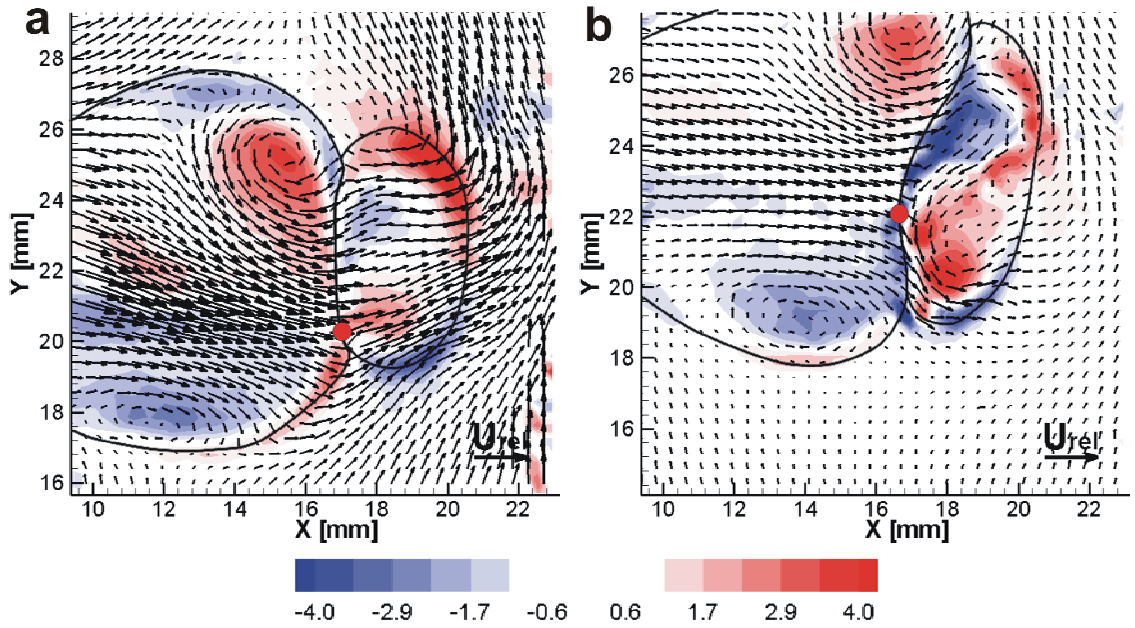


**Figure 3.57** The vector and vorticity fields at the time of rupture: (a) *We** = 14 ($D_s/D_L$ = 0.47), t* = 1.51, (b) *We** = 34 ($D_s/D_L$ = 0.47), t* = 1.62. Vectors show in-plane velocity relative to the falling drops. Colors show normalized vorticity. Red is counterclockwise, and blue is clockwise rotation. The Red dots show the film rupture location.

of the small drop. Therefore, when the velocity ratio ($u_L/u_s$) is below 1, the vortex ring pair is less symmetric.

The film ruptures near its center where the downflow is strong and curvature of the film changes. In Fig. 3.57, the rupture location is higher for $We^* = 34$ than for $We^* = 14$. As discussed earlier, the rupture location varies for unequal size drop collisions depending on the intervening film shape, velocity vectors and vorticity near the film. In Fig. 3.57, the relative velocity vectors in the small drop for $We^* = 34$ differ from those for $We^* = 14$. The vectors in Fig. 3.57b show the circulation of fluid in the small drop corresponding with the vortex ring and bent interface. However, the vectors in the small drop in Fig. 3.57a point to the right as both drops translate to the right. After coalescence, the top and bottom of the small drop fluid enclose the large drop fluid at $t^* = 2.54$ (Fig. 3.56c) and the large drop fluid moves toward the lower portion of small drop fluid. Counterclockwise circulation at the upper part of the resulting drop is observed (Figs. 3.56c and d). The small drop fluid eventually moves to the top of the resulting drop and mixes with the large drop fluid (Fig. 3.56d).

In summary, for higher Weber number cases, the curvature of the intervening film is deformed more inward toward the large drop than for lower $We^*$ cases when the drops collide and deform. As $We^*$ decreases, the deformation of the film is weaker, and it becomes flattened before coalescence. Also, a subsequent horizontal elongation of the small drop fluid after coalescence is observed for $We^* = 14$. This may be because the velocity ratio ($u_L/u_s = 1.61$) is higher than for $We^* = 34$ ($u_L/u_s = 0.81$). For $We^* = 34$, the small drop fluid expands vertically after coalescence. For both cases, the upper portion of the vortex ring in the large drop and the lower portion of the ring in the small drop are more focused. When $We^* = 34$, the interface decrease in curvature but is still not flat before the film ruptures. In contrast, for $We^* = 14$, the concavely deformed interface changes to convexly deformed just before coalescence. Observation of additional cases suggests that at the higher $We^*$ ($We^* = 34$), even if the velocity ratio $u_L/u_s > 1$, the concavely deformed interface does not become convex. Instead, it becomes flat before coalescence. Further details are discussed below.

For previous depictions when *We** = 34, the initial velocity of the large drop has been slower than the small drop: $u_s$ = 18.3 cm/s and $u_L$ =14.9 cm/s ($u_L/u_s$ = 0.81). In the following paragraphs, *We** = 34 ($u_L/u_s$ = 2.12), a case where the large drop is faster than the small drop is compared. Figure 3.58 shows the coalescence sequence for *We** = 34 from the large field of view: $D_s/D_L$ = 0.44 where $D_s$ = 0.54 cm and $D_L$ = 1.22 cm, $U_{rel}$ = 22.3 cm/s ($u_L/u_s$ = *2.12*, $u_s$ = 7.7 cm/s and $u_L$ = 16.3 cm/s), B = 0. For this case, small view sequences and vector fields are not available. To match the Weber number and impact parameter, the incidence tube angles and tube heights were adjusted so that the collision angles of the large and small drop were 23° and 24°, respectively. For *We** = 34 ($u_L/u_s$ = 0.81), the collision angles of the large and small drop were 22° and 5°, respectively.

As the drops approach, in Fig. 3.58a, the small drop is initially elongated with tails similar to the case with $u_L/u_s$ = 0.81 (Fig. 3.54a). The drop later separates into a main drop with two satellite drops during the initial collision. After the drops initially make contact, unlike $u_L/u_s$ = 0.81, the interfacial film between them is flat at t* = 0.56. The film remains flat as the small drop changes from prolate to oblate (Figs. 3.58c and d). The drops move more to the right than for $u_L/u_s$ = 0.81 due to the higher velocity ratio ($u_L/u_s$ = 2.12). The drops coalesce at t* = 1.55. Unlike $u_L/u_s$ = 0.81, the film is flat and the small drop is vertically elongated at coalescence. Similar to $u_L/u_s$ = 0.81, the no significant elongation of the small drop fluid after coalescence is observed in Fig. 3.58f, although it forms a slight cusp on the right. After coalescence, the small drop fluid rotates counterclockwise and moves toward the top of the resulting drop (Fig. 3.48g). The coalesced drop falls downward to the right as it oscillates to form a spherical drop (Figs. 3.58g and h).

The key effects of the velocity ratio are that, when $u_L/u_s > 1$, the drops deform less and the interface is near flat through the drop deformation sequence before coalescence. After coalescence, the small drop fluid forms a tail and later retracts toward the large drop fluid to mix. When $u_L/u_s < 1$, the drops deform significantly. The interface is initially curved toward the large drop after the drops initial collide. As the small drop changes from prolate to oblate, the interface decreases in curvature and reverts to the

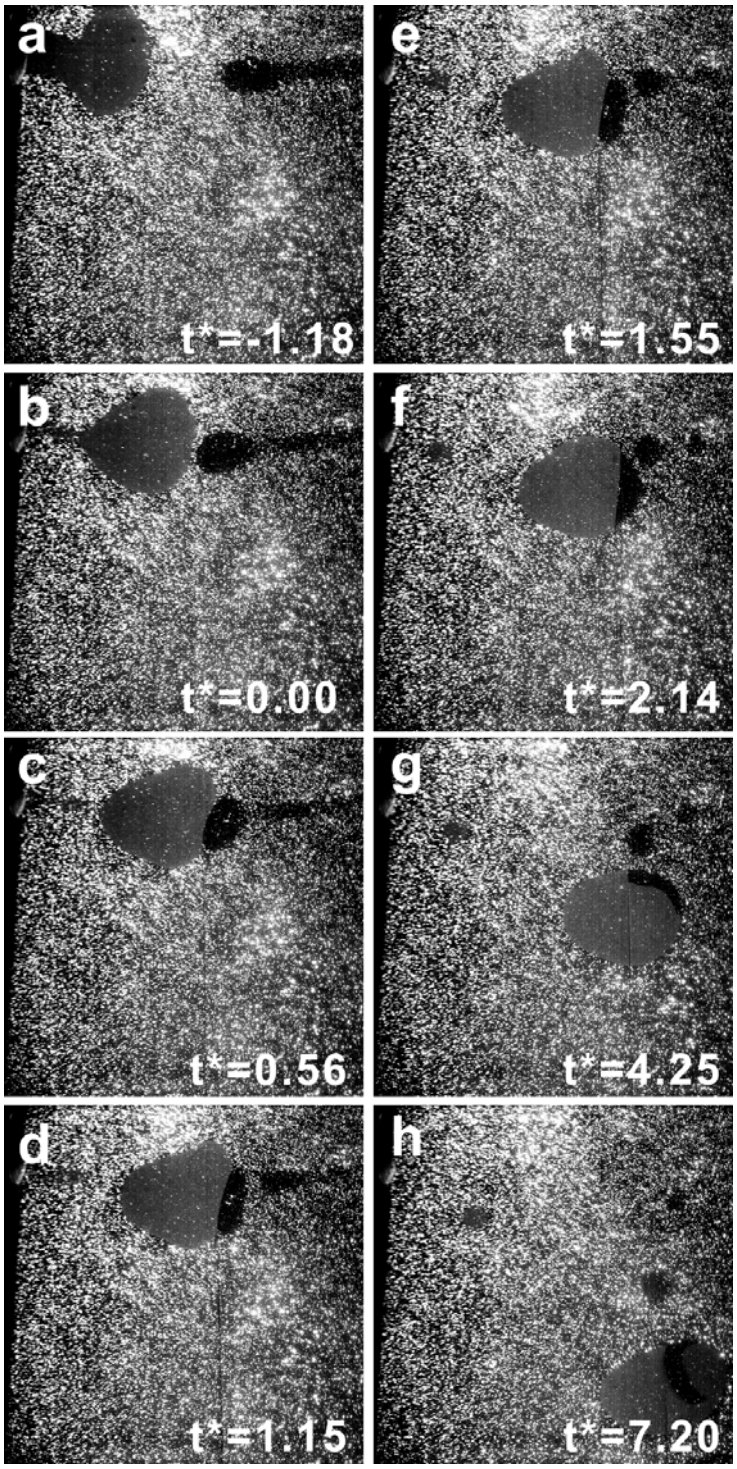


**Figure 3.58** The time evolution of unequal size drop collision: *We** = 34 (coalescence), B = 0, $D_s/D_L$ = 0.44, and $u_L/u_s$ = 2.12 where $D_L$ and $u_L$, and $D_s$ and $u_s$ are the diameter and horizontal components of velocity for the large and small drops, respectively.

initial state. However, the interface is still bent when it ruptures. After coalescence, no tail or strong cusp is observed at the edge of the small drop fluid.

Unlike in previously discussed coalescence cases, an exceptional coalescence case was observed for *We** = 8 as shown in Fig. 3.59: $D_s/D_L$ = 0.53 where $D_s$ = 0.58 cm and $D_L$ = 1.10 cm, $U_{rel}$ = 14.7 cm/s ($u_s$ = 8.0 cm/s and $u_L$ = 8.8 cm/s), B = 0.15.

In this case, the drops collide and deform over t* = 0.00-0.86 (Fig. 3.59b-d). The small drop deforms less than in previous cases with unequal size drops. The intervening film remains flat through the collision event. The drops move apart at t* = 1.68. When the drops almost separate from each other at t* = 2.80, they coalesce. This is similar to the coalescence seen when *We* = 3 (equal size drops, Fig. 3.14). The time evolution of drop images and velocity vector fields are presented for completeness in Fig. 3.60 and 3.61. The film ruptured in the lower end of the film as shown in Fig. 3.61b. As in Fig. 3.61, the coalescence mechanism in this case is unclear. Figure 3.62 shows the vorticity and downward velocity contours at the time of rupture at t* = 2.80. The most important point noted is that there is one local maximum downward velocity at the outer edge of the large drop at this frame (Fig. 3.62b). Similarly, for coalescence when *We* = 3 (equal size drops, Fig. 3.16b), there are two local maxima away from the interface through the entire sequence. Before the drops coalesce, the two drops rotate clockwise as they fall downward. In subsequent images (Fig. 3.61c), the film near the rupture location retracts rapidly upward and downward. Therefore, the upper and lower cusp in the curvature disappear at t* = 2.90 (Fig. 3.61c). At t* = 3.37 (Fig. 3.61d), the small drop fluid rapidly moves into the resulting drop.

### 3.3.4 Effect of impact parameter, B

All drop collisions were near head-on (B = 0) for the previous coalescence cases in Sections 3.3.2 and 3.3.3. However, in realistic situations, drop collisions usually are off-center (B > 0). In this section, the characteristics of off-center collisions are presented.

Figure 3.63 shows the coalescence sequence when *We** = 22 with B = 0.51 from a large field of view: $D_s/D_L$ = 0.47 where $D_s$ = 0.57 cm and $D_L$ = 1.21 cm, $U_{rel}$ = 17.2

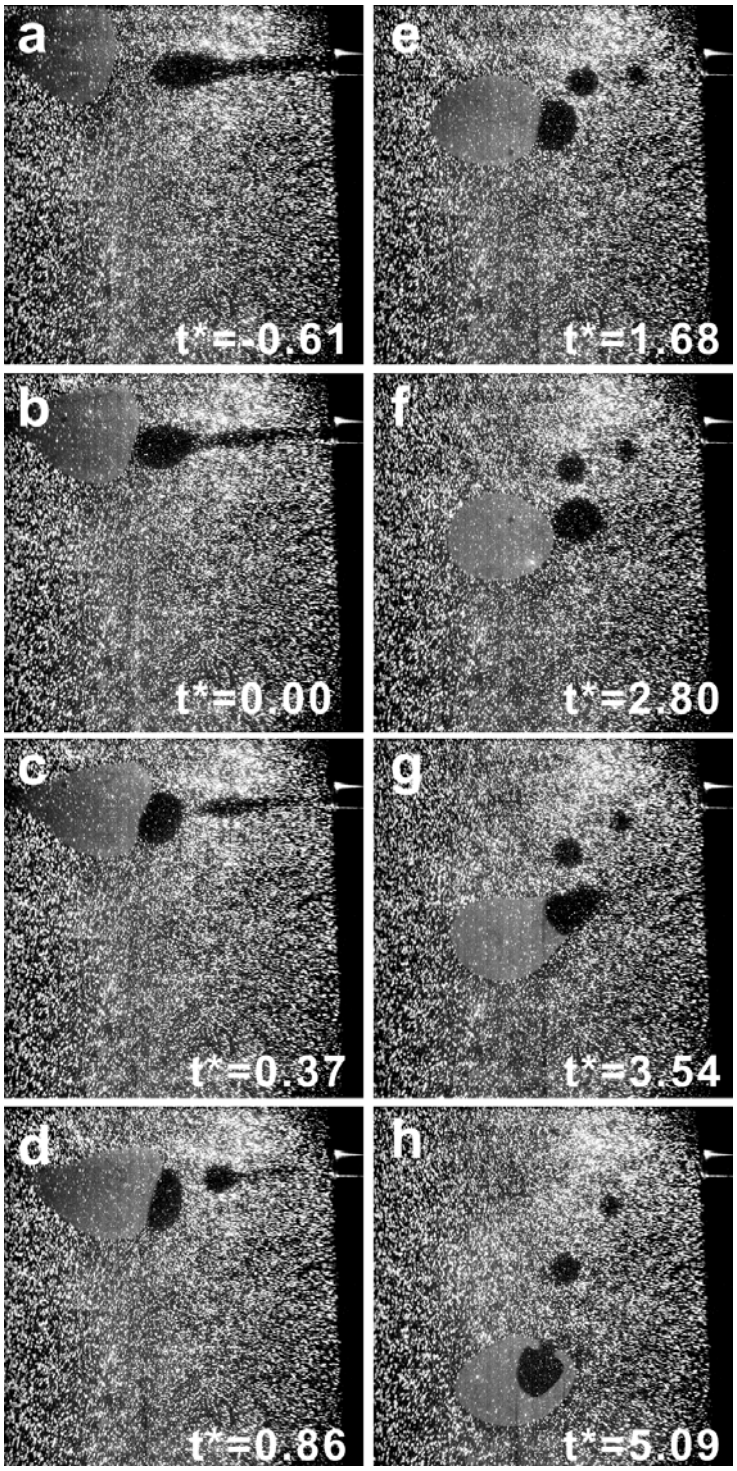


**Figure 3.59** The time evolution of unequal size drop collision: *We** = 8 (coalescence), B = 0.15, $D_s/D_L$ = 0.53 where $D_L$ and $D_s$ are the diameter of the large and small drops, respectively.

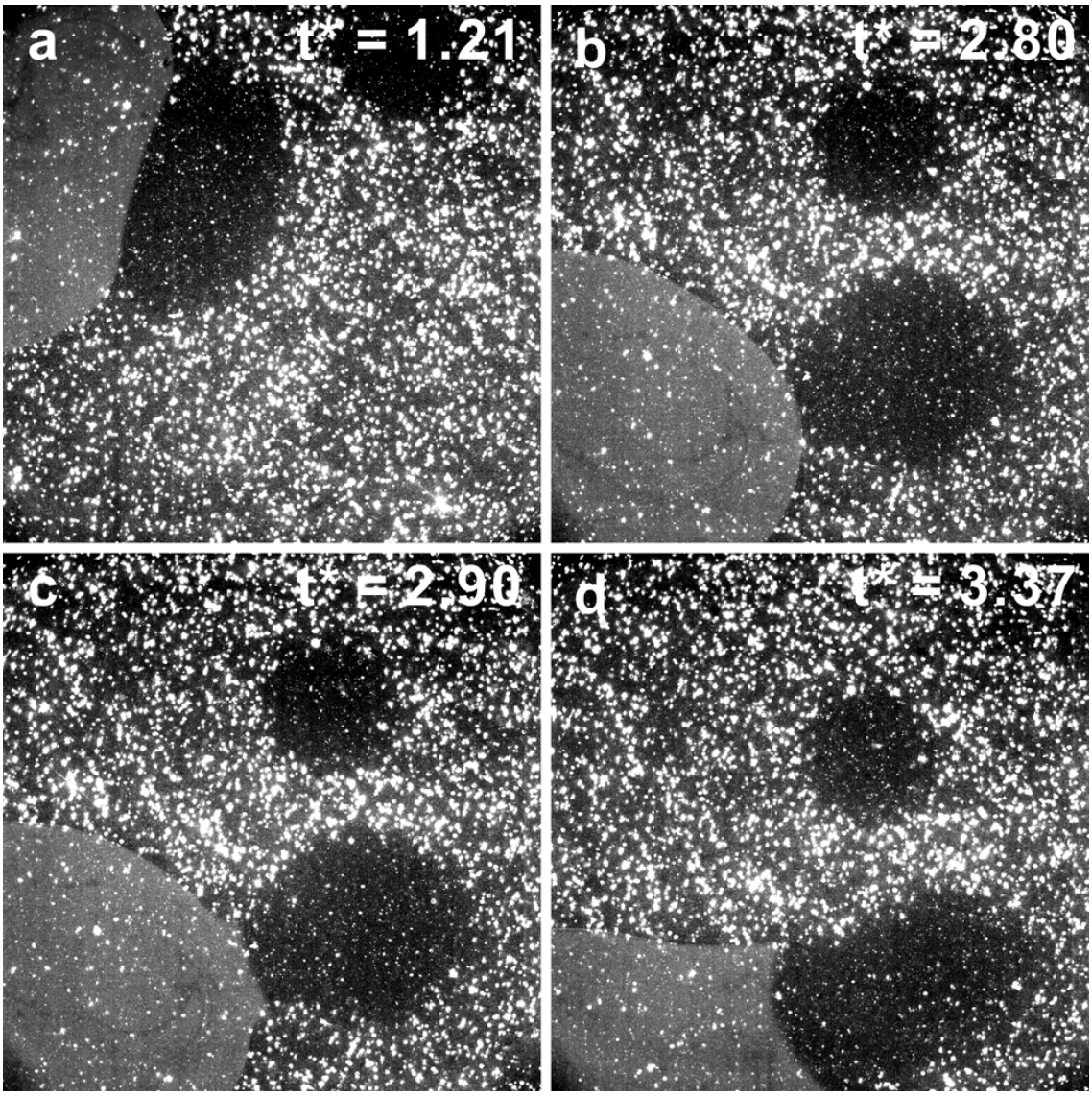


**Figure 3.60** The sequential zoomed views during the coalescence event when *We** = 8 ($D_s/D_L$ = 0.53).

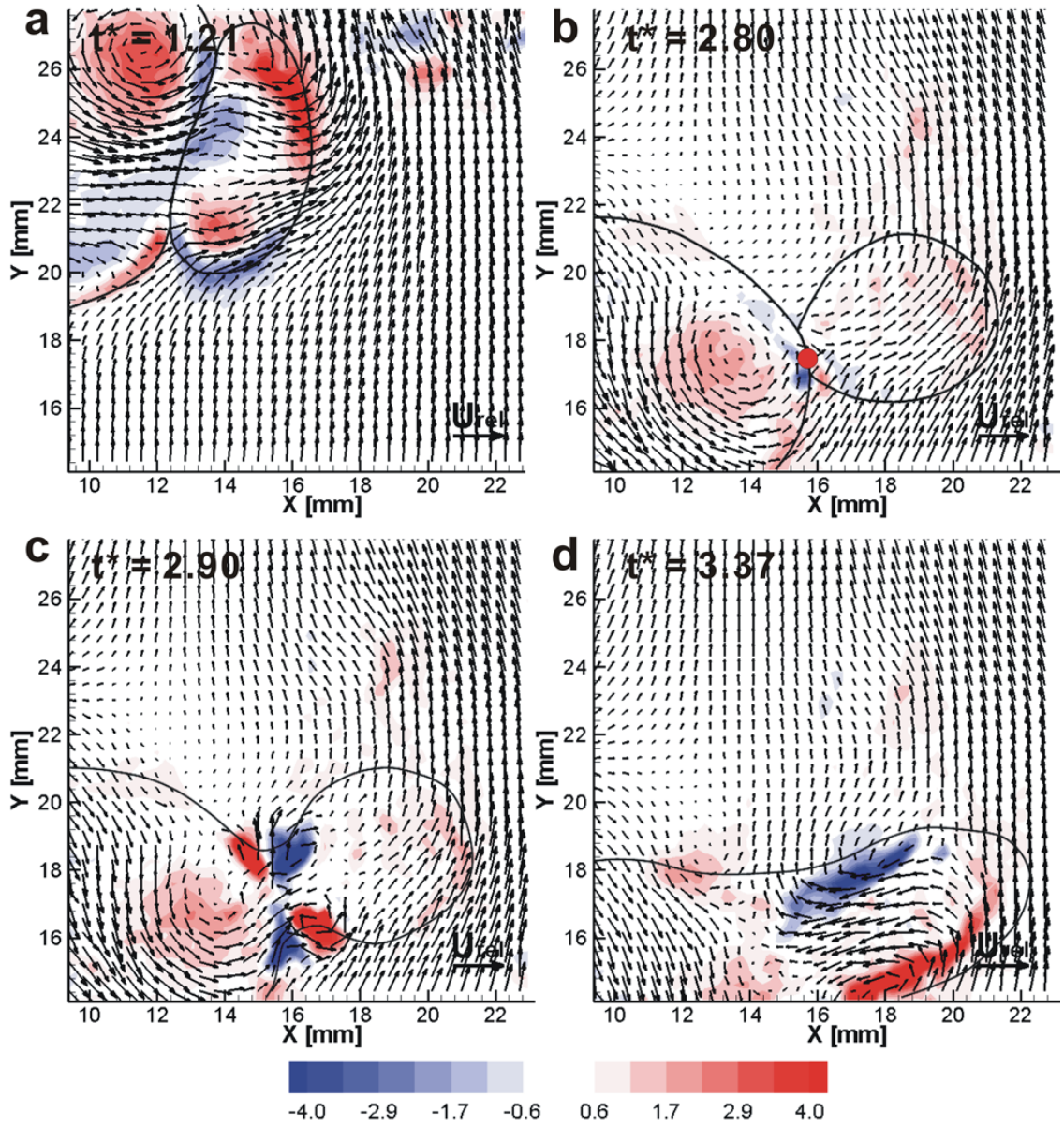


**Figure 3.61** The in-plane vectors and normalized vorticity contours during coalescence event for *We** = 8 ($D_s/D_L$ = 0.53). Vectors show the velocity relative to the falling drops. Colors show normalized vorticity. Red is counterclockwise, and blue is clockwise rotation. The red dot in b shows the film rupture location (Film ruptures at t* = 2.80).

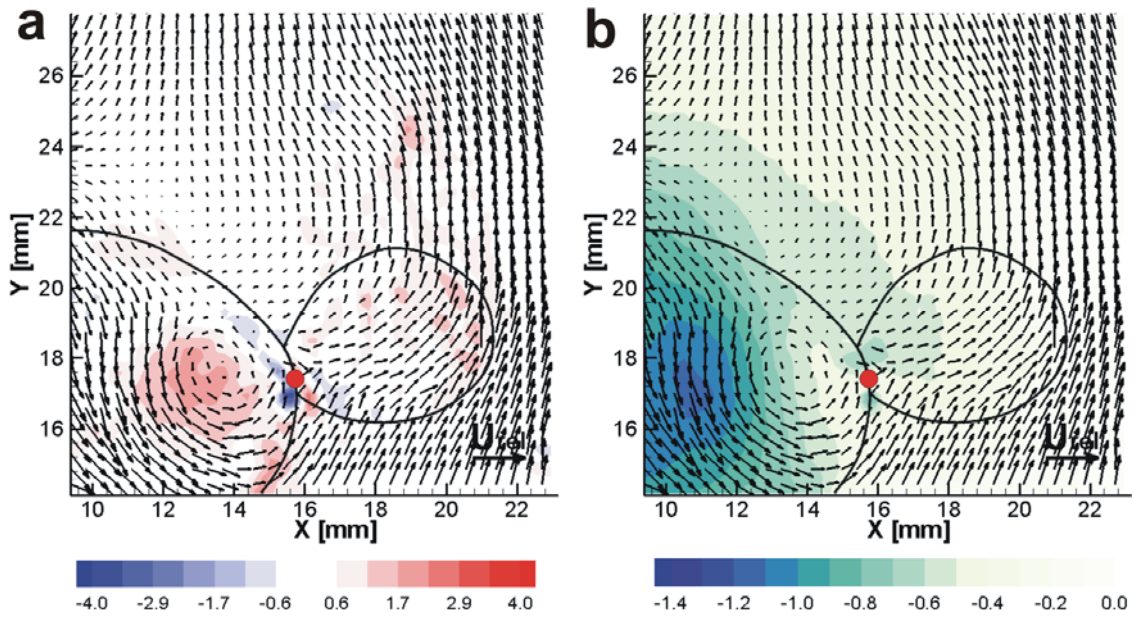


**Figure 3.62** The fields at the time of the film rupture (t* = 2.80) for *We** = 8 ($D_s/D_L$ = 0.53): (a) Normalized vorticity contour. Red is counterclockwise, and blue is clockwise. (b) Normalized vertical velocity contour. Blue is downflow. Vectors show velocity relative to the falling drops. The red dots show the film rupture location.

cm/s ($u_s$ = 4.5 cm/s and $u_L$ = 13.3 cm/s). In Fig. 3.64, the boundary of the small drop is not clear due to the low concentration of fluorescent dye within the drop. Therefore, a zoomed view and movie are used to track the boundary of the small drop.

When the drops approach, both are initially elongated with tails. In this case, the collision is not head-on as shown in Fig. 3.63b. The small drop collides at the upper head of the large drop (B = 0.51). After the initial collision, the large drop deforms slightly while the small drop pushes the interface film into the large drop. The small drop changes from prolate to oblate, rotates counterclockwise and moves to the upper part of the large drop as shown in Fig. 3.63c. The drops coalesce at t* = 0.70. A dimple at the back of each drop is not observed. Compared to previous coalescing cases, the rupture time is shorter (t* = 0.70). In general, for B > 0, the film ruptures earlier than in a head-on collision case with the same Weber number. After coalescence, the small drop fluid moves downward into the large drop fluid at t* = 1.76. Then, the small drop fluid rotates counterclockwise within the coalesced drop to mix (Figs. 3.63d-f). Unlike B = 0 cases, the coalesced drop rotates counterclockwise while it falls downward as shown in Fig. 3.63f. Overall mixing of the two drop fluids is enhanced for B > 0 compared to previous B = 0 cases.

Figures 3.64 and 3.65 show a time sequence during the coalescence event from the small field of view and corresponding vector fields for the same event: $We^*$ = 22 ($D_s/D_L$ = 0.47). Figure 3.66 shows the vorticity and vertical velocity relative to the falling drops when the film ruptures. At t* = 0.40 (Fig. 3.64a), the tail of the small drop is observed. The small drop moves close to interface, and the large drop rotates counterclockwise as it moves to the right. At the time of contact in Fig. 3.65a, the vortex ring of the small drop is close to the interface while only the upper part of the ring in the large drop is located close the interface. At this time, the vorticity in the vortex ring in the small drop is stronger than that in the large drop: The vorticity values at the upper and lower part of vortex ring in the large drop are 7.1D/$U_{rel}$ and 4.6D/$U_{rel}$, and The values at the upper and lower part of the ring in the small drop are 8.1D/$U_{rel}$ and 9.8D/$U_{rel}$.

The vorticity magnitudes associated with the vortex ring of the small drop

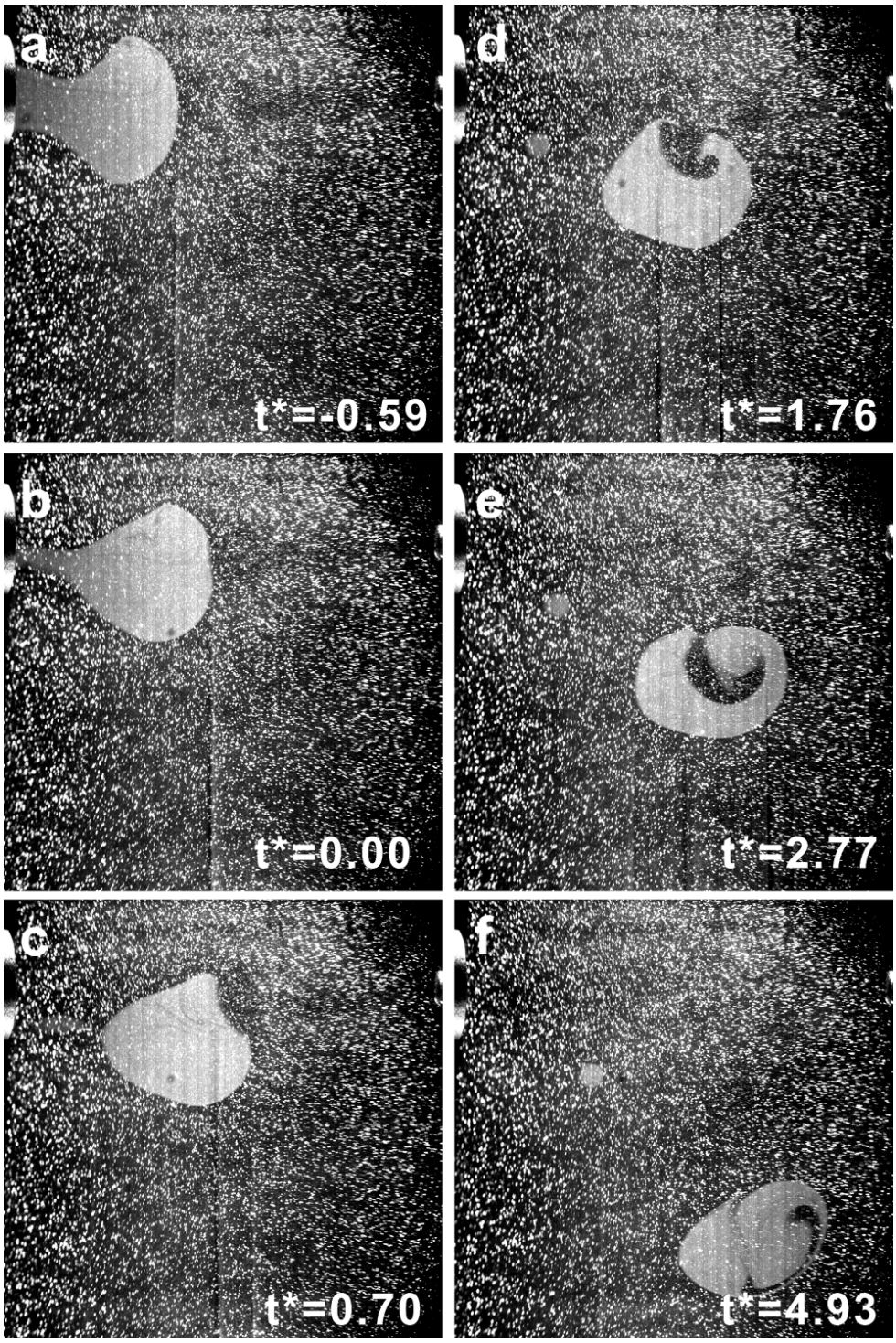


**Figure 3.63** The time evolution of unequal size drop collisions: *We** = 22 (coalescence), B = 0.51, $D_s/D_L$ = 0.47 where $D_L$ and $D_s$ are the diameter of the large and small drops, respectively.

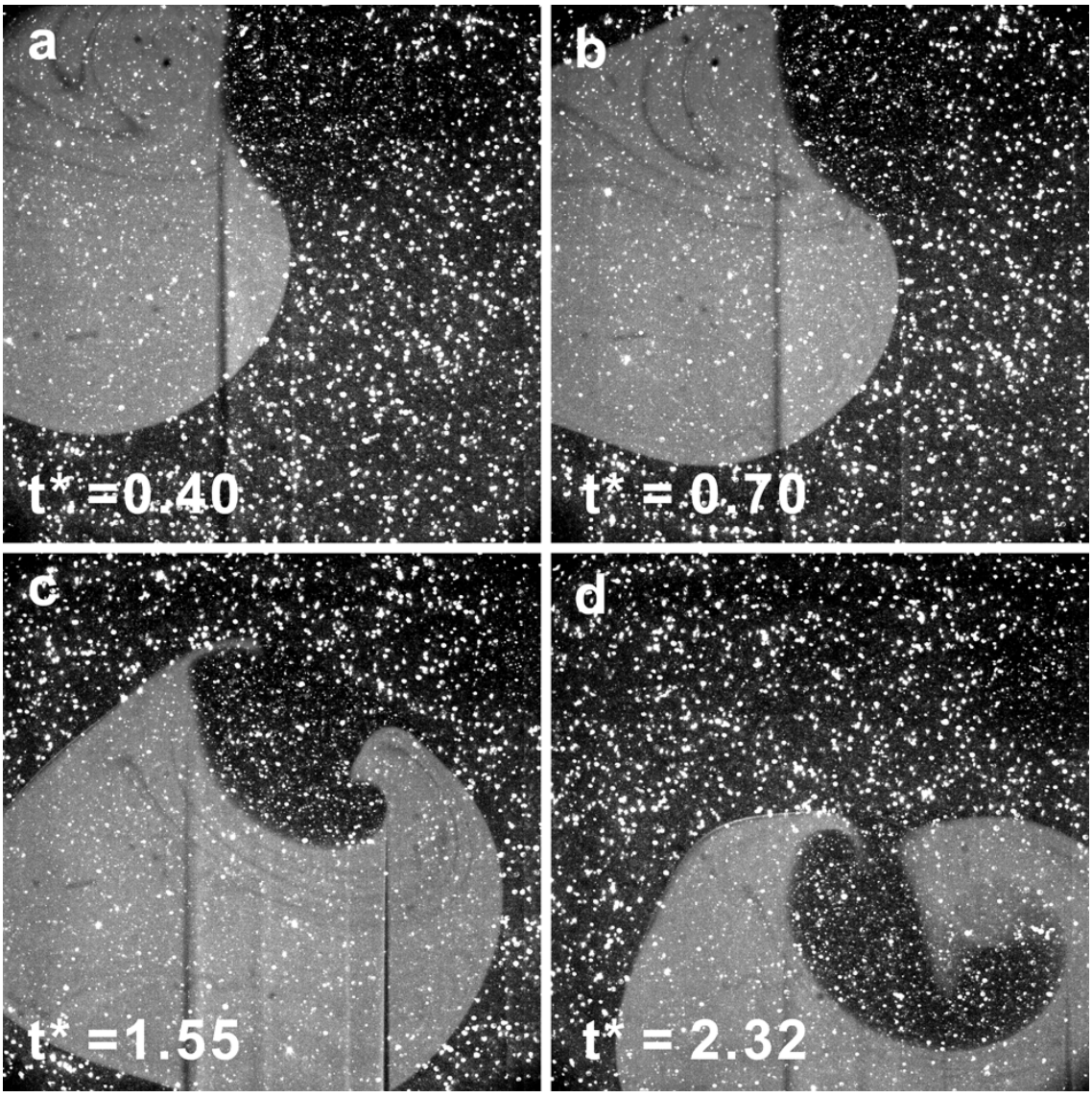


**Figure 3.64** The sequential zoomed views during the coalescence event when *We** = 22 (B = 0.51 and $D_s/D_L$ = 0.47).

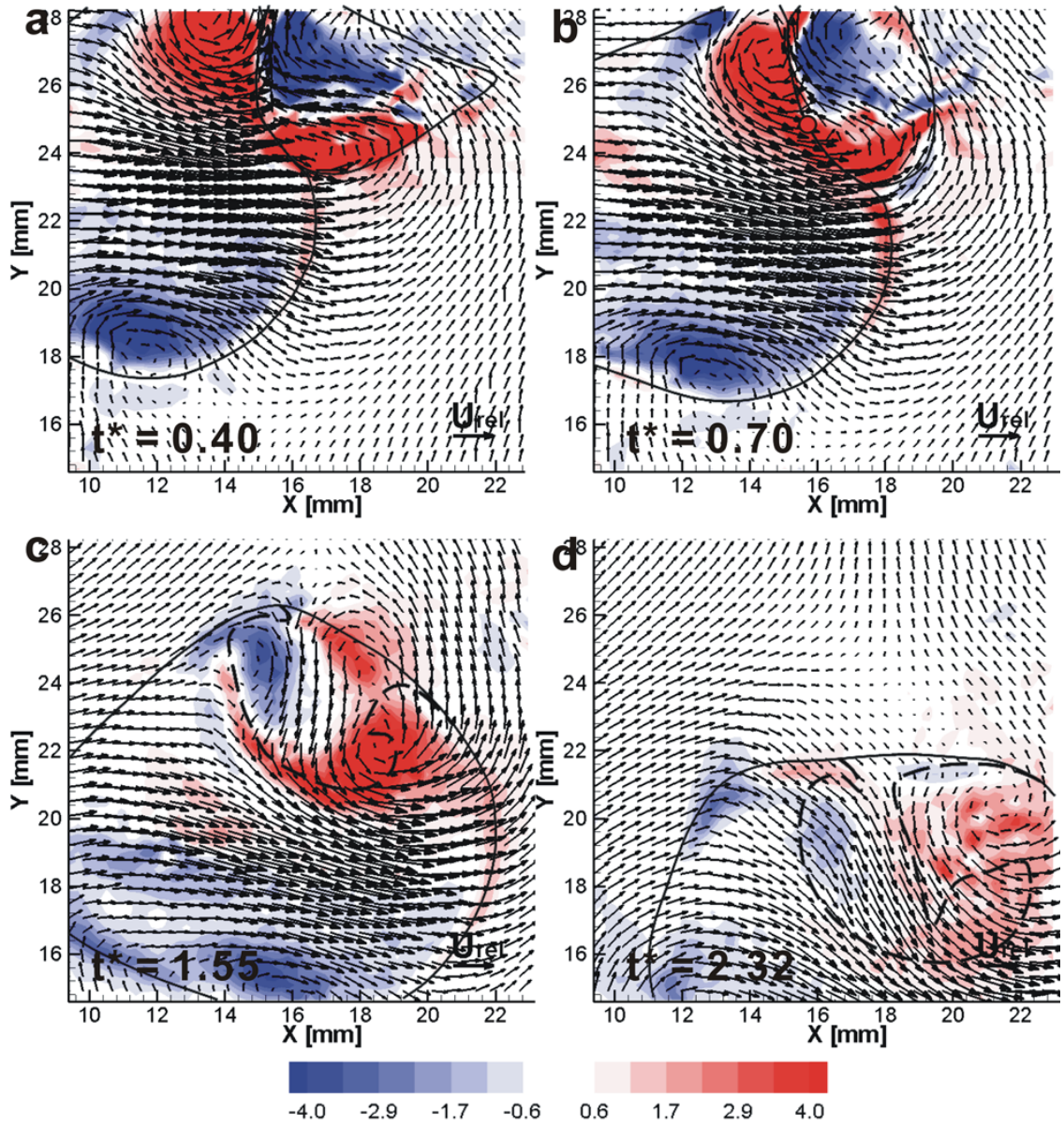


**Figure 3.65** The in-plane vectors and normalized vorticity contours during coalescence event for *We** = 22 (B = 0.51, $D_s/D_L$ = 0.47). Vectors show velocity relative to the falling drops. Colors show normalized vorticity. Red is counterclockwise, and blue is clockwise rotation. The red dot in b shows the film rupture location (Film ruptures at t* = 0.70). Dashed line shows boundary of fluid from small drop.

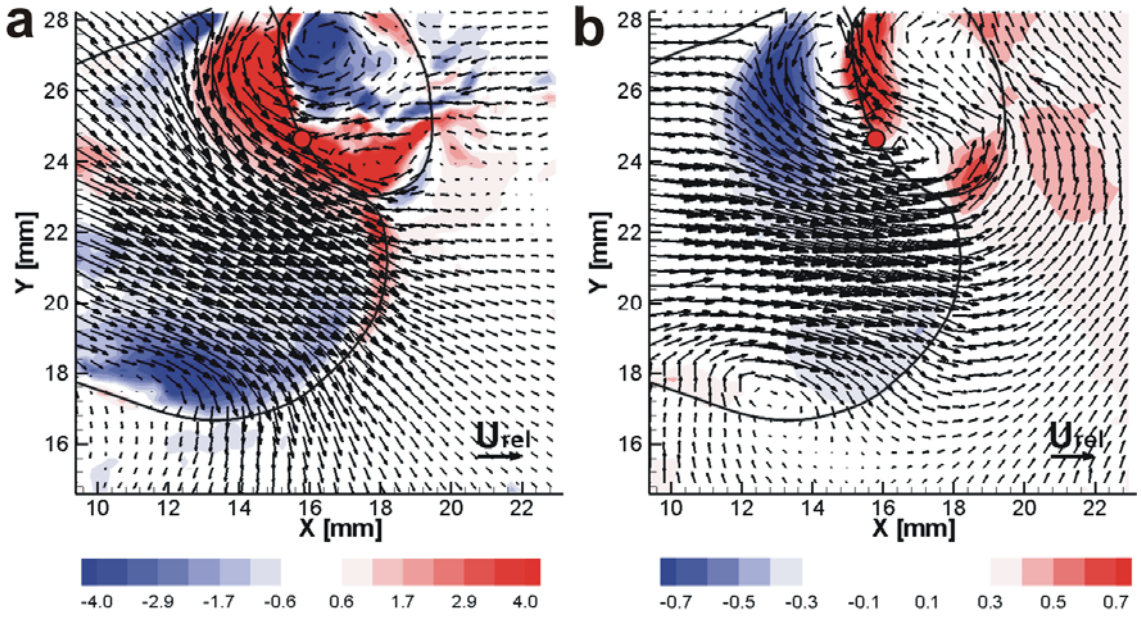


**Figure 3.66** The fields at the time of film rupture (t* = 0.70) for when *We** = 22 (B = 0.51, $D_s/D_L$ = 0.47): (a) Normalized vorticity contour. Red is counterclockwise, and blue is clockwise. Vectors show absolute velocity. (b) Normalized vertical velocity relative to the falling drops. Red is upflow, and blue is downflow. Vectors show the in-plane velocity relative to the falling drops. The red dots show the film rupture locations.

decrease at t* = 0.70. In Figs. 3.65a through 3.65b, the vorticity strength decreases from 8.1D/$U_{rel}$ to 5.2D/$U_{rel}$ in the upper part of the ring, and from 9.8D/$U_{rel}$ to 7.9D/$U_{rel}$ in the lower part of the ring. By contrast, unlike previous cases, the vorticity values of the vortex ring increase for the large drop at t* = 0.70. The vorticity strength increases from 7.0D/$U_{rel}$ to 8.1D/$U_{rel}$ in the upper part of the ring, and from 4.9 to 5.1 in the lower part of the ring. The film ruptures at t* = 0.70 while the film remains slightly curved. The vectors show a strong upflow located at the upper end of the film while the fluid is draining out (Fig. 3.65b). Figure 3.66b shows the vertical velocity relative to the falling drops when the film ruptures. Strong upflow near the interface of the small drop can be observed. Also, there is strong downflow in the upper part of the large drop. Compared with Fig. 3.66a (absolute velocity vector field), the vortex ring of the small drop drives fluid to move toward the interface film, and together with the vortex ring of the large drop, the fluid near the film rapidly moves upward. The upper part of vortex ring for the large drop induces the fluid near the film to move upward to drain out and also causes the fluid away from the film to move downward. This downflow merges with the lower part of the large drop flow, and causes the drop to fall and rotate counterclockwise. The rupture location is near the center of the film.

After coalescence, the large drop fluid continues to move to the right, and the small drop fluid rotates counterclockwise and moves downward into the large drop fluid as shown in Fig. 3.65c. As the resulting drop falls, the two fluids mix as shown in Fig. 3.65d, and eventually the remaining drop rotates counterclockwise.

In summary, as B increases, the film rupture time occurs earlier than for head-on collision cases with the same *We*. The coalesced drop rotates as it falls downward while the resulting drops do not rotate for B = 0 cases. The mixing of the drops after coalescence is enhanced as B increases. After the drops collide, the interface between them moves. This is because the strong upflow near the interface of the small drop and the strong downflow in the upper part of the large drop drain the fluid out from the interface. For B = 0 cases, this strong upflow region is not observed. For B > 0, the interface is not flat when it ruptures. Similar to previous unequal size drop collisions, the rupture location varies.

## 3.4 The effects of tracer particles

The characteristics of coalescence for both equal and unequal size drops have been previously investigated using the particle image velocimetry (PIV) technique. Tracer particles of approximately 1 μm in diameter were applied for all of the experiments. It has been reported that the presence of liquid surface contaminants can affect the collision behavior of the colliding drop pairs (Hu et al. 2000 and Ha et al. 2003). However, there has been little discussion concerning surface contaminants such as tracer particles for PIV on the interfacial surface. Therefore, it is necessary to understand how tracer particles affect drop coalescence. In this section, cases with tracer particles which measure 1 μm diameter are used and compared with cases without tracer particles in the fluid surrounding the drops. Also, cases with tracer particles of 10 μm diameter in the surrounding fluid are tested to see whether larger sized particles affect the collision outcomes. In this study, silver coated hollow spheres (diameter $D_p \sim 10$ μm, density $\rho_p = 1.05 – 1.15$ g/cm$^3$, index of refraction n =1.5) were used. For all the cases, the drop fluid was seeded with tracer particles ($TiO_2$) of 1 μm diameter. All drop collisions were head-on (B = 0), and used two drops of equal size.

Figure 3.67 shows the results of equal size drop collisions over which *We* and collision angle were varied. The closed symbols represent coalescing cases and open symbols represent rebounding cases. Red symbols are drop collisions with tracer particles ($TiO_2$) of 1 μm diameter in the surrounding fluid (including all cases from Fig. 3.1), blue symbols are collisions with no tracer particles in the surrounding fluid, and black symbols are collisions with tracer particles of 10 μm diameter in the surrounding fluid.

The boundary between rebound and coalescence was drawn for the cases with 1 μm tracer particles in the ambient fluid as previously described in Section 3.1.1. The critical Weber number is *We* = 10. The drops rebound when *We* is below 10 and coalesce when *We* is greater than 10. For cases in which there are no tracer particles in the silicone oil, overall outcomes are similar to the cases with tracer particles. However, when compared to cases with tracer particles, the boundary between rebound and coalescence is not obvious. Rebound can be observed up to *We* = 18. The lowest

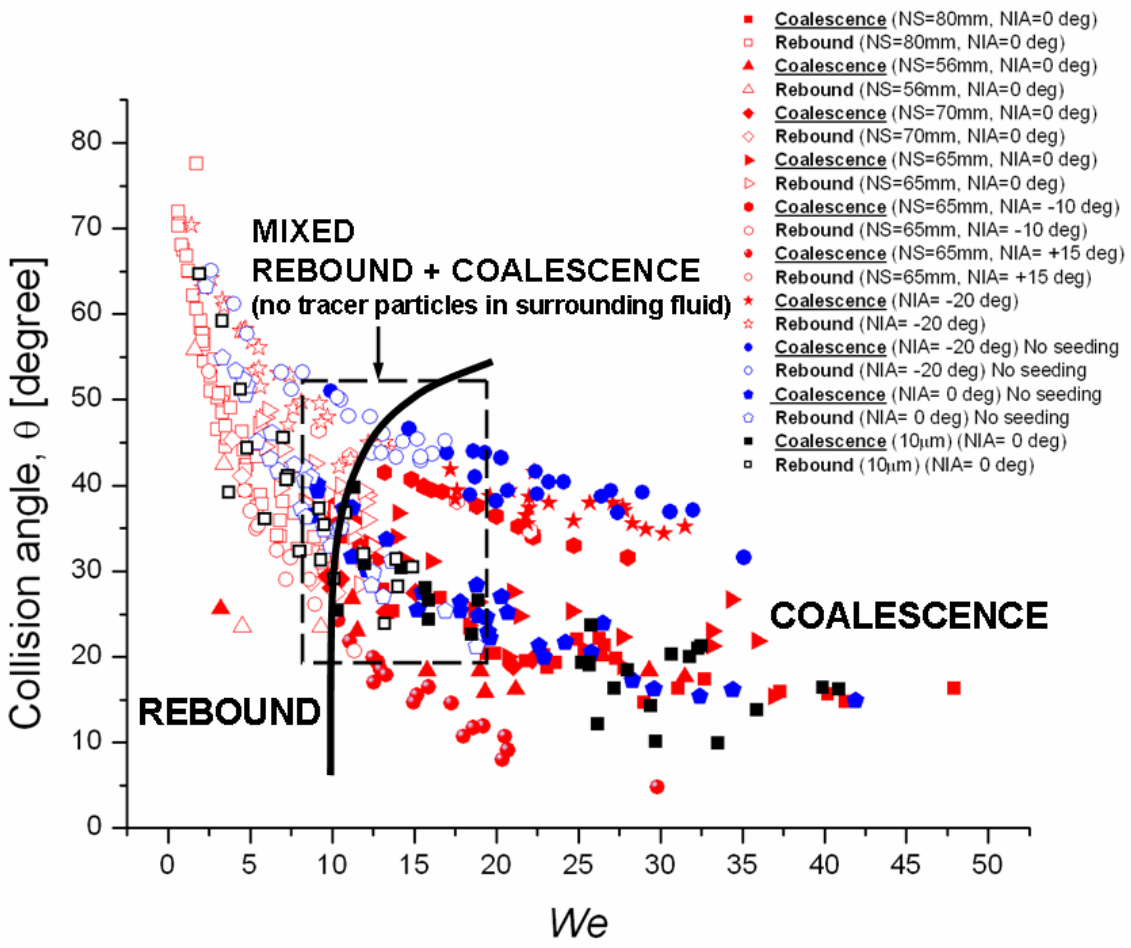


**Figure 3.67** The region of rebound and coalescence for equal size drops. Closed symbols represent coalescing cases and open symbols represents rebounding cases. The red symbols are drop collisions with tracer particles ($TiO_2$) of 1 μm diameter in the surrounding fluid, blue symbols are collisions with no tracer particle in the surrounding fluid, and black symbols are collisions with tracer particles (silver coated hollow spheres) of 10 μm diameter in the surrounding fluid. The drop fluid used for all cases is seeded with tracer particles ($TiO_2$) of 1 μm diameter. NS represents initial nozzle separation and NIA is the initial nozzle injection angle.

Weber number in which the drops coalesce is $We \sim 8$ which is below the previous critical $We = 10$. The dotted block in Fig. 3.67 shows the region where both rebound and coalescence can occur for cases with no tracer particle in surrounding fluid. Therefore, for cases with no tracer particles, the drops obviously rebound below $We = 8$

and coalesce above *We* = 18, but exhibit mixed results in between.

Figure 3.67 shows that cases with tracer particles of 10 μm diameter correspond closely with the cases with tracer particles of 1 μm diameter, i.e. the minimum *We* for coalescence is consistent. Thus, it does not appear that particle size difference significantly affects the drop collisions. However, some rebounding cases are seen above *We* = 10 in Fig. 3.67. When adding 10 μm particles in surrounding fluid, the number of particle is less than that of 1 μm particles cases. If the same number of 10 μm particles were added to the fluid, the particles would scatter too much light for proper imaging. The possibility for the 10 μm particles to be in the right location within the thin film during the collision is less than in the 1 μm particle cases. Therefore, the lack of particles in the film may cause a rebound occasionally above *We* = 10. Since vector and vorticity fields are not available, it is hard to understand the flow motion inside of the drops, but, by examining several cases, the drop shapes at the time of coalescence are similar to those in the 1 μm particle cases. The image sequences suggest that the difference in particle size in this experiment does not significantly affect the time of coalescence. In the following discussion, collisions with and without tracer particles are compared to study how the particles affect coalescence.

Figure 3.68 shows coalescence when *We* = 16 (D = 0.86 cm, trajectory angle θ = 28°, and $U_{rel}$ = 21.7 cm/s). For this case, tracer particles in the silicone oil were removed. Although the tank was cleaned before the experiments, tracer particles were not completely removed. Thus, a few particles can be still seen in Fig. 3.68. However, compared with the particle density in the drops, the relative number of particles in silicone oil is very small. Comparing Figure 3.68 with the coalescence case where *We* = 15 in Fig. 3.10, both cases have similar *We* and collision angle. Overall drop shape evolution is very similar for both cases, but there are some small differences. In Fig. 3.68, the drops initially elongate as they approach. After the drops collided, they change from prolate to oblate in Fig. 3.68b-d. The drops reach the maximum film length between them at t* = 1.21. For *We* = 15 in Fig. 3.10, the film length is maximum at t* = 1.37, and the drops coalesce in this time frame. However, for the case with no tracer particles in Fig. 3.68, the drops move apart after they reach the maximum film

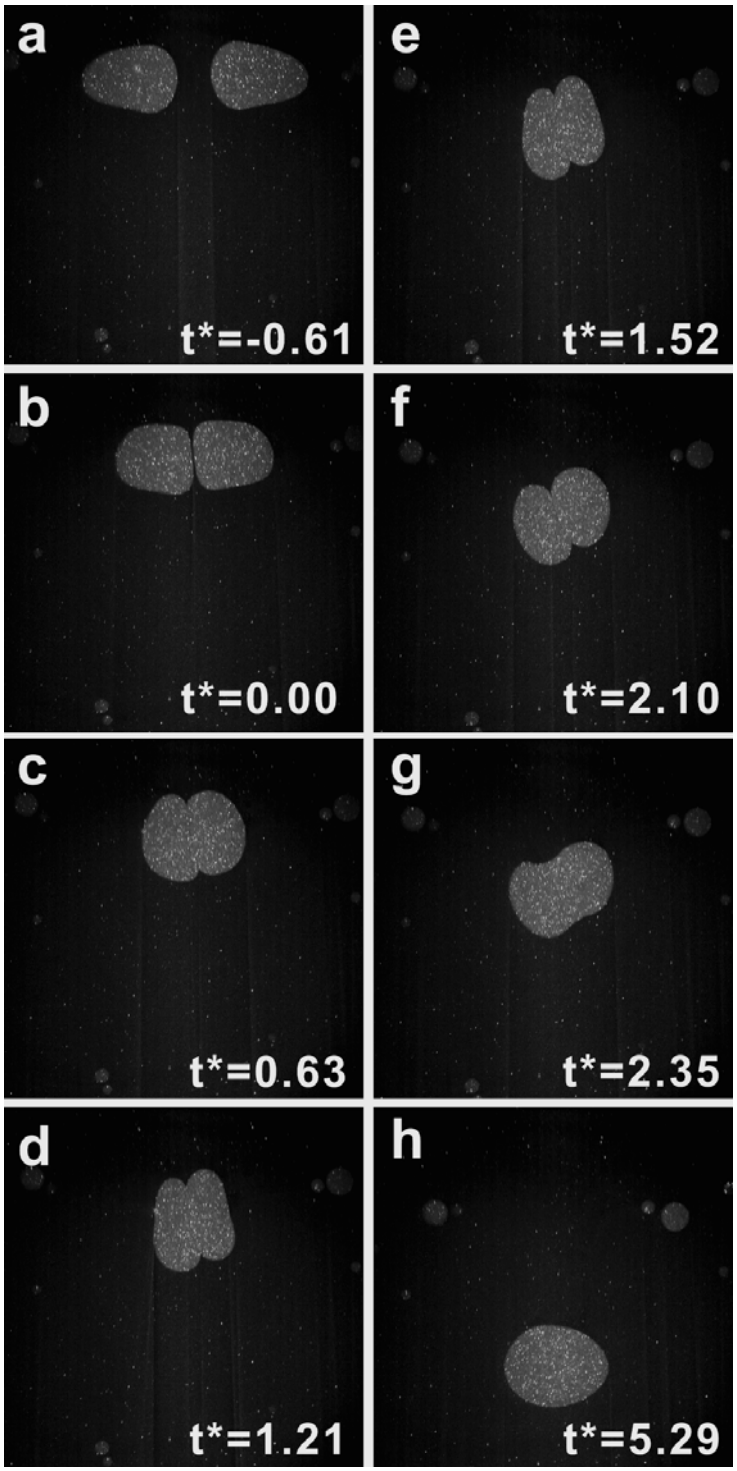


**Figure 3.68** The time evolution of drop collision for *We* = 16 (with no tracer particle in the surrounding fluid), θ = 28° (coalescence). t* = t$U_{rel}$/D, where D is drop diameter and $U_{rel}$ is relative velocity.

length (Fig. 3.68e). While the drops move apart, they coalesce at t* = 2.10 (Fig. 3.68f). For the cases with no tracer particles in the ambient fluid, coalescence occurs later than in cases with tracer particles. Therefore, the absence of tracer particles in the film may delay coalescence.

Figures 3.69-3.72 show the detailed view of the thin film region for small fields of view. Figures 3.69-3.71 show the fields at the maximum film length, and Fig. 3.72 shows the film rupture time for drops with no tracer particles in the surrounding fluid. Figures 3.69, 3.70, and 3.72a show vorticity contours, and Figs. 3.71 and 3.72b show vertical velocity contours relative to falling drops. The vectors in Fig. 3.69 are normalized absolute velocity and in Figs. 3.70-3.72, velocity is relative to the falling drops.

When the drops reach the maximum film length, the vector distributions for both cases are similar. There are some minor differences because the collision is slightly off-center for the case with no tracer particles. In Figs. 3.69 and 3.70, fluid flows into the centerplane for *We* = 15. Vectors in the left drop in Figs. 3.69 and 3.70 are directed somewhat downward while the vectors in the right drop are directed toward the centerplane. At this time, the two drops are tilted counterclockwise that the fluid in the left drop flows somewhat downward and the vector distribution in the right drop is similar to *We* = 15. Overall, the drop orientation slowly rotates counterclockwise. The vortex ring pair is symmetrical for *We* = 15. A pair of vortex rings for *We* = 16 lose symmetry due to the drop orientation. The lower part of the vortex in the left drop is located away from the centerplane and induces the flow to point more downward along with the upper part of the vortex ring when compared to the right drop. In this case, a dimple at the back of each drop is not observed while dimples for each drop are viewed for *We* = 15. These differences are probably because of initial offset (B > 0) and the rotation of the drops after they collide. The times at the maximum film length for two cases are different. However, as discussed in Fig. 3.17, the time at the maximum film length, even for like *We*, varies somewhat between events. Therefore, the differences observed here are probably not caused by the lack of tracer particles. Instead, with or without tracer particles, the velocity and vorticity fields are relatively similar up to this

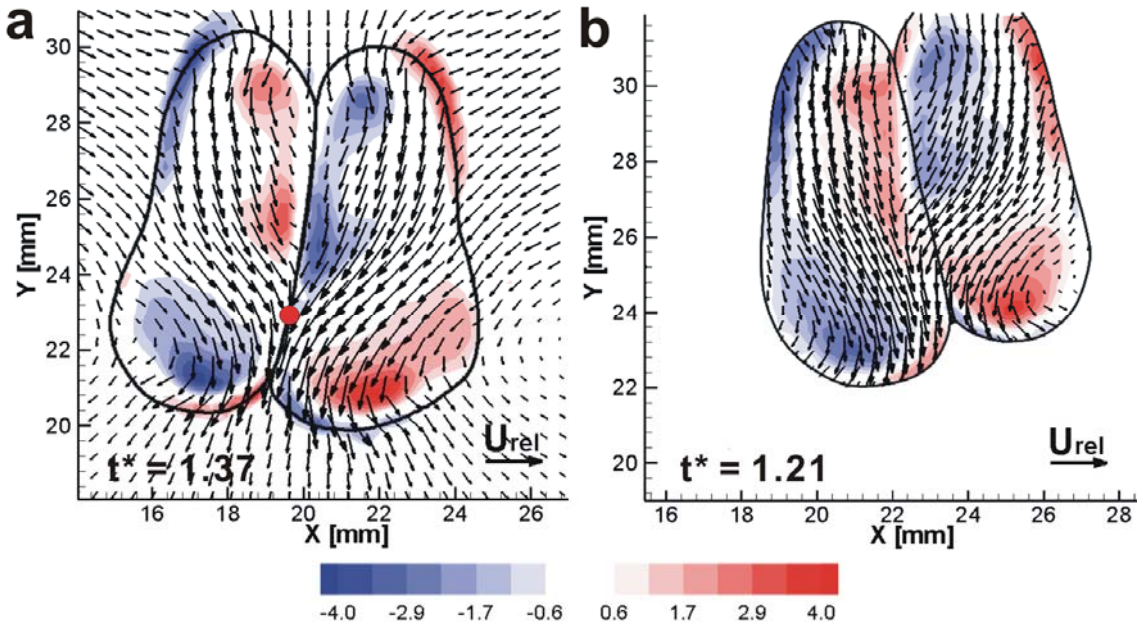


**Figure 3.69** The vector and vorticity fields at the maximum film length: (a) *We* = 15 (with tracer particles in the surrounding fluid), θ = 28°, t* = 1.37, (b) *We* = 16 (without tracer particles in the surrounding fluid), θ = 28°, t* = 1.21. Vectors show normalized absolute velocity. Colors show normalized vorticity. Red is counterclockwise rotation and blue is clockwise rotation.

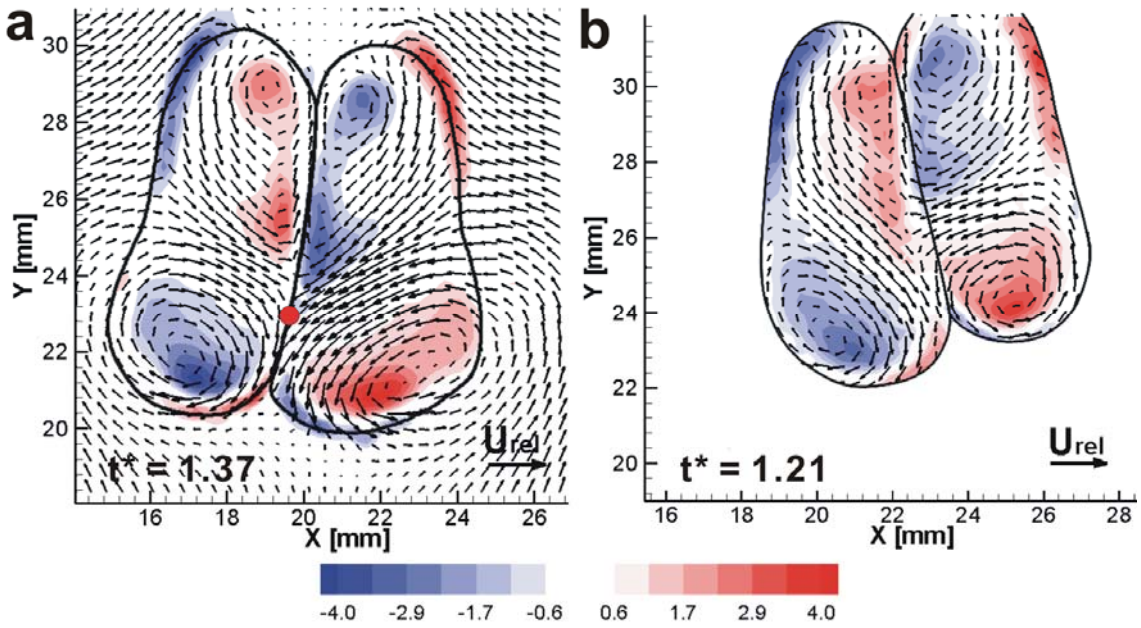


**Figure 3.70** The vector and vorticity fields at the maximum film length: (a) *We* = 15 (with tracer particles in the surrounding fluid), θ = 28°, t* = 1.37, (b) *We* = 16 (without tracer particles in the surrounding fluid), θ = 28°, t* = 1.21. Vectors show in-plane velocity relative to the falling drops. Colors show normalized vorticity. Red is counterclockwise rotation and blue is clockwise rotation. The red dot shows the film rupture location.

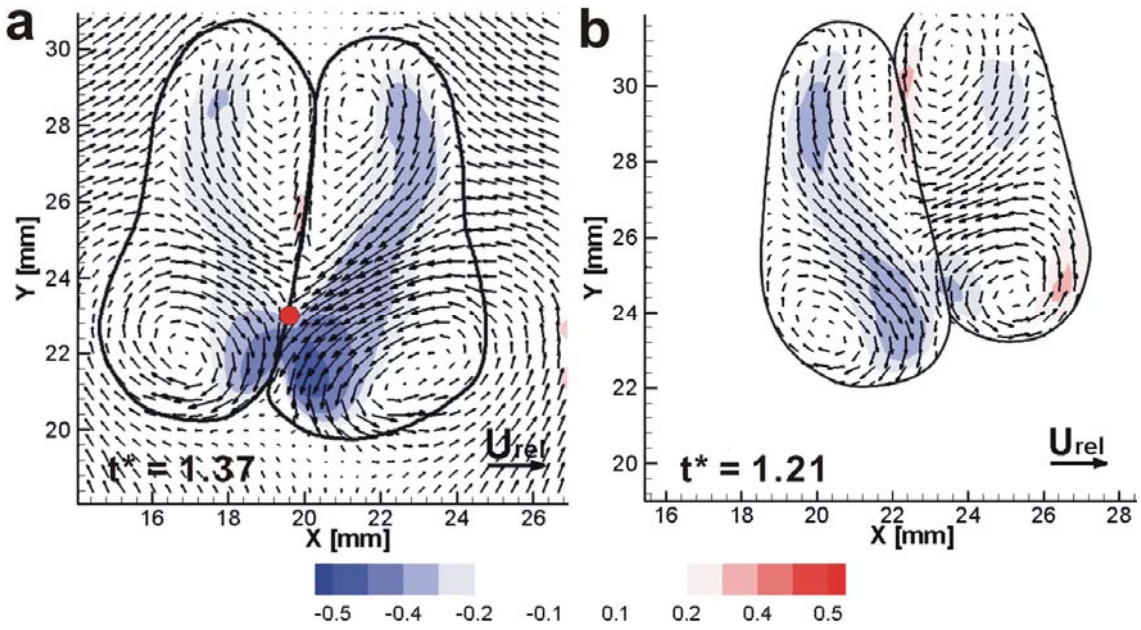


**Figure 3.71** The vector and vertical velocity fields at the maximum film length: (a) *We* = 15 (with tracer particles in the surrounding fluid), θ = 28°, t* = 1.37, (b) *We* = 16 (without tracer particles in the surrounding fluid), θ = 28°, t* = 1.21. Vectors show in-plane velocity relative to the falling drops. Colors show normalized vertical velocity relative to the falling drops. Red is upflow, and blue is downflow. The red dot shows the film rupture location.

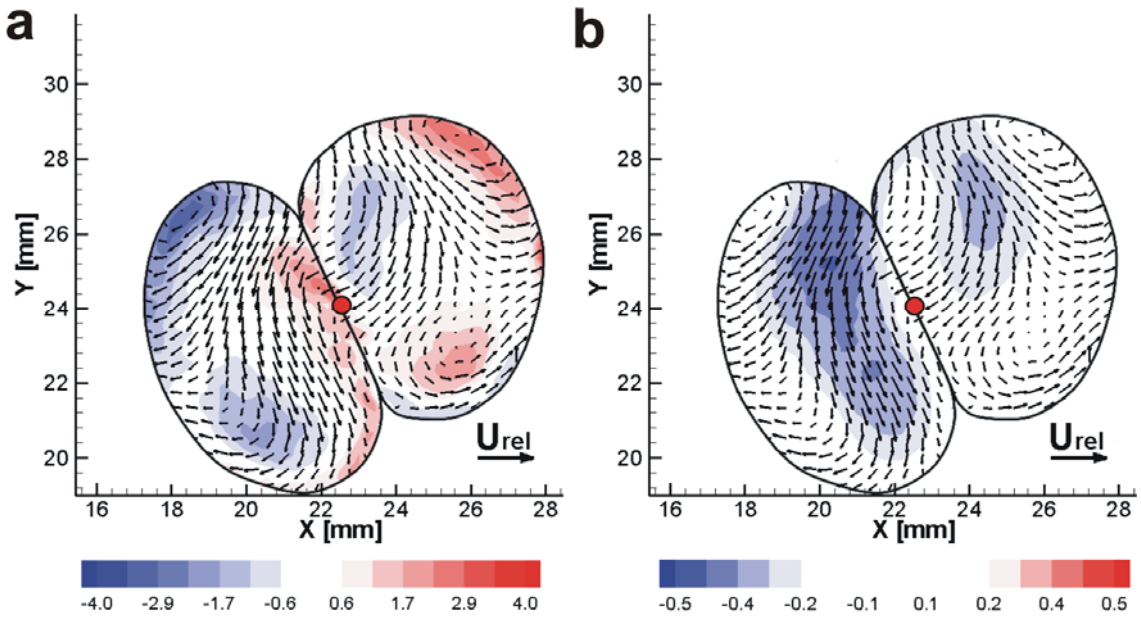


**Figure 3.72** Velocity field at the time of the film rupture (t* = 2.10) for *We* = 16 (with no tracer particles in the surrounding fluid): (a) Normalized vorticity contour. Red is counterclockwise, and blue is clockwise. (b) Absolute vertical velocity contour. Blue is downflow. Vectors show velocity relative to the falling drops. The red dots show the film rupture location.

point.

The vertical velocity in Fig. 3.71 shows that local maximum upflow is located near the center for *We* = 15 and at the upper end of the film for *We* = 16. Strong downflow occurs at the end of film for *We* = 15. Near this downflow zone, the film ruptures. For *We* = 16, maximum downflow is slightly away from the centerplane, similar to the rebounding cases described earlier in Section 3.1.2, and causes the drops to move apart instead of coalescing at the maximum film length. For *We* = 15, the maximum relative downward velocity near the downstream edge at the interface is $0.47U_{rel}$ and the maximum relative upward velocity is $0.34U_{rel}$. For *We* = 16, the maximum relative downward velocity away from the interface is $0.33U_{rel}$ and the maximum relative upward velocity is $0.31U_{rel}$. As described earlier, the small differences are because of the rotation of the drops. Otherwise, the vertical velocity distribution is similar for both cases.

Afterward, the drops with no tracer particles move apart, and coalesce at t* = 2.10 as shown in Fig. 3.72. The rupture location is at the center of the interfacial film. The drops without tracer particles at t* = 2.10 continues to rotate counterclockwise. The vertical velocity contours show that strong downflow is located in the upper part of the left drop, and this downflow encourages the drops to move apart before they actually coalesce..

When comparing the two cases, there are some small differences in the initial behavior after collision. But, these differences are due to the difference in drop evolution during the collision, and it is unlikely that these are related to the presence of tracer particles. On the other hand, for cases with no tracer particles in the silicone oil, the coalescence is obviously delayed, and the rupture location is typically higher and variable compared with the tracer particle cases. The following compares another two cases for the same *We*, collision angle, and similar drop evolution, but a higher *We* and steeper collision angle than in previous cases, to confirm that the delay of coalescence and variation of rupture location are due to the existence of tracer particles in the intervening film between the drops. For both cases, the drops do not rotate during the collision.

Two sequences of coalescing cases with like Weber number (*We* = 21) and collision angle (θ = 40°) are compared in Figs. 3.73 and 3.74: $U_{rel}$ = 24.4 cm/s and D = 0.91 cm with tracer particles in silicone oil (Fig. 3.73) vs. $U_{rel}$ = 24.5 cm/s and D = 0.89 cm without tracer particles in the silicone oil (Fig. 3.74). The initial injection angles are -20° (downward).

For both cases, the drop heads point downward due to the initial trajectory (Figs 3.73a and 3.74a). After the drops initially come in contact, they compress into oblate shapes (Figs 3.73b-d and 3.74b-d). At t* = 1.02 in Fig. 3.73 and t* = 1.21 in Fig. 3.74, the film length is maximum. The bottom section of each drop is wider than the top at this frame of time. Note that, for the case with no tracer particles, the drops take longer to reach the maximum film length (t* = 1.02 vs. 1.21). After the drops reach the maximum film length, they move apart. The drops coalesce while they are rebounding at t* = 1.45 for the tracer particle case (Fig. 3.73e) and later at t* = 2.39 for the no tracer particle case (Fig. 3.74f), similar to *We* = 16 in Fig. 3.68. After coalescence, for both cases, the resulting drop oscillates to form a spherical drop and falls downward.

Generally, the initial drop evolutions for both cases are very similar. The time to reach the maximum film length is somewhat shorter for the case with tracer particles (t* = 1.02 vs t* = 1.21 for the case with no tracer particles). However, as discussed in Section 3.1.6, the time of maximum film length for like Weber number can vary from event to event. Hence, the difference in the time at the maximum film length for these cases may be uncertainty due to other parameters. However, the times to rupture for the two cases are obviously different. Therefore, the tracer particles in the film appear to cause earlier coalescence. The detailed view of flow fields when the drops reach the maximum film length and coalesce will be presented next to view the velocity and vorticity fields near the thin film region.

Figures 3.75-3.78 show the zoomed view of the rupture region. Figures 3.75 and 3.76 show vorticity and vertical velocity fields at the maximum film length. Figures 3.77 and 3.78 show the fields at the film rupture. The vectors show the velocity relative to falling drops. The two cases are very alike that the vorticity and vector fields are similar. But, there are some small differences.

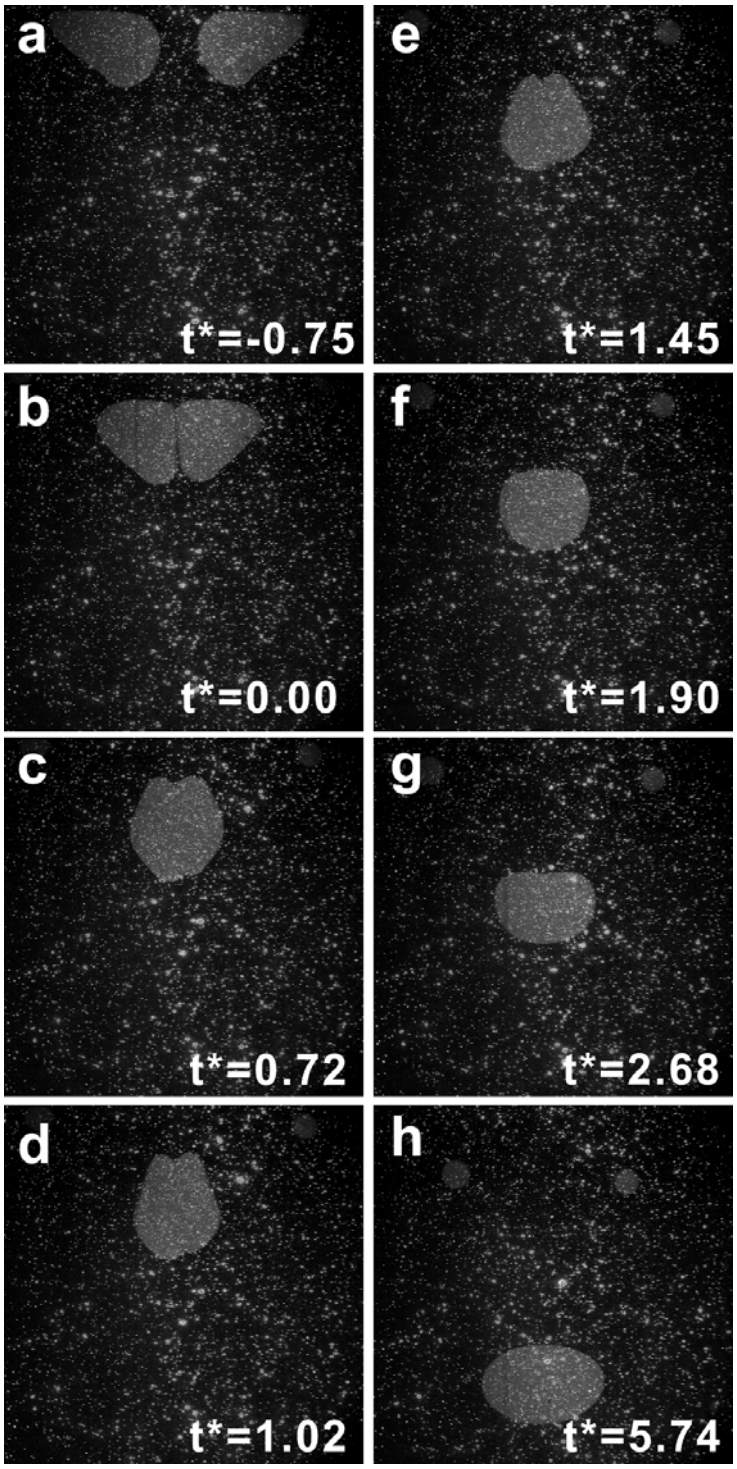


**Figure 3.73** The time evolution of drop collision: *We* = 21 (with tracer particles in the surrounding fluid), θ = 40° (coalescence). t* = t$U_{rel}$/D, where D is the drop diameter and $U_{rel}$ is relative velocity.

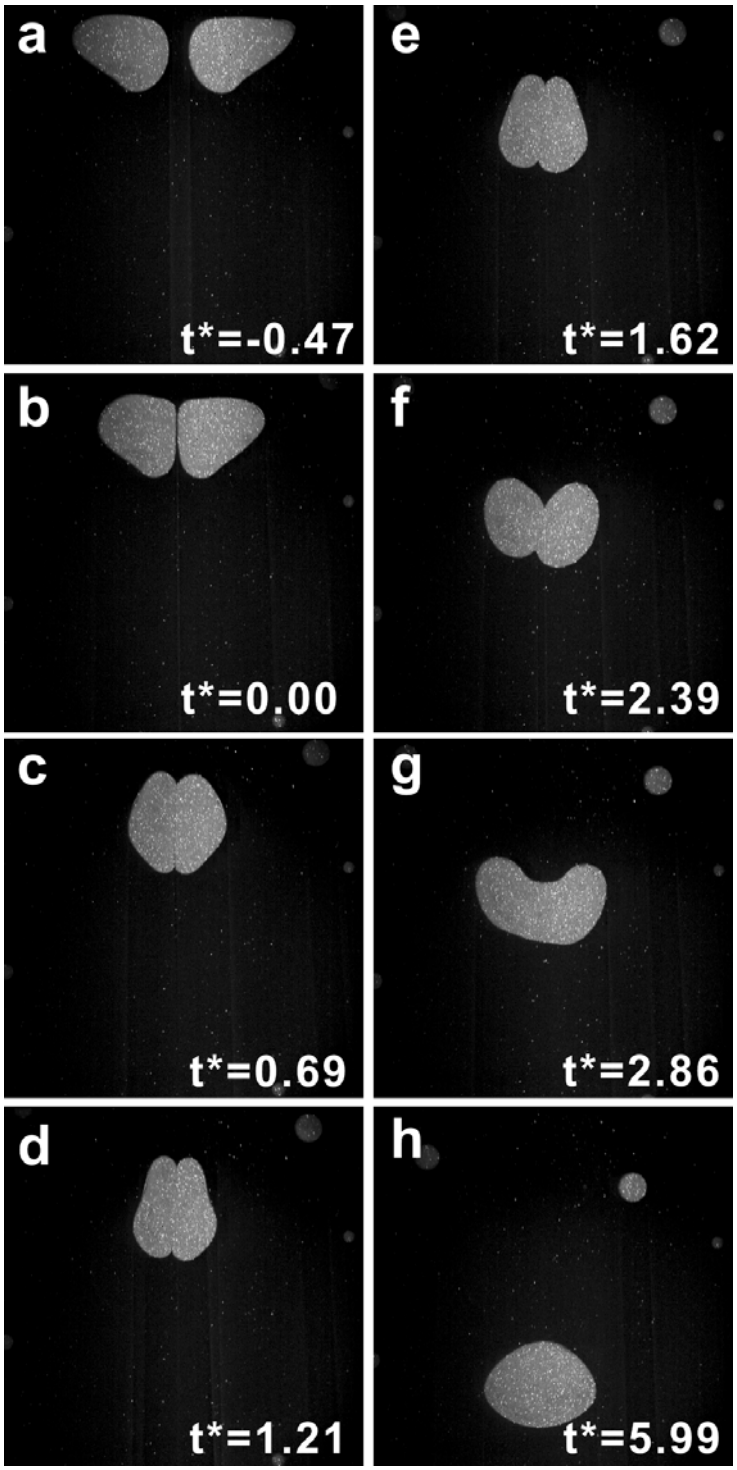


**Figure 3.74** The time evolution of drop collision: *We* = 21 (with no tracer particle in the surrounding fluid), θ = 40° (coalescence). t* = t$U_{rel}$/D, where D is the drop diameter and $U_{rel}$ is relative velocity.

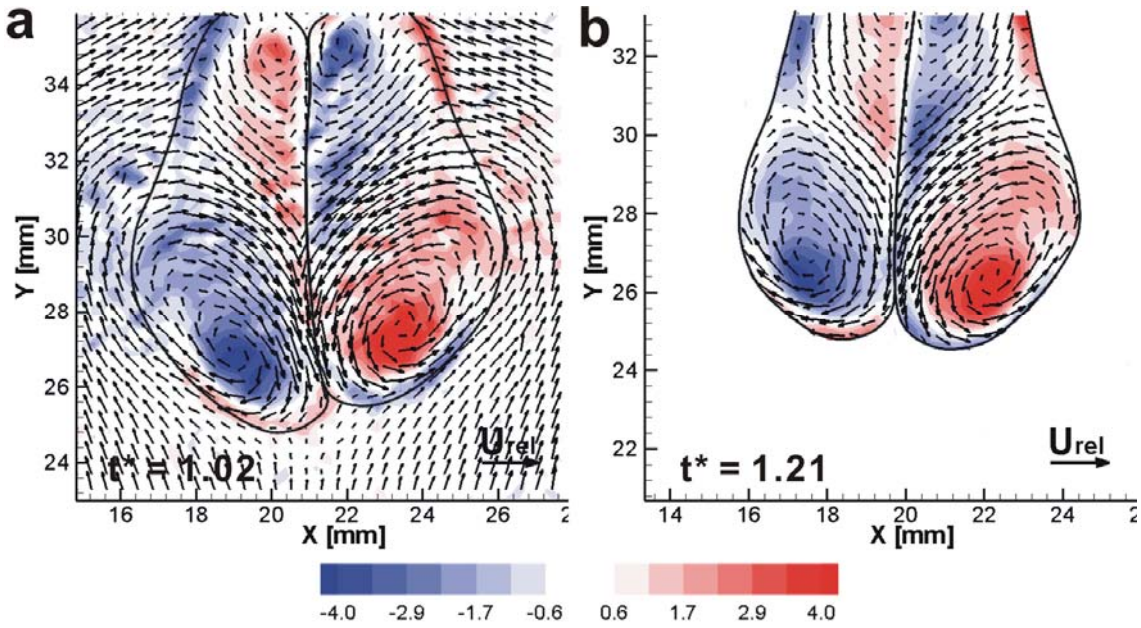


**Figure 3.75** The vector and vorticity fields at the maximum film length: (a) *We* = 21 (with tracer particles in surrounding fluid), θ = 40°, t* = 1.02, (b) *We* = 21 (with no tracer particle in surrounding fluid), θ = 40°, t* = 1.21. Vectors show in-plane velocity relative to the falling drops. Colors show normalized vorticity. Red is counterclockwise rotation and blue is clockwise rotation. The red dot shows the film rupture location.

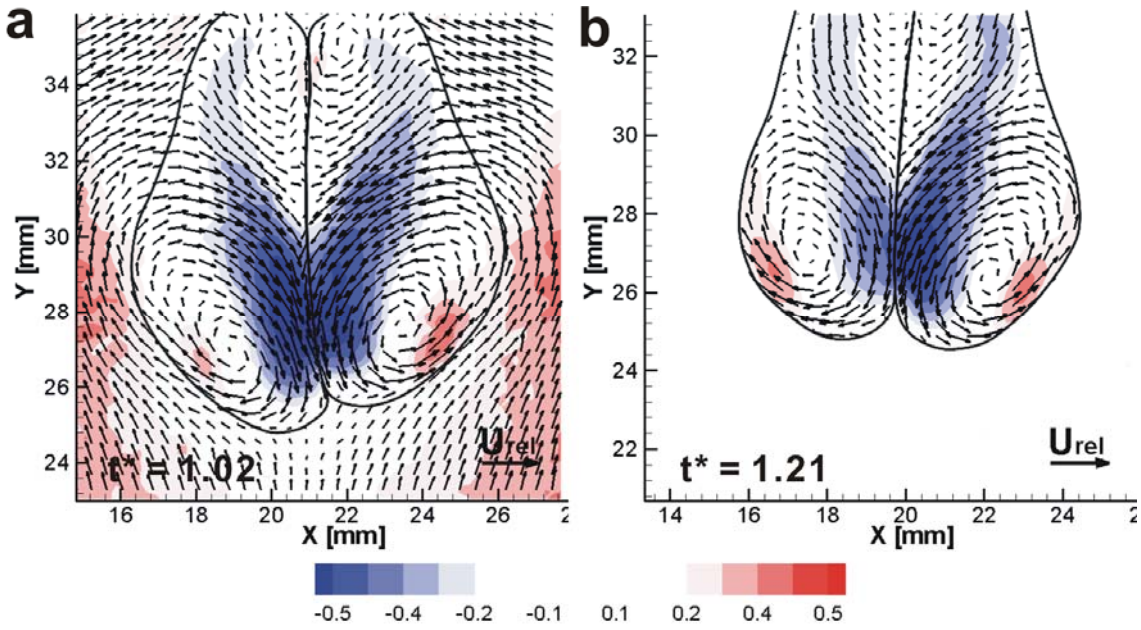


**Figure 3.76** The Vector and vertical velocity fields at the maximum film length: (a) *We* = 21 (with tracer particles in surrounding fluid), θ = 40°, t* = 1.02, (b) *We* = 21 (with no tracer particle in surrounding fluid), θ = 40°, t* = 1.21. Vectors show in-plane velocity relative to the falling drops. Colors show normalized vertical velocity relative to falling drops. Red is upflow, and blue is downflow. The red dot shows the film rupture location.

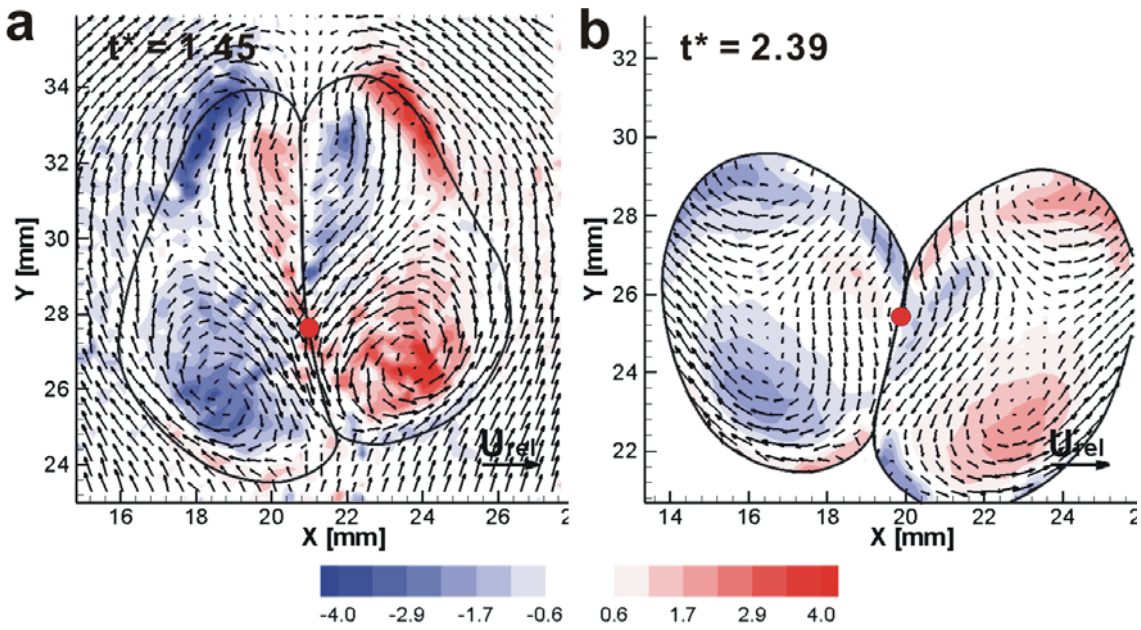


**Figure 3.77** The vector and vorticity fields at the time of rupture: (a) *We* = 21 (with tracer particles in surrounding fluid), θ = 40°, t* = 1.45, (b) *We* = 21 (with no tracer particle in surrounding fluid), θ = 40°, t* = 2.39. Vectors show in-plane velocity relative to the falling drops. Colors show normalized vorticity. Red is counterclockwise rotation and blue is clockwise rotation. The red dot shows the film rupture location.

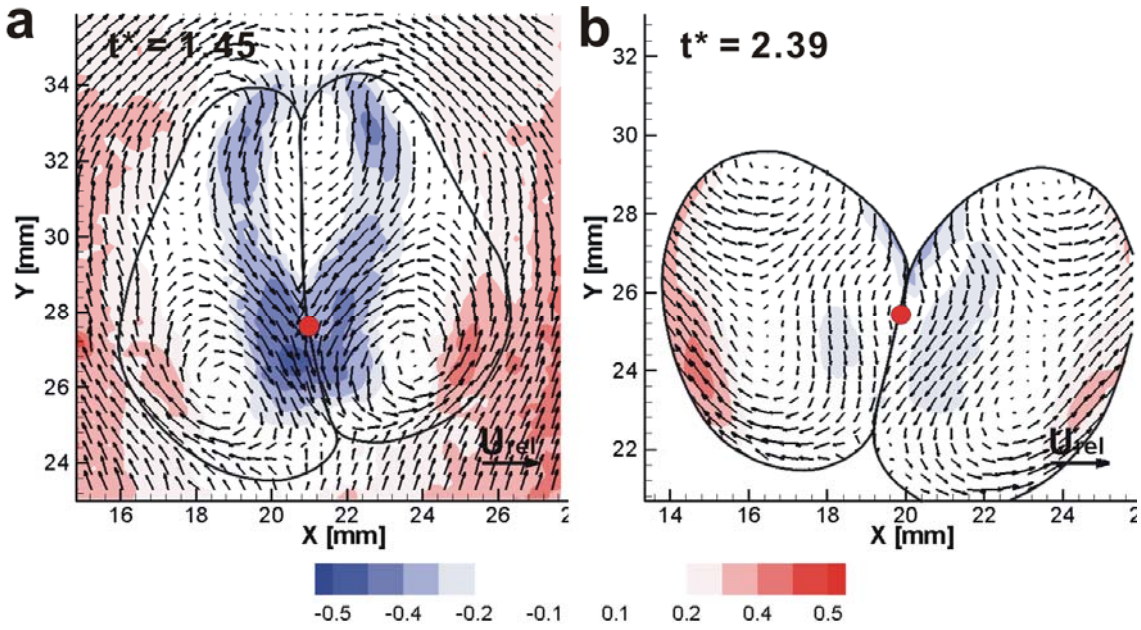


**Figure 3.78** The vector and vertical velocity fields at the time of rupture: (a) *We* = 21 (with tracer particles in surrounding fluid), θ = 40°, t* = 1.45, (b) *We* = 21 (with no tracer particle in surrounding fluid), θ = 40°, t* = 2.39. Vectors show in-plane velocity relative to the falling drops. Colors show normalized vertical velocity relative to falling drops. Red is upflow, and blue is downflow. The red dot shows the film rupture location.

The drop shapes and vortex ring orientation for both cases are similar in Fig. 3.75. The lower parts of the vortex ring for both cases are stronger than the upper parts. The vorticity magnitudes in the vortex ring pair are very similar: the maximum vortex strength of the lower part of the ring is $4.9U_{rel}$/D in Fig. 3.75a and $4.7U_{rel}$/D in Fig. 3.75b. The vector distribution for both cases are very similar such that the streaming flow through the vortex ring moves toward the centerplane and induces the downflow at this region. The dimples at the back of the drops are similar in shape for both cases, but the drops are slightly more elongated in the vertical direction in Fig. 3.75a. The velocity variation near the thin film is be examined in more detail in Fig. 3.76. In Fig. 3.76, the maximum relative downward velocity of ~$0.59U_{rel}$ occurs at the center plane between the vortices in Fig. 3.76a while the maximum downward velocity of approximately $0.57U_{rel}$ occurs slightly away from the interface in the streaming region inside of right drop vortex ring in Fig. 3.76b. At the centerplane, the downward velocity is $0.53U_{rel}$ in Fig. 3.76b. However, the vertical velocity contours for both cases are very similar. At this point, it is unclear whether the difference is due to the presence of the tracer particles. Instead, it is more reasonable to say that these differences maybe caused by variability in other parameters.

Figures 3.77 and 3.78 show the fields when the drops coalesce. Compared with Fig. 3.75 when the film length was maximal, the vortex strengths decrease at this time: the lower parts of vortex ring decrease from $4.9U_{rel}$/D to $4.0U_{rel}$/D for tracer particle cases (Fig. 3.77a) and from $4.7U_{rel}$/D to $2.2U_{rel}$/D (Fig. 3.77b) for cases in which there is no tracer particle. The vortex ring orientation for each drop is still located close to the interface for the tracer particle case. The lower parts of the vortex ring pair are distributed and tilted closer to the interface film than in the no tracer particle case, and induce downflow at the centerplane. For the case with no tracer particles in Fig. 3.77b, the upper parts of the vortex ring significantly decrease and the lower parts move away from the interface. The streaming flow between the rings points downward, but is weak. The circulation becomes strong at the upper part of outer edge of the drops as they move apart. The film ruptures at the lower portion of the centerplane in Fig. 3.77a. At this region, the local downflow is strong as shown in Fig. 3.78a; the maximum vertical

velocity is $0.49U_{rel}$. By contrast, the rupture location is higher in Fig. 3.77b above the center of the film. In this case, the maximum downflow ($0.26U_{rel}$) is away from the interface. In the coalescing case, the thin film ruptures in the lower portion where the local downflow is strong.

The drops with tracer particles in the silicone oil coalesce shortly after they reached the maximum film length at t* = 1.45. The drops with no tracer particles coalesce much later at t* = 2.39. Examination of additional collisions in the case with no tracer particles suggested that coalescence is often delayed. The film ruptures after the drops reach the maximum film length and are moving apart. Figure 3.77b shows one example which is obviously different from the case with tracer particles. For other cases with no tracer particles for $10 < We < 20$, the drops generally coalesce while they are moving apart. The film ruptures sometimes shortly after it reaches the maximum length or some time later similar to Fig. 3.77b. Although the coalescence time for the cases with no particles varies from event to event, it is generally later than in the cases with tracer particles. Some collisions for $10 < We < 20$ with no tracer particles result in rebounds. Above, $We > 20$, the drop evolution before coalescence and the coalescence time are very similar for both cases with and without tracer particles.

Mohamed-Kassim and Longmire (2004) reported that the tracer particles enhanced earlier coalescence by bridging the gap between the interfaces. Similar behavior is observed for this inertia driven drop coalescence. Therefore, it can be concluded that the existence of tracer particles in the intervening film between the colliding drops may reduce the coalescence time. However, the coalescence time varies from case to case.

Several works have previously studied the solid particles at the interface between drop pairs (Pickering 1954, Tambe and Sharma 1994 and 1995, Ashby et al. 2004, Stancik, et al 2004, Denkov et al 1992, Aveyard et al. 2003, and Horozov and Binks 2006). These studies were conducted to investigate interfacial film stabilization with densely packed solid particles in the liquid drop interfaces to prevent coalescence. The results of these studies were opposite to the result from the current study, which demonstrates that the presence of particles in the film delays rupture.

In general when drops collide, an intervening film is formed between them. In numerical analysis, the two drop interfaces are bridged by either multiple particle layers (Tambe and Sharma 1994 and 1995) or a single layer of particles (Denkov et al 1992, Ashby et al. 2004, Stancik, et al 2004, and Horozov and Binks 2006). When some particles in the ambient fluid are caught in the film between the drops, the pressure difference between the inside and outside of the drops creates capillary pressure. Due to the capillary pressure, the film around each particle deforms to form a dimple region around the particles (Denkov et al 1992). When this dimpled film reaches a critical minimal distance between the two opposing interfaces and the capillary pressure reaches a critical value, the film ruptures. If the particles in the film are densely packed, they resist displacement within the film and eventually the emulsion is stabilized. Aveyard et al. (2003) also report that different fluids affect the interfacial tension, the contact angle of the particles in the film, and the molecular interactions between the particles and the liquids. Previous studies show that as the diameter of particles decreases, the critical capillary pressure increases such that the film is more stable and does not rupture (Tambe and Sharma 1994, and Denkov et al 1992).

The results of the present study may depend on the specific fluid and particle material properties. These properties can affect parameters, such as the contact angle of the particle and intermolecular interaction. Although the particles in the film in the current study were not viewed completely, the images show that particle concentration in the ambient fluid is not dense enough to form a densely packed layer in the film. Therefore, the particles in the film do not contribute to stabilization of the drops, but rather enhance coalescence and may accelerate the film rupture when compared to coalescence without tracer particles.

# Chapter 4

# Conclusions and recommendations for future work

## 4.1 Summary and conclusion

A dual-field high-speed PIV measurement system was applied to investigate binary drop collisions in an ambient liquid so that drop trajectories and small-scale motion within drops could be studied simultaneously. In this way, the initial conditions for collision simulations as well as details of drop behavior in the impact zone could be provided. In this study, a number of collision cases were described and compared. All drops (water and glycerin mixture) were injected into silicone oil and were moving downward when they collided because of gravitational effects. After collision, the drops changed from prolate to oblate as they deformed. Drop trajectories and overall collision outcomes as well as detailed velocity fields at the collision interface were quantified.

### 4.1.1 Equal size drop collisions

For equal size drops, collisions over different Weber numbers were compared first to understand the characteristics of rebound and coalescence. For head-on collisions, the drops, in general, rebounded when $We < 10$, and coalesced when $We > 10$. This boundary shifted to higher *We* as the collision angle increased.

For *We* below 10, the drop collisions resulted in a rebound. The colliding drops did not deform significantly, and once they reached the maximum intervening film

length, they moved apart. For rebounding cases, there were two local maxima in the vertical velocity contours through the entire sequence. The maximum downward velocity occurred close to, but away from the interface.

Coalescence occurred for $We > 10$. The drops were initially elongated with tails due to the higher injection velocities when they approached each other. As *We* increased, dimples at the back of the drops were observed. The drops coalesced, when or shortly after, they reached the maximum film length. After coalescence, the resulting drop deformed vertically and eventually oscillated and fell downward. At the lower end of the interface, a strong local downflow region was formed.

As the downward drop collision angle was increased, the bottom section of each drop became wider than the top, and the vortex ring inside of each drop tilted more downward. The location of strongest downflow near the film interface moved upward as the angle was steepened, and the location of film rupture moved upward as well. Examination of additional collisions in which the collision angle was varied independently of *We* by tilting the injection tubes suggests that the rebound/coalescence of $We \sim 10$ boundary is insensitive to this angle over the range $20° < \theta < 40°$. Further, observation of multiple events lead to the conclusion that the film always ruptures close to the plane of symmetry, lending evidence that the rupture location is determined more by the macroscopic flow dynamics than by random instabilities.

The variations in kinetic and deformation energy during collisions showed that deformation energy first decreased as the drops approached and then increased after they collided and deformed. As *We* increased, the maximum deformation energy increased. The deformation energy was maximal when the film length was near maximum. The inertia of the drop affected the compression of the drops so that the deformation energy sharply increased as the horizontal kinetic energy distinctly decreased. The horizontal kinetic energy decreased as the drops collided, and continued to decrease until the drops reached the maximum film length and coalesced. When $We > 30$, the kinetic energy decreased as the drops collided and compressed each other. However, the thin film ruptured before the drops lost all of their horizontal kinetic energy. For $We > 30$, the drops coalesced before they changed from prolate to oblate in

shape, such that the tails of the drops remained when they coalesced and inertia continued to drive the fluid to the center, which was not observed for $We < 30$.

Coalescence time increased with the Weber number. When the two drops collided, they rebounded or coalesced when or shortly after the intervening film length was maximal. As *We* increased, the drops took a longer time to reach the maximum film length (longer t*). For higher *We* cases, coalescence was delayed as the drops continued to deform after they reached the maximum film length due to their higher initial velocity. For coalescing cases with $We < 30$, the times to reach the maximum film length and rupture increased as *We* increased. However, for $We > 30$, the drops took a shorter time to reach the maximum film length and coalescence occurred earlier than for $We < 30$. Therefore, the film drainage time was not the only parameter that determined the time of coalescence.

A detailed view of the thin film regions showed that two key factors are important in the coalescence mechanism. First, the vortex rings within colliding drops must be oriented such that they induce a streaming flow oriented toward the centerplane. Secondly, the drops must collide with sufficient inertia such that they deform significantly, increasing the velocity magnitude in the streaming flow. If the large velocities in the streaming flow approach the center plane, then they can induce a faster outflow in the thin film between the drops. The vortex interaction combined with strong drop deformation causes a strong relative downflow in the lower portion of the film so that the film ruptures in this region.

### 4.1.2 Unequal size drop collisions

In this study, the drop pair had an approximate size ratio ($D_s/D_L$) of either 0.71 or 0.48 for unequal size drop collisions. As shown in Fig. 3.44, two boundaries were found. At B = 0, when $We^* < 8$, the drops rebounded, and when $We^* > 11$, the drops coalesced. In between these two boundaries, the collisions could result in either rebound or coalescence. The boundary of coalescence for unequal size drops was similar to the one for equal size drops. In this study, the drop size ratio did not affect the critical $We^*$.

As the drop size ratio ($D_s/D_L$) decreased, the intervening film changed shape as the drops collided and deformed. The interface initially deformed inward toward the large drop and then the curvature decreased as the small drop changed from prolate to oblate, and the opposing pair of vortex rings lost its symmetry. The asymmetrical vortex ring orientations, associated with strong downflow near the upper portion of the film, along with the moving interface caused the film to rupture in this region. The film rupture location for unequal size drops varied, while the location for equal size drops was typically at the lower end of the interface.

As *We** increased, the curvature of the intervening film was deformed more inward toward the large drop as the drops deformed. As *We** decreased, the deformation of the film was weaker and it became flattened before coalescence. If the Weber number was low (for example *We** = 14), the concavely deformed interface reverted to a convex shape before coalescence. For *We** = 34, the interface decreased in curvature but remained concave when the film ruptured.

When $u_L/u_s > 1$, the interface deformed less after the initial collision, and the curvature of the interface decreased with time before coalescence. The interface was nearly flat through drop deformation sequence. After coalescence, when $u_L/u_s > 1$, an outward elongation of the small drop fluid was observed, and afterward, the small drop fluid retracted toward the resulting drop.

As B increased, the film rupture time was earlier than for head-on collision cases at the same *We**. Also, the mixing of the drops after coalescence was enhanced as B increased. Similar to previous head-on collisions (B = 0) for unequal size drops, the rupture location varied.

### 4.1.3 The effects of tracer particles in the thin film

In all of the experiments described above, 1 μm diameter tracer particles were used for PIV. Separate studies were conducted to determine whether the presence of tracer particles in the ambient fluid (and thin film between colliding drops) affected coalescence boundaries or dynamics. Collision cases with tracer particles of 1 μm and

10 μm diameters were compared with cases with no tracer particles in the surrounding fluid.

For the case with 10 μm particles, some rebounding cases with 10 μm particles were seen for $10 < We < 15$. This might be because of the smaller number of particles in the film. Compared to 1 μm particles, the concentration of 10 μm particles in the ambient fluid was much smaller so that the chance for the particles to be in the right location in the film was lower. However, the outcomes of using 1 μm and 10 μm diameter particles showed that the particle size difference did not significantly affect drop collisions or the minimum Weber number for coalescence in this study.

For cases without tracer particles, the drops always rebounded when $We < 8$ and coalesce when $We > 18$. Between these values, the collision could result in either a rebound or coalescence. When $8 < We < 18$, the lack of particles in the film might vary the outcomes such that some rebounds occurred above critical minimum Weber number for coalescence ($We = 10$) and coalescence occurred for $We < 10$. For cases with seeded ambient fluid, the rupture location was always in the lower portion of the thin film between the drops. The presence of the tracer particles in the intervening film did not affect the coalescence boundaries, but the rupture location was more variable.

The coalescence time for the cases without tracer particles varied from event to event similar to the cases with tracer particles, but the presence of tracer particles in the film induced earlier coalescence than the cases with no tracer particles at similar *We*.

## 4.2 Recommendations for future work

The study presented here resolves some characteristics of binary drop coalescence in liquids. This work is important for two reasons. First, it provides new understanding of when and how drops coalesce. Second, the results provide unique initialization and test data for numerical models. Improved understanding and accurate numerical codes will lead to more efficient processes in energy extraction, production of fuels, and cleanup of nuclear and chemical wastes. In addition, the ability to model coalescence can lead to new methods to control biochemical synthesis and new ideas for pollution reduction.

Future works will reveal more details on collision dynamics. For example, although the small zone of the rupture was studied in this work, the intervening film is microscopic when it actually ruptures, and the detailed flow and particle behaviors in the film were not resolved. In this study, using non-square interrogation zones to examine the specific variations along and normal to the interface enabled the velocity pattern close to the interface to be analyzed more thoroughly. However, better PIV resolution or novel flow visualization methods, such as tomographic PIV, might enable one to capture the film motion more accurately. Also, different PIV views, such as a horizontal view or an inclined view of the drop motion would shed more light on the rebound or coalescence process. Drop collisions in higher or lower viscosity fluids, or drop collisions with two different materials, such as water and oil drops with significant surface tension difference, would also be interesting as succeeding experiments.

# Bibliography


Aarts, D. G.A.L. and Lekkerkerker, H. N.W., 2008 Droplet coalescence: drainage, film rupture and neck growth in ultralow interfacial tension systems. *J. Fluid Mech.* **606**, 275-294

Abbott, C. E., 1977 A survey of waterdrop interaction experiments. *Rev. Geophys. Space Phys*. **15**, 363–374

Adam, J. R., Lindblad, N. R., and Hendricks, C. D., 1968 The collision, coalescence, and disruption of water droplets. *J. Appl. Phys.* **39**(11), 5173-5180

Ashby, N. P., Rinks, B. P., and Paunov, V. N., 2004 Bridging interaction between a water drop stabilized by solid particles and a planar oil/water interface. *Chem. Commun*. **4**, 436-437

Ashgriz, N. and Poo, J. Y., 1990 Coalescence and separation in binary collisions of liquid drops. *J. Fluid Mech.* **221**, 183-204

Aveyard, R., Binks, B. P., and Clint, J. H., Adv. 2003 Emulsions stabilized solely by colloidal particles. *Adv. Colloid Interf. Sci.* **100-102**, 503-546

Beard, K. V. and Ochs, H. T., 1983 Measured collection efficiencies for cloud drops. *J. Atmos. Sci.* **40**, 146

Borrell, M., Yoon, Y., and Leal, L. G., 2004 Experimental analysis of the coalescence process via head-on collisions in a time-dependent flow. *Phys. Fluids* **16**, 3945-3954

Bradley, S. G. and Stow, C., 1978 Collisions between liquid droplets. *Phil. Trans. R. Soc. London* **287**, 635–675

Brazier-Smith, P. R., Jennings, S. G., and Latham, J., 1972 The interaction of falling water drops: Coalescence. *Proc. Roy. Soc. London*, **326**, 393-408.

Brenn, G. and Frohn, A., 1989 Collision and merging of two equal droplets of propanol. *Exp. Fluids* **7**, 441–446

Brenn, G. and Kolobaric, V., 2006 Satellite droplet formation by unstable binary drop collisions. *Phys. Fluids* **18**(8), 087101

Brenn, G., Valkovska, D., and Danov, K. D., 2001 The formation satellite droplets by unstable binary drop collisions. *Phys. Fluids* **13**(9), 2463-2477

Charles, G. E. and Mason, S. G., 1960 The mechanism of partial coalescence of liquid drops at liquid/liquid interfaces. *J. Colloid Sci.* **15**, 105.

Chen, R-H. and Chen, C-T., 2006 Collision between immiscible drops with large surface tension difference: Diesel oil and water. *Exp. Fluids* **41**, 453-461

Chesters, A. K., 1991 The modelling of coalescence process in fluid–fluid dispersion: A review of current understanding. *Trans. Inst. Chem. Eng.* **69**, 259–270

Chesters, A. K. and Bazhlekov, I. B., 2000 Effect of Insoluble Surfactants on Drainage and Rupture of a Film between Drops Interacting under a Constant Force. *J. Colloid Interface Sci.* **230**, 229-243

Chevaillier, J-P., Klaseboer, E., Masbernat, O., and Gourdon, C., 2006 Effect of mass transfer on the film drainage between colliding drops. *J. Colloid Interface Sci.* **299**, 472-485

Cliff, R., Grace, J. R., and Weber, M. E. 1978 *Bubble, Drops, and Particles*. Academic Press, London

Dai, M. and Schmidt, D. P., 2005 Numerical simulation of head-on droplet collision: Effect of viscosity on maximum deformation. *Phys. Fluids* **17**, 041701

Denkov, N. D., Ivanov, I. B., Kralchevsky, P. A., and Wasan, D. T. 1992 A possible mechanism of stabilization of emulsions by solid particles. *J. Colloid Interf. Sci.* **150**, 589-593

de Sousa, F. S., Mangiavacchi, N., Nonato, L. G., Castelo, A., Tomé, M. F., Ferreira, V. G., Cuminato, J. A., and McKee, S., 2004 A front-tracking/front-capturing method for the simulation of 3D multi-fluid flows with free surfaces. *J. Comput. Phys.* **198**(2), 469-499

Eggers, J., Lister, J. R., and Stone, H. A., 1999 Coalescence of liquid drops. *J. Fluid Mech.* **401**, 293-310

Faeth, G. M., 1977 Current status of droplet and liquid combustion. *Prog. Energy Combust. Sci.* **3**, 191–224

Foote, G. B., 1975 The water drop rebound problem: Dynamics of collision. *J. Atomos. Sci.* **32**, 390-402

Fujimoto, H., Hata, N., and Takuda, H., 1997 Collision dynamics of two droplets. Proceedings of the ASME Fluid Engineering Division, FED-Vol. 244

Gerzina, K. 2005 Studies of Binary Liquid Droplet Collion. B.A.E.M. Honors Thesis, Department of Aerospace Engineering and Mechanics, University of Minnesota

Guido, S. and Simeone, M., 1998 Binary collision of drops in simple shear flow by computer-assisted video optical microscopy. *J. Fluid Mech.* **357**, 1-20

Gunn, R., 1965 Collision characteristics of freely falling water drops. *Science* **150**, 695-701

Ha, J. W., Yoon, Y., and Leal, L. G., 2003 The effect of compatibilizer on the coalescence of two drops in flow. *Phys. Fluids* **15**, 849-867

Hartland, S., 1967a The coalescence of a liquid drop at a liquid-liquid interface. Part II: Film thickness. *Trans. Instn. Chem. Engrs.* **45**, 102-108

Hartland, S., 1967b The coalescence of a liquid drop at a liquid-liquid interface. Part III: Film rupture. *Trans. Instn. Chem. Engrs.* **45**, 109-114

Horozov, T. S. and Binks, B. P., 2006 Particle-stabilized emulsions: a bilayer or a bridging monolayer? *Angew. Chem. Int. Ed. 45*, 773-776

Hu, Y. T., Pine, D. J. , and Leal, L. G., 2000 Drop deformation, breakup, and coalescence with compatibilizer. *Phys. Fluids* **12**, 484-489

James, A. J., and Lowengrub, J., 2004 A surfactant-conserving volume-of-fluid method for interfacial flows with insoluble surfactant. *J. Comput. Phys.* **201**(2), 685-722

Jiang, Y. J., Umemura, A., and Law, C. K., 1992 An experimental investigation on the collision beavior of hydrocarbon droplets. *J. Fluid Mech.* **234**, 171-190

Kapur, N. and Gaskell, P. H., 2007 Morphology and dynamics of droplet coalescence on a surface. *Phys. Rev. E* **75**, 056315

Klaseboer, E., Chevaillier, J. Ph., Gourdon, C., and Masbernat, O., 2000 Film drainage between colliding drops at constant approach velocity: Experiments and modeling. *J. Colloid Interface Sci* 229:274-285

Ko, G. H. and Ryou, H. S., 2005 Modelling of droplet collision-induced breakup process. *Int. J. Multiphase Flow* **31**, 723-738

Lekkerkerker, H. N. W., de Villeneuve1, V. W. A., de Folter1, a, J.W.J., Schmidt, M., Hennequin, Y., Bonn, D., Indekeu, J. O., and Aarts, D. G. A. L., 2008 Life at ultralow interfacial tension: wetting, waves and droplets in demixed colloid-polymer mixtures. *Eur. Phys. J. B* **64**, 341−347

Lide, D. R., 2008 *CRC Handbook of Chemistry and Physics - 89th Edition*. CRC press, Inc.

Low, T. B. and List, R., 1982 Collision, coalescence, and breakup of raindrops. Part I: Experimentally established coalescence efficiencies and fragment size distributions in breakup. *J. Atmos. Sci.*, **39**, 1591–1606

Mackay, G. D. M. and Mason, S. G., 1963 The gravity approach and coalescence of fluid droplets and liquid interfaces. *Can. J. Chem. Eng.* **41**, 203-212

Mashayek, F. and Ashgriz, N., 1995 A hybrid finite-element-volume-of-fluid method for simulating free surface flows and interfaces. *Int. J. Numer. Methods Fluids* **20**, 1363-1380

Mashayek, F. and Ashgriz, N., 1995 A spine-flux method for simulating free surface flows. *J. Comput. Phys.* **122**, 367-379

Mashayek, F., Ashgriz, N., Minkowycz, W. J., and Shotorban, B., 2003 Coalescence collision of liquid drops. *Int. J. Heat Mass Transfer* **46**, 77-89

Meleán, Y. and Sigalotti, L. Di. G., 2005 Coalescence of colliding van der Waals liquid drops. *Int. J. Heat Mass Transfer* **48**, 4041-4061

Mohamed-Kassim, Z. and Longmire, E. K., 2003 Drop impact on a liquid/liquid interface. *Phys. Fluids* **15**, 3263-3272

Mohamed-Kassim, Z. and Longmire, E. K., 2004 Drop coalescence through a liquid/liquid interface. *Phys. Fluids* **16**, 2170-2181

Nobari, M. R., Jan, Y-J., Tryggvason, G., 1996 Head-on collision of drops - a numerical investigation. *Phys. Fluids* **8** (1), 29-42

Nobari, M. R. and Tryggvason, G., 1996 Numerical simulations of three-dimensional drop collision. *AIAA J.* **34**, 750-755

Orme, M., 1997 Experiments on droplet collisions, bounce, coalescence and disruption. *Prog. Energy Combust. Sci.* **23**, 65–79

O'Rourke, P. J. and Bracco, F. V., 1980 Modelling of drop interactions in thick sprays and a comparison with experiments. *Stratified Charge Automotive Engines Conf.*, IMechE, London, 101–116

Pan, Y. and Suga, K., 2005 Numerical simulation of binary liquid droplet collision. *Phys. Fluids* **17**, 082105

Pickering, S. U., 1907 Emulsions. *J. Chem. Soc.* **91**, 2001-2021

Post, S. L. and Abraham, J., 2002 Modelling the outcome of drop-drop collisions in Diesel sprays. *Int. J. Multiphase Flow* **28**, 997-1019

Premnath, K. N. and Abraham, J., 2005 Simulations of binary drop collisions with a multiple-relaxation-time lattice-Boltzmann model. *Phys. Fluids* **17**, 122105

Qian, J. and Law, C. K., 1997 Regime of coalescence and separation in droplet collision. *J. Fluid Mech*. **331**, 59-80

Reynolds, O., 1886 On the theory of lubrication and its application to Mr. Beauchamp tower's experiments, including an experimental determination of the viscosity of olive oil. *Philos. Trans. R. Soc. London* **177**, Pt. 1

Rieber, M. and Frohn, A., 1995 Three-dimensional Navier-Stokes simulations of binary collision between droplets of equal size. *J. Aerosol Sci.* **26**, S929-S930

Roisman, I. V., 2004 Dynamics of inertia dominated binary drop collisions. *Phys. Fluids* **16**, 3438-3449

Sakakibara, B. and Ianmuro, T., 2008 Lattice Boltzmann simulation of collision dynamics of two unequal-size droplets. *Int. J. Heat Mass Transfer* **51**, 3207-3216

Salber, S., 2004 Drop Collision in a liquid-liquid flow with surface tension. M.S. thesis, Department of Aerospace Engineering and Mechanics, University of Minnesota

Schelkle, M. and Frohn, A., 1995 Three-dimensional lattice Boltzmann simulations of binary collision between equal droplets. *J Aerosol Sci.* **26**, S145-S146

Sethian, J. A., 1999 *Level Set Methods and Fast Marching Methods : Evolving Interfaces in Computational Geometry, Fluid Mechanics, Computer Vision, and Materials Science.* 2nd Edition. Cambridge University Press.

Stancik, E. J., koukhan, M., and Fuller, G. G., 2004 Coalescence of particle-laden fluid interfaces. *Langmuir*, **20**(1), 90-94

Tambe, D. E. and Sharma, M. M., 1994 The effect of colloidal particles on fluid-fluid interfacial properties and emulsion stability. *Adv. Colloid Interf. Sci*. **52**, 1-63

Tambe, D. E. and Sharma, M. M., 1995 Factors controlling the stability of colloid-stabilized emulsions – III. Measurement of the rheological properties of colloid-laden interfaces. *J. Colloid Interf. Sci*. **171**, 456-462

Tanguy, S. and Berlemont, A., 2005 Application of a level set method for simulation of droplet collision. *Int. J Multiphas Flow* **31**, 1015-1035

Thoroddsen, S. T., Qian, B., Etoh, T. G., and Takehara, K., 2007 The initial coalescence of miscible drops. *Phys. Fluids* **19**, 072110

Tryggvason, G., Bunner, B., Esmaeeli, A., Juric, D., Al-Rawahi, N., Tauber, W., Han, J., Nas, S., and Jan, Y.-J., 2001 A front-tracking method for the computations of multiphase flow. *J. Comput. Phys.* **169**(2), 708-716

Tobin, T., Muralidhar, R., Wright, H., and Ramkrishna, D., 1990 Determination of coalescence frequencies in liquid-liquid dispersions: Effect of drop size dependence. *Chem. Eng. Sci.* **45** (12), 3491-3504

Verdier, C. and Brizard, M., 2002 Understanding droplet coalescence and its use to estimate interfacial tension. *Rheol. Acta.*, *41*, 514-523

Whepdale, D. M. and List, R., 1971 The coalescence process in raindrop growth. *J. Geophys. Res.*, **76**, 2836-2856

Wieneke, B., 2005 Stereo-PIV using self-calibration on particle images. *Exp. Fluids* **39**, 267-280

Willis, K. and Orme, M., 2000 Experiments on the dynamics of droplet collisions in a vacuum. *Exp. Fluids* **29**, 347-358

Willis, K. and Orme, M., 2003 Binary droplets collision in a vacuum environment: An experimental investigation of the role of viscosity. *Exp. Fluids* **34**, 28-41

Yang, H., Park, C. C., Hu, Y. T., Leal, L. G., 2001 The coalescence of two equal-sized drops in a two-dimensional linear flow. *Phys. Fluids* **13**, 1087-1106

Yeo, L. Y., Matar, O. K., Susana Perez de Ortiz, E., Hewitt, G. F., 2003 Film drainage between two surfactant-coated drops colliding at constant approach velocity. *J. Colloid Interface Sci.* **257**, 93-107

Yiantsios, S. G. and Davis, R. H., 1991 Close approach and deformation of two viscous drops due to gravity and van der Waals forces. *J. Colloid Interface Sci.* **144** (2), 412-433

Yoon, Y., Borrell, M., Park, C. C., and Leal, L. G., 2005 Viscosity ratio effects on the coalescence of two equal-sized drops in a two-dimensional linear flow. *J. Fluid Mech.* **525**, 355-379

Yoon, Y., Hsu, A., and Leal, L. G., 2007 Experimental investigation of the effects of copolymer surfactants on flow-induced coalescence of drops. *Phys. Fluids* **19**, 023102

Zdravkov, A. N., Peters, G. W. M., and Meijer, H. E. H., 2006 Film drainage and interfacial instabilities in polymeric systems with diffuse interface. *J. Colloid Interface Sci*. **296**, 86-94